ATOMIC STRUCTURE AND NON-ELECTRONIC PROPERTIES OF SEMICONDUCTOR

Spatially inhomogeneous oxygen precipitation in silicon

S. V. Bulyarskiĭ, V. V. Svetukhin, and O. V. Prikhod'ko

Ul'yanovsk State University, 432700 Ul'yanovsk, Russia

A theoretical model for point-defect precipitation in crystals, which is a generalization of the well-know Ham model, has been proposed. The equations obtained are helpful in describing the kinetics of oxygen precipitation in silicon, and in determining the kinetics of variation of the mean geometrical dimensions of clusters. A theoretical model of spatially inhomogeneous precipitation has been developed. This model can be used to describe processes of internal gettering and creation of insulating layers in silicon. © *1999 American Institute of Physics.*
[S1063-7826(99)00111-8]

1. INTRODUCTION

Oxygen precipitation lies at the basis of such production processes as internal gettering[1,2] and the creation of insulating layers in a crystal.[3] Hartzell *et al.*[4] proposed a method of simulating the process of precipitation, based on solution of the Fokker–Planck equation for the cluster size distribution function. This method was subsequently developed further by Schrems *et al.*[5] and Senkander *et al.*[6] They used a combined simulating method based on solution of differential equations for the small clusters and the Fokker–Planck equation for the large clusters. In these equations the kinetic coefficients were determined[4–6] from the condition that growth of the precipitate is limited by the rate of monomer attachment to the cluster surfaces. In what follows, we show that the form of the kinetic coefficients chosen in these works is ill-advised. However, in Refs. 7–10, for example, it was shown that the growth of oxygen precipitates is described by Ham's theory, which uses a different model: growth of the precipitates is limited by monomer diffusion. At the same time, Ham's theory cannot be used to describe spatially inhomogeneous precipitation. We have been able to eliminate this drawback: the proposed model generalizes Ham's theory to the case of a spatially inhomogeneous precipitate and allows one to simulate important production processes.

2. THEORY OF DECAY OF SOLID SOLUTIONS

It is assumed that the growth kinetics of clusters of point defects is governed by their geometry and is essentially independent of their internal structure. In what follows we therefore do not draw a sharp boundary between clusters and precipitates.

Let us consider the growth kinetics of clusters taking place according to the following reversible scheme:

$$A_i C + A \underset{g(i)}{\overset{k(i)}{\rightleftarrows}} A_{i+1} C, \tag{1}$$

where $k(i)$ and $g(i)$ are the kinetic rates of capture and ejection of a monomer for a nucleation center that has picked up i particles.

This model corresponds to growth of precipitates at nucleation centers C with concentration N_C. We assume that the given concentration does not vary over the course of time and can be determined experimentally.

Taking into account the importance of the choice of the kinetic coefficients, let us consider this factor in more detail. The kinetic coefficients should include two steps of the process: diffusion and reaction. Since these steps occur sequentially, the kinetic coefficient has the form

$$k(i) = \frac{V}{\tau^{\text{dif}}(i) + \tau^{\text{reac}}(i)}, \tag{2}$$

where V is the unit volume, $\tau^{\text{dif}}(i)$ and $\tau^{\text{reac}}(i)$ are respectively the mean time that a particle takes to diffuse to a cluster and to attach to it.

The diffusion term can be found from the standard Smoluchowski relation[11]

$$\frac{V}{\tau^{\text{dif}}(i)} = 4\pi R(i) D, \tag{3}$$

where D is the monomer diffusion coefficient, and $R(i)$ is the radius of a cluster of i particles. In Ref. 12 it was shown that the dependence of the radius on the number of particles can be represented as

$$R(i) = b(i+m)^\alpha, \tag{4}$$

where b is a quantity on the order of the distance between the particles in the cluster. The quantity m is determined by the condition that the radius of the nucleation centers be equal to $R(0) = bm^\alpha$. The value of the parameter α is determined from simple geometric arguments (see Table I).

The time required by a particle to attach to a cluster is[13]

TABLE I. Dependence of the parameters α and β on cluster geometry.

Cluster geometry		α	β	$\dfrac{\alpha}{1-\alpha}$	$\dfrac{\beta}{1-\beta}$
Sphere		1/3	2/3	1/2	2
Fractal cluster of dimensionality D_F		$1/D_F$	$\dfrac{D_F+1}{2D_F}$	$\dfrac{1}{D_F-1}$	$\dfrac{D_F+1}{D_F-1}$
Disk, diameter D,	$d=$const	1/2	1	1	*
thickness d $(D \ll d)$	$d/D=$const	1/3	2/3	1/2	2
Cylinder, diameter d,	$d=$const	1	1	*	*
length L $(d \ll L)$	$d/L=$const	1/3	2/3	1/2	2
Growth of clusters in sinks of unbounded capacity		0	0	0	0

Note: *This case corresponds to a power law.

$$\frac{V}{\tau^{\mathrm{reac}}(i)} = \frac{S(i)D}{r_0}\exp\left\{-\frac{E(i)}{kT}\right\}, \tag{5}$$

where E_i is the activation energy of capture of a particle to a cluster of i particles, r_0 is the lattice period, and $S(i)$ is the surface area of the cluster,

$$S(i) = 4\pi b^2(i+m)^\beta. \tag{6}$$

Values of the parameter β for clusters of different geometries are listed in Table I.

Expressions (3) and (4) allow one to find the general form of the kinetic coefficient:

$$k(i) = \frac{4\pi DR(i)}{1+[4\pi R(i)r_0/S(i)]\exp\{E(i)/kT\}}$$
$$= \frac{4\pi Db(i+m)^\alpha}{1+(r_0/b)(i+m)^{\alpha-\beta}\exp\{E(i)/kT\}}. \tag{7}$$

If $E(i) < kT\ln[b(i+m)^{\beta-\alpha}/r_0]$, then the process of cluster growth is diffusion-limited:

$$k(i) = 4\pi DR(i) = 4\pi Db(i+m)^\alpha. \tag{8}$$

If the inequality sign is reversed, the time required to surmount the energy barrier determines the form of the kinetic coefficients:

$$k(i) = \frac{S(i)D}{r_0}\exp\left\{-\frac{E(i)}{kT}\right\}$$
$$= \frac{4\pi b^2(i+m)^\beta D}{r_0}\exp\left\{-\frac{E(i)}{kT}\right\}. \tag{9}$$

Kinetic coefficients in the form (9) were used in Refs. 4–6; however, those studies considered only spherical precipitates.

The Fokker–Planck equation is used to describe a process taking place in accordance with the equation (1) (Refs. 4 and 14)

$$\frac{\partial C(i,t)}{\partial t} = -\frac{\partial}{\partial i}[k(i)N(t)-g(i)]C(i,t)$$
$$+ \frac{\partial^2}{2\partial i^2}[k(i)N(t)+g(i)]C(i,t), \tag{10}$$

where $C(i,t)$ is the concentration of the nucleation centers that have picked up i particles. The principle of detailed balance yields a relation between the kinetic coefficients

$$g(i) = k(i-1)N_E C_E(i-1)/C_E(i) \approx k(i)N_E.$$

In addition, at any instant for a system described by scheme (1), the laws of conservation of nucleation centers and the total number of particles in the system are obeyed. These laws allow us to find the mean number of particles at the nucleation centers $\langle i \rangle$:

$$\langle i \rangle = \frac{\int_{i=0} iC(i,t)di}{\int_{i=0} C(i,t)di} = \frac{n(0)-N(t)}{N_C}. \tag{11}$$

2.1. Diffusion-limited precipitation

In this case, the kinetic coefficients are given by formula (8). For the mathematical expectation value $\langle i(t) \rangle$ it is possible to use the so-called macroscopic equation[14]

$$\frac{d\langle i \rangle}{dt} = k_D(N-N_E)[\langle i(t) \rangle + m]^\alpha, \tag{12}$$

where $k_D = 4\pi Db$.

Equations (11) and (12) are used to write a differential equation which describes the variation of the concentration during decay of a solid solution:

$$\frac{dN(t)}{dt} = -k_D N_C^{1-\alpha}[N(t)-N_E]\{N(0)+mN_C-N(t)\}^\alpha. \tag{13}$$

Equation (13) has the exact solution

$$t = C + {}_2F_1\left(\alpha,\alpha,1+\alpha,-\frac{N(0)+mN_C-N_E}{N_E-N}\right)$$
$$\times\left(\frac{N(0)-N+mN_C}{N_E-N}\right)^\alpha \frac{[N(0)-N+mN_C]^{-\alpha}}{k_D N_C^{1-\alpha}}, \tag{14}$$

$$C = -{}_2F_1\left(\alpha,\alpha,1+\alpha,-\frac{N(0)+mN_c-N_E}{N_E-N(0)}\right)$$
$$\times\left(\frac{mN_C}{N_E-N(0)}\right)^\alpha \frac{(mN_C)^{-\alpha}}{k_D N_C^{1-\alpha}}. \tag{15}$$

Here ${}_2F_1$ is the hypergeometric function.

For practical purposes it is more convenient to use approximations describing the initial and final stages of precipitation:

$$\frac{N(t)-N_E}{N(0)-N_E} = \exp\{-N_C\{(1-\alpha)[N(0)-N_E]^\alpha k_D t$$
$$+ (s)^{1-\alpha}\}^{\frac{1}{1-\alpha}} - s\}, \tag{16}$$

$$N(t)-N_E=A\exp\{-N_C^{1-\alpha}[N(0)+mN_C-N_E]^\alpha k_D t\},$$
$$\tag{17}$$

where $s=mN_C/[N(0)-N_E]=m/\langle i\rangle_E$, and the constant A is found from experiment. The quantity $\langle i\rangle_E$, according to Eq. (11), is the equilibrium value of the mean number of particles at the nucleation centers.

If we disregard the initial size of the precipitations ($m=0$), then the kinetics of the decrease in the monomer concentration in the first stage of the decay of the solid solution has the form

$$\frac{N(t)-N_E}{N(0)-N_E}=\exp\{-N_C\{(1-\alpha)[N(0)-N_E]^\alpha k_D t\}^{\frac{1}{1-\alpha}}\},$$
$$\tag{18}$$

where $\alpha\in[0,1)$. The formulas found by Ham on the basis of the diffusion equations[15–17] follow from Eq. (18).

For the case $\alpha=1$, Eq. (13) can be solved exactly:

$$\frac{N(t)-N_E}{N(0)-N_E}=\frac{C_1}{N(0)-N_E+(mN_C-N_E)\exp\{C_1 k_D t\}},$$
$$\tag{19}$$

where $C_1=N(0)+mN_C-2N_E$.

Comparison of Eqs. (11) and (18) allows us to delineate the trend in the variation of the mean number of particles in the clusters and their mean geometrical size in the initial stage of the decay of the solid solution:

$$\langle i\rangle\sim t^{\frac{1}{1-\alpha}},\quad \langle R\rangle\sim\langle i\rangle^\alpha\sim t^{\frac{\alpha}{1-\alpha}}.\tag{20}$$

2.2. Precipitation limited by the rate of the attachment reaction

The given problem simplifies substantially if we assume that the energy barrier to particle capture to a precipitate is independent of its size: $E_i=E_0=$ const.

The expression for the kinetic coefficient (9) then takes the form

$$k_i=4\pi D\exp\left\{-\frac{E_0}{kT}\right\}\frac{b^2}{r_0}(i+m)^\beta.\tag{21}$$

In this case, the results obtained in the preceding section can be used. It is sufficient in these formulas to replace α by β and k_D by $k_R=4\pi D\exp\{-E_0/kT\}(b^2/r_0)$.

The initial and final stages of precipitation can then be described by the formulas

$$\frac{N(t)-N_E}{N(0)-N_E}=\exp\{-N_C\{(1-\beta)[N(0)-N_E]^\beta k_R t\}^{\frac{1}{1-\beta}}\},$$

$$\langle R\rangle\sim t^{\frac{\beta}{1-\beta}};\tag{22}$$

$$N(t)-N_E=A\exp\{-N_C^{1-\beta}[N(0)+mN_C-N_E]^\beta k_R t\}.$$
$$\tag{23}$$

The power-law dependence of the variation of the size of the clusters makes it possible to diagnose the mechanism of their formation. The exponents for the reaction and diffusion mechanism for the formation of clusters of different geometries are given in Table I.
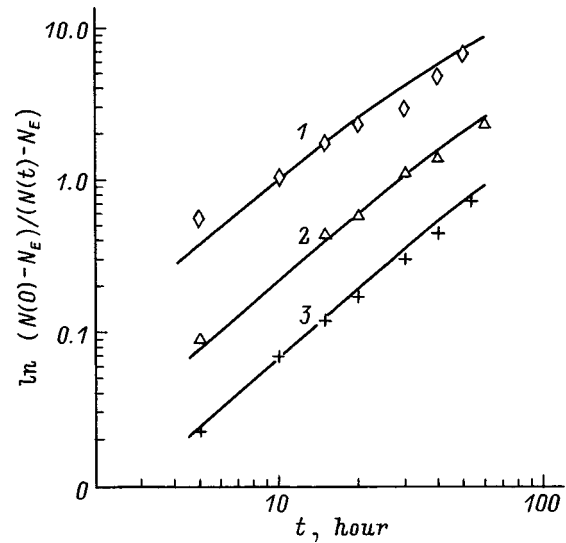

FIG. 1. Kinetics of variation of the interstitial oxygen concentration in silicon. Curves — numerical calculation based on Eq. (13). Annealing temperature, °C: *1* — 1100, *2* — 950, *3* — 850.

For the case of spherical clusters, this problem was considered by Turnbull.[18] His result can be obtained from relation (22) if one sets $\beta=2/3$. Note that the laws governing the decrease of the monomer concentration in the case of diffusion-limited precipitation and in the case of rate-limited precipitation are different.

3. THE KINETICS OF OXYGEN PRECIPITATION IN SILICON

In the preceding section we proposed a microscopic model for the decay of solid solutions. To test this theory, we carried out an experiment on the annealing of dislocation-free silicon in a nitrogen atmosphere. We used Czochralski-grown silicon wafers of *n*-type ($8\,\Omega\cdot$cm) with initial oxygen content 1.4×10^{18} cm^{-3}.

The concentration of interstitial oxygen in the silicon wafers was recorded by following the variation of the absorption at the maximum of the band near 9 μm at 300 K (Ref. 1). The kinetics of the decrease in the oxygen concentration for three annealing temperatures is plotted in Fig. 1.

The temperature dependence of the concentration of nucleation centers N_C was determined from microscopic observations. It was assumed that the concentration of nucleation centers is equal to the concentration of precipitation centers in the final stage of decay. Our result is in good agreement with the microscopic data:[1]

$$N_C=0.15\exp\{2.65/kT\},\text{ cm}^{-3}.\tag{24}$$

There are several different opinions about their nature. It is believed that nucleation centers can form both on lattice defects (the heterogeneous mechanism; Ref. 19) and by aggregation of several near-lying atoms of interstitial oxygen (homogeneous nucleus formation; Ref. 20).

Let us consider the homogeneous precipitation scheme, realized by successive aggregation of monomers. Taking into account that only clusters of size *m* (nucleation centers) are

stable, we can use the following approximation for the law of monomer conservation: $N(0) \approx N + mN_m$. Thus, the law of mass action is written as follows:

$$N_C \equiv N_m = \frac{[N(0) - mN_C]^m}{N_f^{m-1}} \exp\{-E_m/kT\}, \qquad (25)$$

where m is the number of oxygen atoms in the nucleus, $N(0)$ is the initial interstitial oxygen concentration, $N_f = 5 \times 10^{22}$ is the number of interstitials per unit volume of the silicon crystal, and E_m is the energy of formation of a complex of m particles.

Comparison of expressions (24) and (25) gives the value $m = 5$; i.e., in this model a nucleation center consists of five oxygen atoms.

We determined the equilibrium monomer concentration N_E from experimental kinetic curves at later times. Of the four parameters of Eq. (13), in reality it is necessary to choose only one parameter, k_D.

The found parameter values provide a good description of the experimental data on the decrease of the interstitial oxygen concentration during precipitation (Fig. 1).

Experimental data at different temperatures make it possible to find the temperature dependence of the given kinetic coefficient:

$$k_D = 3.08 \times 10^{-8} \exp\{-2.44/kT\}, \text{ cm}^3/\text{s}. \qquad (26)$$

The activation energy in expression (26) is equal to the activation energy of diffusion of interstitial oxygen in silicon.[21] If we adopt the model of Refs. 4–6, according to which growth of precipitates is limited by the surface attachment reaction, then the experimentally found activation energies of the temperature coefficient should be larger by the activation energy of attachment. Thus, the model adopted in Refs. 4–6 contradicts experiment.

Since the diffusion model is realized, it is possible to find the diffusion coefficient: $D = k_D/4\pi b$. The parameter $b = 2.5\,\text{Å}$ can be estimated from the density of the SiO_2 phase. The obtained value

$$D = 0.05 \exp\{-2.44/kT\}, \text{ cm}^2/\text{s} \qquad (27)$$

is in good agreement with the data of other authors.[21]

Solving Eq. (13) numerically together with Eq. (11), it is possible to calculate the mean radius at any time:

$$R(t) = \sqrt[3]{\frac{3b^3 \langle i(t) \rangle}{4\pi}}. \qquad (28)$$

The radius found with the help of Eqs. (11), (13), and (28) is compared in Fig. 2 with the data of Ref. 22. The experimental data on the time dependence of the mean radius of the precipitates at various temperatures, collected by Vanhellemont,[9] show that it increases in the initial stage of precipitation according to the law $R(t) \sim t^2$, consistent with Eq. (20) and also confirms the diffusion mechanism for the formation of oxygen precipitates.

4. SPATIALLY INHOMOGENEOUS PRECIPITATION

A very simple model which explains the effect of internal gettering is based on a solution of the one-dimensional
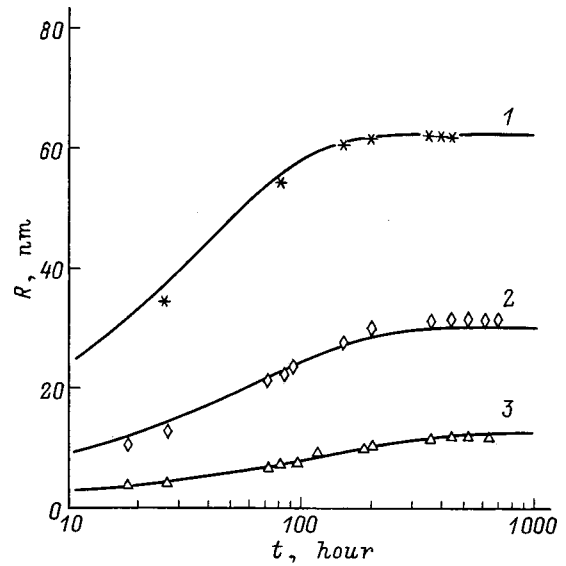

FIG. 2. Kinetics of variation of the mean radius of the precipitates. Lines — numerical calculation based on Eqs. (13) and (28), points — data of Ref. 22. Annealing temperature, °C: *1* — 900, *2* — 700, *3* — 600.

diffusion equation.[1] However, oxygen precipitation takes place simultaneously with diffusion since these two processes are indissolubly linked. Therefore, it is necessary to augment the diffusion equation by a term which accounts for the oxygen precipitation:

$$\begin{cases} \dfrac{\partial N(x,t)}{\partial t} = -k_0 N_C [N(x,t) - N_E]\{\langle i(x,t) \rangle + m\}^\alpha \\ \qquad\qquad + D(\partial^2 N(x,t)/\partial x^2), \\ \dfrac{\partial \langle i(x,t) \rangle}{\partial t} = k_0 [N(x,t) - N_E]\{\langle i(x,t) \rangle + m\}^\alpha. \end{cases} \qquad (29)$$

The initial conditions of the problem can be represented in the form

$$N(x,0) = \begin{cases} N(0), & x>0 \\ N_E, & x=0 \end{cases}, \quad \langle i(x,0) \rangle = \begin{cases} m, & x>0 \\ 0, & x=0. \end{cases} \qquad (30)$$

We assume that the nucleation centers are uniformly distributed throughout the wafer, and that their concentration is given by Eq. (25).

Solving system of equations (29) numerically, we calculate the distribution of oxygen with depth in the sample after annealing as a function of time t for any temperature.

The concentration profiles allow us to estimate the width of the defect-free zone (DFZ) which is obtained as a result of annealing. As a criterion of our estimate of the DFZ from the calculated concentration profiles, we chose a quantity proportional to the dispersion of the concentration profile:

$$\Delta = \left(\frac{2 \int x^2 [N_E - N(x,t)] dx}{\int [N_E - N(x,t)] dx} \right)^{1/2}. \qquad (31)$$

Results of this estimate are compared in Fig. 3 with experimental data taken from Ref. 1. Despite the large error in the experimental determination of the DFZ (this quantity is determined from the results of microscopic observations of a
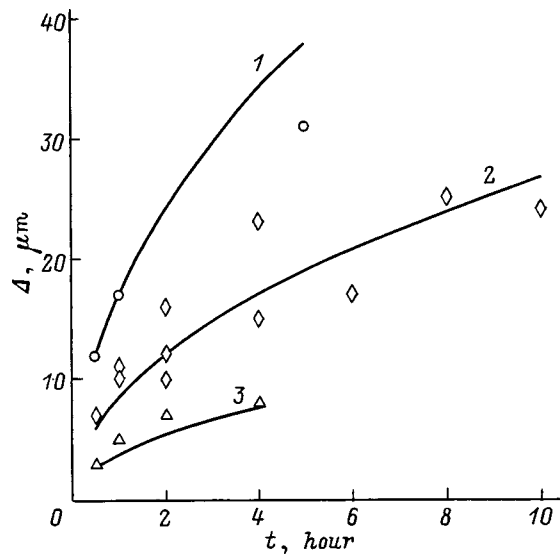
FIG. 3. Dependence of the width of the defect-free zone on temperature and annealing time. Curves — numerical calculation based on Eqs. (31), points — data of Ref. 1. Annealing temperature, °C: *1* — 1200, *2* — 1100, *3* — 1000.

FIG. 4. Oxygen depth profile in the wafer after annealing at $T = 900$ °C for 40 min. Curves — numerical calculation based on Eqs. (29), points — data of Ref. 23. Doses, cm^{-2}: *1* — 10^{15} *2* — 3×10^{13}.

cleavage face of the wafer after selective etching) and the uncertainty in the criterion (31), we find the agreement to be satisfactory.

The technology of ''silicon deposited on an insulator'' is now under active development. In this technology a layer of high-quality semiconductor (silicon) is formed on an insulating layer of silicon dioxide. A promising method of fabricating silicon-on-insulator structures for very-large-scale integrated circuits (VLSIC's) is oxygen implantation in the silicon skin layer with subsequent annealing. An insulating layer of the required thickness is formed during annealing for the right time at the right temperature.

The theory of oxygen precipitation proposed in this paper makes it possible to simulate such annealing with the help of a system of equations (30) and aids in the choice of the appropriate times and temperatures.

Figure 4 plots the total oxygen concentration (both interstitial and precipitated) as a function of depth for two different implantation doses after annealing. The points plot experimental data[23] and the solid lines plot the result of simulation using Eqs. (29). As the initial conditions, we assumed that the interstitial oxygen is distributed over the wafer according to a Gaussian law, and the concentration of nucleation centers is given by formula (25). It can be clearly seen that for a small oxygen dose, precipitation does not occur and the profiles have a purely diffusional form. As the dose is increased past a critical value, oxygen begins to combine into precipitates, which, as they increase in size, are converted into an insulating layer. One may choose the following criterion of coalescence of precipitates into an insulating layer: the mean radius of the precipitates should become larger than half the distance between precipitates:

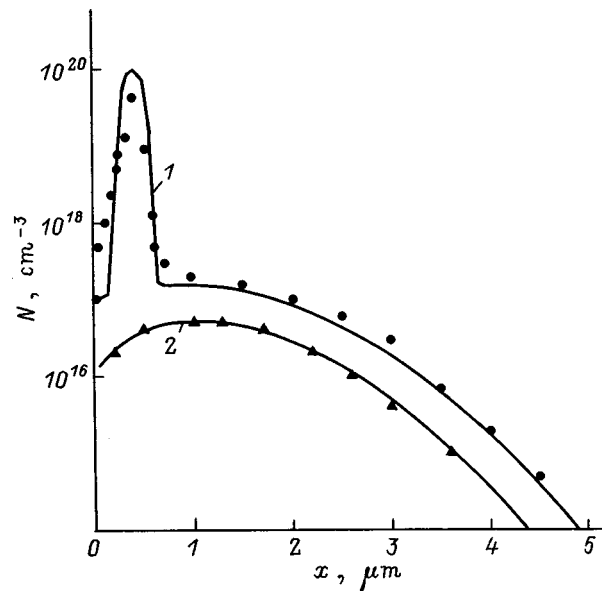$$b \frac{\sqrt[3]{3\langle i \rangle}}{4\pi} > \frac{N_C^{-1/3}}{2}.$$

5. CONCLUSION

The proposed kinetic model of decomposition of solid solutions not only affords a good description of the available experimental data on oxygen precipitation in silicon, but also allows one to simulate production processes connected with oxygen precipitation.

[1] A. Borghesi, B. Pivac, A. Sassella, and A. Stella, J. Appl. Phys. **77**, 4196 (1995).

[2] R. A. Craven, Mater. Res. Soc. Symp. Proc. **36**, 159 (1985).

[3] B.-Y. Tsaur, Mater. Res. Soc. Symp. Proc. **36**, 641 (1985).

[4] R. A. Hartzell, H. F. Schaake, and R. G. Massey, Mater. Res. Soc. Symp. Proc. **36**, 217 (1985).

[5] M. Schrems, M. Budil, G. Hobler, H. Potzl, and J. Hage, Proc. Simulation of Semicond. Dev. Proc. **4**, 113 (1991).

[6] S. Senkander, J. Esfandyari, and G. Hobler, J. Appl. Phys. **78**, 6469 (1995).

[7] M. J. Binns, W. P. Brown, J. G. Wilkes, R. C. Newman, F. M. Livingston, S. Messoloras, and R. J. Stewart, Appl. Phys. Lett. **42**, 525 (1983).

[8] P. M. Grinshteĭn, M. A. Il'in, and V. I. Fistul', Elektron. Tekh., Mater., No. 9, 70 (1978).

[9] J. Vanhellemont, J. Appl. Phys. **78**, 4295 (1995).

[10] S. V. Bulyarskiĭ, V. V. Svetuhin, and O. V. Prihod'ko, Izv. Vuzov. Elektron., No. 5, 24 (1997).

[11] M. V. Smoluchowski, Z. Phys. Chem. **92**, 192 (1917).

[12] S. V. Bulyarskiĭ, A. N. Georgobiani, and V. V. Svetuhin, Krat. Soobshch. Fiz., No. 5–6, 93 (1997).

[13] J. W. Christian, *The Theory of Transformation of Metals and Alloys* (Pergamon, Oxford, 1975).

[14] N. G. Van Kampen, *Stochastic Processes in Physics and Chemistry* (North-Holland, 1992).

[15] F. S. Ham, J. Phys. Chem. Solids **6**, 335 (1958).

[16] F. S. Ham, J. Appl. Phys. **30**, 1518 (1959).

[17] V. I. Fistul', *Decay of Supersaturated Semiconductor Solid Solutions* [in Russian], Metallurgiya, Moscow, 1977.

[18] D. Turnbull, Acta Metall. **1**, 764 (1953).

[19] T. Y. Tan and C. Y. Kung, J. Appl. Phys. **59**, 917 (1986).

Bulyarskiĭ *et al.*

[20] J. Vanhellemont and C. Claeys, J. Appl. Phys. **71**, 1073 (1992).

[21] W. Kaiser, H. L. Frisch, and H. Reiss, Phys. Rev. **112**, 1546 (1958).

[22] F. M. Livingstone, S. Messoloras, R. C. Newman, B. C. Pike, R. J. Stewart, and N. J. Binns, J. Phys. C **17**, 6253 (1984).

[23] Lee S. Tong and D. Nichols, in *Proceedings of Mater. Res. Soc. Symposium*, Vol. 59 (1986), p. 31.

Translated by Paul F. Schippnick

Enhanced formation of thermal donors in irradiated germanium: local vibrational mode spectroscopy

A. A. Klechko and V. V. Litvinov

Belarus State University, 220050 Minsk, Belarus

V. P. Markevich and L. I. Murin

Institute of Solid-State and Semiconductor Physics, Academy of Sciences, 220013 Minsk, Belarus

Oxygen-rich Ge samples were bombarded with fast electrons ($E = 4$ MeV) at 80 °C and subjected to isochronal (100–340 °C) and isothermal (350 °C) annealing. Infrared absorption spectra were measured at room temperature. Preliminary irradiation of the samples is found to strongly enhance the development of the absorption bands in the range 600 to 780 cm^{-1} when the Ge⟨Sb,O⟩ crystals are heated to 350 °C. The bands are assigned to local vibrational modes of thermal donors. It is inferred from the annealing studies that a radiation-induced complex with the local vibrational modes at about 770–780 cm^{-1} is probably responsible for the enhanced growth of the thermal donors. Oxygen dimers are proposed as such a complex. © *1999 American Institute of Physics.* [S1063-7826(99)00211-2]

Thermal donors (TD's), formed during heat treatment (300–500 °C) of oxygen-enriched crystals of silicon[1] and germanium,[2] are among the most well-studied defects in semiconductors. However, despite the extended history (more than 40 years) of such studies,[3,4] their structure and the mechanism of their formation remain unclear.

Most current models of thermal donors represent these centers as complexes consisting of an electrically active nucleus with a varying number of attached oxygen atoms. The successive formation of a series (up to 16 types in Si) of double donors with distinct energy levels near the conduction band[5,6] correlates well with the behavior of the group of local vibrational modes (LVM's) in the spectral ranges 975−1015 and 724−748 cm^{-1} in Si (Ref. 7), and at 786 and 600 cm^{-1} in Ge (Refs. 6 and 8). Two groups of vibration bands of thermal donors are linked with two different vibrational modes of oxygen atoms at the nucleus of a thermal donor.[7]

It is thought[3,4] that oxygen dimers play an important role in processes of thermal-donor formation. Recently, the existence of these complexes in Si has been proved experimentally, and their local vibrational modes have been identified.[9–11] It was also determined that irradiation of Si crystals at elevated temperatures (280–400 °C) enhances dimer formation and hence the generation of thermal donors.[11,12]

Oxygen dimers have not yet been identified in Ge, although the effect of enhanced formation of thermal donors was observed earlier after irradiation of crystals with ^{60}Co γ rays at room temperature.[13,14] The results reported in Refs. 13 and 14 were based on measurements of the Hall coefficient. These results do not give any information about the behavior of electrically inactive centers that participate in the formation of thermal donors. In view of this circumstance, it

would be useful to carry out a study of the influence of prior irradiation on the formation of thermal donors in Ge using the more informative method of spectroscopy of local vibrational modes. It should be noted that this method was first successfully applied in the 1960s in the study of processes of radiation defect formation in oxygen-containing germanium.[15,16] In irradiated Ge⟨O⟩ crystals a whole series of vibrational bands, attributable to oxygen-containing centers, was observed and their transformation during isochronous annealing was traced.[15,16] However, only one of these bands (620 cm^{-1}) was conditionally identified as a vibrational mode of a vacancy–oxygen complex (an A center). The nature of the remaining bands still remains unclear.

In this study we investigated crystals of Ge⟨Sb,O⟩ (resistivity $\rho = 4.3 \ \Omega \cdot$ cm) with a concentration of interstitial oxygen (O$_i$) 1.65×10^{17} cm^{-3}, which was introduced during growth of the crystals in an atmosphere of water vapor. As a comparison we used samples of Ge⟨Sb⟩ ($\rho = 10 \ \Omega \cdot$ cm) with low ($\leqslant 5 \times 10^{15}$ cm^{-3}) O$_i$ content. The O$_i$ concentration was determined from measurements of the absorption at the maximum of the 855 cm^{-1} band using as the calibration factor 1.25×10^{17} cm^{-2} (Ref. 17). Samples of 6 mm thickness were bombarded on both sides by 4-MeV electrons at a temperature ~ 80 °C. The total radiation dose was $2 \times 3 \times 10^{17}$ cm^{-2}. Isochronous (25 min with a 20 °C step in the temperature interval 100−340 °C) and isothermal (at 350 °C) anneals were performed in air. Infrared (IR) absorption spectra were recorded at room temperature on a Specord 75 IR spectrophotometer and on a Fourier spectrometer with a resolution of 1 cm^{-1}.

Bombardment of Ge⟨Sb,O⟩ crystals with fast electrons led to a drop in the interstitial oxygen concentration by 4 $\times 10^{16}$ cm^{-3} and the appearance of a series of radiation-defect bands. The most intense of these bands were observed
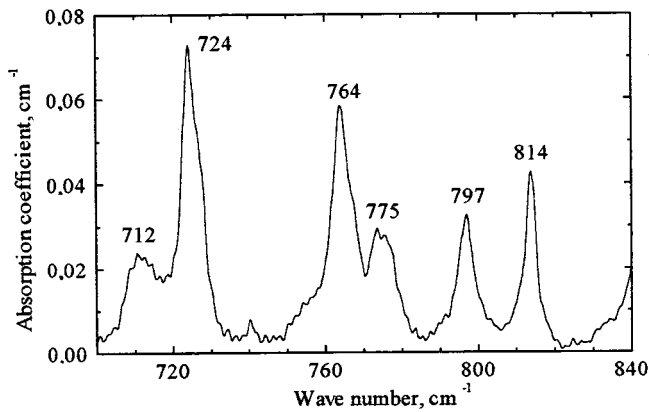
FIG. 1. Infrared absorption spectra of Ge⟨Sb,O⟩ after electron bombardment with a flux of 3×10^{17} cm^{-2}.

in the spectral region $700-820$ cm^{-1} (Fig. 1). None of the bands shown in Fig. 1 was observed in the spectra of irradiated Ge⟨Sb⟩ crystals with low oxygen content. This allows us to link these bands with the vibrational modes of oxygen-containing defects. Note that in the spectrum of the irradiated Ge⟨Sb,O⟩ crystals the band at 620 cm^{-1}, i.e., the band of the A centers ($V-O$), was absent. It is known that these centers possess relatively low thermal stability in Ge ($\leqslant 100$ °C; Ref. 16). Therefore, already during irradiation of crystals annealing of the A centers could have taken place, i.e., they could have dissociated and/or transformed into $V-O_2$ and O_{2i} complexes, as is the case in Si at elevated irradiation temperatures.[12] These complexes are apparently responsible for some of the observed bands (see Fig. 1). It is also highly likely that the interaction of intrinsic interstitial atoms with oxygen in Ge also leads to the formation of optically active complexes which are stable at temperatures $T > 100$ °C, which is the reason for the variety of observed bands.

In irradiated Ge⟨Sb,O⟩ samples subjected to isochronal anneals no noticeable changes in the IR absorption spectrum were observed up to temperatures of $240-260$ °C. At the stage $260-340$ °C the bands at 712, 724, 764, 797, and 814 cm^{-1} disappeared with simultaneous increase of the total absorption in the range $770-780$ cm^{-1} and the appearance of new low-intensity bands at 767 and 790 cm^{-1}. Subsequent isothermal annealing at 350 °C led to the formation of two wide bands with maxima at 777 and 600 cm^{-1} (Fig. 2, curve *1*). Their formation correlates well with the lowering of the resistivity of the samples, i.e., with the generation of thermal donors. Such bands also show up during heat treatment of unirradiated crystals of Ge⟨Sb,O⟩ (Fig. 2, curve *2*). These results, taken together with the earlier data,[6–8] allow one to unambiguously link the given bands with the two vibrational modes of the thermal donors in Ge.

From the spectra shown in Fig. 2 it can be seen that the total intensity of the thermal-donor absorption bands in the pre-irradiated crystals greatly exceeds the total intensity for the unirradiated crystals that were subjected to the same heat treatment (350 °C, 15 h). It is noteworthy that the maximum of both thermal-donor bands in the pre-irradiated samples are shifted by $7-8$ cm^{-1} into the high-energy region relative to the maxima of the thermal-donor bands for the unirradiated
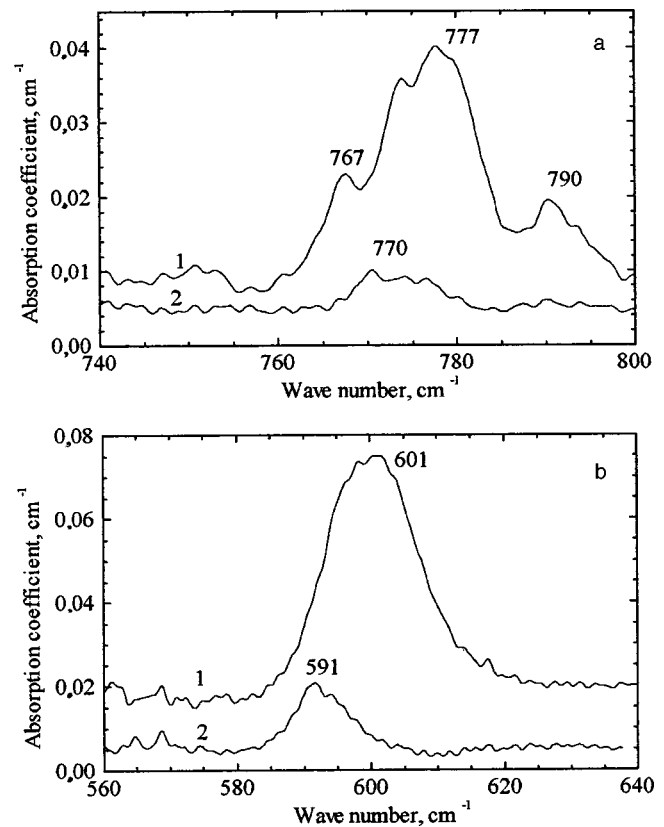

FIG. 2. Infrared absorption spectra in the regions of the high-energy (a) and low-energy (b) thermal-donor modes in pre-irradiated (*1*) and unirradiated (*2*) samples of Ge⟨Sb,O⟩ after heat treatment at 350 °C for 15 h.

crystals. To achieve the same intensity and obtain the same spectral position of the thermal-donor bands in the unirradiated crystals requires more extended (>50 h) annealing at 350 °C. The shift of the maxima of the thermal-donor bands with increase of the duration of heat treatment at 350 °C was observed earlier[18] and correlates with the subsequent formation in prevailing concentrations of thermal-donors of a higher order. Consequently, the difference in the intensities and positions of the maxima of the thermal-donor bands for the unirradiated and irradiated crystals indicates that prior irradiation of Ge⟨Sb,O⟩ not only leads to an increase in the total rate of thermal-donor generation but also substantially enhances the entire process of their subsequent formation (transformation).

In summary, the results of spectroscopic studies confirm the electrical measurement data[13,14] on the enhanced formation of thermal donors in pre-irradiated Ge crystals. This enhancement is most likely due to the formation during irradiation and subsequent annealing of complexes with local vibrational modes in the range $770-780$ cm^{-1}. In the irradiated crystals these centers precede the thermal donors and, according to Ref. 16, contain two oxygen atoms. In addition, the position of the local vibrational modes of these centers nearly coincide with the position of the high-energy mode of the thermal donors; i.e., these centers may be a structural unit that forms a thermal donor. All these factors, taken together, allow us to assume that these centers are oxygen dimers.

[1] C. S. Fuller, N. B. Ditzenberger, N. B. Hannay, and E. Buhler, Phys. Rev. **96**, 833 (1954).

[2] J. Bloem, C. Haas, and P. J. Penning, J. Phys. Chem. Solids **12**, 22 (1959).

[3] *Proceedings of the NATO Advanced Workshop on the Early Stages of Oxygen Precipitation in Silicon* (Exeter, U. K., 1996), edited by R. Jones, NATO ASI Series, 3. High Technology (Kluver Academic Publishers, Dordrecht, 1996), Vol. 17.

[4] *Oxygen in Silicon*, edited by F. Shimura, Semiconductors and Semimetals (Academic, London, 1994), Vol. 42.

[5] W. Gotz, G. Pensl, and W. Zulrhner, Phys. Rev. B **46**, 4312 (1992).

[6] P. Clauws, Mater. Sci. Eng., B **36**, 213 (1996).

[7] T. Hallberg and J. L. Lindstrom, J. Appl. Phys. **79**, 7570 (1996).

[8] W. Kaiser, J. Phys. Chem. Solids **23**, 255 (1962).

[9] L. I. Murin and V. P. Markevich, in *Proceedings of the NATO Advanced Workshop on the Early Stages of Oxygen Precipitation in Silicon* (Exeter, U.K., 1996), edited by R. Jones (Kluver Academic Publishers, Dordrecht, 1996), p. 103.

[10] L. I. Murin, T. Hallberg, V. P. Markevich, and J. L. Lindstrom, Phys. Rev. Lett. **80**, 93 (1998).

[11] L. I. Murin and V. P. Markevich, in *Proceedings of the Seventh International Conference on Shallow-Level Centers in Semiconductors*, edited by C. A. J. Ammerlaan and B. Pajot (World Scientific, Singapore, 1997), p. 339.

[12] J. L. Lindstrom, T. Hallberg, D. Aberg, B. G. Svensson, L. I. Murin, and V. P. Markevich, Mater. Sci. Forum **258–263**, Pt. 1 (1997).

[13] V. V. Litvinov and V. I. Urenev, Fiz. Tekh. Poluprovodn. **18**, 716 (1984) [Sov. Phys. Semicond. **18**, 445 (1984).

[14] V. V. Litvinov, G. V. Pal'chik, and V. I. Urenev, Phys. Status Solidi A **115**, K9 (1989).

[15] R. E. Whan, Phys. Rev. **140**, A 690 (1965).

[16] R. E. Whan, Appl. Phys. Lett. **6**, 221 (1965).

[17] E. I. Millet, L. S. Wood, and G. Bew, Br. J. Appl. Phys. **16**, 159 (1965).

[18] V. V. Litvinov, V. A. Bykovski, and N. I. Dolgikh, in *Proceedings of the 23rd International Conference on the Physics of Semiconductors* (Berlin, July 1996), edited by M. Scheffler and R. Zimmermann (World Scientific, Singapore), Vol. 4, p. 2609.

Translated by Paul F. Schippnick

ELECTRONIC AND OPTICAL PROPERTIES OF SEMICONDUCTORS

Radiation defects in semiconductors under hydrostatic pressure

V.N. Brudnyĭ*)

V. D. Kuznetsov Siberian Physicotechnical Institute, 630050 Tomsk, Russia
(Submitted July 6, 1998; accepted for publication March 30, 1999)
Fiz. Tekh. Poluprovodn. **33**, 1290–1294 (November 1999)

The effect of hydrostatic pressure on the sensitivity of the electrical properties of irradiated semiconductors as functions of the position of the Fermi level in the band gap of the crystal has been investigated. A numerical analysis of the experimental data has been performed. This analysis is based on a model of the crystal as having an isotropic band gap $\langle E_G \rangle$, where $\langle E_G \rangle$ is the average energy interval between the conduction band and the valence band. It is shown that varying the pressure results in hardly any change in the position of the radiation defect levels relative to the energy corresponding to the center of the isotropic gap $\langle E_G \rangle/2$, which is identical to the value of the ''limiting'' position of the Fermi level ($F_{\lim}$) in an irradiated semiconductor. © *1999 American Institute of Physics.* [S1063-7826(99)00311-7]

INTRODUCTION

It is known that native lattice defects or chemical impurities with deep levels as a rule enhance the sensitivity of semiconductors to hydrostatic pressure. This result is attributable to the peculiarities of the formation of ''deep'' states in semiconductors. The present paper reports the results of an investigation of the influence of hydrostatic pressure on the electrical properties and energy position of the levels of radiation defects (RD) in semiconductors subjected to high-energy radiation. A definite body of experimental data has accumulated in recent years on this subject, which requires systematization and interpretation. This paper generalizes not only the results of our research group,[1–5] but also the data of other authors. The analysis of the results presented is based on experimental and calculated data on pinning of the Fermi level (F) in its limiting position ($F_{\lim}$) in semiconductors irradiated by electrons, protons, and fast neutrons.[6] This should make it possible, by varying the initial doping level, type of conductivity, and radiation dose, to study the sensitivity of the characteristics of the irradiated semiconductor to subsequent application of hydrostatic pressure P as functions of the position of the Fermi level F over the entire band gap of the crystal.

EXPERIMENTAL TECHNIQUE

GaAs, InP, GaSb, and GaP, irradiated at $T \simeq 300 \, \text{K}$ by electrons (with energies $E \simeq 2 \, \text{MeV}$) and H^+ ions (with energy $E = 5 \, \text{MeV}$) were investigated experimentally (see Table I). We estimated the pressure coefficient of the resistivity (ρ), defined as

$$\alpha_\rho = \partial(\ln \rho)/\partial P,$$

which, taking into account the bipolar (electron and hole) conductivities $\sigma_n(D)$ and $\sigma_p(D)$ (D is the radiation dose)

and the contribution of the hopping conductivity of the carriers via local states of the radiation defects, $\sigma_{\text{RD}}(D)$, to the total conductivity of the crystal

$$\rho(D)^{-1} = \sigma_n(D) + \sigma_p(D) + \sigma_{\text{RD}}(D),$$

can be written in the form

$$\alpha_\rho(D) = \frac{\alpha_n(D)}{(1 + p/nb)} + \frac{\alpha_p(D)}{(1 + nb/p)}$$
$$+ \frac{\alpha_{\text{RD}}(D)}{(1 + \sigma_n/\sigma_{\text{RD}} + \sigma_p/\sigma_{\text{RD}})}, \quad (1)$$

where $\alpha_n = -\partial(\ln \sigma_n)/\partial P$, $\alpha_p = -\partial(\ln \sigma_p)/\partial P$, $\sigma_{\text{RD}} = -\partial(\ln \sigma_{\text{RD}})/\partial P$, and $n(p)$ is the concentration of free electrons (holes), $b = \mu_n/\mu_p$ is the ratio of the electron and hole mobilities. In a material with n-type conductivity $n \gg p$, $\sigma_n \gg \sigma_p$, and $\alpha_\rho \simeq \alpha_n$; analogously for crystals with p-type conductivity $\alpha_\rho \simeq \alpha_p$. The third term in expression (1) is important only in heavily irradiated samples, e.g., for electron fluxes ($E = 2 \, \text{MeV}$) greater than $10^{18} \, \text{cm}^{-2}$ for GaAs, for which $\rho(D)^{-1} \simeq \sigma_{\text{RD}}(D)$ (Fig. 1). In the present work we restrict the discussion to the case $\sigma_n(D)$, $\sigma_p(D) > \sigma_{\text{RD}}(D)$; therefore, the third term in expression (1) is ignored.

For α_n we can write $\alpha_n = (\gamma_n/kT) - \partial(\ln N_c)/\partial P - \partial(\ln \mu_n)/\partial P$, where $\gamma_n = \partial(E_c - F)/\partial P$ is the coefficient of isothermal variation of the position of the Fermi level with pressure (the pressure coefficient), and N_c is the effective density of states referenced to the bottom of the conduction band. In the expression for α_n the second and third terms are quantities of second order of smallness in comparison with the quantities γ_n/kT ($\sim 10^{-4} \, \text{bar}^{-1}$) in the irradiated samples. For high-resistance samples the contribution of the term $\partial(\ln \mu_n)/\partial P$ to α_n can reach $5 - 7\%$, which amounts up to 10% of the contribution to the total variation of the conductivity under hydrostatic pressure. Irradiation has almost

TABLE I. Experimental values of $F_{\lim}$ in irradiated semiconductors, the Schottky barrier heights (F_{bS}), calculated values of the minimum band gap E_g, the mean isotropic energy gap $\langle E_G \rangle$, the insulating gap of the crystal E_P, and $\langle E_G \rangle/2$ in eV, and calculated values of the pressure coefficients of the minimum band gap of the semiconductor $\gamma(E_g)$, the isotropic energy gap $\gamma(\langle E_G \rangle)$ and $\gamma(\langle E \rangle/2)$ in units of 10^{-6} eV/bar. The values of $F_{\lim}$, F_{bS}, $\langle E_G \rangle/2$, and $\gamma(\langle E_G \rangle/2)$ are referenced to the top of the valence band (the level Γ_{8v}).

Semiconductor	E_g	$F_{\lim}$	F_{bS}	$\langle E_G \rangle/2$	$\langle E_G \rangle$	E_P	$\gamma(\langle E_g \rangle)$	$\gamma(\langle E_G \rangle)$	$\gamma(\langle E_G \rangle/2)$
C	5.45	⋯	1.71	2.32	10.47	12.9	0.5	4.90	1.37
Si	1.20	0.39	0.32–0.4	0.37	4.98	4.8	−2.2	4.21	0.50
Ge	0.78	0.13	0.07–0.18	0.06	4.56	4.3	4.2	5.18	−0.17
AlP	2.48	⋯	⋯	1.31	6.05	5.7	−2.4	3.13	0.46
AlAs	2.24	⋯	0.96	1.07	5.11	5.1	−2.4	4.02	0.36
AlSb	1.60	0.5	0.55	0.45	5.15	4.5	−4.0	5.40	−0.19
GaP	2.37	1±0.2	0.94–1.17	1.03	5.57	5.8	−2.6	5.52	−0.06
GaAs	1.51	0.6	0.52–0.62	0.70	5.25	5.2	9.5	4.94	−0.56
GaSb	0.87	0.02	0.07–0.1	0.00	4.58	4.1	14.9	6.68	−0.79
InP	1.42	1.0	0.76–0.98	0.90	5.25	5.2	7.7	4.41	−0.38
InAs	0.39	0.51	0.47	0.50	4.79	4.6	11.5	5.91	−0.74
InSb	0.14	0.0	~0.0	0.05	4.30	3.7	12.5	6.95	−1.02
CdTe	1.48	⋯	0.9–1.1	1.56	4.76	5.8	6.5	5.12	−2.65
ZnTe	2.33	⋯	⋯	1.72	5.37	5.5	10.3	5.25	−3.04
HgTe	0.23	⋯	⋯	0.76	3.86	5.0	5.8	7.41	−4.28

Note: The values of E_g demonstrate the accuracy of the calculations of the energy gaps in the band spectrum of the crystal, and the values of $\gamma(E_g)$ demonstrate the accuracy of the estimates of the pressure coefficients $\gamma(\langle E_G \rangle)$ and $\gamma(\langle E_G \rangle/2)$.

no effect on the sensitivity of *p*-type samples to pressure; therefore, the contribution of the second and third terms ($\sim 10^{-5}$ bar^{-1}) to such expression for α_p only limits the accuracy of the numerical estimates for the *p*-type samples. All this allows us to use the following approximate expression to estimate the values of γ (γ_n and γ_p):

$$\alpha_\rho(D) \simeq (\gamma_n/kT)/[1+p(D)/n(D)b]$$
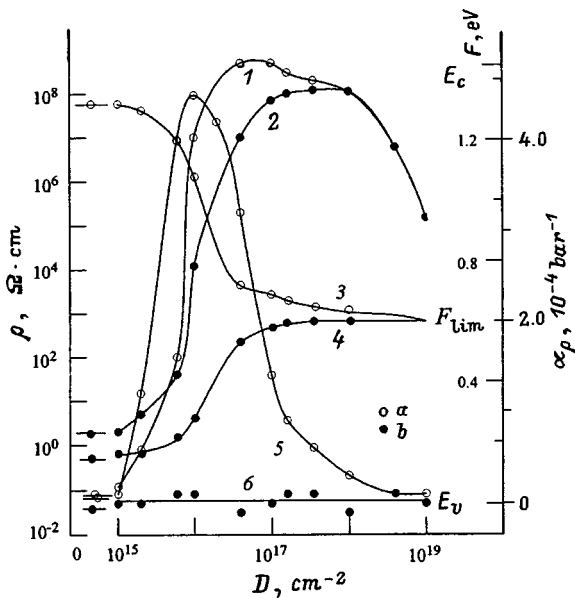$$+ (\gamma_p/kT)/[1+n(D)b/p(D)], \qquad (2)$$

FIG. 1. Variation with radiation dose of the resistivity $\rho(D)$ (*1, 2*), position of the Fermi level $F(D)$ (*3, 4*) and pressure coefficient of the resistivity $\alpha_\rho(D)$ (*5, 6*) for crystals of *n*- and *p*-GaAs (a and b, respectively) for bombardment by 2-MeV electrons. $T = 300$ K. Solid curves — calculation according to expressions (1)–(4) based on the known spectrum of E and H traps in GaAs (trap spectrum shown in Fig. 2).

where γ_n is reckoned from the nearest extremum of the conduction band, and γ_p is reckoned from the top of the valence band.

EXPERIMENTAL RESULTS

Since detailed studies of the radiation-defect spectrum have been carried out for GaAs, we present a quantitative analysis of the experimental results for this material.

Gallium arsenide. When *n*-GaAs is irradiated by high-energy particles, the value of ρ grows to $(3-5) \times 10^8 \, \Omega \cdot$cm (at 300 K) followed by $n-p$ conversion of the conductivity type and pinning of the Fermi level near $F_{\lim} = E_v + 0.6$ eV (Ref. 6). This is accompanied by a simultaneous increase in α_ρ up to values $\sim 4.5 \times 10^{-5}$ bar^{-1}, which corresponds to $\gamma_n \simeq 11.7 \times 10^{-6}$ eV/bar and is close in value to the pressure coefficient of the (Γ_{8v}–Γ_{6c}) gap.[1] For crystals of *p*-GaAs the value of α_ρ varies hardly at all as a result of irradiation (Fig. 1).

The experimental data were analyzed on the basis of numerical solution of Eq. (2) and the equation of electrical neutrality

$$n + N_a^- + \sum_{j=1}^{5} N_{RAj}^- = p + N_d^+ + \sum_{i=1}^{2} N_{RDi}^+ \qquad (3)$$

for the known set of traps $E1-E5$ and $H0$ and $H1$ in irradiated GaAs, inferred from DLTS measurements (shown in Fig. 2).[2] Here N_d and N_a are the unirradiated concentrations of the chemical impurities, donors, and acceptors, N_{RD} and N_{RA} are the concentrations of the donor and acceptor radiation defects, respectively. Numerical analysis of the experimental dependences $R_H(D)$ (R_H is the Hall coefficient) and $\alpha_\rho(D)$ with the aid of Eqs. (2) and (3) enabled us to construct the calculated curves $\rho(D)$, $F(D)$, $\alpha_\rho(D)$, and $\alpha_\rho(F)$ (Figs. 1 and 2) and estimate the values of γ_n^i. Here
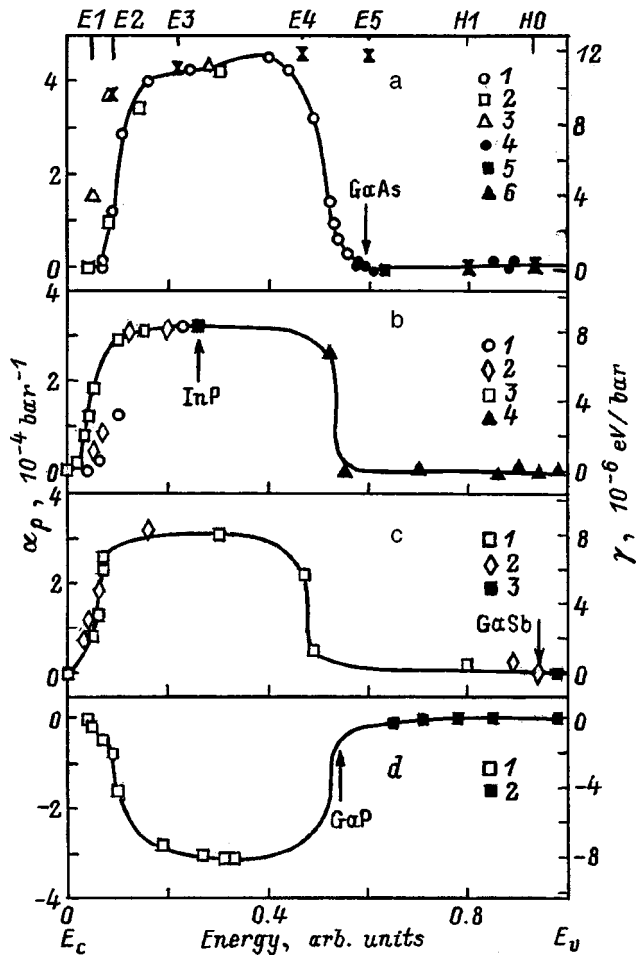
FIG. 2. Energy dependence of $\alpha_\rho(F)$ and $\gamma(F)$ in the irradiated semiconductors GaAs (a), InP (b), GaSb (c), and GaP (d). a: (1–3) — n-GaAs, (4–6) — p-GaAs; n, p 10^{16} cm^{-3}: 1 — (1–2), 2 — (8–16), 3 — (300–390), 4 — (500–900). b: (1–3) — n-InP, 4 — p-InP; n, p, 10^{16} cm^{-3}: 1 — 2, 2 — 5, 3 — 30, 4 — 100. c: 1, 2 — n-GaSb, 3 — p-GaSb; n, p, 10^{16} cm^{-3}: 1 — (16–36), 2 — (50–90), 3 — (100–400). d: 1 — n-GaP, 2 — p-GaP; n, p, 10^{16} cm^{-3}: 1 — 30, 2 — 150. Arrows indicate positions of $F_{\lim}$ in the irradiated crystals. For GaAs the calculated curve $\alpha_\rho(F)$ and values of γ_n and γ_p are plotted for the E and H traps (crosses); Qualitative curves of $\alpha_\rho(F)$ are shown for the remaining materials. For GaP the values of α_ρ and γ are multiplied by 5.

$\gamma^i = dE_i/dP$, E_i are the ionization energies of the defect levels for the traps $E2 - E5$ $(9.6, 11.0, 11.6, 11.6) \times 10^{-6}$ eV/bar relative to the level Γ_{6c} (crosses in Fig. 2). These values are similar to the corresponding experimental values $(8.8, 13.5, 10.5) \times 10^{-6}$ eV/bar for the energies of electron emission from the traps $E2 - E4$ in n-GaAs according to the hydrostatic-pressure measurements of the deep-level transient spectra.[7] Note that the obtained values of γ_n for the E traps are close to the value $\gamma_n \simeq 9.5 \times 10^{-6}$ eV/bar for the well-known defect $EL2$ (As$_{Ga}$ − X) in GaAs (Ref. 8). For the hole traps $H1$ and $H0$ the calculated values of γ_p^i are in the range $(1-2) 10^{-6}$ eV/bar. These data demonstrate that the levels of the E and H traps in GaAs within the limits of accuracy of the experiment (and calculation) are "fixed" relative to the top of the valence band (the Γ_{8v} level) under variation of the hydrostatic pressure. The results obtained are compared with experimental data on the height of the

Schottky barrier (F_{bS}) at a metal/GaAs contact under hydrostatic pressure, e.g., for Al/p-GaAs barriers $\partial(F_{bS}^p)/\partial P \simeq (0.2 - 0.3) \times 10^{-6}$ eV/bar and for Au/p-GaAs it is about 0.6×10^{-6} eV/bar.[8,9] This shows that regardless of the nature of the defects responsible for pinning of the Fermi level in irradiated bulk GaAs or at a metal/GaAs interface, the levels of the native lattice defects are shifted only slightly relative to the top of the valence band under hydrostatic pressure.

A detailed numerical analysis of the experimental results for other materials was not carried out since the data on the radiation-defect spectra for them are insufficient, and since the experimental dependences are qualitatively similar to those for GaAs.

Indium phosphide. In irradiated indium phosphide samples pinning of the Fermi level takes place near $E_v + 1.0$ eV (Ref. 6); i.e., n-InP crystals preserve their original conductivity type, and p-InP crystals are characterized by $p - n$ conversion of their conductivity type. In irradiated p-InP crystals, the value of α_ρ remains essentially unchanged, and under $p - n$ conversion of its conductivity type it attains a maximum value of 3.2×10^{-4} bar^{-1}, as in the case of n-InP. This corresponds to $\gamma_n \simeq 8.3 \times 10^{-6}$ eV/bar and is close to the value of the pressure coefficient of the $(\Gamma_{8v} - \Gamma_{6c})$ gap. Thus, in irradiated InP, as in the case of GaAs, regions of high (the Fermi level is located above $E_g/2$) and low (the Fermi level is located below $E_g/2$) sensitivity of ρ to pressure are revealed. (Here E_g is the minimum width of the band gap.)

Gallium antimonide. In irradiated gallium antimonide the Fermi level is pinned near the top of the valence band, near $E_v + 0.02$ eV (Ref. 6). The maximum values of $\alpha_\rho(F)$ $(\simeq 3.1 \times 10^{-4}$ bar$^{-1})$ are reached for irradiation of samples with n-type conductivity, which corresponds to $\gamma_n \simeq 8.05 \times 10^{-6}$ eV/bar, and for $n - p^+$ conversion of the conductivity type α_ρ falls to values of 5×10^{-6} bar^{-1}, which is close to the corresponding values of α_ρ in unirradiated and irradiated p-GaSb. A peculiarity of GaSb is the close position of the Γ_{6c} and L_{6c} minima in the band spectrum of the crystal: for the gap $\Delta E_{\Gamma L}$ we have $\Delta E_{\Gamma L}(T) = 0.084 - 3.4 \times 10^{-5}T$ and $\partial(\Delta E_{\Gamma L})/\partial P = (7.4 - 10.0) \times 10^{-6}$ eV/bar. Therefore, the value of γ_n was calculated with allowance for the partial contribution of the pressure coefficients of the gaps $\gamma(\Gamma_{6c} - \Gamma_{8v}) = 14 \times 10^{-6}$ eV/bar and $\gamma(L_{6c} - \Gamma_{8v}) = 6.6 \times 10^{-6}$ eV/bar.[10] This puts the calculated value of $\gamma_n = (\gamma_\Gamma + 4\gamma_L) \simeq 8.1 \times 10^{-6}$ eV/bar close to the experimental data values ($\sim 8.05 \times 10^{-6}$ eV/bar) in irradiated n-GaSb.

Gallium phosphide. In irradiated gallium phosphide the Fermi level is shifted into the band gap and "pins" at energies near $E_v + (1.0 \pm 0.2)$ eV. In irradiated GaP crystals the resistivity reaches large values. Therefore, the measurements of $\alpha_\rho(F)$ were performed for $\rho < 10^{10}$ Ω·cm, and in the region of large values of ρ the value of $\alpha_\rho(F)$ was extrapolated as was done for the GaAs, InP, and GaSb crystals (Fig. 2). In irradiated n-GaP we reached the maximum value $\alpha_\rho(D) \simeq -6.6 \times 10^{-5}$ bar^{-1}, which corresponds to $\gamma \simeq -1.7 \times 10^{-6}$ eV/bar and is similar to the pressure coefficient of the $(\Gamma_{8v} - X_{6c})$ gap in this semiconductor.[11] For crystals of p-GaP the value of γ showed very little change as a result of irradiation (Fig. 2).

DISCUSSION OF THE DATA

The measurements and analysis show that in irradiated semiconductors there are regions of high ($E_c > F > E_g/2$) and low ($E_g/2 > F < E_v$) sensitivity of ρ to hydrostatic pressure, due to peculiarities in the formation of ''deep'' states of the native lattice defects in the semiconductors. To describe the behavior of these states under hydrostatic pressure, we have made use of a model of a semiconductor with an effective isotropic ''band gap'' $\langle E_G \rangle$ ($\langle E_G \rangle = \langle E_c \rangle - \langle E_v \rangle$ is the mean energy interval between the lower conduction band E_c and the upper valence band E_v), which we developed earlier to describe the effects of radiation modification of the electrical properties of semiconductors.[6] In this model the variation of the properties of a semiconductor as a result of high-energy bombardment is considered as a radiation ''self-compensation'' phenomenon. As a result, the Fermi level pins at the level $\langle E_G \rangle/2$ ($\sim F_{\lim}$). Calculated values of $\langle E_G \rangle$ and $\langle E_G \rangle/2$, obtained by using ten special points to take into account the lower conduction band and the upper valence band, are presented in the table; here we simply present the values of the insulating gap (the Penn gap E_P) for the given materials. It follows from the calculations that the quantity $\langle E_G \rangle/2$ serves as an estimate of $F_{\lim}$ in an irradiated semiconductor.

Taking into account the partial contribution of the pressure coefficients of the interband Γ, X, and L energy gaps,[12]

$$\gamma(\langle E_G \rangle) \simeq (\gamma_\Gamma + 3\gamma_X + 4\gamma_L)/8 \qquad (4)$$

we estimated the pressure coefficient of the isotropic energy gap $\gamma(\langle E_G \rangle) = \partial(\langle E_G \rangle)/\partial P$ and the pressure coefficient of the energy corresponding to the middle of the isotropic energy gap $\gamma(\langle E_G \rangle/2) = \partial(\langle E_G \rangle/2)/\partial P$. The estimates assume that the radiation-defect levels that form $F_{\lim}$ ($\sim \langle E_G \rangle/2$) originate from all the states of the Brillouin zone of the crystal (such an expression was used earlier to describe the behavior of the so-called DX centers in n-Ga$_{1-x}$Al$_x$As under hydrostatic pressure[13]). Since there is significant spread in the values of the pressure coefficient in the literature for the Γ, X, and L gaps in semiconductors, their values were estimated from the expressions $\gamma^i = 3D_n^i/(c_{11} + 2c_{12})$. Here D_n^i are constants of the deformation potential for the Γ, X, and L extrema,[14] and c_{11} and c_{12} are the elastic moduli of the crystal, $i = \Gamma$, X, and L. It was shown that the quantity $\gamma(\langle E_G \rangle/2)$ in the majority of semiconductors of groups IV and III–V is equal to $\pm 0.5 \times 10^{-6}$ eV/bar (relative to the level Γ_{8v}), which is close to the experimental values for γ_p in unirradiated and irradiated crystals of p-type conductivity.

Thus, in the investigated materials the value of $\langle E_G \rangle/2$ ($\sim F_{\lim}$) undergoes hardly any change when subjected to hydrostatic pressure (relative to the Γ_{8v} level); i.e., for deep levels of the native lattice defects, the majority of semiconductors of groups IV and III–V satisfy the conditions $\partial(E_c - E_i)/\partial P \simeq \partial(E_g)/\partial P$ and $\partial(E_i - E_v)/\partial P \simeq \pm 0.5 \times 10^{-6}$ eV/bar. The consequence of this circumstance is the low sensitivity of the irradiated crystals of p-type conductivity to hydrostatic pressure, $n - p$ conversion of the conductivity type under hydrostatic pressure of irradiated crystals of n-type conductivity (e.g., InSb at $P > 10$ kbar; Ref. 15), and

''ejection'' of the resonance states of the native lattice defects from the conduction band into the band gap of the crystal under hydrostatic pressure (e.g., in n-InSb and n-InAs; Refs. 16 and 17).

Numerical estimates show that in contrast to semiconductors of groups IV and III–V, in compounds of the group II–VI, in particular II–Te, irradiated samples with both n- and p-type conductivity can exhibit a high sensitivity to pressure since they satisfy the condition $\partial(E_c - E_i)/\partial P \simeq \partial(E_i - E - v)/\partial P \simeq (1/2)\partial(E_g)/\partial P$. The absence of the necessary data for IV–VI semiconductors—the lead chalcogenides (PbS, PbSe, and PbTe)—prevents us from obtaining the corresponding numerical estimates for these materials. However, experimental studies on these materials[18] have revealed $n - p$ conversion of the conductivity type in the irradiated solid solutions PbTe–SnTe and PbSe–SnSe under hydrostatic pressure (up to 16 kbar). This indicates that a shift of the radiation-defect levels takes place in these compounds under pressure in the direction of the valence band, like in semiconductors of the group II–Te.

CONCLUSIONS

The results of this experimental study show that in semiconductors the native lattice defect levels, regardless of their nature and location in the band spectrum of the crystal, remain essentially the same relative to the energy $\langle E_G \rangle/2$ ($\sim F_{\lim}$) under variation of the hydrostatic pressure. Here the dielectric model of the crystal correctly describes the main trends of the electrical properties of irradiated semiconductors subjected to subsequent application of hydrostatic pressure, makes it possible to estimate the pressure coefficients for deep levels, and opens up possibilities of *a priori* choice of materials for the development of static and dynamic pressure sensors based on irradiated semiconductor materials and structures. We note that despite the different conditions of pinning of the Fermi level in an irradiated bulk semiconductor and at a metal/semiconductor interface, $F_{\lim} \approx F_{bS}$ (Ref. 19) and $\partial(F_{\lim})/\partial P \simeq \partial(F_{bS})/\partial P$.

*)E-mail: brudnyi@ic.tsu.ru; Fax: (3822) 233034

[1] V. N. Brudnyĭ, A. A. Vilisov, V. M. Diamant, and N. P. Krivorotov, Fiz. Tekh. Poluprovodn. **14** (1), 13 (1980) [Sov. Phys. Semicond. **14**, 7 (1980)].
[2] V. N. Brudnyi and V. M. Diamond, Solid State Commun. **54**, 355 (1985).
[3] V. N. Brudnyĭ and V. M. Diamant, Izv. Vuzov. Fizika **29**, 81 (1986).
[4] V. N. Brudnyĭ and V. A. Novikov, Izv. Vuzov. Fizika **34**, 911 (1991).
[5] V. N. Brudnyĭ, P. N. Drobot, and V. A. Novikov, Dep. VINITI N6854-B87 (1987).
[6] V. N. Brudnyi, S. N. Grinyaev, and V. E. Stepanov, Physica B: Condens. Matter. **212**, 429 (1995).
[7] R. H. Wallis, A. Zylbersztein, and J. M. Besson, Appl. Phys. Lett. **38**, 698 (1981).
[8] P. Phatak, N. Newman, P. Dreszer, and E. R. Weber, Phys. Rev. B **51**, 18003 (1995).
[9] W. Shan, M. F. Li, P. Y. Yu, W. L. Hansen, and W. Walukiewicz, Appl. Phys. Lett. **53**, 974 (1988).
[10] *Numerical Data and Functional Relationships in Science and Technology,*

edited by O. Madelung (Springer-Verlag, Berlin/Heidelberg/New York/London/Paris/Tokyo,1987), Vol. 22: *Semiconductors*.

[11] V. N. Brudnyĭ and V. A. Novikov, Izv. Vuzov. Fizika **41**, 124 (1998).

[12] R. A. Évarestov, *Quantum-Chemical Methods in Solid State Theory* [in Russian], Leningrad State Univ. Press, Leningrad, 1982.

[13] D. J. Chadi and K. J. Cheng, Phys. Rev. B **39**, 10 063 (1989).

[14] M. Cardona and N. E. Christensen, Phys. Rev. B **35**, 6182 (1987).

[15] V. V. Dmitriev and E. P. Skipetrov, Fiz. Tekh. Poluprovodn. **24**, 897 (1990) [Sov. Phys. Semicond. **24**, 564 (1990)].

[16] I. Booth, M. H. Hawton, and W. J. Keller, Phys. Rev. B **25**, 7713 (1982).

[17] A. Kadri, R. L. Aulomhard, K. Zitouni, and L. Konczewicz, Physica B & C **139−140**, 426 (1986).

[18] N. B. Brandt and E. P. Skipetrov, Fiz. Niz. Temp. **22**, 870 (1996) [Low Temp. Phys. **22**, 665 (1996)].

[19] V. N. Brudnyĭ and S. N. Grinyaev, Fiz. Tekh. Poluprovodn. **32**, 315 (1998) [Semiconductors **32**, 284 (1998)].

Translated by Paul F. Schippnick

Photoconductivity spectral characteristics of semiconductors with exponential fundamental absorption edge

A. I. Vlasenko,*) Z. K. Vlasenko, and A. V. Lyubchenko

Institute of Semiconductor Physics, National Academy of Sciences of the Ukraine, 252028 Kiev, Ukraine

An analysis has been performed of photoconductivity spectral characteristics of semiconductors with an exponential fundamental absorption edge as functions of the surface recombination rate and sample thickness. It is shown, in particular, that in crystals of $Cd_xHg_{1-x}Te$ ($x \approx 0.2$) the spectral position of the photoconductivity maximum over a wide range of values of these parameters can be used, with an error not exceeding 1%, to determine the effective band gap and, consequently, the composition of the material. © *1999 American Institute of Physics.*
[S1063-7826(99)00411-1]

Chemically complex semiconductors are characterized by microfluctuations of their composition and, as a consequence, a smooth falloff of their intrinsic absorption coefficient (α) as a function of photon energy.[1–6] This makes it difficult to determine the band gap (E_g) from the long-wavelength falloff of the photoconductivity spectrum and raises the question, from which of its elements can the E_g values, and correspondingly the composition of the material, be most dependably and accurately determined.

In most general form, the specific photoconductivity $\Delta\sigma$ is

$$\Delta\sigma = e(\mu_n \Delta n + \mu_p \Delta p)G(\alpha) = e\mu_n(\tau_n + b^{-1}\tau_p)G(\alpha), \tag{1}$$

where Δn and Δp are the concentrations, μ_m and μ_p are the mobilities ($b = \mu_m/\mu_p$), τ_n and τ_p are the lifetimes of the nonequilibrium charge carriers (NCC's)—electrons and holes, and $G(\alpha)$ is the rate of optical generation of pairs per unit volume expressed as a function of α and the surface recombination rate s. Its magnitude in a sample of thickness d

$$G(\alpha) = \beta(1-R^0)\frac{\Phi}{d}[1 - \exp(-\alpha d)] \tag{2}$$

is determined by the spectral dependence of the absorption coefficient $\alpha(h\nu)$, the quantum yield of the photocurrent β, the reflection coefficient $R^0(h\nu)$, and the photon flux density Φ.

If recombination of the NCC's at the surface ($s=0$) is disregarded, the quantity $G(\alpha)$,

$$G(\alpha) = \begin{cases} G_0 = \beta(1-R^0)(\Phi/d), & \alpha d \gg 1, \tag{3a} \\ G_0(\alpha d), & \alpha d \ll 1, \tag{3b} \end{cases}$$

increases with increasing α in the transparency region (3b) of the fundamental absorption edge and then saturates for total photon absorption (3a).

When $s \neq 0$, the quantities G (2) and $\Delta\sigma$ (1) can be written in the form[7]

$$G(\alpha, s) = G_0 F(\alpha, s), \quad \Delta\sigma(\alpha, s) = \Delta\sigma_0 F(\alpha, s), \tag{4}$$

where $\Delta\sigma_0 = e\mu_n(\tau_n + b^{-1}\tau_p)G_0$ is the value of $\Delta\sigma$ in the strong absorption region, $F(\alpha, s)$ is a dimensionless function of the effect of the surface on the bulk recombination rate of NCC's under conditions of their nonuniform excitation.

Solution of the diffusion equation for the minority NCC's with boundary conditions $d\Delta p/dy = \pm s \cdot (\Delta p_\pm / D)$ (the rates s on both surfaces are equal) with the above relations taken into account gives[8]

$$F(\alpha, s) = \frac{\alpha L}{1 - \alpha^2 L^2} \left\{ \frac{1 - e^{-\alpha d}}{\alpha L} \right.$$
$$\left. + \frac{[(\alpha L - S)e^{-\alpha d} - (\alpha L + S)][S(\cosh\chi - 1) + \sinh\chi]}{2S\cosh\chi + (S^2 + 1)\sinh\chi} \right\}, \tag{5}$$

where $S = sL/D = s\tau_p/L$ is the dimensionless surface recombination rate, L is the diffusion length of the minority NCC's, and $L = (D\tau_p)^{1/2}$; here D is the diffusion coefficient of the minority NCC's; and $\chi = d/L$ defines a relation between the sample thickness d and L. Taking all the above relations into account, we have: for a diffusion-thick sample ($\chi \gg 1$)

$$F(\alpha, s) = \frac{\alpha L}{1 - \alpha^2 L^2} \left\{ \frac{1 - e^{-\alpha d}}{\alpha L} \right.$$
$$\left. + \frac{[(\alpha L - S)e^{-\alpha d} - (\alpha L + S)]S}{(S+1)^2} \right\}, \tag{6a}$$

for a diffusion-thin sample ($\chi < 1$)

$$F(\alpha, s) = \frac{\alpha L}{1 - \alpha^2 L^2}$$
$$\times \left\{ \frac{1 - e^{-\alpha d}}{\alpha L} + \frac{[(\alpha L - S)e^{-\alpha d} - (\alpha L + S)]}{1 - S} \right\}. \tag{6b}$$
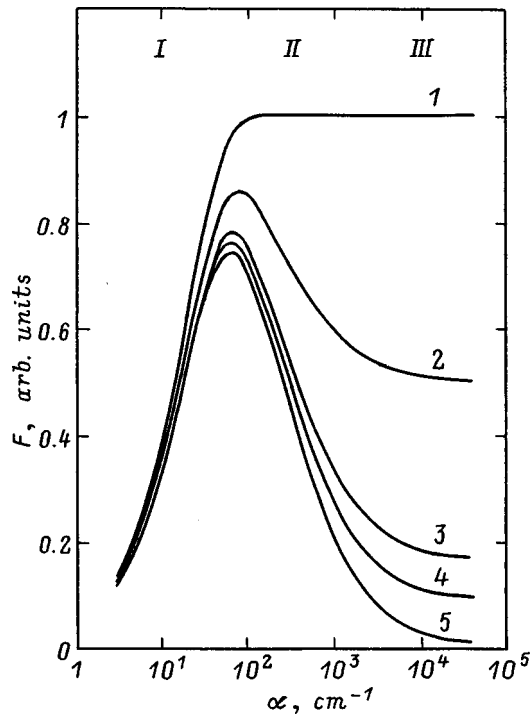
FIG. 1. Spectral characteristics of the photoconductivity in the coordinates $F(\alpha)$ for a diffusion-thick sample ($d=5\times10^{-2}$ cm, $L=4\times10^{-3}$ cm), calculated according to formula (5). Curves *1–5* correspond, respectively, to $S=0$, 1, 5, 10, and 100. *I, II, III* indicate, respectively, segments of growth and decay, and ledge of the spectral characteristic.

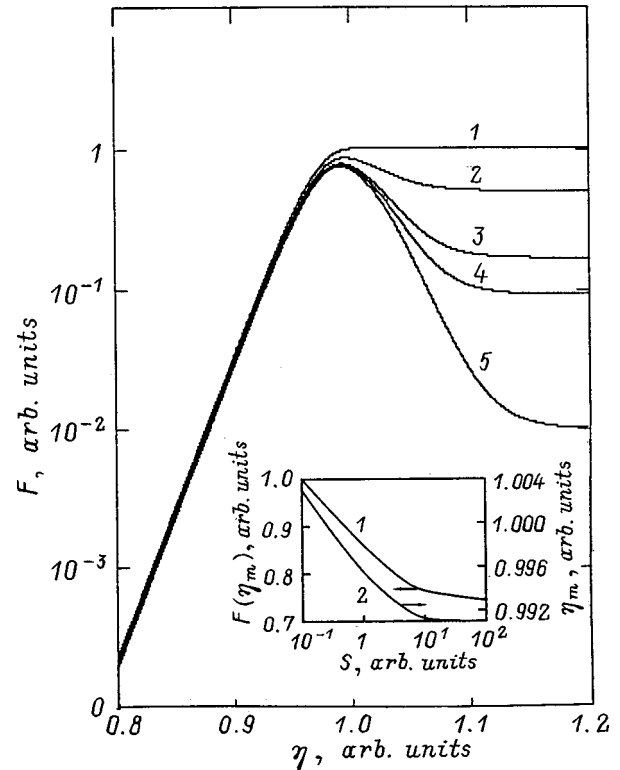

FIG. 2. Spectral characteristics of the photoconductivity in the coordinates $F(\eta)$ for a diffusion-thick sample ($d=5\times10^{-2}$ cm, $L=4\times10^{-3}$ cm), calculated according to formula (5) with dependence (10) taken into account. Curves *1–5* correspond to $S=0$, 1, 5, 10, and 100. The inset plots the maximum of the spectral characteristic $F(\eta_m)$ (*1*) and the value of the parameter η at which F takes its maximum (η_m) (*2*) as functions of the reduced surface recombination rate S.

For a $Cd_xHg_{1-x}Te$ (CMT) wafer ($x\simeq0.2$) of n-type conductivity with standard parameters (at 77 K) $n_0=(2-5)\times10^{14}$ cm^{-3}, $\tau_n\simeq\tau_p=(1-4)\times10^{-6}$ s, $\mu_p\simeq400-800$ cm$^2/(V\cdot s)$, $D=10-20$ cm^2/s, $L=(3-9)\times10^{-3}$ cm, and $1.5\times10^{-2}<S<10^2$ for $s=10^3-10^5$ cm/s (Refs. 9 and 10). Thus, samples with thickness $d<20\,\mu$m can be assumed to be diffusion-thin, and samples with thickness $d>100\,\mu$m can be assumed to be diffusion-thick.

As a rule, the above-mentioned studies were restricted to an analysis of the spectral characteristic of the photoconductivity as a function of α, which made it possible to determine only the general outline of the spectrum, regardless of the concrete form of the function $\alpha(h\nu)$ determined by the type (types) of optical transitions at the fundamental absorption edge. Let us review the main points of this analysis.

In the photoconductivity spectral characteristics for diffusion-thick samples, calculated according to formula (5) (Fig. 1), the photoconductivity saturates at $S=0$: $F\rightarrow1$, $\Delta\sigma=\Delta\sigma_0$ (4); for $S\neq0$ the photoconductivity reaches a maximum with increasing α (where $F\rightarrow1$) with subsequent falloff to a short-wavelength "ledge." The dependence $\Delta\sigma(\alpha,S)$ is approximated by the functions

$$F(\alpha,s)=\begin{cases}\alpha d; & \alpha d\ll1, \quad \alpha L\ll1, \quad L<d; & (7a)\\[2mm] \dfrac{1}{\alpha L}\dfrac{S+\alpha L}{S+1}; & \alpha L>1, \quad \alpha L<S; & (7b)\\[2mm] 1/(S+1); & \alpha L\gg S. & (7c)\end{cases}$$

in the different segments of its variation (growth, falloff, and the short-wavelength ledge).

According to relations (7a) and (7b), on the rising segment the quantity $\Delta\sigma(\alpha,S)$ is directly proportional, and on the falling segment, inversely proportional to $\alpha(h\nu)$. This makes it possible to estimate the spectral position of the photoconductivity maximum (α_m) from the intersection of the corresponding approximate dependences:

$$\alpha_m\simeq\sqrt{\frac{1}{dL}\frac{S}{S+1}}. \tag{8}$$

For large values of S the position α_m depends only weakly on S, but very strongly on the sample thickness, shifting toward smaller values of α (less than the photon energies) with increasing d, as is confirmed experimentally, in particular, for crystals of CMT.[10–13] It can be easily seen that the value of $\Delta\sigma$ (4) on the ledge determines the effective "surface" lifetime

$$\tau_{\text{eff}}=\frac{\tau_n+b^{-1}\tau_p}{1+S}, \tag{9a}$$

which is less than the bulk lifetime by a factor of $(1+S)$ (Ref. 12). In semiconductors with $b\gg1$

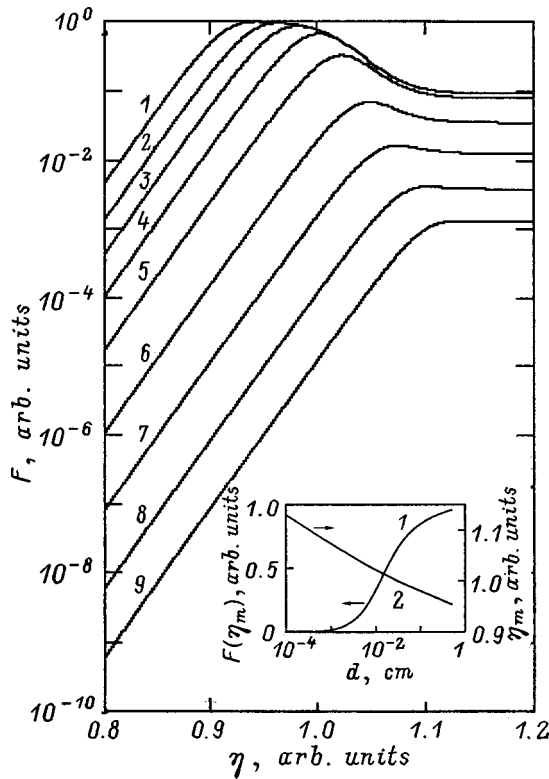$$\frac{1}{\tau_{\text{eff}}}=\frac{s}{L}+\frac{1}{\tau_n}. \tag{9b}$$

FIG. 3. Spectral characteristics of the photoconductivity in the coordinates $F(\eta)$ — calculation according to formula (5) with dependence (10) taken into account for $L=4\times10^{-3}$ cm and $S=10$. Curves *1–9* correspond to $d=3\times10^{-1}$, 1×10^{-1}, 3×10^{-2}, 1×10^{-2}, 3×10^{-3}, 1×10^{-3}, 3×10^{-4}, and 1×10^{-4} cm. The inset plots the maximum of the spectral characteristic $F(\eta_m)$ (*1*) and the value of the parameter η at which F takes its maximum (η_m) (*2*) as functions of the sample thickness d.

The influence of the surface [the first term in Eq. (9b)] is significant for $s/L \gtrsim 1/\tau_n$. For a sample with $\tau_n=10^{-6}$ s and $L=4\times10^{-3}$ cm the required value of the recombination rate is $s>4\times10^3$ cm/s.

In insensitive samples (short lifetimes) the influence of the surface is small. For fixed values of s this leads to a narrowing of the falloff segment and to its disappearance at $1/\tau_n < s/L$ and $\tau_n \simeq \tau_{\text{eff}}$ (9). A dependence of this type, as calculation shows, is characteristic of diffusion-thin samples (6b), in which the lifetime of the NCC's is independent of their bulk values even for uniform absorption ($1/\alpha>d$) of light.

The next element of the analysis is an account of the concrete form of the dependence $\alpha(h\nu)$ at the fundamental absorption edge. Let us consider it in the case where the dependence $\alpha(h\nu)$ is exponential, as is the case in solid-solution semiconductors. For crystals of CMT the dependence $\alpha(h\nu)$ at the fundamental absorption edge is described by the expression[4–6]

$$\alpha(h\nu)=\alpha_0\exp\left(\frac{h\nu-E_s}{W}\right)=\alpha_0\exp\left[\frac{E_s}{W}(\eta-1)\right],$$

$$\eta=\frac{h\nu}{E_s}, \tag{10}$$

where α_0, W, and E_s are spectrum-independent parameters. The quantity E_s is similar to the optical band gap E_g. The difference between them is given by the variance $[\overline{(\Delta E_g)^2}]^{1/2}$ due to spatial fluctuations of the lattice potential of different nature in the solid solutions—primarily microfluctuations of the composition.[14] For CMT with $x\simeq0.2$ ($E_g\simeq100$ meV) $[\overline{(\Delta E_g)^2}]^{1/2}\approx13.7$ meV. The dependence of E_g and E_s on T essentially coincide, and the dependence $W(T)$ is approximated by the expression

$$W=W_0+\delta T, \tag{11}$$

where $W_0\simeq1.8-3.1$ meV (Ref. 14) and the parameter δ is determined by the chemical bond and decreases with decreasing role of the ionic component of the chemical bond, $\delta=2\times10^{-2}$ meV/K. At 80 K $W\simeq3.8$ meV (CMT, $x\simeq0.2$).

The quantity α_0 in expression (10) is independent of T and can be estimated using the expressions given in Refs. 5 and 15. According to the data of Ref. 4, the photoconductivity maximum is realized for $\alpha_0\simeq(2-5)\times10^2$ cm^{-1}, which corresponds to the condition $h\nu_m\approx E_s$.

For the photoconductivity spectral characteristics calculated from formula (5) taking formula (10) into account (Figs. 2 and 3) the following trends are characteristic.

1) In diffusion-thick samples with $S\neq0$ the maximum of the function $F(\eta)$ is formed at $\eta\simeq1$; S has only a weak effect on the value of the function at its maximum $F(\eta_m)$ and on its spectral position η_m; as S varies from 10^2 to 10^{-1} $0.75\leqslant F(\eta_m)\leqslant1$ and $0.992\leqslant\eta_m\leqslant1.003$.

2) For fixed S decreasing the thickness of the sample leads to a short-wavelength shift of the characteristic and its maximum value $F(\eta_m)$; the photoconductivity decreases simultaneously over the entire spectral range, and most steeply in the region of the transition to the condition of a diffusion-thick sample ($d<L$).

3) For small S ($S\ll1$) and large d, calculation gives values of η_m somewhat less than unity, which corresponds to $h\nu_m<E_s$; in contrast, for large S and small d we have $\eta_m>1$, which corresponds to $h\nu_m>E_s$; over wide ranges of the mean values of S and d the values of η_m differ only slightly from unity; all this is confirmed by the statistics of the experiment.[10–13]

4) The dependence $F(\eta)$ for $\eta>\eta_m$ disappears in a diffusion-thin sample, where the bulk lifetime τ (8) is governed by surface recombination (9).

Let us analyze an actual metrological question—the connection of the characteristic elements of a spectral characteristic with the band gap of a semiconductor, in the analyzed case with the quantity E_s (10). Among the characteristic elements we may include, in particular, the spectral position of the longest segment of long-wavelength edge of the dependence $F(\eta)$, which corresponds to the maximum of the derivative $dF/d\eta=F'(\eta)$ (Fig. 4). Since the spectral positions of the extrema of the derivatives $F'(\eta)$ do not correspond to the condition $\eta=1$ ($h\nu=E_s$), they cannot be used to determine E_s. Small deviations of $h\nu$ from E_s due to the factor E_s/W entering into the exponential in expression (10) and defining the scale of the photoconductivity spectrum can lead
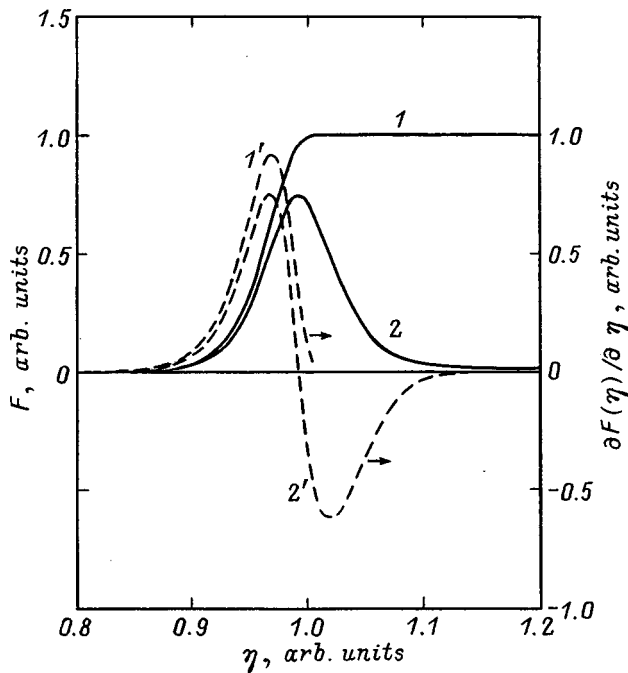
FIG. 4. Spectral dependence of the photoconductivity in the coordinates $F(\eta)$ (*1*, *2*) and the corresponding derivatives $F'(\eta)$ (*1'*, *2'*) for $S=0$ ((*1*, *1'*) and $S=100$ ((*2*, *2'*). Calculated according to formula (5) for the parameter values $d=5\times10^{-2}$ cm and $L=4\times10^{-3}$ cm.
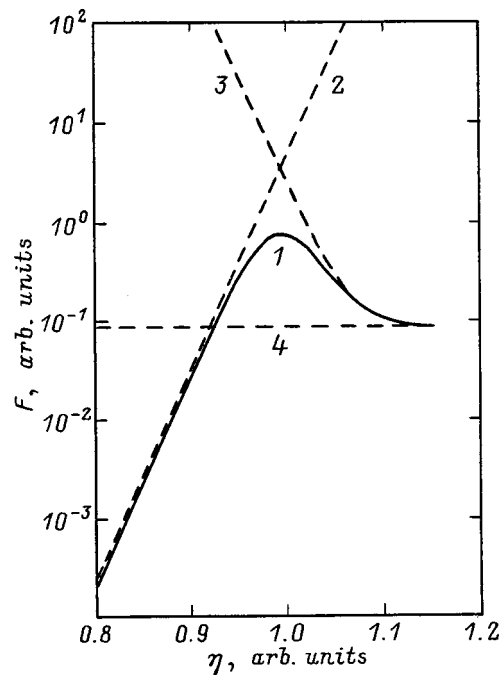

FIG. 5. Spectral dependence of the photoconductivity in the coordinates $F(\eta)$ for a diffusion-thick sample with $S=10$, $d=5\times10^{-2}$ cm, and $L=4\times10^{-3}$ cm. *1* — calculation according to formula (5), dashed lines — extrapolation of different segments of the dependence of the function $F(\eta)$ corresponding to the formulas: *2* — (7a), *3* — (7b), and *4* — (7c).

to substantial changes in the absolute values of $F(\eta)$. For this reason, and also because of the variation of the parameters E_s and W from sample to sample as functions of their degree of structural perfection, the determination of the value of E_s from its long-wavelength edge is also invalid.

Let us consider the conditions for the existence of a maximum of the curve $F(\eta)$ for a diffusion-thick sample with $S\neq0$ (8). To determine $F_m(\eta)$ to first order, we use condition (8)—the intersection point of the extrapolations of the functions (7a) and (7b) that form the maximum (Fig. 5). Using relation (10), we have

$$\alpha_m=\alpha_0\exp\left[\frac{E_s}{W}(\eta-1)\right]\simeq\sqrt{\frac{1}{dL}\frac{S}{S+1}}. \quad (12)$$

If the condition $1<\alpha L<S$ is satisfied, i.e., in a sample with a pronounced photoconductivity maximum, the difference between E_s and the position of the maximum, $h\nu_m$, is given by

$$\Delta E_s=h\nu_m-E_s=W\ln\left(\frac{1}{\alpha_0}\sqrt{\frac{1}{dL}\frac{S}{S+1}}\right). \quad (13)$$

The accuracy with which formula (13) gives E_s depends on the parameters of the sample and increases with growth of the values of α_0, d, and L. Let us estimate ΔE_s for CMT ($x=0.2$) with the parameters $L=10^{-2}$ cm, $d=10^{-1}$ cm, $S=10$, $\alpha_0=10^2$ cm^{-1}, $W=2$ meV, and $E_s=100$ meV. Substituting these quantities into formula (13) gives $\Delta E_s/E_s \simeq 4\times10^{-3}<1\%$, which is a more-than-satisfactory result.

Thus, in crystals with exponential dependence of the long-wavelength absorption edge the effective band gap can be determined with good accuracy over wide limits of the

sample thickness and surface recombination rate from the maximum of the photoconductivity spectral characteristic.

*)E-mail: micle@semicond.kiev.ua; Fax: (044) 265-8324

[1] M. D. Blue, Phys. Rev. A **134**, 226 (1964).
[2] J. L. Schmit and E. L. Stelzer, J. Appl. Phys. **40**, 4865 (1969).
[3] I. M. Nesmelova, L. F. Kovalenko, K. Ya. Shtivel'man, and I. S. Aver'yanov, Zh. Prikl. Spektrosk. **17**, 894 (1972).
[4] L. D. Saginov, V. P. Ponomarenko, V. I. Stafeev, and V. A. Fedirko, Fiz. Tekh. Poluprovodn. **13**, 1039 (1979) [Sov. Phys. Semicond. **13**, 608 (1979)].
[5] E. Finkman and Y. Nemirowski, J. Appl. Phys. **50**, 4356 (1979).
[6] L. D. Saginov, V. P. Ponomarenko, V. A. Fedirko, and V. I. Stafeev, Fiz. Tekh. Poluprovodn. **16**, 470 (1982) [*sic*].
[7] V. A. Petrusevich, Fiz. Tverd. Tela (Leningrad) **1**, 1095 (1959).
[8] N. A. Zakhlenyuk, E. A. Sal'kov, and V. N. Sokolov Ukr. Fiz. Zh. **31**, 268 (1986).
[9] N. N. Belyĭ, N. S. Baryshev, I. N. Tarasova, and B. V. Panasenko, Opt. Mekh. Promst. **10**, 13 (1978) [*sic*].
[10] A. I. Vlasenko, E. P. Matsas, A. V. Lyubchenko, E. A. Sal'kov, and A. V. Sachenko, Poluprovodn. Tekh. Mikroelektron. **33**, 67 (1981).
[11] A. I. Vlasenko, A. V. Lyubchenko, and E. A. Sal'kov, Ukr. Fiz. Zh. **25**, 431 (1980).
[12] A. V. Lyubchenko, E. A. Sal'kov, and F. F. Sizov, *Physical Principles of Semiconductor Photo-Electronics* [in Russian], Naukova Dumka, Kiev, 1984.
[13] A. I. Vlasenko, K. R. Kurbanov, A. V. Lyubchenko, and E. A. Sal'kov, Ukr. Fiz. Zh. **27**, 1392 (1982).
[14] L. D. Saginov, V. A. Fedirko, V. I. Stafeev, V. P. Ponomarenko, and V. L. Egorov, Fiz. Tekh. Poluprovodn. **16**, 1266 (1982) [Sov. Phys. Semicond. **16**, 808 (1982)].
[15] J. Chu, B. Li, and D. Tang, J. Appl. Phys. **75**, 1234 (1994).

Translated by Paul F. Schippnick

The electron density of semiconductors with charged dislocations placed in external fields

Z. A. Veliev

Nakhichevan University, 373630 Nakhichevan, Azerbaijan

Variations in the electron density due to variations in the capture cross section and the thermal ionization upon application of an external electric field and a quantizing magnetic field are considered. Analytical expressions for the electron density in arbitrary electric and quantizing magnetic fields and also in crossed electric and quantizing magnetic fields are obtained. It is assumed that the electrons relax in energy as a result of interacting with acoustic phonons. Calculations for a quantizing magnetic field in the ultraquantum limit are presented. © *1999 American Institute of Physics.* [S1063-7826(99)00511-6]

The electron density in nondegenerate *n*-type semiconductors in the absence of an external electric field obeys Boltzmann statistics. In this case the relation linking the thermal ionization of a dislocation center β and the cross section σ for capture of electrons at a charged dislocation center can be derived from the condition of equality of the thermal-ionization and recombination fluxes

$$\beta = \sigma \langle v_c \rangle N_c \exp(-E_D / kT). \tag{1}$$

Here $\langle v_c \rangle = \sqrt{8kT/\pi m}$ is the mean electron velocity, $N_c = 2(mkT/2\pi\hbar^2)^{3/2}$ is the density of states in the conduction band, T is the lattice temperature, k is the Boltzmann constant, m is the effective mass of the electron, and E_D is the ionization energy of a dislocation.

Upon the application of external fields, the coefficients σ and β vary independently and there is no simple relation between them of the type (1). However, under steady-state conditions, as at equilibrium, the thermal-ionization and recombination fluxes are equal, and this equality determines the steady-state concentration in the presence of external fields.

In our study we have calculated the electron density in nondegenerate semiconductors with charged edge dislocations under the following steady-state conditions: a) in the presence of an external electric field, and b) in the presence of external crossed electric and quantizing magnetic fields.

1. As was shown in Refs. 1–5, in external electric fields the carrier capture cross section σ and the thermal ionization coefficient β become functions of the field strength $\mathcal{E}$ of the applied electric field, with the coefficients $\sigma(\mathcal{E})$ and $\beta(\mathcal{E})$ varying independently as functions of the applied electric field. Correspondingly, the free electron density becomes a function of $\mathcal{E}$.

Let us consider the case where the dislocations are distributed in such a way that the axis of the Read cylinders is perpendicular to the xy plane and they do not intersect, i.e., the dislocation centers act independently. The equation of particle balance can then be written in the form

$$J - \beta(\mathcal{E}) N_d = 0, \tag{2}$$

where the total recombination flux per unit volume J is related to the concentration of the dislocations N_d and the capture cross section σ of the carriers by the equation

$$J = n N_D \sigma \langle v_c \rangle. \tag{3}$$

Here N_D is the dislocation density, and $\langle v_c \rangle$ is the mean electron velocity in the external electric field. The capture cross section of the carriers $\sigma(\mathcal{E})$ in the presence of a field decreases for two reasons. First, the mean energy of the free electrons is increased and, consequently, the number of carriers at the bottom of the conduction band, which directly determine capture, is decreased. Second, the dislocation well is deformed in strong electric fields, which leads to the destruction of bound states with binding energy less than

$$\Delta = -U_0 \ln \frac{U_0 R}{2 W_0 b} ((1 + 4 W_0 b e \mathcal{E}/U_0^2)^{1/2} - 1)$$

$$+ U_0 \left(1 + \frac{4 W_0 b \mathcal{E} e}{U_0^2} \right)^{1/2}, \tag{4}$$

$$r_s = \frac{U_0}{2 e \mathcal{E}} ((1 + 4 W_0 b e \mathcal{E}/U_0^2)^{1/2} - 1),$$

and consequently, in strong electric fields the cross sections for capture at a dislocation center are decreased ($U_0 = e^2/2\pi\varepsilon\varepsilon_0 a$, $W_0 = E_c(1-2\nu)/(1+\nu) = E_c\alpha$, where ν is the Poisson coefficient, and E_c is the effective constant of the deformation potential).

As was shown in Ref. 5, the probability for ionization of a dislocation center in the presence of an electric field $\beta(\mathcal{E})$ varies not only due to a lowering of the ionization energy E_D by virtue of the so-called Poole–Frenkel' dislocation effect, but also due to a change in the rate of diffusion of the free electrons into the space of the total energy of highly excited states of the dislocation center. As follows from Eqs. (2) and (3), for the carrier concentration we obtain

$$n = \frac{\beta(\mathcal{E})}{\sigma \langle v_c \rangle}. \tag{5}$$

In the presence of an external electric field the quantities $\sigma(\mathcal{E})$ and $\beta(\mathcal{E})$ were calculated by the method of cascade capture[1] under the assumption that the electrons relax in energy as a result of interacting with acoustic phonons and are given by

$$\sigma = B(\mathcal{E}) \left(\frac{2}{\pi m_c kT} \right)^2 \frac{\pi^3 \hbar^3 [(\Delta/kT)^2 + \mu_1]^{\mu_1} e^{\frac{\Delta}{kT}}}{2 \langle v_c \rangle \mu_1^{\mu_1 + 3/2} U(3/2, \mu_1 + 5/2, \mu_1)}, \tag{6}$$

$$\beta = B(\mathcal{E}) e^{-\frac{E_D - \Delta}{kT}}, \tag{7}$$

where

$$B(\mathcal{E}) = \frac{b^2 m_\perp^2 m_\parallel c^2 W_0^2}{\pi \rho_0 \hbar^7} \ln \frac{r_s}{a},$$

$$\mu_1 = \frac{(e\mathcal{E})^2}{6 m_c S_e^2 kT} \left(\frac{\pi \rho_0 S_e^2 \hbar^7}{E_0 E_c m_\perp^{3/2} m_\parallel^{1/2} kT} \right)^2, \tag{8}$$

$$c = \frac{1}{3} [3 m_\perp E_d^2 + m_\parallel (E_d + E_u)^2],$$

$$E_0 = c/m_\perp, \quad \langle v_c \rangle = \sqrt{8kT/\pi m_c},$$

$$\frac{1}{m_c} = \frac{3}{m_\parallel} + \frac{3}{2m_\perp},$$

E_d and E_u are the constants of the deformation potential, introduced by Herring[6] (the z axis is aligned with the axis of the energy ellipsoid), $m_\parallel$ and $m_\perp$ are the components of the mass tensor parallel and transverse to the axis of the ellipsoid, and S_e is the speed of sound in the crystal. Substituting expressions (6) and (7) into relation (5), we obtain for the electron density in an electric field

$$n(\mathcal{E}) = \frac{1}{2\pi^3 \hbar^3} \left(\frac{\pi m_c kT}{2} \right)^2 \frac{\mu_1^{\mu_1 + 3/2} U(3/2, \mu_1 + 5/2, \mu_1)}{[(\Delta/kT)^2 + \mu_1]^{\mu_1}}. \tag{9}$$

Employing Kummer's asymptotic limit of the hypergeometric function $U(3/2, \mu_1 + 5/2, \mu_1)$ (Ref. 7), we find for $\mu_1 \gg 1$ in strong electric fields that $n \sim T_e^2 \exp(\Delta/kT)^2$; i.e., the free electron density in a strong electric field grows in comparison to the equilibrium density for the same sample temperature as a result of growth of the mean energy of the free electrons and a lowering of the energy of the dislocation barrier.

As follows from Eq. (9), the free-carrier concentration grows exponentially with growth of the field when $\Delta > kT$. If, on the other hand, $\Delta < kT < kT_e$, then the field dependence of the concentration is governed mainly by the pre-exponential factor. The quantity T_e (T_e is the temperature of the electron subsystem in strong electric fields) is given by

$$kT_e = e\mathcal{E} l_\mathbf{p} \delta_0^{1/2},$$

where

$$l_\mathbf{p} = \pi \hbar^4 \rho_0 S_e^2 / m_c^2 E_c kT,$$

$$\delta_0 = \sqrt{2 m_c S_e^2 / kT}.$$

2. The cross section for capture of electrons in a quantizing magnetic field was calculated by the method developed in Ref. 5. If the thermal energy of the carriers kT is much greater than the characteristic phonon energy $\sqrt{\hbar \omega_H \cdot m_\perp S_e^2}$, then the process of electron capture can be described as a continuous descent from the region of positive values of the total energy into the region of negative values. The capture cross section when the condition $\hbar \omega_H \gg kT \gg \sqrt{\hbar \omega_H \cdot m_\perp S_e^2}$ is satisfied in the case of an anisotropic electron spectrum is given by

$$\sigma(H) = \frac{(2\pi)^{3/2}}{12\pi^3} \frac{b^2 \langle E_c^2 \rangle \alpha^2}{\rho_0 \sqrt{m_\parallel kT} U_0^3} \left(\frac{eH}{c\hbar} \right)^2 (m_\perp + m_{\omega_H})$$

$$\times \left[\ln \frac{U_0}{3\sqrt{\hbar \omega_H \cdot m_\perp S_e^2}} + \frac{1}{3} \right.$$

$$\left. + \frac{4U_0}{\hbar \omega_H} c(\theta) \right] \cosh \frac{3\sqrt{\hbar \omega_H \cdot m_\perp S_e^2}}{U_0}, \tag{10}$$

where

$$c(\theta) = [\sin^2 \theta \cdot \cos^2 \theta (m_\parallel - m_\perp)^2 + m_z^2] / $$
$$m_\perp ((m_z m_\parallel)^{1/2} + m_z),$$

$$\langle E_c^2 \rangle = E_d^2 + \frac{2}{3} E_d E_u + \frac{1}{3} E_u^2, \tag{11}$$

$$\frac{1}{m_{\omega_H}^2} = \frac{\cos^2 \theta}{m_\perp^2} + \frac{\sin^2 \theta}{m_\parallel m_\perp},$$

$$m_z = m_\perp \sin^2 \theta + m_\parallel \cos^2 \theta.$$

The magnetic field is aligned with the z axis and makes an angle θ with the rotation axis of the ellipsoid.

In the presence of a quantizing magnetic field the Boltzmann distribution of the carriers over the highly excited dislocation levels and energy levels in the band is preserved. However, the free carrier concentration in a magnetic field is changed in comparison with its equilibrium value since the density of states in the band is changed. If the distance between the dislocation levels is large in comparison with kT and if the ionization energy of a dislocation center is greater than kT ($E_D > kT$), then the condition of electrical neutrality yields the following expression for the electron density in the ultraquantum limit

$$n(H) = \frac{\gamma}{(2\pi)^{3/2}} \frac{m_\perp m_\parallel^{1/2} \omega_H (kT)^{1/2}}{\hbar^2} \exp(-E_D/kT)$$

$$= \frac{1}{2} N_{\omega_H} \exp(-E_D/kT), \tag{12}$$

where γ is the number of valleys in the conduction band. Note that expression (12) is valid if the applied quantizing magnetic field does not alter the ground-state energy of a bound electron, which indeed is the case provided $\hbar \omega_H \ll E_D$.

The formula for the thermal ionization in a quantizing magnetic field $\beta(H)$, which is derived from equality of the thermal-ionization and recombination fluxes under conditions of a Boltzmann carrier distribution, has the form

$$\beta(H) = \frac{1}{2} N_{\omega_H} \langle v_c \rangle \sigma \, e^{-\frac{E_D}{kT}}. \tag{13}$$

3. Let us consider a sample placed in crossed electric and quantizing magnetic fields. The electric field, on the one hand, deforms the dislocation well, i.e., it promotes an increase in the ionization process and a decrease in the capture process; on the other hand, it heats up the current carriers. The electron capture cross section is calculated in the ultraquantum limit as

$$\sigma(\mathcal{E}, H) = \sigma(H)\left(\frac{T}{T_e}\right)^{1/2}. \tag{14}$$

The electron density in this case is given by

$$n(\mathcal{E}, H) = n(H)\left(\frac{T_e}{T}\right)^{1/2}.$$

Here the electron temperature is given by

$$T_e = T\left[1 + \frac{1}{2}\left(\frac{c\mathcal{E}}{S_e H}\right)^2\right].$$

4. The limits of applicability of the results obtained are found from the condition of the possibility of using the method of cascade capture in external fields. For example, Eq. (9) is valid when the inequality $1 < r_s(\mathcal{E})/l \ll \delta_0^{-1}$ is satisfied. This inequality corresponds, on the one hand, to ap-plicability of the model of cascade capture and, on the other, to the dependence of the distribution function of electrons bound to a dislocation on their total energy. In quantizing magnetic fields the region of applicability of the obtained formulas is determined by the inequality $\hbar \omega_H \cdot m_\perp S_e^2)^{1/2} < kT \ll \hbar \omega_H$. We thus find $1 < H/H_{char} \ll kT/m_\perp S_e^2$.

In conclusion, let us estimate the values of the parameters $\mu_\perp$ and H_{char}. For example, in a germanium crystal $E_u \sim 16$ eV, $E_D \sim -6.5$ eV, $a \simeq 5.7 \times 10^{-10}$ m, $m_\parallel \sim 1.66 m_0$, $m_\perp \sim 0.082 m_0$, $\rho_0 \sim 2.3 \times 10^3$ kg/m^3, $T \sim 300$ K, and $S_e \sim 10^3$ m/s; for the parameters μ_1 and H_{char} we have $\mu_1 \sim (10^{-3}\mathcal{E})^2$ and $H_{char} \sim 10^5$ Oe, i.e., the system of electrons in a germanium crystal can be assumed to be heated if $\mathcal{E} > 10^3$ V/m; for values of $\mathcal{E} < 10^3$ V/m the external electric field can be assumed to be weak. For values of the magnetic field $H > H_{char}$ the quantization condition is satisfied, i.e., the formulas derived for a quantizing magnetic field are valid when $H > 10^5$ Oe.

[1] Z. A. Veliev, Fiz. Tekh. Poluprovodn. **32**, 36 (1998) [Semiconductors **32**, 29 (1998)].

[2] Z. A. Veliev, J. Fizika, **13**, No. 1 (1997).

[3] Z. A. Veliev, Fiz. Tekh. Poluprovodn. **17**, 1351 (1983) [Sov. Phys. Semicond. **17**, 858 (1983)].

[4] Z. A. Veliev, Fiz. Tekh. Poluprovodn. **19**(6), 1141 (1985) [Sov. Phys. Semicond. **19**, 700 (1985)].

[5] Z. A. Veliev, Fiz. Tekh. Poluprovodn. **24**, 553 (1990) [Sov. Phys. Semicond. **24**, 347 (1990)].

[6] B. K. Ridley, *Quantum Processes in Semiconductors* (Oxford Univ. Press, New York, 1986).

[7] *Handbook of Special Functions* [in Russian], Nauka, Moscow (1978), p. 321.

Translated by Paul F. Schippnick

Activation of impurities in ZnSe crystals, stimulated by a laser shock wave

A. Baĭdullaeva,*) A. I. Vlasenko, B. L. Gorkovenko, and P. E. Mozol'

Institute of Semiconductor Physics, National Academy of Sciences of the Ukraine, 252650 Kiev, Ukraine
(Submitted April 1, 1999; accepted for publication April 26, 1999)
Fiz. Tekh. Poluprovodn. **33**, 1303–1306 (November 1999)

The effect of a laser shock wave on the photoconductivity spectra and the thermally stimulated conductivity spectra and also on the temperature dependence of the photocurrent and dark current of ZnSe single crystals with different residual impurity levels is investigated. It is shown that a temperature dependence of the dark currents after passage of a shock wave is observed at higher shock-wave pressures for the less defective crystals, while activation of the photocurrent and dark current is due to the release of residual impurities from clusters during passage of the shock wave. © *1999 American Institute of Physics.*
[S1063-7826(99)00611-0]

Irradiation of II–VI crystals by laser pulses with power density below the threshold for destruction of the material leads to a substantial change in their physical properties. These changes are due to the formation, decay, or diffusion of defects due to heating, formation of an acoustic wave—or shock wave—as a result of the action of the laser radiation on the crystals.[1–3] On the other hand, defect formation depends on the initial state of the crystal; for example, the effect of the laser shock wave depends on the number of native lattice defects and dopant impurities in the initial sample.[2,3]

It is accordingly of interest to investigate the effect of a laser shock wave on the physical properties of crystals as a function of their level of structural perfection and impurity state. As our object of study we chose high-resistance ZnSe single crystals of varying degree of purity. The samples were divided into two groups: ZnSe-1 and ZnSe-2, depending on the residual impurity concentration $n = 10^{15}, 10^{14} \, \text{cm}^{-3}$. The impurity concentration was estimated from the electron spin resonance (ESR) spectra and from features in the low-temperature photoluminescence (PL) spectra. As the laser, we used a ruby laser operating in the Q-switched regime with pulse duration $t = 2 \times 10^{-8} \, \text{s}$ and power density $10^7 - 10^8 \, \text{MW/cm}^2$. The investigated sample, which had dimensions $2 \times 3 \times 1.5$ mm, was placed between a copper foil and a quartz substrate. The space between the foil and the substrate was then filled with an epoxy resin so that the distance from the crystal to the foil and to the substrate was $\sim 25 \, \mu$m. Ohmic contacts were deposited on the end-faces of the crystal. The copper foil served to prevent an unwanted photoelectric effect from direct or scattered laser light, and the quartz substrate served to absorb the unloading wave. The samples were irradiated at room temperature. The depth of formation of the shock waves and their pressure were estimated using formulas given in Refs. 4 and 5. The depths of shock wave formation in ZnSe for power densities of 40 and 80 MW/cm^2 were 110 and 77 μm, and the shock-wave pressure was $P_1 = 3.64$ and $P_2 = 5.14$ kbar, respectively. Measurements relating to the photoelectric effect in the unirradi-ated and irradiated crystals were performed on the side opposite the irradiated surface.

EXPERIMENTAL RESULTS

Two maxima are observed in the photoconductivity spectrum (I_{PC}) of the unirradiated sample ZnSe-1: $\hbar \omega_1 = 2.7$ eV, which corresponds to interband absorption of light, and $\hbar \omega_2 = 2.53$ eV, which is attributable to absorption on impurities (Fig. 1a, curve *1*). Passage of a shock wave with pressure P_1 of nondestructive amplitude in the crystal is followed by a decrease in the photoconductivity (PC) in the region of the fundamental absorption while in the region of impurity absorption the photoconductivity remains constant (Fig. 1a, curve *2*). When the pressure of the shock wave is increased to P_2, only the impurity band, whose magnitude is much less than that observed in the unirradiated crystal, is observed in the photoconductivity spectra (Fig. 1a, curve *3*).

Only one maximum is observed in the photoconductivity spectrum of an unirradiated ZnSe-2 crystal, corresponding to the fundamental absorption of light, whose magnitude is increased after the first irradiation, and is decreased after the second, but remains higher than its unirradiated value (Fig. 1b). After passage of a shock wave, a change is again observed in the magnitude of the photoconductivity, but this time accompanied by a shift of its red edge toward longer wavelengths by 27 meV.

Figure 2 presents spectra of the thermally stimulated current (I_{TSC}) of the ZnSe-1 and ZnSe-2 crystals before and after passage of the shock wave. In the initial ZnSe-1 spectra two peaks of the thermally stimulated conductivity are observed at $T = 148$ and 243 K (Fig. 2a, curve *1*). The energy position of the centers, determined by the Bube method, is $E_1 = 0.061$ eV at $T = 148$ K. Passage of a shock wave with pressure P_1 is followed by a decrease in the magnitude of the low-temperature thermally stimulated conductivity peak and an increase in the intensity of the high-temperature peak (Fig. 2a, curve *2*), whose energy position is $E_2 = 0.336$ eV.

In the initial thermally stimulated conductivity spectra of ZnSe-2 crystals, two peaks are observed at the temperatures
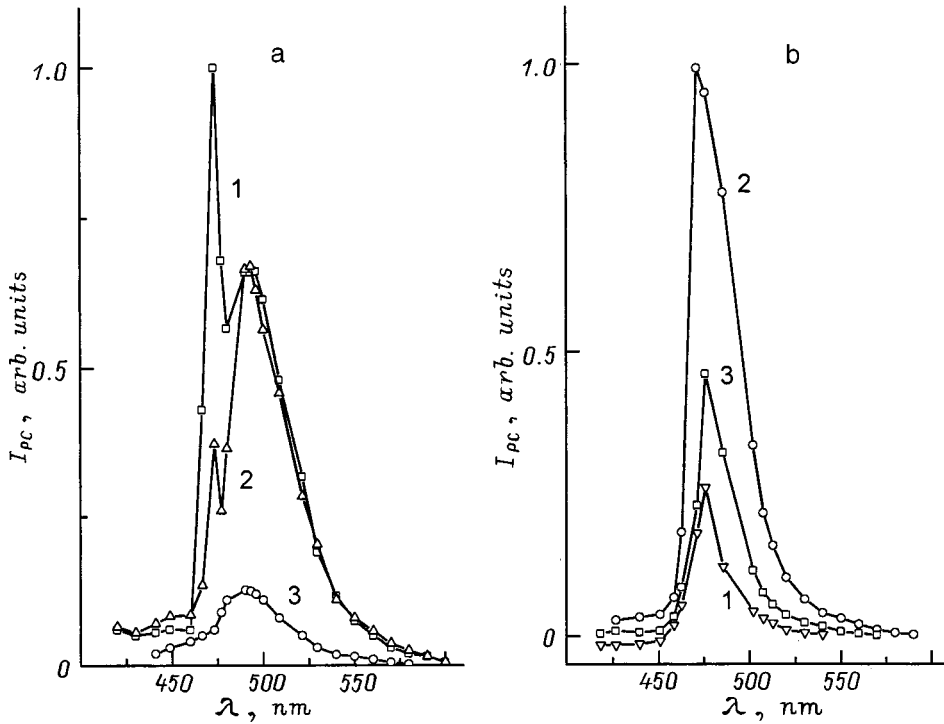
FIG. 1. Photoconductivity spectra of ZnSe crystals before (*1*) and after (*2, 3*) passage of the shock wave: a — ZnSe-1, b — ZnSe-2, $T = 300$ K.

166 and 243 K (Fig. 2b, curve *1*). After passage of the first shock wave, with pressure P_1, the magnitude and position of the thermally stimulated conductivity peaks remain almost unchanged, but after passage of the second shock wave, with pressure P_2, a high-temperature peak with $E_3 = 0.11$ eV is distinctly seen, and with further increase in the temperature the equilibrium conductivity is observed to grow, with activation energy $E_a = 0.68$ eV (Fig. 2, curve *2*).

Typical temperature curves of the photocurrents of ZnSe crystals of both groups are shown in Fig. 3. In the initial

crystals the photocurrent depends weakly on the temperature in the interval $80 - 200$ K, above which the effect of thermal quenching of the photocurrent (TQP) begins to play a role. Below this interval, the region of the maximum photoconductivity is bounded by thermal activation of the photocurrent (TAP), which depends exponentially on the temperature, with the photocurrent activation energy within the limits $E_4 = 0.03 - 0.06$ eV (Figs. 3a and 3b, curve *1*).

After passage of a shock wave with pressure P_1 through a ZnSe-1 crystal, the magnitude of the photocurrent falls.
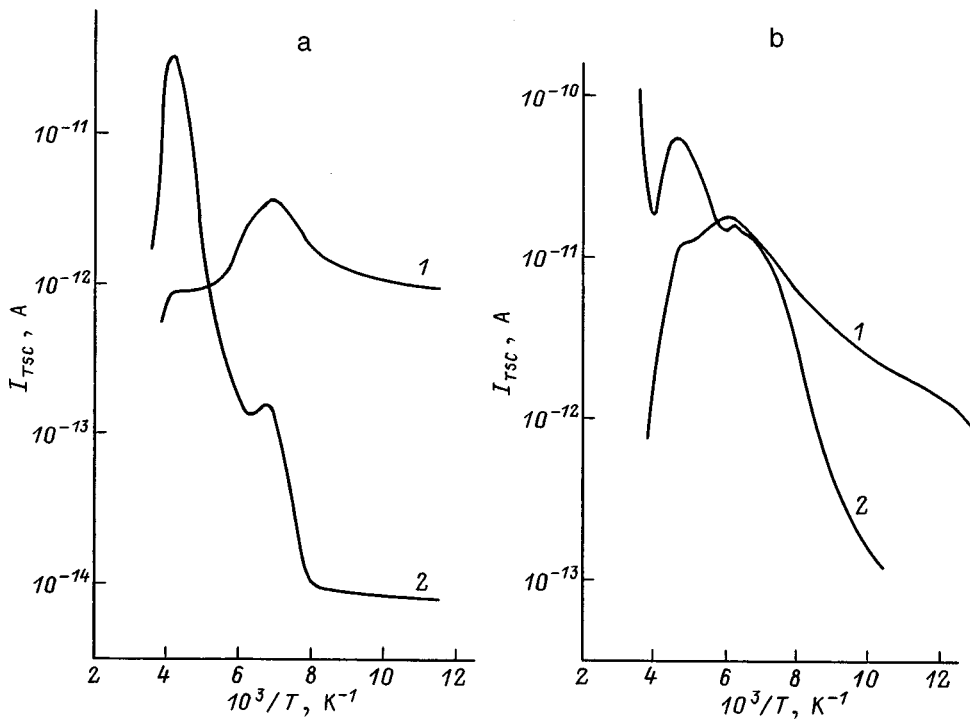

FIG. 2. Thermally stimulated conductivity spectra of ZnSe crystals before (*1*) and after (*2*) passage of the shock wave: a — ZnSe-1, b — ZnSe-2.
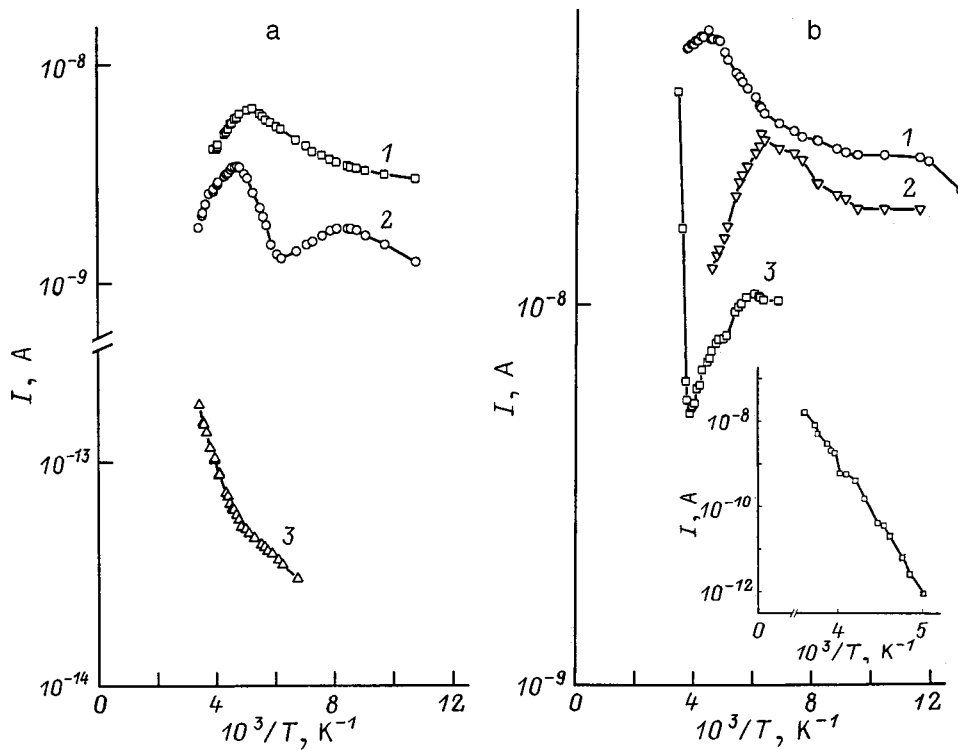
FIG. 3. Temperature dependence of the photocurrents and dark currents of ZnSe crystals before (*1*) and after (*2, 3,* and the inset) passage of the shock wave: a — ZnSe-1, *1, 2* — photocurrent, *3* — dark current; b — ZnSe-2, *1–3* — photocurrent, inset — dark current.

Besides the initial TQP region, an additional region of thermal quenching of the photocurrent is observed at 130 K (Fig. 3a, curve *2*). The TQP energy at low temperatures is the same as in the unirradiated sample, and at high temperatures $E_5 = 0.132$ eV. Upon passage of the shock wave with pressure P_2, the photocurrent continues to fall, preserving the form of its temperature dependence.

In the ZnSe-2 crystals after the passage of a shock wave with pressure P_1 the TQP region shifts toward lower temperatures ($T = 160$ K). The magnitude and activation energy of the photocurrent in the low-temperature region remain nearly constant in this case (Fig. 3b, curve *2*). After passage of the shock wave with pressure P_2, the photocurrent falls, all the while preserving the position of the TQP region. But above the TQP temperature interval ($T = 220$ K) the photocurrent is observed to grow, with activation energy of the photocurrent $E_a = 0.68$ eV (Fig. 3b, curve *3*), which coincides with the TQP activation energy at higher temperatures.

We were not able to record the temperature dependence of the dark currents of the unirradiated ZnSe crystals of either group. After passage of a shock wave, the dark current in both ZnSe-1 and ZnSe-2 exhibits a temperature dependence, but for different pressures of the shock wave. In the more defective crystals (ZnSe-2) temperature dependences of the dark current with activation energies of the impurity $E_6 = 0.03$ eV and $E_7 = 0.11$ eV (Fig. 3a, curve *3*) are observed at a lower pressure and a smaller shock wave than in the less defective ZnSe-2 crystals. In the latter the temperature dependence of the dark current with $E_a = 0.68$ eV appears upon the second irradiation (see the inset in Fig. 3b) and corresponds to the activation energy of the centers, found from the thermally stimulated conductivity spectra and the temperature dependence of the photocurrent.

DISCUSSION OF EXPERIMENTAL RESULTS

The decrease in the magnitude of the photoconductivity, the appearance of thermal quenching of the photoconductivity and activation of the dark current at low temperatures in the ZnSe-1 crystals after passage of the first shock wave can be explained by a transformation or increase of the native point defects already present in the starting crystal. According to Refs. 3–5, the energy of the shock wave is scattered by inhomogeneities of the solid (impurities, defects, thermal fluctuations). In our case, the initial scattering centers for the shock wave can be residual impurities and point defects (in ZnSe crystals, these are usually elements of group I and group III, interstitial atoms, and vacancies). Lagging behind the shift of the surrounding lattice in the shock-wave front, impurity atoms knock atoms out of their positions, thereby creating additional defects. As the shock wave passes through the crystal, in addition to the formation of interstitial atoms and vacancies, the release of residual impurities from complexes is possible with subsequent formation of defect complexes. Evidence of this behavior takes the form of the appearance of a temperature dependence of the dark current and the thermal quenching of the photoconductivity at low temperatures after passage of the shock wave, i.e., the passage of the shock wave is followed by the appearance of additional levels (0.03 and 0.11 eV). From their energy positions, these levels can be linked with atoms of group-III elements, which create donor levels, and can play the role of recombination *S*-centers. Thus, the introduction of *S* centers in high-resistance *n*-ZnSe, despite their relatively small number, can substantially alter the electron fluxes at the recombination *r*-centers. The contribution of the recombination flux through the recombination *r*-centers falls; this leads to a

decrease of the lifetime of the current carriers and, consequently, to a decrease of the photocurrent. This explains the observed spectral dependence of the photoconductivity upon passage of the first shock wave: The magnitude of the photoconductivity in the intrinsic absorption region is less than in the impurity region.

In high-resistance ZnSe crystals the recombination *r*-centers are deep acceptor levels responsible for the photosensitivity of the material. Their energy depths relative to the top of the valence band have been determined in many studies. They amount to $E_a = 0.6 - 0.7$ eV and are linked with a residual copper impurity which is present in the crystals.[6,7] Recombination *S*-centers with $E_3 = 0.11$ eV are also present in the crystals, and thermal quenching of photoconductivity at low temperatures is associated with these centers. Consequently, the increase in the photocurrent and the shift of thermal quenching of photoconductivity into the low-temperature region with a change in the dark current in the less defective ZnSe-2 crystals after passage of the first shock wave may be due to a restructuring of these centers. This is indicated by the distinct appearance of a high-temperature peak in the thermally stimulated conductivity spectrum after passage of the first shock wave. Growth of the photocurrent (relative to its initial value), the appearance of a temperature dependence of the dark current, activation regions in the temperature dependence of the photocurrent and the thermally stimulated conductivity at high temperatures after passage of the second shock wave may be due to the appearance or increase of the concentration of pre-existing *r*-centers in the crystal. According to the data in the literature, residual copper impurities are responsible for the level appearing after passage of the second shock wave. In this case the increase in the concentration of these centers may be due to the release of residual impurities from clusters as the shock wave passes through the crystal. The decrease in the photoconductivity in both groups of crystals after passage of the second shock wave is possibly also connected with damage to the crystals.

The diverse nature of the change in the photoconductivity of ZnSe crystals due to passage of shock waves with the same pressure can be explained by a different defect state of the starting material. It is known that the larger the number of scattering centers, the higher the probability for defect formation and damage to the material.[7] Upon passage of the second shock wave, the defects formed during passage of the first shock wave serve as new scattering centers. This leads to their accumulation and to an increase in their concentration. Since the ZnSe-1 crystals are more defective than the ZnSe-2 crystals, obviously the effect of a shock wave is manifested more strongly already upon first irradiation in ZnSe-1.

In summary, passage of a laser shock wave through ZnSe crystals of both groups is accompanied by an increase in the defect concentration due to a release of residual impurities from complexes. The effect of the shock wave on the electrical and photoelectric properties of the crystals depends on the original defect state of the material.

*)E-mail: baildulla@class.semicond.kiev.ua; Phone: (38044) 265 1875

———

[1] A. Baĭdullaeva, A. I. Vlasenko, Yu. V. Vlasenko, B. K. Dauletmuratov, and P. E. Mozol', Fiz. Tekh. Poluprovodn. **30**, 1438 (1996) [Semiconductors **30**, 1395 (1996)].
[2] V. A. Yanushkevich, Fiz. Khim. Obrab. Mater., No. 2, 47 (1979).
[3] Yu. N. Nikiforov and V. A. Yanushkevich, Fiz. Tekh. Poluprovodn. **14**, 534 (1980) [Sov. Phys. Semicond. **14**, 496 (1980)].
[4] V. A. Yanushkevich, Fiz. Khim. Obrab. Mater., No. 5, 9 (1975).
[5] *High-Speed Collision Phenomena,* edited by V. N. Nikolaevskiĭ (Mir, Moscow, 1973).
[6] V. V. Borshch, P. E. Mozol', I. I. Patskun, and I. V. Fekeshgazi, Fiz. Tekh. Poluprovodn. **16**, 339 (1982) [Semiconductors **16**, 213 (1982)].
[7] V. A. Korotkov, L. V. Malikova, and G. P. Grin'ko, *Physics of Semiconductors and Insulators*, Kishinev, Fiz. Nauki, 1982.

Translated by Paul F. Schippnick

Effects of heavy p doping on the polarized emission spectra and low-temperature luminescence spectra of GaAs/GaAsP strained-layer structures

A. V. Subashiev, Yu. A. Mamaev,*) B. D. Oskotskiĭ, and Yu. P. Yashin

St. Petersburg State Technical University, 195251 St. Petersburg, Russia

V. K. Kalevich

A. F. Ioffe Physicotechnical Institute, Russian Academy of Sciences, 194021 St. Petersburg, Russia

The optical orientation of electron spins in heavily doped, strained GaAs/GaAsP layers with a deformation-split valence band is studied experimentally. The observed polarized luminescence spectra and polarized photoemission (electron emission) spectra are shown to be described well by a model which allows for smearing of the edges of the bands by the fluctuation potential due to impurities, degeneracy of the carriers at low temperatures, and indirect electron–phonon optical transitions. The dominant mechanism of electron spin relaxation in strained layers is found to be the Bir–Aronov–Pikus mechanism. The parameters of the fluctuation potential and the parameters governing carrier spin relaxation are determined. © *1999 American Institute of Physics.* [S1063-7826(99)00711-5]

INTRODUCTION

The effect of heavy doping is observed in semiconductors in kinetic phenomena, by virtue of the sharp decrease of the contribution to the mobility from carriers below the mobility threshold, and in the optical absorption and luminescence spectra as a consequence of 1) narrowing of the band gap, 2) smearing of the band edges, and 3) changes in the optical matrix elements of the transition.[1]

In the optical spectra the enumerated effects of doping are hard to separate. This leads to ambiguity in the interpretation of the experimental results (see the discussion about the magnitude of the narrowing of the band gap[2,3] and the mechanism of edge absorption[4,5]). In p-doped materials, there are additional difficulties in the interpretation and analysis of the spectra, associated with the complex structure of the valence band and the acceptor states.[6]

New possibilities for studying the effects of doping have appeared in directed layers with a split valence band[7] in connection with studies of the optical orientation of the carriers. The interest that has been shown in these studies is connected with the use of directed p-doped structures to create lasers and spin-polarized electron emitters.[8]

Depending on the symmetry of the states of the valence band, during optical excitation of electrons from the heavy-hole subband by circularly polarized light (of negative helicity) near the absorption edge the polarization of the excited electrons $P_{c,\mathrm{ex}}$ turns out to be close to $P_{c,\mathrm{ex}}=1$ (i.e., the mean value of the projection of the electron spin onto the direction of the outer normal to the film surface is opposite the direction of the angular momentum of the exciting photon, which is $S_z=1/2$). Excitation from the light-hole subband produces electrons with oppositely directed spin.

For a large enough hole density the edge absorption from the heavy-hole subband is shifted as a consequence of the Moss–Burstein effect so that near the edge transitions from the detached light-hole subband become important.

The change in the dominant mechanism as a result of doping is accompanied by a dramatic change in the mean spin of the excited electrons, which is manifested in dramatic changes in the polarization in the polarized luminescence spectra and in the polarized electron emission spectra. This effect, predicted in Ref. 7, was observed in the polarized luminescence spectra of directed layers[9,10] and quantum wells.[11]

The dependence of the electron polarization on the excitation energy in the directed layers, by virtue of its dramatic variation, is very sensitive to peculiarities of the edge absorption associated with the position of the Fermi level, fluctuation smearing of the absorption edge, and Coulomb interaction effects. A study of polarization spectra can therefore be used to obtain information about these effects.

In the present paper we report the results of an experimental study of the effects of p doping in polarized low-temperature luminescence spectra and the spectra of polarized emission of electrons to vacuum. A comparison of the experimental spectra with the calculated spectra makes it possible to estimate the structure parameters and the parameters of the fluctuation potential, and to elucidate the mechanisms of electron spin relaxation.

MEASUREMENT PROCEDURE AND EXPERIMENTAL RESULTS

We investigated strained GaAs and $GaAs_{1-x}P_x$ layers of thickness $d=0.12-0.15\,\mu\mathrm{m}$, grown on $GaAs_{1-y}P_y$ buffer layers by vapor-phase epitaxy (chemical vapor deposition) from metallo-organic compounds (MOCVD) with $x=0-0.05$ and $y=0.28-0.32$. To obtain uniformly strained layers on (100) GaAs substrates, we grew a $GaAs_{1-y}P_y$ transi-

tional layer with a smoothly increasing phosphorus concentration (to match the lattice constants of the substrate and the buffer layer) and a sequence of layers $GaAs_{0.55}P_{0.45}$–$GaAs_{0.85}P_{0.15}$ (Ref. 12); the buffer layer and the strained layer were *p*-doped with Mg impurity, $N_a = (0.8-3) \times 10^{18}$ cm^{-3}. An arsenic coating was deposited on the surface of the layers to protect them from adsorption of impurities and oxidation. We examined the polarized luminescence spectra and luminescence excitation spectra at liquid-helium temperature. In addition, we measured at room temperature the spectral dependence of the quantum yield and polarization of the electrons emitted to vacuum. To observe photoemission, the atomically pure (after heating in vacuum to $T=600\,°C$) surface of the strained layer was activated by deposition of Cs(O) until a negative electron affinity was obtained.

The low-temperature ($T=4$ K) luminescence spectrum of the strained $GaAs/GaAs_{0.72}P_{0.28}$ layer (type-1 sample) with excitation energy 1.7 eV is shown in Fig. 1a. The points in this figure plot the luminescence polarization at the maxima of the two emission lines (corresponding to edge emission and emission during recombination at a shallow acceptor level) as a function of the excitation energy. The observed additional line, shifted toward longer wavelengths, can be assigned to luminescence from the space charge region near the surface. The extremely small width (for the given level of doping and deformation of the layers) of the luminescence lines testifies to the high degree of structural perfection of the strained layer. The abrupt falloff of the polarization is connected with the threshold for excitation from the detached light-hole band. The dip in this dependence, by virtue of its relatively large width, cannot be explained as an exciton effect, but is rather connected with the Moss–Burstein effect and the partial suppression of excitation from the heavy-hole subband.

The energy interval between the emission line at 1.545 eV and the position of the dip in the polarization enables us to estimate the magnitude of the deformation splitting of the valence band $\Delta_{def} \approx 40$ meV. This estimate of the splitting coincides with the value obtained by comparing the luminescence polarization spectra, and also the polarization spectra of the emitted photoelectrons, with the calculation presented below.

For a higher doping level it is possible to observe polarization of the emitted radiation close to zero, and even a change of sign in the polarization.[9,11] Note that the shape of the polarization spectra is completely similar for both lines, and the observed larger (by $\approx 10\%$) value of the polarization of the edge luminescence in the region of excitation from the heavy-hole subband are evidence of a somewhat larger interband recombination rate in comparison with recombination at an acceptor center. This interpretation is in accord with the magnitude of the polarization difference ($\approx 5\%$) in the excitation region above the threshold of absorption from the light-hole subband by virtue of the lower (close to 50%) electron polarization for excitation in this energy region.

For comparison, Fig. 1b plots luminescence spectra and luminescence polarization spectra of a $GaAs_{1-x}P_x/GaAs_{1-y}P_y$ layer with $x=5\%$ and $y=32\%$

(type-2 sample). The shift in the spectrum (by ≈ 50 meV) into the higher-energy region is a result of the phosphorus content of the layer and corresponds to the observed shift of the spectra of polarized electron emission. Note the smearing of the luminescence lines, the lower polarization at the maximum of the luminescence line, and the absence of a dip in the excitation spectrum, all attributable to the greater inhomogeneity of the structure.

Figure 2 plots the spectral dependence of the quantum yield and the polarization of the emitted electrons for a type-2 sample. The maximum value of the polarization ($P_{emi}=86\%$) was reproduced in a number of samples after repeated cycles of surface activation, including extended (one-hour) heating at $600\,°C$. The excitation energy corresponding to maximum polarization of the emitted electrons was $\hbar\omega_{max}=1.505$ eV. The quantum yield of photoemission (electron emission) at the excitation energy $\hbar\omega_{max}$ is sensitive to the particular features of the surface activation and the quality of the vacuum. It changed upon reactivation, reaching $Y_{max}=0.1\%$ under optimal conditions. The high value of the electron polarization observed is evidence of preservation in the layer of a uniform, strongly deformed state, and the high value of Y_{max} indicates that a negative electron affinity was obtained and that a high-quality Cs(O) activating layer was formed.

SPECTRAL DEPENDENCE OF THE POLARIZATION LUMINESCENCE AND THE PHOTOEMISSION

In the strained, heavily doped layers examined by us the energy relaxation time of the optically excited electrons amounts to fractions of a picosecond,[13] which is much less than the mean transport time of the carriers to the surface and the spin relaxation time. Therefore, the luminescence excitation spectrum and the emission spectrum reflect mainly electron polarization in the conduction band $P_{c,ex}(\hbar\omega)$ at the instant of excitation, which in turn is determined by the mean electron density $\langle n_\uparrow(\mathbf{r},\hbar\omega)\rangle$ and $\langle n_\downarrow(\mathbf{r},\hbar\omega)\rangle$ in the two spin states of the conduction band:

$$P_{c,ex}(\hbar\omega) = \frac{\langle n_\uparrow(\mathbf{r},\hbar\omega)\rangle - \langle n_\downarrow(\mathbf{r},\hbar\omega)\rangle}{\langle n_\uparrow(\mathbf{r},\hbar\omega)\rangle + \langle n_\downarrow(\mathbf{r},\hbar\omega)\rangle}. \tag{1}$$

The observed edge luminescence comes from the transition to the optical heavy-hole band, and the circular polarization of the emitted radiation (luminescence) P_{lum} (in the Faraday geometry) is proportional to the mean value of the degree of orientation of the electrons in the working layer. Electron emission into vacuum occurs from the space charge region at the surface. Therefore, polarization of the electrons emitted into the vacuum P_{emi} is determined by the degree of orientation of the electrons that have arrived at the surface. The quantities P_{lum} and P_{emi} are proportional to the electron polarization under excitation,

$$P_{lum}(\hbar\omega) = B_l P_r R_1 R_T P_{c,ex}(\hbar\omega),$$

$$P_{emi}(\hbar\omega) = B_s R_2 R_T P_{c,ex}(\hbar\omega), \tag{2}$$

where the coefficient B_l is governed by the degree of depolarization of the radiation emitted from the sample, the
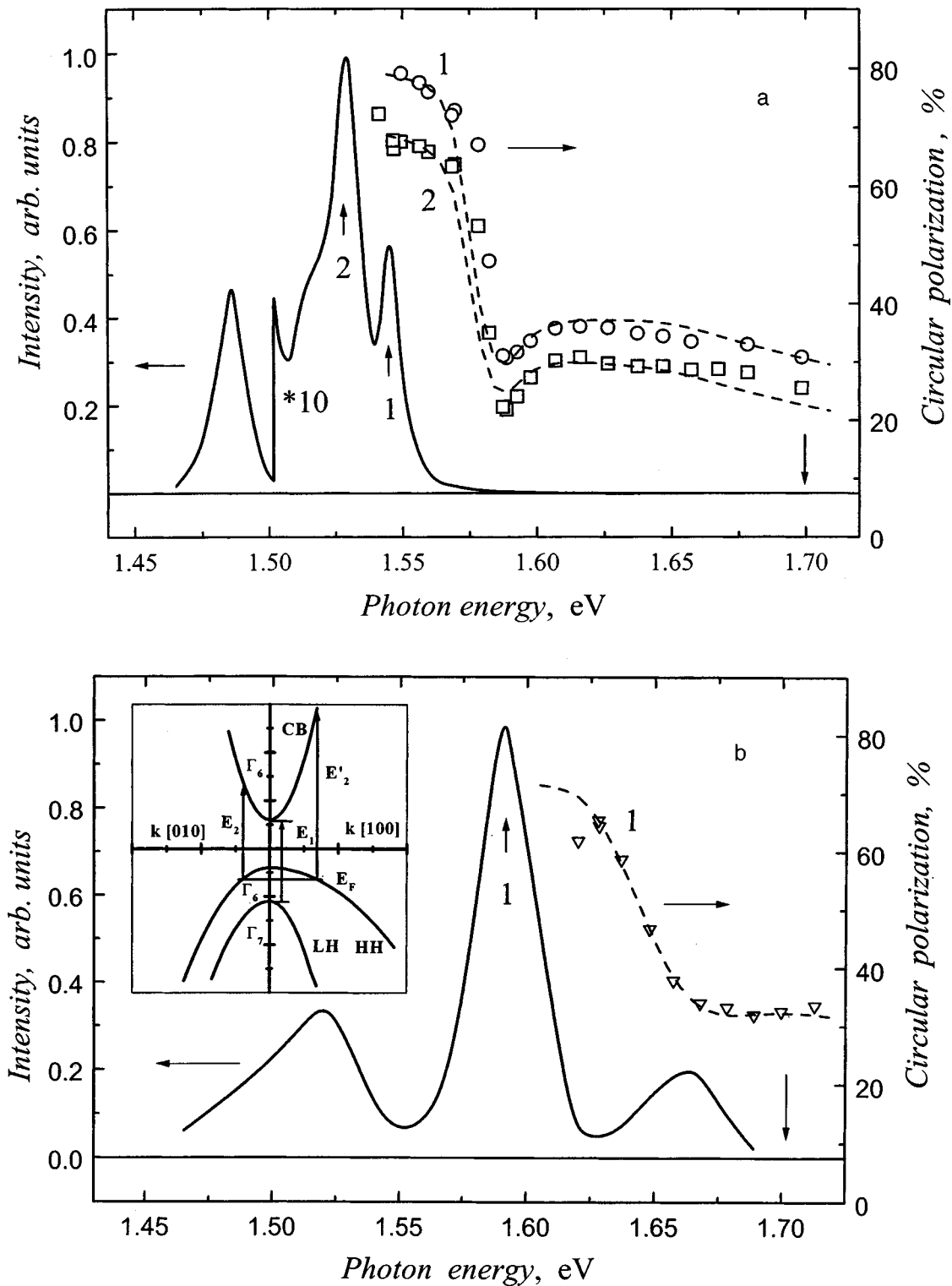
FIG. 1. Photoluminescence spectra (solid curves; arrow indicates excitation energy) and dependence of the luminescence polarization on the excitation energy (plotted as data points for the emission lines marked by arrows): for the structure GaAs/GaAsP (a) and the structure $GaAs_{0.95}P_{0.05}/GaAs_{0.78}P_{0.32}$ (b), $T = 4.2$ K; dashed curves — result of calculation of the polarization spectra for the parameter values shown in the table. The inset shows the band structure diagram of a (100) GaAs film compressed in the (100) plane. The vertical lines indicate thresholds of direct optical transitions from split states of light holes (E_1) and heavy holes (E_2, E_2') of the valence band to states of the conduction band; E_F is the Fermi energy.

coefficient B_s governs the loss of electron polarization due to electron relaxation in the space charge region and their emission into the vacuum, the factor R_T describes spin relaxation of carriers during thermalization, and the factors R_1 and R_2 describe spin relaxation of the thermalized electrons in the

working region. It is important that the coefficients B_l and B_s, and also the factors R_1 and R_2, do not depend on the excitation energy. The dependence of the luminescence observation function P_r on the energy of the emitted photons coincides with the dependence of $P_{c,ex}(\hbar\omega)$ on the excita-
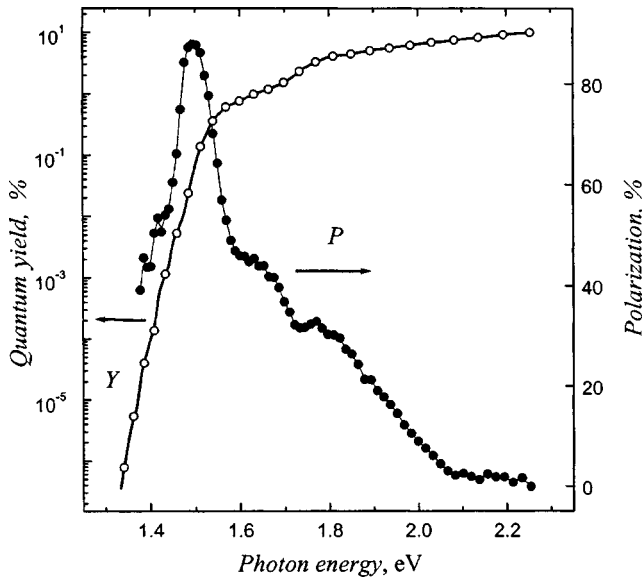
FIG. 2. Spectral dependence of the quantum yield $Y(\hbar\omega)$ and polarization of the emitted electrons $P_{emi}(\hbar\omega)$ in a *p*-doped structure with a strained GaAs$_{0.95}$P$_{0.05}$/GaAs$_{0.78}$P$_{0.32}$ layer, $T = 300$ K.

tion energy.[14] Near the edge of the interband transitions in the strained layer both quantities are close to unity.

The quantities $n_\uparrow$ and $n_\downarrow$ in Eq. (1) are proportional to the sum of the probabilities of the optical transitions $W_{J,\mu}^m$ with excitation of electrons to the states $m = \uparrow, \downarrow$ of the conduction band from different states J, μ with total angular momentum $J = 3/2$ of the *hh* and *lh* subbands of the valence band.

The resulting electron polarization $P_{c,\text{ex}}(\hbar\omega)$ is determined by the contribution of transitions from the light-hole and heavy-hole subbands. For an undoped semiconductor, the particular features of the calculation of the spectral dependence $P_{c,\text{ex}}(\hbar\omega)$ for direct optical transitions from a split valence band to the conduction band are given in Ref. 15. Features of the polarization spectrum due to heavy (*p*-type) doping were discussed in Ref. 7.

The steady state values of $n_\uparrow$ and $n_\downarrow$ should be calculated with allowance for the multistep nature of the kinetics of spin relaxation, recombination, and escape of electrons from the working layer to its boundaries ($x = 0, d$). The decrease in the polarization due to spin relaxation during thermalization of electrons is described by the dependence of the factor R_T on the energy of the excited electrons[14]

$$R_T = \exp(-\Phi), \quad \Phi = \int_{3kT/2}^{E} \frac{d\epsilon}{\epsilon} \frac{\tau_\epsilon}{\tau_s(\epsilon)}. \tag{3}$$

Here E is the energy of the excited electrons, τ_ϵ is the energy relaxation time, and $\tau_s(\epsilon)$ is the spin relaxation time. If the Bir–Aronov–Pikus mechanism is assumed to be the dominant mechanism of energy relaxation due to emission of optical phonons,[16] the quantity Φ takes the form

$$\Phi = \frac{\tau_{ph}}{\tau_{s,0}} \frac{E^{3/2} - (3kT/2)^{3/2}}{\hbar\Omega\sqrt{E_b}}, \tag{4}$$

where τ_{ph} is the time it takes an electron to emit an optical phonon with energy $\hbar\Omega$ and E_b is the binding energy of an acceptor. The quantity $1/\tau_{s,0}$ is proportional to the acceptor concentration and can be expressed in terms of the spin–spin exchange interaction constant.[16] Since $1/\tau_{s,0}$ varies in a complicated manner in a heavily doped, strained layer, this quantity was assumed to be a parameter of the calculations.

Steady-state values of $n_\uparrow$ and $n_\downarrow$ can be found by solving the diffusion equation[17] with allowance for spin relaxation of thermalized electrons, diffusion of electrons toward the surface, and their capture into the space charge region and at the heterojunction. For a thin working layer of thickness $d \ll L$, $1/\alpha$ (where L is the diffusion length, and α is the optical absorption coefficient) this gives

$$R_{1,2} = \frac{\tau_s^*}{\tau_s^* + \tau_{1,2}}, \tag{5}$$

where τ_s^* is the spin relaxation time of the thermalized electrons in the working layer; the quantities

$$\tau_{1,2} = [d/(S_{1,2} + S_h) + d^2/D]$$

govern the escape time of the electron from the working layer, $S_{1,2}$ is the surface recombination rate in respectively an unactivated sample and activated sample, S_h is the recombination rate at the heteroboundary with the buffer layer, and D is the diffusion coefficient. The surface recombination rate in activated samples is generally higher than in the unactivated samples used in the luminescence measurements, so $\tau_1 \geqslant \tau_2$.

The quantum yield of photoemission $Y(\hbar\omega)$ is defined in terms of the total concentration of electrons $n_\uparrow$ and $n_\downarrow$ excited into the two spin states of the conduction band, which is proportional to the total absorption coefficient α. Accordingly, for a thin layer we have[17]

$$Y = B_n(1 - R)\alpha d \frac{S_2}{S_2 + S_h} \frac{\tau}{\tau + \tau_2}, \tag{6}$$

where R is the reflection coefficient at the excitation frequency, τ is the lifetime, and the coefficient B_n is equal to the ratio of the flux of electrons emitted to vacuum and the flux of electrons arriving at the surface.

Smearing of the band edges due to the tails of the density of states leads to a change in the spectral dependence of the absorption and the mean electron polarization at the instant of excitation. It can be taken into account by averaging the quantities $n_\uparrow$ and $n_\downarrow$ over the fluctuations of the random potential of the electrons and holes. The results of such a calculation depend on the mechanism for the appearance of tails of the density of states of the bands. The results of calculations for a series of models of band tails were compared with experiment.

A large-scale potential, which is attributable to local fluctuations in the concentration of ionized acceptors, and which leads to a parallel random shift of the edges of both bands, arises in heavily *p*-doped structures. This potential can be taken into account by averaging the probability of excitation over the distribution of fluctuations of the hole Fermi level.[1] Another form of smearing of the interband absorption edge arises in the presence of a random potential

TABLE I. Parameters of strained doped GaAs and GaAsP layers, reconstructed from the luminescence and polarized-electron emission spectra.

Samples	1		2		SLAC-1	
T, K	4	293	4	293	12 (Ref. 9)	293 (Ref. 10)
E_g, eV	1.54	1.46	1.62	1.505	1.585	1.455
Δ_{def}, meV	43	43	40	40	50	50
γ_{lh}, meV	5	18	13	20	16	26
γ_{hh}, meV	7	19	16	21	18	28
S_0, 10^5 cm/s	2	100	5	100	1	10
τ_s, ps	200	23	143	27	100	80
B_N	$\cdots$	0.05	$\cdots$	0.2	$\cdots$	0.15
N_a, 10^{18} cm^{-3}	1.7	2.3	3	4	4	5.6

FIG. 3. Spectral dependence of the quantum yield Y and polarization of the emitted electrons P_{emi} in the structure GaAs$_{0.95}$P$_{0.05}$/GaAs$_{0.78}$P$_{0.32}$ with the strained layer near the absorption edge (points), $T = 300$ K. The solid curves were calculated using the parameters listed in the table. The dashed curve plots the polarization calculated without account of the contribution of indirect transitions.

field in the sample, leading to fluctuations of the width of the band gap. Such a potential arises in heavily doped p-type semiconductors with a small electron-to-hole mass ratio as a result of the small size and small capacity of the electron tails. In this case, fluctuations of the width of the band gap are governed by the tails in the valence band.

In the region near the absorption threshold, where the initial and final electron states are comparatively large-scale, fluctuations of the potential can be taken into account in the semiclassical approximation by averaging the transition probabilities over a Gaussian distribution of fluctuations of the band gap, so that

$$\langle W_i^\alpha \rangle = \int_{-\infty}^{\infty} W_i^\alpha(E_g + V) f(V) \, dV, \tag{7}$$

$$f(V) = \frac{1}{\sqrt{2\pi}\gamma} \exp\left(-\frac{V^2}{2\gamma_i^2} \right), \tag{8}$$

where γ_i are the tail parameters of the heavy-hole ($i = hh$) and light-hole ($i = lh$) bands. Comparison of the results of these calculations with experiment points in favor of this type of tail model. The remaining types of models of the fluctuation potential usually considered lead to results that are in poorer agreement with experiment.

DISCUSSION OF RESULTS AND PARAMETERS OF THE FLUCTUATION POTENTIAL

Experimentally obtained spectral dependences were used to determine the parameters of the photoemitter structures. Results of calculations of the luminescence polarization spectra for the two investigated samples are represented by the dashed lines in Figs. 1a and 1b. Values of the main parameters of the samples giving best agreement with experiment are given in Table I. Equation (4) is used to describe the decrease in the polarization of the luminescence line with growth of the excitation energy in the region of high excitation energies for typical parameter values: $\tau_{\text{ph}} = 0.15$ ps, $\hbar\Omega = 36.9$ meV, $E_b = 17$ meV, and $\tau_{s,0} = 60$ ps. Thus, in strained layers at low temperatures and high acceptor concentrations, the BAP mechanism, which is attributable to the electron–hole exchange interaction, is the dominant mechanism.
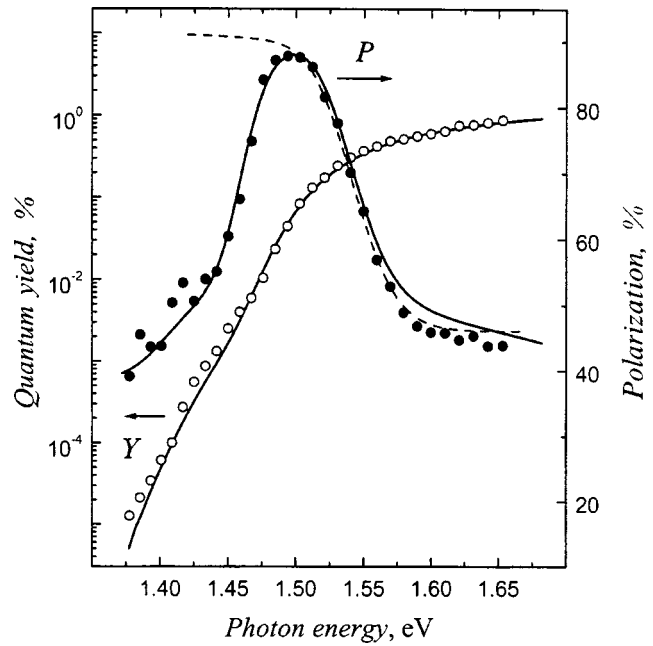
The second calculated curve, which is shown in Fig. 1a and which corresponds to recombination via acceptor states, was obtained using a larger value of the lifetime τ^* ($\tau/\tau^* = 0.6$) with all the other parameters of the sample the same.

Results of our comparison of the experimental and calculated spectral dependences of the quantum yield of photoemission and polarization of the emitted electrons ($T = 300$ K) in the absorption region of the working layer are shown in Fig. 3 for a type-2 sample. The parameters of the samples, determined from a comparison of the experimental and calculated dependences, are given in Table I (in particular, $L = 10^{-4}$ cm, $D = 50$ cm^2/s, and $S_1 = 10^5$ cm/s) were chosen in line with their characteristic values for photocathode structures.[9]

Spin relaxation under conditions of thermalization of carriers also turns out to be substantial at room temperature, and leads to a decrease of the polarization with growth of the excitation energy. An alternative mechanism of polarization loss (which could be identified in experiments recording polarization of hot electrons and polarized emission resolved in energy) consists in excitation of electrons with opposite spin from the fluctuation states of tails of an extended transitional layer on the back side of the working layer.

In comparison with the low-temperature values of the parameters inferred from the luminescence spectra, the degree of smearing of the band gap is markedly increased.

The emission spectra make it possible to determine the polarization of the electrons excited by radiation with energy less than the mean value of E_g. The steep falloff of the polarization observed may be due to an increase in the escape time of the electrons excited into the tails of the con-

duction band from the working layer to the surface (i.e., a decrease in R_2) and to a lower degree of polarization of the electrons at the moment of their creation. Calculations and comparison with experiment show that the magnitude of the electron tails of the density of states is small, which points in favor to the latter mechanism of the polarization falloff.

The polarization of the electrons when they are excited near the interband absorption edge and below it is determined not only by direct interband transitions, but also by transitions with absorption of optical phonons, with a virtual transition of a hole to an intermediate state of a heavy-hole band or a detached light-hole band. Such transitions lead to population of both states of the conduction band and a substantial decrease of the polarization of the electrons at the moment of their creation. In addition, these transitions alter the absorption spectrum in a doped layer (and hence the frequency dependence of the photoemission quantum yield) in the region of the tails.

Results of calculation of the polarization of emission and the quantum yield for type-2 samples, with allowance for indirect transitions with the participation of optical phonons, are shown in Fig. 3.

Note that to obtain similar behavior of the experimental and calculated dependences it is necessary to allow for narrowing of the band gap due to doping, which for a type-1 sample amounts to roughly 0.03 eV at low temperatures and ≈ 0.01 eV at room temperature.

The shape of the emission spectra for $\hbar \omega \lesssim E_g$ is sensitive to the behavior of the absorption coefficient in this region, i.e., to the form of the tails of the density of states. Calculation using Urbach tails, tails of the Gal'perin–Lax model, and the model in which smearing of the absorption edge is due to local fluctuations of the hole Fermi level[1] are in noticeably poorer agreement with experiment. The difference in the parameters characterizing the samples at the two measurement temperatures is in reasonable agreement with their expected temperature dependence.

According to the calculated results, emission of electrons into vacuum from the space charge region is accompanied by minimal polarization losses, which do not exceed 2% ($B_s \geqslant 0.98$).

We carried out analogous calculations for the low-temperature luminescence data and polarized emission data presented in Refs. 9 and 10. The photocathode structure parameters (SLAC-1) recovered from a comparison of the calculated spectra with the experimental data of Refs. 9 and 10 are listed in the table. The parameter values determined by us correspond to a significantly greater acceptor concentration than in our samples (of types 1 and 2) (which is in line with the data presented in Refs. 9 and 10) and similar values of the remaining parameters. This testifies to the similar quality of the samples and the reliability of the chosen calculational model.

CONCLUSIONS

Our study of polarized luminescence spectra and polarized electron emission spectra in strained, heavily doped, thin layers of GaAs and GaAsP shows that the observed spectral features are well described within the framework of the diffusion model.

An important mechanism for the decrease of electron polarization when they are excited into the tails of the density of states near the absorption edge is loss of polarization at the instant of excitation, determined by the contribution of indirect transitions with participation of optical phonons. With growth of the excitation energy, we see a decrease of the polarization, which indicates that the Bir–Aronov–Pikus mechanism is the dominant mechanism for spin relaxation.

Comparison of calculation with experimental data allowed us to determine the deformational splitting of the valence band, the carrier concentration, the tail parameters of the bands, and the parameters governing carrier spin relaxation.

*)E-mail: mamaev@spes.stu.neva.ru; Fax: +7(812) 552 67 06

[1] B. I. Shklovskiĭ and A. L. Efros, *Electronic Properties of Doped Semiconductors* (Springer-Verlag, New York, 1984).

[2] D. N. Bychkovskiĭ, O. V. Konstantinov, and B. V. Tsarenkov, Fiz. Tekh. Poluprovodn. **24**, 1848 (1990) [Sov. Phys. Semicond. **24**, 1151, (1990)]; O. V. Konstantinov, O. I. Obolenskiĭ, and B. V. Tsarenkov, Fiz. Tekh. Poluprovodn. **31**, 571 (1997) [Semiconductors **31**, 484 (1997)].

[3] S. C. Jain and D. J. Roulson, Solid-State Electron. **28**, 11 (1985).

[4] A. A. Klochichin, Phys. Rev. B **52**, 10 979 (1995).

[5] H. S. Bennet and J. R. Lowney, Appl. Phys. **62**, 521 (1987).

[6] A. Balderesci and N. O. Lipari, Phys. Rev. B **8**, 2697 (1973); Phys. Rev. B **9**, 1525 (1974).

[7] A. V. Subashiev and E. P. German, in *Proceedings of the International Symposium ''Nanostructures: Physics and Technology''* (St. Petersburg, Russia 1997), p. 130; E. P. German and A. V. Subashiev, JETP Lett. **65**, 909 (1997).

[8] A. V. Subashiev, Yu. A. Mamaev, Yu. P. Yashin, and J. C. Clendenin, Phys. Low-Dimens. Semicond. Struct. **1/2**, 1 (1999).

[9] R. Mair, *A Polarized Photoemission Study of Strained-Layer* GaAs *Photocathodes*, SLAC–Reprint-448 (1996).

[10] T. Maruyama, E. L. Garwin, R. Prepost, and G. H. Zapalac, Phys. Rev. B **46**, 4261 (1992).

[11] S. Wongmanerod, P. O. Holtz, K. Reginski, B. Sernelius, B. Monemar, M. Bugajski, O. Mauritz, and M. Godlewski, in *Proceedings of the 24th International Conference on Physics of Semiconductors*, Tel-Aviv, 1998 (World Scientific, Singapore, 1998).

[12] Yu. A. Mamaev, Yu. P. Yashin, A. V. Subashiev, M. S. Galaktionov, B. S. Yavich, O. V. Kovalenkov, D. A. Vinokurov, and N. N. Faleev, Phys. Low-Dimens. Semicond. Struct. **7**, 27 (1994).

[13] D. N. Mirlin and V. I. Perel', ''Hot-Electron Photoluminescence under CW Pumping.'' in *Spectroscopy of Nonequilibrium Electrons and Photons*, edited by C. V. Shank and B. P. Zakharchenya (North-Holland, 1992), p. 269.

[14] M. I. D'yakonov and V. I. Perel', Zh. Éksp. Teor. Fiz. **60**, 1954 (1971) [Sov. Phys. JETP **33**, 1053 (1971)].

[15] G. L. Bir and E. L. Ivchenko, Fiz. Tekh. Poluprovodn. **9**, 1300 (1975) [Sov. Phys. Semicond. **9**, 1275 (1975)].

[16] G. L. Bir, A. G. Aronov, and G. E. Pikus, Zh. Éksp. Teor. Fiz. **67**, 1386 (1975) [*sic*].

[17] B. D. Oskotskij, A. V. Subashiev, and Yu. A. Mamaev, Phys. Low-Dimens. Semicond. Struct. **1/2**, 77 (1997).

Translated by Paul F. Schippnick

Deep-level transient spectroscopy of radiation-induced levels in 6H-SiC

V. S. Ballandovich

St. Petersburg State Electrotechnical University, 197376 St. Petersburg, Russia

The methods of capacitance and current deep level transient spectroscopy are used to investigate single crystals of Leli n-SiC($6H$) irradiated by 5-MeV electrons at doses of $10^{16} - 10^{18}\,cm^{-2}$. Eleven deep levels belonging to the resulting radiation-induced intrinsic defects were observed in the energy range 0.18–1.44 eV from the bottom of the conduction band. Isochronous annealing of various samples showed that most of the observed defects were stable up to a temperature of $\sim 1000\,°C$. In addition, annealing of a deep level with ionization energy $E_i = 0.48 - 0.53$ eV was observed in the temperature range $150 - 250\,°C$. It is believed that this center is caused by a vacancy in the carbon sublattice. © *1999 American Institute of Physics.* [S1063-7826(99)00811-X]

Silicon carbide, by virtue of its unique physical and chemical properties, is an attractive material for making high-reliability electronic devices. In particular, its high stability against irradiation ensures that devices based on it can operate at high radiation levels. The characteristics of such devices under these conditions will be for the most part determined by the presence of electrically active structural defects induced in the material during irradiation. Therefore, the parameters of these centers, the conditions under which they appear, and their annealing are of considerable interest. A further stimulus for the study of these questions is the use of ion doping technology to create various structural elements based on SiC.

A method for determining the parameters of deep levels that is especially popular these days is deep level transient spectroscopy (DLTS).[1] Use of this method to study radiation-induced defects in SiC has revealed that irradiating silicon carbide with high-energy particles leads to the formation of a large number of intrinsic defects with energy levels located in the upper half of the band gap. The parameters of these centers have been enumerated in Refs. 2–4. However, despite the accumulating experimental material, many questions remain open regarding the identification of radiation-induced deep levels, their energy positions, charge states, etc.; therefore, the need for continuing investigations in this area remains.

In the overwhelming majority of papers devoted to deep levels in silicon carbide, the signal that records the DLTS spectra comes from capacitive relaxation of a $p-n$ junction or Schottky barrier. However, it is well known that many of the radiation-induced deep levels in silicon carbide have similar ionization energies, so that DLTS spectra of irradiated crystals obtained by capacitive DLTS consist of broad bands formed by overlapping peaks, which hinders the processing of the results. In this case, DLTS spectra obtained by measuring current relaxation can be more informative. Since current signals are the first derivative with respect to time of the change in space charge, current DLTS makes it possible to improve the energy resolution of closely spaced deep lev-

els, since the relative width of the DLTS peaks corresponding to them decreases. An additional advantage of this method is its low sensitivity to changes in the series resistance of the sample, a matter of no small importance in view of the strong dependence of the resistivity of SiC on temperature.

In this paper we describe our studies of radiation-induced deep levels in n-SiC single crystals using capacitive and current DLTS. We paid particular attention to low-temperature annealing of radiation-induced defects in light of the information published in Ref. 3. We discuss how low-temperature annealing affects the DLTS spectrum of irradiated SiC crystals, taking into account the results of ESR studies of primary defects.[5,6]

SAMPLES AND EXPERIMENTAL METHODS

In our studies we used single crystals of Leli $6H$-SiC doped with nitrogen. Initial concentrations of weakly compensated donors in our samples, as derived from capacitance-voltage characteristics, were in the range $3 \times 10^{16} - 8 \times 10^{17}\,cm^{-3}$ The samples were separated into three groups and irradiated with 5-MeV electrons at doses of 10^{16}, 10^{17}, and $10^{18}\,cm^{-2}$. Electron bombardment is the most convenient way to create point defects, since the concentration of induced centers is relatively small and uniformly distributed over the crystal volume. Because the samples were attached to a cooled copper holder with low-temperature solder, their temperature never exceeded $50\,°C$ in the course of the irradiation, after which the solder was removed at $T \simeq 75\,°C$. The characteristics of these samples are presented in Table I.

Before irradiation, Cr–SiC Schottky barriers ($\phi = 0.5$ mm) were grown on the crystals, starting with an all-carbon crystal surface. The measurements were made in the temperature range 85–650 K. A reverse bias of 3–5 V was applied to the barrier, and the traps were filled by decreasing this bias to 0 V. The duration of the filling pulses was 1 ms. The ionization energy and capture cross section of the centers under study were determined from Arrhenius

TABLE I. Irradiation dose and starting concentration of uncompensated donors in the test samples.

	Radiation dose, cm^{-2}				
	10^{16}		10^{17}		10^{18}
Sample	$N_D - N_A$, 10^{16} cm^{-3}	Sample	$N_D - N_A$, 10^{17} cm^{-3}	Sample	$N_D - N_A$, 10^{17} cm^{-3}
$e16-1$	8.0	$e17-1$	0.55	$e18-1$	7.3
$e16-2$	3.1	$e17-2$	2.3	$e18-2$	3.0
$e16-3$	4.6	$e17-3$	1.9	$e18-3$	4.6
		$e17-4$	3.9		
		$e17-5$	2.3		

plots. In making these plots, the ''discrimination window'' was varied from 6.7×10^4 s^{-1} to 67×10^4 s^{-1} for current DLTS, and 1.63×10^3 s^{-1} to 9.19×10^3 s^{-1} for capacitive DLTS. In the temperature range 85–500 K we mostly used current DLTS. At higher temperatures, where recording current DLTS spectra becomes difficult due to increasing leakage current, the deep-level parameters were determined from capacitive measurements. The DLTS spectra were measured for $\tau_m = 1.49$ and 10.88 ms in the current and capacitive relaxation regimes. The spectra of current DLTS were reduced to the form $J_0 / \Delta W$, where J_0 is the initial current density through the barrier at the maximum of the DLTS peak and $\Delta W = W(V) - W(0)$ is the change in the width of the space-charge region at the instant the filling pulse passes through it.

In order to study the thermal stability of the induced defects, the samples were subjected to isochronous 10-min anneals up to a temperature of 1600 °C. In the range 100–500 °C they were annealed in vacuum while in the cryostat of the measurement apparatus. All spectra in this temperature range were measured using the same barrier structure, allowing us to eliminate the effects of spatial nonuniformity of the crystal properties on the measurement results. At higher temperatures the crystals were annealed in a special graphite furnace in an argon atmosphere. In this case the barriers were first removed and then re-made after each annealing stage.

RESULTS OF EXPERIMENTS AND DISCUSSION

Figure 1 shows current DLTS spectra of one of the n-SiC($6H$) samples irradiated with electrons at a dose of 10^{16} cm^{-2} and annealed in the temperature interval 75–250 °C. For comparison, we also show a DLTS spectrum of this sample measured in the capacitive relaxation regime (curve $1'$).

Two features usually dominate the low-temperature portions ($T \lesssim 300$ K) of DLTS spectra taken from irradiated single crystals of n-SiC($6H$) that are not subjected to special annealing (the solid curves in Fig. 1). One is a wide band consisting of two overlapping peaks L_3 and L_4 with maxima near 200 and 220 K, respectively, and an isolated peak denoted by L_6. The band $L_3 - L_4$ is well known from the earliest publications on radiation-induced defects in n-SiC($6H$) crystals irradiated by electrons and investigated by DLTS.[7,8] In Ref. 7 this band was assigned to a level $E_c - 0.35$ eV. Zhang et al.[8] showed that this band had a structure and was

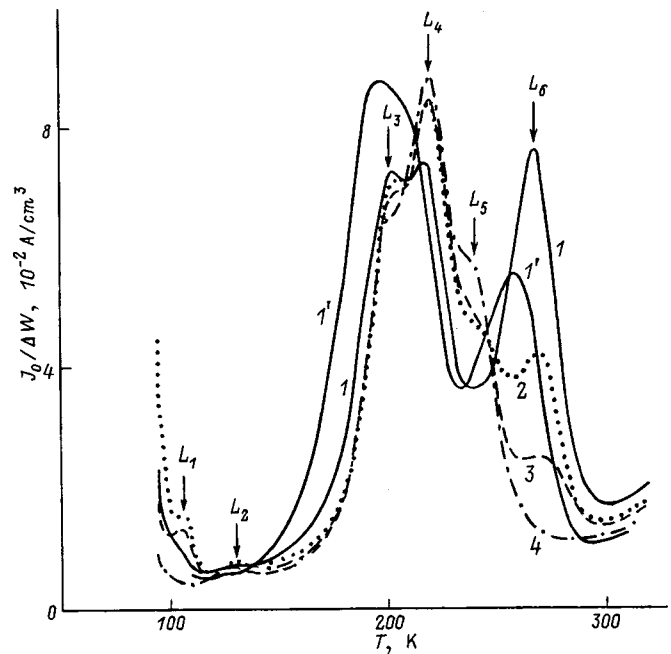FIG. 1. DLTS spectra for sample $e16-1$ irradiated with electrons ($E = 5$ MeV) at a dose 10^{16} cm^{-2} and annealed in the temperature range 75–250 °C. Measurement methods: 1–4— current DLTS, $\tau_m = 1.49$ ms; $1'$—capacitance DLTS, $\tau_m = 10.88$ ms. Anneal temperature T_a, °C: $1,1'$—75, 2—150, 3—200, 4—250 K. Dependences $1'$, 1–4 are denoted by: $1,1'$—solid curves, 2—dotted curve, 3—dashed curve, 4—dotted-dashed curve.

due to two centers, labeled E_1 / E_2, with similar ionization energies. It is difficult to resolve the energy positions of these centers when recording DLTS spectra in the capacitive relaxation regime (see the curve $1'$ in Fig. 1); therefore, the ionization energy reported in the literature is an average of both centers. Based on data from various sources in which T^2 corrections were used, this amounts to 0.35–0.39 eV.[4,8] It is clear from Fig. 1 that the resolution of peaks L_3 and L_4 is greatly improved by recording the DLTS spectra in the current relaxation regime, making it possible to determine the following values of the ionization energies of the centers: (0.37–0.40) and (0.40–0.44 eV). Here and in what follows, the data are presented as pairs of numbers in parentheses, where the first number is derived by assuming that σ_n = const, the second by assuming that $\sigma_n \sim T^{-2}$. These numbers are average values calculated from the results of measurements in various crystals. Scatter in the experimental data for each deep level did not exceed ± 5%. The peak L_6 was previously observed by the authors in Ref. 5. Capacitive measurements imply that the position of the deep level corresponding to this peak was $E_c - 0.44$ eV. This peak appears only in DLTS spectra of those samples for which barrier structures were created before irradiation. The results of our current DLTS measurements imply that the ionization energy of the center corresponding to the peak L_6 equals (0.48–0.53) eV.

A commonly encountered question is: to what extent do the results of capacitance and current measurements correspond to one another? In order to answer this question, we made comparative measurements on samples whose DLTS
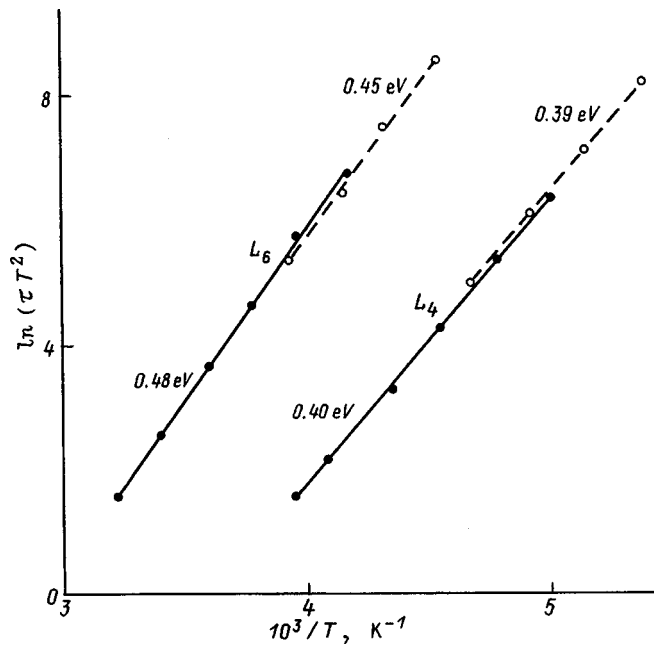
FIG. 2. Arrhenius plots for two deep levels L_4 and L_6 in $6H$-SiC, plotted on the basis of measurements of current-DLTS spectra (solid curves) and capacitance DLTS spectra (dashed curves). The corresponding activation energies are printed next to the straight lines.

FIG. 3. Current-DLTS spectra ($\tau_m = 1.49$ ms) of sample $e18$–1 irradiated by electrons ($E = 5$ MeV) at a dose 10^{18} cm^{-2} and annealed in temperature range $75 - 250$ °C. Anneal temperature T_a, °C: 1—75, 2—250.

spectra contained well-expressed isolated peaks. Figure 2 shows Arrhenius plots for levels L_4 and L_6, using data from current DLTS spectra (solid curves) and capacitive DLTS spectra (dashed curves). Comparing the results, we note that the activation energy (shown in Fig. 2) and capture cross section of the deep levels calculated from capacitance measurements are as a rule somewhat smaller than the same parameters obtained from current DLTS spectra. An analogous difference was observed in Ref. 9 in investigations of deep levels in light-emitting diodes made from $6H$-SiC. The reason for this discrepancy is probably the nonexponential nature of the transient process, which is rather typical of silicon carbide.

Increasing the radiation dose leads to broadening of the DLTS spectra; in this case, the band $L_3 - L_4$ can merge either partially or completely with peak L_6 (Fig. 3). The observed broadening of the DLTS peaks allows us to assert that when the concentrations of radiation-induced defects are large, the energy states corresponding to them are not discrete but rather are distributed in some way over the band gap. Measurements show that the rate of filling of deep levels slows down with increasing irradiation. The total concentration of defect levels L_3 and L_4 in samples irradiated at doses of 10^{16}, 10^{17} and 10^{18} cm^{-2} are found to be in the ranges $(3-5) \times 10^{15}$, $(2-4) \times 10^{16}$, and $(5-8) \times 10^{16}$ cm^{-3}, respectively. The concentrations of L_6 centers in samples from the same groups were $(2-4) \times 10^{15}$, $(1-4) \times 10^{16}$, and $(5-9) \times 10^{16}$ cm^{-3}.

Annealing these crystals leads to a considerable transformation of the spectra (Fig. 1), even at temperatures as low as $150 - 200$ °C. The height of the peak L_6 decreases while the band $L_3 - L_4$ shifts by several degrees to high temperatures, and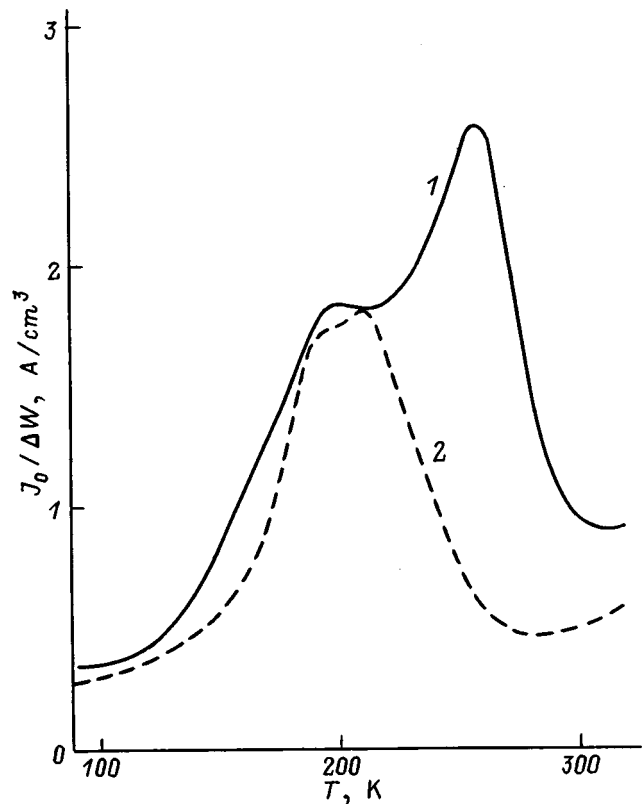 an additional peak L_5 caused by a center with ionization energy $0.42 - 0.46$ eV appears in the neighborhood of 242 K. In the majority of cases the peak L_5 is observed as a "shoulder" on the high-temperature slope of band $L_3 - L_4$. The intensities of the two signals that make up peaks $L_3 - L_5$ are related to one another in arbitrary ways in different samples. This indicates that all three levels belong to different centers, whose relative concentrations depend on the individual features of the crystal. Peak L_6 disappears completely when the samples are heated to a temperature of 250 °C. Subsequent annealing of these crystals at temperatures in the range $250 - 500$ °C produces no further significant changes in the DLTS spectra near the band $L_3 - L_5$.

High-temperature annealing of point defects in SiC has been observed by a number of authors who used electron spin resonance (ESR) and positron diagnostics to investigate silicon carbide irradiated by nuclear particles.[5,6,10,11] These authors established that simple point defects, i.e., Frenkel pairs and single vacancies, are annealed out in the range $100 - 750$ °C; i.e., the thermal stability of these defects in SiC is considerably higher than in other diamond-lattice semiconductors. Vacancy associates and impurity-defect complexes have characteristic annealing temperatures that exceed 100 °C. Judging from these data we may conclude that the centers responsible for level L_6 are a few primary intrinsic defects, some of which transform at a temperature $150 - 250$ °C into more complicated centers, while the rest recombine or are captured at sinks (for example, dislocations).

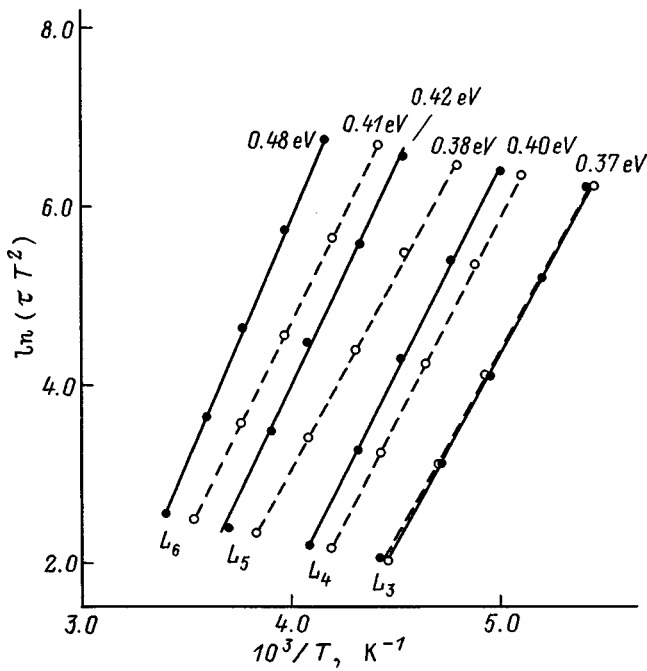The annealing dynamics of level L_6 coincides with the

FIG. 4. Influence of electric field intensity E on the ionization energy of radiation-induced deep levels in $6H$-SiC. Approximate value of E, 10^4 V/cm: solid curve—8, dashed curve—40.

FIG. 5. DLTS spectra of sample $e17-1$ irradiated with electrons ($E = 5$ MeV) at a dose 10^{17} cm^{-2} and annealed in the temperature range 900-1600 °C. Measurement methods: a—current DLTS, $\tau_m = 1.49$ ms; b—capacitance DLTS, $\tau_m = 10.88$ ms. Annealing temperature T_a, °C: solid curves—1000, dashed curves— 1500.

behavior of a carbon vacancy V_C in $3C$-SiC.[5,6] Both in the former and the latter cases, the majority of induced defects are annealed out in the temperature range 100–200 °C. This correspondence leads us to think that both centers are identical, a conclusion that is not contradicted by studies of charge states of the L_6 center using the double-correlation DLTS method. Figure 4 shows Arrhenius plots for levels L_3-L_6 made from current DLTS spectra for two values of the electric field intensity: $E \approx 8 \times 10^4$ V/cm (solid curves) and $E \approx 4 \times 10^5$ V/cm (dashed curves). These plots show that the position of peak L_3 and activation energy of the corresponding center do not depend on the electric field intensity, while for $E > 10^5$ V/cm the other peaks shift to lower temperatures; this shift, which is most significant for level L_4, is not accompanied by changes in activation energy. Thus, the behavior of levels L_3 and L_4 in an electric field suggests electron capture by neutral centers, implying that L_3 and L_4 are levels of acceptor type. This conclusion agrees with the description of the charge state of centers E_1/E_2 given in Ref. 4. The presence of acceptor levels located not far from the bottom of the conduction band explains the fact that irradiation of n-SiC crystals leads to compensation of the primary doping impurity, i.e., nitrogen, without decreasing the concentration of uncompensated donors enough to account for the room-temperature concentration deduced from capacitance-voltage characteristics.[7] Conversely, the activation energy of levels L_5 and L_6 decreases with increasing electric field intensity, indicating capture of electrons at positively charged centers; i.e., the center L_6 behaves like a deep donor, which corresponds to the charge state of the carbon vacancy V_C^+ and V_C^0 in p- and n-type $3C$-SiC, respectively.

Much weaker peaks caused by charging of electronic traps with activation energies 0.18–0.25 eV can be observed
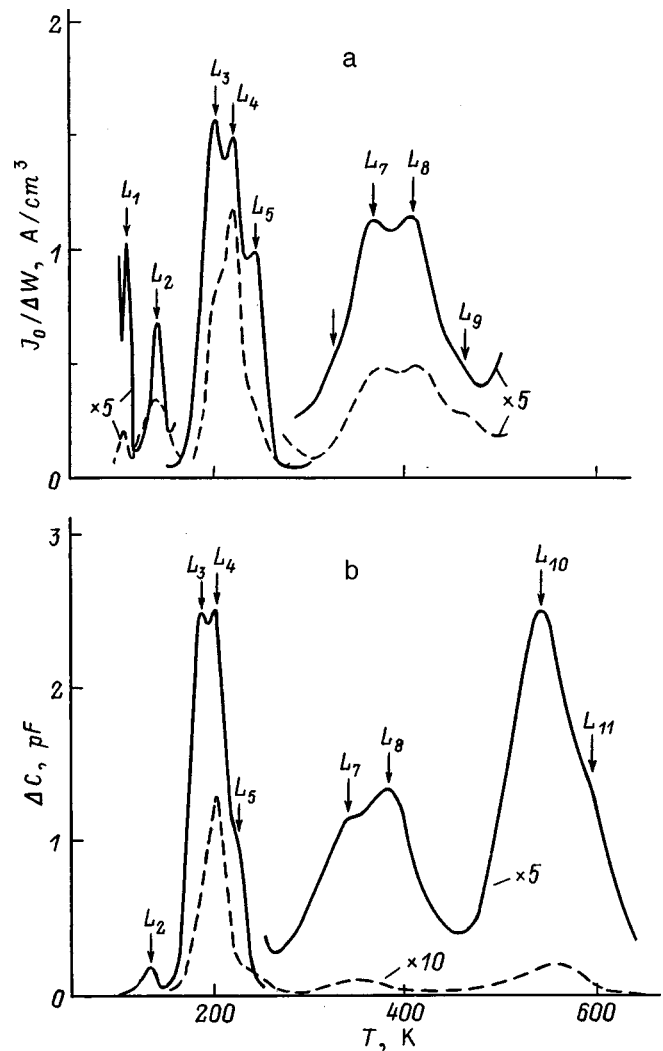
in the DLTS spectra of irradiated crystals in the temperature range 100–150 K (Figs. 1 and 5). The concentrations of these defects, as a rule, are more than an order of magnitude smaller than those of centers L_3, L_4, and L_6. On the other hand, there are deep centers whose recharging occurs at $T > 300$ K. In samples that are not subjected to a special annealing, the presence of these centers can be seen from an increase in the barrier capacitance when the structures are illuminated by impurity-energy light.

Figure 5 shows DLTS spectra of one of the samples annealed in the temperature range 900$-$1600 °C. In addition to peaks L_1-L_5, the current DLTS spectra of irradiated samples measured above room temperature exhibit a wide band with two maxima L_7 and L_8 near 370 and 410 K (Fig. 5a), which correspond to deep levels at $E_c-(0.60-0.66)$ eV and $E_c-(0.63-0.70)$ eV. The energy positions of these levels are close to those reported for centers Z_1/Z_2.[3,4] The intensities of peaks L_7 and L_8 are not related in any definite way; therefore, the shape of the band L_7-L_8

TABLE II. Ionization energies E_i and cross sections σ_n for capture of radiation-induced deep levels in single crystals of n-SiC($6H$) irradiated with electrons at energies of 5 MeV. Results of calculations based on models $\sigma_n = \text{const}$ and $\sigma_n \sim T^{-2}$ are shown.

| Level | $\sigma_n = \text{const}$ | | $\sigma_n \sim T^{-2}$ | |
	E_i, eV	σ_n, cm^2	E_i, eV	σ_n, cm^2
L_1	0.18	4×10^{-15}	0.20	2×10^{-14}
L_2	0.21	1×10^{-15}	0.23	8×10^{-15}
L_3	0.37	5×10^{-15}	0.40	4×10^{-14}
L_4	0.40	4×10^{-15}	0.44	3×10^{-14}
L_5	0.42	2×10^{-15}	0.46	1×10^{-14}
L_6	0.48	4×10^{-15}	0.53	3×10^{-14}
L_7	0.60	2×10^{-16}	0.66	1×10^{-15}
L_8	0.63	4×10^{-17}	0.70	5×10^{-16}
L_9	0.73	7×10^{-17}	0.81	6×10^{-16}
L_{10}	1.17	5×10^{-15}	1.27	2×10^{-14}
L_{11}	1.34	5×10^{-15}	1.45	4×10^{-14}

varies from sample to sample. In a number of cases a ''shoulder'' L_9 is observed on the high-temperature slope of band L_7-L_8, caused by recharging of a deep level at $E_c - (0.73-0.81)$ eV. Still another peak, labeled L_{10}, with a shoulder L_{11} on its high-temperature slope, was recorded near a temperature of 545 K when capacitive relaxation measurements were made (Fig. 5b). With regard to intensity, this peak is second only to the band L_3-L_5. Defect level L_{10} is well known from previous studies: in single crystals of $6H$-SiC irradiated with electrons it was observed for the first time in Ref. 7. The ionization energies of levels L_{10} and L_{11} computed from capacitance DLTS spectra equal (1.17–1.27) and (1.34–1.45) eV, respectively. Structural defects responsible for these levels are probably vacancy associates.[12]

Most of the radiation-induced deep-level centers are annealed out at temperatures above 1000 °C. From Fig. 5 it is easy to see that annealing of defects responsible for bands L_3-L_5 occurs at varying rates. The most intense annealing of centers L_3 and L_5 is characteristic at the start of the process, so that the peak L_4 becomes dominant in this band. Although fewer in number, the defects that make up the primary peaks in DLTS spectra remain in the crystal even after heating to $T_a = 1600$ °C. The residual concentrations of these centers do not depend on the irradiation dose and are approximately 10^{15}, 10^{14}, and 2×10^{14} cm^{-3} for bands $L_3 - L_5$, L_8, L_{10}, and L_{11}, respectively.

The parameters of these deep levels are shown in Table II.

[1] D. V. Lang, J. Appl. Phys. **45**, 3023 (1974).

[2] V. A. Il'in and V. S. Ballandovich, Defect Diffus. Forum **103–105**, 633 (1993).

[3] G. Pensl and W. J. Choyke, Physica B **185**, 264 (1993).

[4] T. Dalibor, G. Pensl, H. Matsunami, T. Kimoto, W. J. Choyke, A. Schöner, and N. Nordell, Phys. Status Solidi A **162**, 199 (1997).

[5] H. Itoh, M. Yoshikava, I. Nashiyama, S. Misava, H. Okumura, and S. Yoshida, J. Electron. Mater. **21**, 707 (1992).

[6] H. Itoh, A. Kawasuso, T. Ohshima, M. Yoshikava, I. Nashiyama, S. Tanigava, S. Misava, H. Okumura, and S. Yoshida, Phys. Status Solidi A **162**, 173 (1997).

[7] V. S. Ballandovich and G. N. Violina, Cryst. Lattice Defects Amorphous Mater. **13**, 189 (1987).

[8] H. Zhang, G. Pensl, P. Glasow, and S. Levenzeder, ECS Extended Abstracts **82–2**, 714 (1989).

[9] N. I. Kuznetsov, Fiz. Tekh. Poluprovodn. **27**, 1674 (1993) [Semiconductors **27**, 925 (1993)].

[10] A. Kawasuso, H. Itoh, S. Okada, and H. Okumura, J. Appl. Phys. **80**, 5639 (1996).

[11] A. I. Girka, V. A. Kuleshin, A. D. Mokrushin, E. N. Mokhov, S. V. Svirida, and A. V. Shishkin, Fiz. Tekh. Poluprovodn. **23**, 2159 (1989) [Sov. Phys. Semicond. **23**, 1337 (1989)].

[12] A. I. Veïnger, V. A. Il'in, Yu. M. Tairov, and V. F. Tsvetkov, Fiz. Tekh. Poluprovodn. **15**, 1557 (1981) [Sov. Phys. Semicond. **15**, 902 (1981)].

Physical properties of CdGeAs₂ crystals grown by solid-state synthesis

V. Yu. Rud'

St. Petersburg State Technical University, 195251 St. Petersburg, Russia

Yu. V. Rud' and T. N. Ushakova

A. F. Ioffe Physicotechnical Institute, Russian Academy of Sciences, 194021 St. Petersburg, Russia
(Submitted April 29, 1999; accepted for publication May 19, 1999)
Fiz. Tekh. Poluprovodn. **33**, 1320–1322 (November 1999)

The authors of this paper offer experimental proof that the method of solid-state reactions can be used to make ternary II–IV–V semiconductors (using CdGeAs₂, for example). In this method, the semiconductor group-IV component reacts with a vapor phase containing the group-II and group-V components of the compound. Initial results of studies of the physical properties of CdGeAs₂ crystals grown in this way and photosensitive heterostructures made from these crystals indicate that this new growth technology promises to improve the quality of II–IV–V semiconductors, thereby enabling novel practical applications of these materials. © *1999 American Institute of Physics.* [S1063-7826(99)00911-4]

Studies of multicomponent semiconductors have led to the discovery of ternary II–IV–V compounds with high values of the nonlinear optics coefficient d_{36}, which opens up new possibilities for increasing the efficiency of nonlinear-optical frequency converters.[1–3] Among these materials, the one with the largest value of $d_{36} = 236$ pm/V turns out to be CdGeAs₂, which is still the most suitable material for doubling the frequency of a CO₂-laser operating in the mid-infrared from 9 to 11 μm.[4] Until now, the only widely used method for growing single crystals of CdGeAs₂ has been the method of directed crystallization from a near-stoichiometric melt of the ternary compound.[5,6] In this paper we report the first results of our investigations of the physical properties of CdGeAs₂ crystals obtained by a novel method which we have developed. It involves solid-phase reaction of germanium with a vapor phase of controlled composition, which eliminates the liquid phase.

1. To obtain CdGeAs₂ we start with plates of *p*-type (111) Ge with chemically polished surfaces. The solid-phase reaction takes place in an evacuated quartz cell (10^{-3} Torr), where the germanium is thermally processed in a vapor phase containing cadmium and arsenic vapors. The partial pressures of the vapors of these elements are controlled by their source temperatures, while the reaction rate is controlled by the temperature of the germanium. In order to suppress condensation of particles onto the plate surfaces, a gradient in temperature is set up in the system in such a way that the highest temperature corresponds to the region in which the germanium plates are located.

Our physical and technological investigations revealed that once the processing is complete a continuous layer forms at the Ge surface, which differs in color from the characteristic color of the original plates. The color of this layer is close to the natural color of CdGeAs₂. The outer surfaces of these layers were found to be rather rugged and uniformly colored, and reflection from them was diffuse.

Once the layers formed, they uniformly covered the surface of the starting plates, and were tightly bound to the substrate. When the films were sheared off or ground off the plates, a microscope clearly revealed a copy of the rugged surface of the original boundary between the germanium plate and the layer that formed on it, which is characteristic of the diffusive mechanism for interface interactions. Measurements showed that the thickness of the layers that form on Ge is in the range 3–7 μm, and is determined by a three-phase synthesis reaction that occurs according to the equation

$$Ge^s + As_4^g + Cd^g \leftrightarrow CdGeAs_2^s. \tag{1}$$
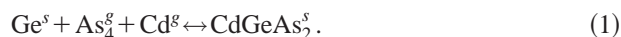
X-ray measurements confirmed the formation of a layer of CdGeAs₂ at the surfaces of the substrates.

2. According to our measurement data on the sign of the thermoelectric power, the layers of CdGeAs₂ that form as a result of reaction (1) have electronic conductivity at $T = 300$ and 77 K.

By removing these layers from all but one side of the Ge plates, we obtained anisotropic heterostructures consisting of n-CdGeAs₂/p-Ge contacts. Figure 1 shows dark I-V characteristics for one of these heterostructures at 300 and 77 K. It is clear that the heterostructures we obtained exhibit rectification, with the forward-bias direction corresponding to positive polarity of the external bias on the *p*-Ge substrates. At bias voltages $U > 0.5$ V, the forward branch of the I-V characteristic usually follows the relation

$$I = (U - U_0)/R_r, \tag{2}$$

where for these heterostructures the reference voltage $U_0 \approx 0.3$ V and the residual resistance $R_r \approx 160\,\Omega$ at $T = 300$ K, which falls to $\approx 100\,\Omega$ when the temperature is lowered to 77 K. This fact leads us to the qualitative conclusion that the resistivity of the synthesized layers of CdGeAs₂ does not increase with decreasing temperature, and hence that the donor centers that determine their conductivity are rather shallow. The falloff in R_r serves as evidence either of degen-
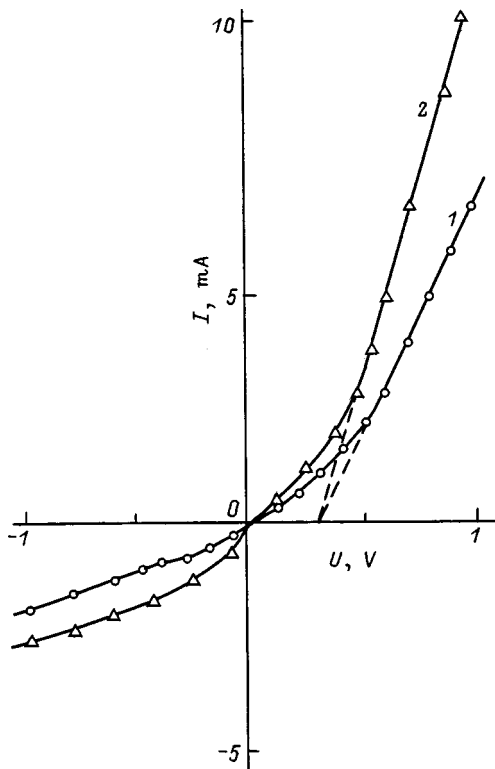
FIG. 1. Steady-state I-V characteristics of a n-CdGeAs$_2$/p-Ge heterostructure (T, K: 1 — 300, 2 — 77). The forward bias direction corresponds to positive polarity of the external bias on the Ge.

FIG. 2. Spectral dependence of the relative photoconversion quantum efficiency of a CdGeAs$_2$/p-Ge heterostructure at $T=300$ K (illumination by unpolarized light at the end of the heterostructure).

eracy of the electron gas or of the decisive role of lattice scattering. It is obvious that an unambiguous explanation of these features in the observed temperature variation of the I–V characteristics of these heterostructures requires an investigation of the conductivities and Hall coefficients in Cd GeAs$_2$ layers, which must be grown on high-resistivity substrates in order to eliminate the influence of the Ge conductivity.

The reverse-bias I–V characteristics of these heterostructures follow a power law $I \sim U^{\alpha}$, where $\alpha \approx 1.1$. This behavior is primarily due to leakage current around the periphery of these structures.

3. When these anisotropic heterostructures were illuminated, we observed a photovoltaic effect. The photovoltage charged the layers of n-CdGeAs$_2$ negatively, consistent with the rectifying direction.

Figure 2 shows a typical spectral dependence of the relative photoconversion quantum efficiency η for one of the n-CdGeAs$_2$/p-Ge heterostructures at $T=300$ K. It is clear that the photosensitivity spectra of these heterostructures has the form of a band with a maximum at $\hbar\omega_m \approx 0.73$ eV and a full width at half-maximum $\delta = 85 - 100$ meV, depending on the structure. The maximum voltage and current photosensitivities in the best heterostructures, which can be as large as 100 mV/W and 50 μA/W at $T=300$ K respectively, occur in the neighborhood of the fundamental absorption edges of the contacting semiconductors, which nearly coincide due to the closeness of the interband transition energies in the two materials.[7,8] In light of this fact, these heterojunctions between different semiconductor materials with similar value
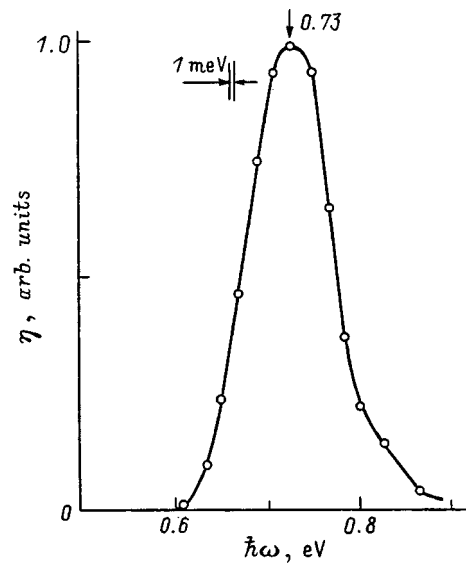
of the band gap resemble homojunctions more than heterojunctions with regard to their photoelectric properties. Therefore, the long-wavelength edge of photosensitivity in these heterostructures must be associated with interband absorption in the thin layer of ternary arsenide and the p-Ge substrate.

Special note should be taken of the fact that the long-wavelength photosensitivity edge of germanium heterostructures obtained by low-temperature solid-phase reactions occurs well within the regions of fundamental absorption of the constituent materials, and that photoabsorption takes place at photon energies that exceed the energy of A transitions ($\hbar\omega_A$) in CdGeAs$_2$ ($\hbar\omega > 0.6$ eV). At the same time, it is important to note that prior efforts to make photosensitive structures using melt-grown p-CdGeAs$_2$ crystals[7] have led to devices with increased long-wavelength photosensitivity beginning at photon energies $\hbar\omega < \hbar\omega_A$. This is evidence for a very far-reaching assertion: namely, that the concentration of centers responsible for the long-wavelength photoconductivity of n-CdGeAs$_2$ layers synthesized by solid-phase reactions is much lower than in crystals obtained from a melt. In our view, this decrease in the concentration of lattice defects in layers of n-CdGeAs$_2$ synthesized on germanium is associated with lowering the temperature at which the ternary arsenide forms. This in turn leads to narrowing of the width of the homogeneity region and a decrease in the concentration of the corresponding lattice defects.

In summary, we report the first successful use of solid-phase synthesis to make the ternary compound CdGeAs$_2$ by thermally processing germanium in the presence of a vapor phase with controlled composition. The results we have obtained in the course of these initial studies of n-CdGeAs$_2$ layers allow us to conclude that increased perfection of this material, which is important for nonlinear optics, is an achievable goal.

[1] N. A. Goryunova, *Chemistry of Diamond-like Semiconductors* (Leningrad State Univ. Publ., Leningrad, 1963).

[2] N. A. Goryunova, S. M. Ryvkin, I. M. Fishman, G. P. Shpen'kov, and I. D. Yaroshetskiĭ, Fiz. Tekh. Poluprovodn. **2**, 1525 (1968) [Sov. Phys. Semicond. **2**, 1272 (1968)].

[3] V. D. Prochukhan and Yu. V. Rud', Fiz. Tekh. Poluprovodn. **12**, 209 (1978) [Sov. Phys. Semicond. **12**, 121 (1978)].

[4] P. G. Schunemann, K. L. Schepler, and P. A. Budni, MRS Bull. **23**, 45 (1998).

[5] R. F. Mekhtiev, E. O. Osmanov, and Yu. V. Rud', Prib. Tekh. Éksp. No. 2, 179 (1964).

[6] P. G. Schunemann and T. M. Pollak, MRS Bull. **23**, 23 (1998).

[7] A. S. Borshchevskiĭ, N. E. Dagina, A. A. Lebedev, K. Obezov, I. K. Polushina, and Yu. V. Rud', Fiz. Tekh. Poluprovodn. **10**, 19095 (1976) [Sov. Phys. Semicond. **10**, 1136 (1976)].

[8] *Physical and Chemical Properties of Semiconducting Materials: Handbook* (Nauka, Moscow, 1979).

Translated by Frank J. Crowne

Change in the energy of Jahn–Teller configurations of vacancy–donor complexes induced by uniaxial strain

N. S. Averkiev, A. A. Gutkin, and M. A. Reshchikov

A. F. Ioffe Physicotechnical Institution, Russian Academy of Sciences, 194021 St. Petersburg, Russia
(Submitted May 14, 1999; accepted for publication May 19, 1999)
Fiz. Tekh. Poluprovodn. **33**, 1323–1329 (November 1999)

Estimates are obtained for the energy splitting of equivalent Jahn–Teller configurations of the light-absorbing state of ⟨vacancy Ga (V_{Ga})⟩−⟨tellurium (Te_{As})⟩ complexes in n-GaAs generated by uniaxial stress along the directions [111] and [001]. These estimates are based on measuring the stress dependence of the polarization of photoluminescence associated with these complexes at $T \simeq 2$ and 77 K. A phenomenological model of the complexes, which describes how the donor (Te_{As}) and the Jahn–Teller effect modify the initial t_2-orbitals of the vacancy component of the complex, is discussed as the effect of uniaxial strain. This model makes it possible to relate measured values of the energy splitting of equivalent configurations relative to the splitting of the original t_2-state of the vacancy arising from the presence of the donor and the Jahn–Teller effect. Comparison of calculations with experimental data shows that the contribution of the Jahn–Teller effect to the formation of the light-absorbing state of the complex $V_{Ga}Te_{As}$ exceeds the contribution due to the donor effect, although the two effects are comparable. © *1999 American Institute of Physics.* [S1063-7826(99)01011-X]

1. INTRODUCTION

It is well known that the local point symmetry of a number of substitutional impurity centers and of very simple intrinsic defects in cubic semiconductors is lower than the point symmetry of the crystal as a whole by virtue of the static Jahn–Teller effect. In this case, for each center there will exist several equivalent configurations that differ in the orientation of the axis or plane of symmetry of the center and (or) its surroundings relative to the symmetry axes of the crystal as a whole. Examples of such centers, which are said to be orientationally degenerate, are vacancies in Si,[1] deep acceptors created by Cu, Ag, or Au atoms replacing Ga in GaAs,[2–5] and Ga vacancies in GaAs.[6]

External uniaxial strain applied to the crystal (like other acceptor-related probes) can disrupt the equivalence of various configurations of the center, i.e., it can change the total energy of these configurations by different amounts, thereby lifting the orientational degeneracy. In cases where spontaneous orientation occurs (transitions between equivalent configurations of the center) at low temperatures, this phenomenon leads to preferential population of the lowest-energy configuration, i.e., the creation of Jahn–Teller distortions involving the entire defect system under study within the crystal. The extent of this induced distortion and its importance as the temperature decreases depend on the value of the configuration energy difference caused by the uniaxial strain.

For relatively small values of uniaxial strain, the lifting of the orientational degeneracy is due to changes in the energy of electronic defect states. This implies that the difference between energies of previously equivalent configurations will be directly related to deformation potential constants that are characteristic of a center that has not undergone a Jahn–Teller distortion. Moreover, the splitting will depend on the symmetry of the distorted center and the direction of the axis of external strain (see, e.g., Refs. 2–5 and 7).

The Jahn–Teller effect and equivalent configurations can also be present in more complex defects, whose initial symmetry may be lower than the crystal symmetry, although still quite high. Complexes of vacancy-donor type in Si (Refs. 8 and 9) and GaAs,[10,11] in which the donor is located in the nearest configuration sphere of the vacancy, belong to this class of centers. However, both the geometric position of the atoms in the equivalent configurations of these complexes at equilibrium and the value of the energy splitting of these configurations under uniaxial strain should differ from those of an isolated vacancy due to the effect of the donor on the vacancy orbitals and the vibrational properties of the complex.

The goal of this work is to experimentally determine the energy splitting of equivalent configurations of $V_{Ga}Te_{As}$ complexes in n-GaAs under the action of uniaxial elastic strain along various directions, and to use these data to understand the electronic properties of complexes and to estimate the relative roles of the donor and Jahn–Teller effect in generating vacancy-ionic states.

2. EXPERIMENT

The energy splitting of various configurations of a Jahn–Teller center under external uniaxial strain can be determined from the associated splitting of photoluminescence (or optical absorption) lines connected with the different configurations of the center, or from changes in the equilibrium populations of these configurations. Because the photoluminescence (and light absorption) spectra of $V_{Ga}Te_{As}$ complexes in n-GaAs consist of wide structureless bands,[10] the

splitting of these bands under uniaxial strain cannot be observed. However, changes in the equilibrium population of various configurations leads to a change in the polarization of the photoluminescence. In our prior work we have observed such changes at low temperatures,[10,12,13] and in this paper we use our results to estimate the value of the energy splitting of different configurations of a complex under the action of uniaxial strain.[1]

Samples for these studies were cut from n-GaAs : Te crystals grown by the Czochralski method and doped with Te during growth. The free electron concentration in these crystals was in the range $5 \times 10^{17} - 2 \times 10^{18}$ cm^{-3}. The light used to excite the photoluminescence had wavelengths both in the intrinsic absorption band of GaAs (photon energy 1.96 eV) and in the band of resonance excitation of the complexes (photon energy 1.43 eV).

In all cases, the photoluminescence spectra exhibited a wide band dominated by a maximum at a photon energy of ~ 1.18 eV and a full width at half-maximum of ~ 170 meV, which was assigned to radiative recombination of electrons from the conduction band or from an excited level of a complex with a hole localized in the ground state of the complex.[10–14] The polarization of this photoluminescence, which propagates perpendicular to the stress axis, was measured at temperatures $T \simeq 2$ and 77 K for various values and directions of the uniaxial stress.

The dependence of the polarization ratio of the photoluminescence r (the ratio of the intensities of light with electric vectors parallel and perpendicular to the strain axis) on the magnitude of the stress P is shown in Figs. 1 and 2. It is clear from Fig. 1 that when $P \| [111]$ and $T \simeq 2$ K, the change in $r(P)$ as P increases from zero is first characterized by rapid growth, which at $P \approx 2$ kbar becomes a relatively slow linear increase that extends to the end of the range of stresses we investigated ($P \lesssim 10$ kbar). According to the results of Refs. 2–5 and 10, we can associate the initial step-like increase in $r(P)$ with the lining up of distortions in the complexes. Experiments show[11,12] that this occurs by spontaneous reorientation of the distortion in the light-absorbing state of the complexes. The region of slow, linear increase of r at $P > 2$ kbar is probably determined by the splitting of the emission bands of complexes with differing orientations of the original vacancy-donor axis relative to the strain axis, and possibly the rather small change in the wave functions of the complexes induced by stress. The value of stress at which the lining up of the distortion is complete ($P \simeq 2$ kbar) does not depend on the intensity of excitation and remains the same when the photoluminescence is resonantly excited (Fig. 1). In this case the lifetime of an individual complex in its light-absorbing state is at least 1 s, i.e., it exceeds by several orders of magnitude the lifetime when the excitation is by intrinsic light. This allows us to assume that the degree of occupancy of the various configurations of the complexes corresponds to thermal equilibrium, and consequently that at ($P \simeq 2$ kbar), for which the lining up is complete, the splitting of the energies of differing configurations is $\sim 4kT_{\mathrm{eff}}$, where T_{eff} is the effective temperature. At low temperatures T_{eff} exceeds the sample temperature, because it includes the effects of internal random stresses and electric fields that
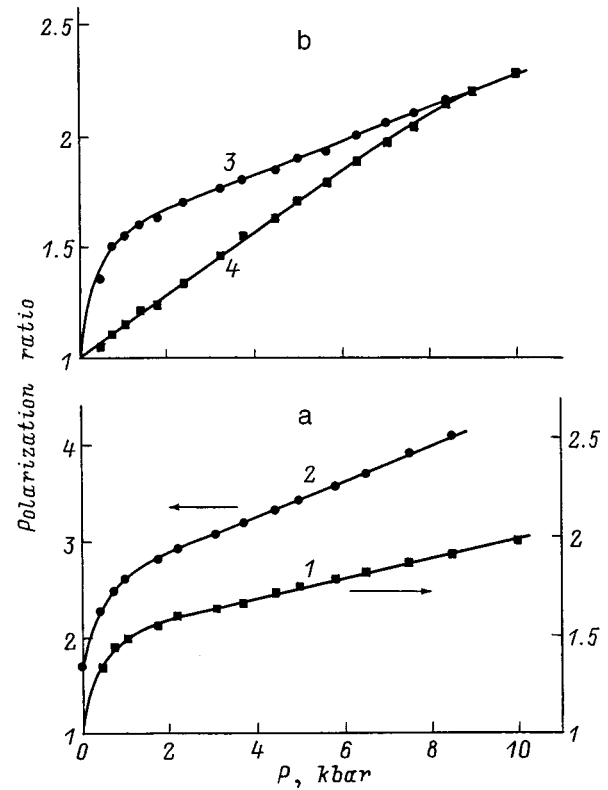

FIG. 1. Dependence of the photoluminescence polarization in the band with a maximum at a photon energy of 1.18 eV in n-GaAs : Te on the value of the stress P along the [111] axis; a—sample 1, b—sample 2; $\hbar\Omega_{\mathrm{ex}}$, eV: *1, 3, 4* — 1.96 and *2* — 1.43. Temperature T, K: *1–3* — 2, *4* — 77. Emission was observed at a photon energy of 1.2 eV (1 and 2) and photon energies corresponding to the maximum of the photoluminescence band (3 and 4).

exist in the crystal on the configuration energy.[15] The large difference between the functions $r(P)$ at 2 and 77 K (Fig. 1) indicates that the energy splitting of different configurations due to random stresses and fields is considerably smaller than kT at 77 K. Therefore, we may assume that the equilibrium populations of the various configurations at 77 K are determined by the sample temperature. Then the fact that the values of $r(P)$ at 2 and 77 K are observed to be equal when the pressure exceeds 9 kbar (Fig. 1) implies that when $T = 77$ K the lining up of the distortions is complete at $P \geqslant 9$ kbar. In other words, at $P \simeq 9$ kbar the energy splitting of equilibrium configurations is $(3.5 - 4)kT$, i.e., 23–26 meV.

When $P \| [001]$ (Fig. 2), no step-like increase is observed in the polarization of the light with increasing P. However, at a temperature of 2 K partial lining up of the distortions of the complexes probably does occur with increasing P, since the polarization of the light in this case is higher than it is at $T = 77$ K. The lack of a noticeable segment of step-like increase in the polarization of the photoluminescence at 2 K, like the analogous segment in the function $r(P)$ for $P \| [111]$, is connected with the relatively slow increase in the energy splitting of equivalent configurations for $P \| [001]$, and also with the small value of the increase in polarization when the lining up of the distortion is complete. The smallness of the polarization increase is due to the relative closeness of the directions of the emitting dipoles for the complexes to the
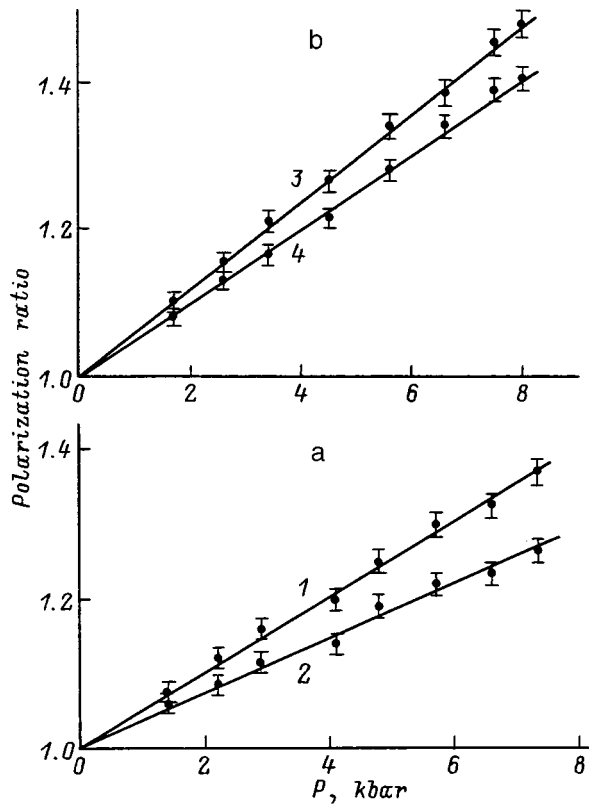
FIG. 2. Dependence of the photoluminescence polarization in the band with a maximum at a photon energy of 1.18 eV in GaAs on the value of the stress along the [001] axis; a—sample 3, b—sample *4*. Temperature *T*, K: *1, 3*— 2, *2, 4*— 77. The photoluminescence was observed at photon energies corresponding to the maximum of the emission band.

FIG. 3. Initial positions of atoms in the complex $V_{Ga}Te_{As}$.

$\langle 111 \rangle$ axis, which qualitatively agrees with an analysis of polarization spectroscopy data for these defects in the single-dipole approximation.[11]

The data shown in Fig. 2 indicate that the values of $r(P)$ at 2 and 77 K continue to differ, with practically no decrease with increasing P, over the entire measurement range ($P \leqslant 8$ kbar). This allows us to conclude that the energy splitting of equivalent configurations at $P = 8$ kbar is smaller than kT at 77 K, i.e., it does not exceed 6 meV.

3. COMPUTATION OF THE ENERGY SPLITTING OF EQUIVALENT CONFIGURATIONS OF VACANCY-DONOR COMPLEXES AS A RESULT OF UNIAXIAL STRAIN

The complex $V_{Ga}Te_{As}$ in GaAs like the vacancy-donor complex in Si,[8,9] contains components that are initially at neighboring lattice sites of GaAs (Fig. 3).[10–14] The piezospectroscopic and polarization properties of photoluminescence connected with this complex can be understood qualitatively if we assume that the complex undergoes a static Jahn–Teller effect at low temperatures it, like the vacancy-donor complex in Si, and has not trigonal, but rather monoclinic $C_{1h}(C_s)$ symmetry with a plane of symmetry {110} that contains the original axis of the complex (the vacancy-donor axis).[10–13] There are three such planes in each complex, and consequently the complex at each instant of time has one out of three equivalent configurations that differ by the positions of their planes of symmetry.
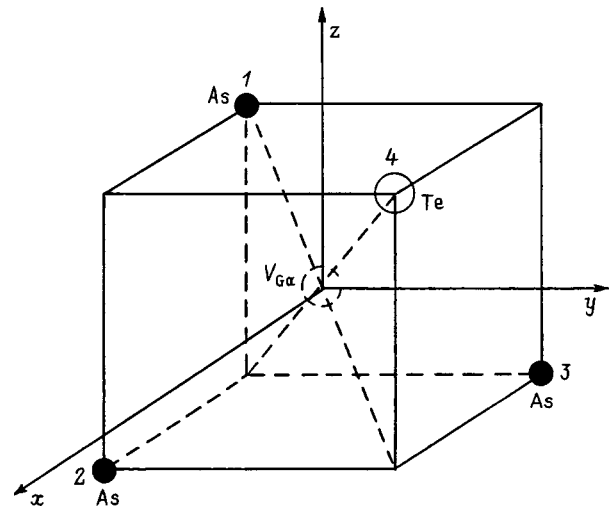
Thus, the initial one-electron t_2-state of the vacancy component of the complex is split both by the presence of the donor (lowering the symmetry of the defect from T_d to trigonal) and by the Jahn–Teller effect (lowering of the symmetry of the defect to monoclinic).

In order to analyze the effect of external uniaxial strain on the energy of the equivalent configurations of the complex, we use the phenomenological model of Ref. 13, which describes the intracenter interactions within a complex (the Jahn–Teller effect and the influence of the donor) as uniaxial strains as well. The splittings of the initial t_2-state caused by these strains equal the splitting of the t_2-state caused by the Jahn–Teller effect alone or the donor-related splitting alone, respectively. In this model it is natural to replace the effect of the donor by a strain along the initial axis of the complex (the [111] axis in Fig. 3), and replace the Jahn–Teller distortion by a strain along another axis of type $\langle 111 \rangle$ that does not coincide with the original complex axis. This model, which incorporates the observed monoclinic symmetry of the complex $V_{Ga}Te_{As}$,[11] and which includes three equivalent configurations corresponding to possible directions of the Jahn–Teller distortion (along any of the three equivalent axes $[\bar{1}\bar{1}1]$, $[1\bar{1}\bar{1}]$, or $[\bar{1}1\bar{1}]$ in Fig. 3), is in qualitative agreement with all the photoluminescence-polarization and piezospectroscopy studies of the $V_{Ga}Te_{As}$ complex,[10–13] since spontaneous reorientation of the Jahn–Teller distortions of the complex, as shown in Ref. 12, takes place only in the light-absorbing state.[2)]

Moreover, this type of model ensures the necessary form of the defect symmetry in limiting cases. In fact, for an isolated vacancy (no donor) the model predicts trigonal symmetry for the distortion due to the Jahn–Teller effect, which is in agreement with experimental data of Ref. 6. In the other limiting case, i.e., no Jahn–Teller interaction, the model also predicts a trigonal center with the axis of symmetry coinciding with the vacancy-donor axis.

Let us consider the change in energy of the various configurations when exposed to an external uniaxial strain within this model of the complex. For the defect with initial

axis [111] shown in Fig. 3, the splitting of the t_2-vacancy state by the donor field is described by a uniaxial strain tensor in which the diagonal elements ε_{ii} equal zero, while the nondiagonal elements $\varepsilon_{ij}(i \neq j)$ equal the same quantity, which we denote by ε_d. An analogous description can be used for the Jahn–Teller effect, with each of the three possible configurations *1, 2, 3* corresponding to uniaxial Jahn–Teller strains along the directions $[\bar{1}\bar{1}1]$, $[1\bar{1}\bar{1}]$ or $[\bar{1}1\bar{1}]$ (Fig. 3). The nondiagonal components of these strain tensors are also equal to one another in absolute value, but they differ in sign. We will denote these components by $+\varepsilon_{JT}$ and $-\varepsilon_{JT}$. Then the components of the total effective strain tensor, which describes intracenter interactions of the complex (Fig. 3), in cofigurations *1*, *2*, and *3* are, respectively,

$$\varepsilon_{xx} = \varepsilon_{yy} = \varepsilon_{zz} = 0, \quad \varepsilon_{xy} = \varepsilon_d + \varepsilon_{JT},$$

$$\varepsilon_{zx} = \varepsilon_{yz} = \varepsilon_d - \varepsilon_{JT}; \tag{1}$$

$$\varepsilon_{xx} = \varepsilon_{yy} = \varepsilon_{zz} = 0, \quad \varepsilon_{xy} = \varepsilon_{zx} = \varepsilon_d - \varepsilon_{JT},$$

$$\varepsilon_{yz} = \varepsilon_d + \varepsilon_{JT}; \tag{2}$$

$$\varepsilon_{xx} = \varepsilon_{yy} = \varepsilon_{zz} = 0, \quad \varepsilon_{xy} = \varepsilon_{yz} = \varepsilon_d - \varepsilon_{JT},$$

$$\varepsilon_{zx} = \varepsilon_d + \varepsilon_{JT}. \tag{3}$$

Such expressions can be written for complexes whose initial axes (the vacancy-donor axis) coincide with axes $[\bar{1}\bar{1}1]$, $[1\bar{1}\bar{1}]$, or $[\bar{1}1\bar{1}]$.

For an external strain along the direction $[\bar{1}\bar{1}1]$ we can assign every complex in the crystal to one of two groups: in the first group the axis of external strain coincides with the initial vacancy-donor axis, while in the second group it coincides with the initial axis of one of the possible Jahn–Teller distortions. In the first group of complexes, the equivalence of all the configurations is preserved, i.e, their energies change by the same amount. In the second group of complexes, those configurations whose main distortion coincides with the axis of the external load have an energy that differs from the energy of the two other configurations. This difference does not depend on the position of the intial vacancy-donor axis. Therefore, in order to determine the energy splitting of the various configurations it is sufficient to consider only one complex of this group, namely that shown in Fig. 3. For the directions of the external load shown above, the components of the strain tensor for this complex in configurations *1*, *2*, and *3* are, respectively,

$$\varepsilon_{xx} = \varepsilon_{yy} = \varepsilon_{zz} = 0, \quad \varepsilon_{xy} = \varepsilon_d + \varepsilon_{JT} + \varepsilon',$$

$$\varepsilon_{yx} = \varepsilon_{zx} = \varepsilon_d - \varepsilon_{JT} - \varepsilon'; \tag{4}$$

$$\varepsilon_{xx} = \varepsilon_{yy} = \varepsilon_{zz} = 0, \quad \varepsilon_{xy} = \varepsilon_d - \varepsilon_{JT} + \varepsilon',$$

$$\varepsilon_{yz} = \varepsilon_d + \varepsilon_{JT} - \varepsilon', \quad \varepsilon_{zx} = \varepsilon_d - \varepsilon_{JT} - \varepsilon'; \tag{5}$$

$$\varepsilon_{xx} = \varepsilon_{yy} = \varepsilon_{zz} = 0, \quad \varepsilon_{xy} = \varepsilon_d - \varepsilon_{JT} + \varepsilon',$$

$$\varepsilon_{yz} = \varepsilon_d - \varepsilon_{JT} - \varepsilon', \quad \varepsilon_{zx} = \varepsilon_d + \varepsilon_{JT} - \varepsilon'. \tag{6}$$

Here ε' is the relative strain in the GaAs for loading along an axis of type $\langle 111 \rangle$,

$$\varepsilon' = \frac{-P}{6 C_{44}}, \tag{7}$$

where C_{44} is the elastic constant of GaAs ($C_{44} = 6 \times 10^{11}$ dyne/cm^2 at temperature 0 K) and P is the magnitude of the uniaxial stress along the trigonal axis (for tension in the crystal the sign of P is negative).

Equations (4)–(6) allow us, following Ref. 16, to write Hamiltonians for the energies of each of the possible configurations. Treating the splitting caused by the external strain as a small perturbation compared to the splitting caused by the Jahn–Teller effect and the donor, the energies of configurations *1* and *2* (or *3*) can be obtained using first-order perturbation theory. The difference between minimal values of these energies gives the energy splitting of the different configurations Δ_{111}, which determines the degree of their population at equilibrium.

If the effect of the donor entering into the complex is such that the triply degenerate single-electron (or single-hole) t_2-state of the vacancy is split in such a way that the ground state becomes a doubly degenerate e-state, then

$$\Delta_{111} = \frac{8\sqrt{3}[\sqrt{8(1+p)^2 + (1-p)^2} + p + 3]d\varepsilon'}{\sqrt{8(1+p)^2 + (1-p)^2}[\sqrt{8(1+p)^2 + (1-p)^2} + 3 - 3p]}, \tag{8}$$

where d is the deformation potential constant for the t_2-state of the vacancy when the strain is along the $\langle 111 \rangle$ axis, and p is the absolute value of the ratio of the splitting of the t_2-state of the vacancy caused by the donor to the same quantity for the Jahn–Teller effect. According to the definition of the relative strains ε_d and ε_{JT}, we have

$$p = \left| \frac{\varepsilon_d}{\varepsilon_{JT}} \right|. \tag{9}$$

In the opposite case, i.e., when the donor-induced splitting of the t_2-state causes the ground state to become the nondegenerate a_1-state, we have

$$\Delta_{111} = \frac{8\sqrt{3}[\sqrt{8(1+p)^2 + (1-p)^2} - p - 3]d\varepsilon'}{\sqrt{8(1+p)^2 + (1-p)^2}[\sqrt{8(1+p)^2 + (1-p)^2} - 3 + 3p]}. \tag{10}$$

When the external uniaxial strain is along the [001] axis, complexes with any possible position of the Te atom are equivalent; however, different configurations of the complex can have different energies, since the positions of their planes of symmetry relative to the stress axis are different. In particular, for the complex shown in Fig. 3 the axes of the effective strains that represent the Jahn–Teller effect and the influence of the donor are in the same plane as the axis of external strain [001] in configuration 1, but are not in the same plane in configurations *2* and *3*. It is well known that strain along the [001] axis leading to splitting of the energy levels is described by the three diagonal components of the strain tensor.[16] For the strain directions we have chosen

$$\varepsilon_{xx} = \varepsilon_{yy} = -\varepsilon'', \quad \varepsilon_{zz} = 2\varepsilon''. \tag{11}$$

Here

$$\varepsilon'' = -\frac{P}{C_{11} - C_{12}}, \tag{12}$$

where C_{11} and C_{12} are elastic constants (for GaAs at $T=0$ K, $C_{11} = 12.26 \times 10^{11}$ dyne/cm^2 and $C_{12} = 5.71 \times 10^{11}$ dyne/cm^2). Thus, in order to compute the energies of the various configurations it is necessary to replace the zero values of the diagonal components in Eqs. (1)–(3) with the expressions (11). Now, by treating the change in energy of the configuration to linear order in ε'' we can obtain an expression for the energy splitting (Δ_{001}) of configurations *1* and *2* (or *3*). If the presence of the donor causes the t_2-state of the vacancy to split so that the ground state becomes a doubly degenerate *e*-state, then

$$\Delta_{001} = \frac{24pb\varepsilon''}{\sqrt{8(1+p)^2 + (1-p)^2}\left[\sqrt{8(1+p)^2 + (1-p)^2} + 3 - 3p\right]}, \tag{13}$$

where b is the deformation potential constant for the t_2-state of the vacancy for strain along the $\langle 001 \rangle$ axis. In the opposite case

$$\Delta_{001} = \frac{24pb\varepsilon''}{\sqrt{8(1+p)^2 + (1-p)^2}\left[\sqrt{8(1+p)^2 + (1-p)^2} - 3 + 3p\right]}. \tag{14}$$

If the initial single-electron (single-hole) state of the vacancy has symmetry Γ_8 rather than t_2, and if the spin-orbit splitting greatly exceeds the splitting due to the presence of the donor and the Jahn–Teller effect, then by using the deformation tensor components given above and the expression for the energy corresponding to this case given in Ref. 16 we obtain

$$\Delta_{111} = \frac{4d\varepsilon'}{\sqrt{3 + 2p + 3p^2}} \quad \text{and} \quad \Delta_{001} = 0. \tag{15}$$

Note also that we have no assurance that configurations of defects equivalent under the Jahn–Teller effect will remain so under prespecified conditions for arbitrary values of p. For example, if a single electron or single hole is present in the initial t_2-state of the vacancy, and if the action of the donor entering into the complex causes the state for which the carrier is localized to be nondegenerate even in the absence of a Jahn–Teller effect, then the appearance of equivalent configurations is possible only for $p < 1$ due to the pseudo-Jahn–Teller effect.[17] For this reason, Eqs. (10), (14), and (15) are meaningful only for $p < 1$, while expressions (8) and (13) are valid for every p.

4. ANALYSIS OF EXPERIMENTAL DATA

As we have already indicated, spontaneous reorientation and the initial lining up of Jahn–Teller distortions of the $V_{\mathrm{Ga}}\mathrm{Te}_{\mathrm{As}}$ complex in *n*-GaAs take place in the light-absorbing state of the complex.[12] The number of electrons present in this state is not precisely known for vacancy-ionic orbitals. In a number of papers (see, e.g., Refs. 18–20) it is asserted that under equilibrium conditions this complex is singly

negatively charged. In such a case it is natural to assume that it consists of $(V_{\mathrm{Ga}}^{2-}\mathrm{Te}_{\mathrm{As}}^{+})^{-}$, i.e., the orbitals that are generated from the a_1- and t_2- states of V_{Ga} bind seven electrons. Since the a_1-state is located ~ 1 eV below the t_2- state in energy, this implies that initially the t_2-orbitals of the vacancy contain five electrons, i.e., one hole. Let us analyze the splitting of the energy of equivalent configurations in this case. Studies of the vacancy-donor complex in Si have shown[8,9] that the splitting of the t_2-state under the influence of the donor causes the ground state of the hole to become a doubly degenerate single-electron *e* state. An analogous conclusion may be inferred from indirect information regarding the ⟨gallium vacancy⟩–donor complexes in GaAs.[21] Within the framework of the phenomenological model used here, this implies that the difference in energy of equivalent configurations for strain along the [111] or[001] axes should be given by expressions (8) or (13) when the spin-orbit interaction can be ignored, or expression (15) when the spin-orbit interaction plays a dominant role. Since for $P\|[001]$ the splitting of the configurations is nonzero, let us consider the first case. It follows from Eqs. (8) and (13) that p can be estimated from the experimental magnitudes for the energy splitting of equivalent configurations in this case if the magnitudes of the initial deformation potential constants d and b are known, or at least their ratio.

For the valence band and many defects in GaAs (see, for example, Ref. 15), b and d should be exactly related by the empirical condition

$$d \simeq (2.7 - 3)b \tag{16}$$

(in the spherical approximation $d = \sqrt{3}b$). Substituting Eq. (16) into Eqs. (8) and (13), we find

$$\frac{\Delta_{001}}{\Delta_{111}} = \frac{kp}{\sqrt{3}\left[\sqrt{8(1+p)^2 + (1-p)^2} + 3 + p\right]}\frac{\varepsilon''}{\varepsilon'}, \tag{17}$$

where the value of the numerical coefficient k lies in the range $k = 1 - 1.11$. From Eq. (17), using Eqs. (7) and (12) and the experimental data for Δ_{001} and Δ_{111} presented in Sec. 2 for specific values of the uniaxial stress, it is easy to show that $p \lesssim 0.8$. Substituting this estimate and the quantities Δ_{111} and ε' into Eq. (8), we then obtain $d \approx -(2.0 - 2.5)$ eV. Using the spherical approximation to replace Eq. (16) in Eqs. (8) and (13) makes the value of p even smaller.

In addition, it should be noted that when Eq. (16) holds roughly, Eqs. (10) and (14) cannot explain the experimentally observed difference in the energy splittings of equivalent configurations for compression along axes [111] and [001] (Sec. 2), since for any values of p and the magnitudes of the stress we have chosen the quantity Δ_{001} obtained for Eq. (14) greatly exceeds the quantity Δ_{111} from Eq. (10). This contradiction shows that the splitting of the t_2-state of the vacancy corresponding to Eqs. (10) and (14) due to the presence of the donor in the complex $V_{\mathrm{Ga}}\mathrm{Te}_{\mathrm{As}}$ cannot be realized, and thus our previous assumptions are confirmed.

Let us now consider the case of another charge state postulated for the light-absorbing state of the complex $V_{\mathrm{Ga}}\mathrm{Te}_{\mathrm{As}}$. In Ref. 21 it was proposed that under equilibrium conditions in *n*-GaAs this complex consists of a doubly

negatively charged defect $(V_{Ga}^{3-} Te_{As}^{+})^{2-}$. In favor of this assumption is the small cross section for capture of an electron by this complex after it captures a hole $(10^{-19} - 10^{-20}\,\mathrm{cm}^2$; see Ref. 22). In this case, all the vacancy-ionic orbitals of the complex are occupied by electrons, and the distortion of the complex in the light-absorbing state can be treated as resulting from the Jahn–Teller effect, which in turn takes place by virtue of the mixing of the light-absorbing and emitting states of the complex due to interaction with incompletely symmetric phonons. Analysis shows that such vibrations, which initially consist of F_2-vibrations of the vacancy environment, give rise to distortions of the light-absorbing state of an isolated vacancy along the trigonal axis as well. An external stress will change the energy minima of the adiabatic potentials of the complex in this state by shifting the analogous minima of the emitting state, in which a single hole is bound in the vacancy-ionic orbitals.

Because of the phenomenological character of the model we are proposing, and the mixing of the light-absorbing state with a state that binds a single hole in the vacancy-ionic orbitals, we can once more use expressions (8) and (13) to describe the behavior of the energy of equivalent configurations under an external stress. For this reason the estimates of the values p, d, and b given above are also correct when the light-absorbing state of the complex has the form $(V_{Ga}^{3-} Te_{As}^{+})^{2-}$.

Note also that only the charged states of the complex we have considered are in qualitative agreement with the results of experimental observations, according to which the Jahn–Teller effect and barriers between equivalent configurations in the emitting state are considerably larger than in the light-absorbing state.

Thus, our investigations show that the Jahn–Teller effect affects the formation of the light-absorbing state of the complex $V_{Ga}Te_{As}$ more than the presence of the donor Te_{As}, although the two effects may be comparable. This conclusion is in agreement with the results of experiments in which the direction of the optical dipole was inferred by describing the complex in the single-dipole approximation,[23] results that also give the magnitude of the relative contribution of the donor, which consists of an effective average of this contribution in the light-absorbing and light-emitting states.

[1)]Measurement of changes in the intensity of a magnetic resonance line corresponding to different configurations[8,9] cannot be used to study the $V_{Ga}Te_{As}$ complex, because no magnetic resonance signal was observed.
[2)]Previously, in Ref. 13, we modeled such a complex using three uniaxial strains, since we assumed that the Jahn–Teller distortion reorients itself at low temperatures both in the light-absorbing and in the light-emitting states. Under these conditions, the results of studies of polarized photoluminescence of complexes could only be explained by assuming that the centers remain monoclinic without any reorienting distortion. For this reason, fixed strains were introduced only along two axes.

---

[1]G. D. Watkins, in *Radiation Damage in Semiconductors*, edited by P. Baruch (Dunod, Paris, 1965), p. 97.

[2]N. S. Averkiev, T. K. Ashirov, and A. A. Gutkin, Fiz. Tekh. Poluprovodn. **17**, 97 (1983) [Sov. Phys. Semicond. **17**, 61 (1983)].

[3]N. S. Averkiev, A. A. Gutkin, E. B. Osipov, V. E. Sedov, and A. F. Tsatsul'nikov, Fiz. Tekh. Poluprovodn. **23**, 2072 (1989) [Sov. Phys. Semicond. **23**, 1282 (1989)].

[4]A. A. Gutkin, V. E. Sedov, and A. F. Tsatsul'nikov, Fiz. Tekh. Poluprovodn. **25**, 508 (1991) [Sov. Phys. Semicond. **25**, 307 (1991)].

[5]A. A. Gutkin, in *Defects in Semiconductors* I. *Proceedings of the 1st National Conference on Defects in Semiconductors*, St. Petersburg, Russia, April 26–30, 1992 (Scitec Publ. Ltd., Switzerland, 1993) [Defect Diffus. Forum **103–106**, 13 (1993)].

[6]Y. Q. Jia, H. J. von Bardeleben, D. Stivenard, and C. Delerue, Phys. Rev. B **45**, 1645 (1992).

[7]N. S. Averkiev, A. A. Gutkin, E. B. Osipov, and V. E. Sedov, Fiz. Tekh. Poluprovodn. **21**, 415 (1987) [Sov. Phys. Semicond. **21**, 258 (1987)].

[8]G. D. Watkins and J. W. Corbett, Phys. Rev. **134**, A1359 (1964).

[9]E. L. Elkin and G. D. Watkins, Phys. Rev. **174**, 881 (1968).

[10]A. A. Gutkin, N. S. Averkiev, M. A. Reshchikov, and V. E. Sedov, *Defects in Semiconductors*, p. 18 (*Proceedings of the 18th International Conference on Defects in Semicond.*, Sendai, Japan, July 23–28, 1995), edited by M. Swezawa and H. Katayama-Yoshida [Mater. Sci. Forum **196–201**, pt. 1, 231 (1995)].

[11]A. A. Gutkin, M. A. Reshchikov, and V. E. Sedov, Fiz. Tekh. Poluprovodn. **31**, 1062 (1997) [Semiconductors **31**, 908 (1997)].

[12]A. A. Gutkin, M. A. Reshchikov, and V. E. Sedov, Zeitschrift für Physikalische Chemie **200**, 217 (1997).

[13]N. S. Averkiev, A. A. Gutkin, E. B. Osipov, M. A. Reshchikov, and V. E. Sedov, Fiz. Tekh. Poluprovodn. **26**, 1269 (1992) [Semiconductors **26**, 708 (1997)].

[14]E. W. Williams and H. B. Bebb, in *Semiconductors and Semimetals*, edited by R. K. Willardson and A. C. Beer (Academic Press, New York, 1972), v. 8, p. 321.

[15]N. S. Averkiev, Z. A. Adamiya, D. I. Aladashvili, T. K. Ashirov, A. A. Gutkin, E. B. Osipov, and V. E. Sedov, Fiz. Tekh. Poluprovodn. **21**, 421 (1987) [Sov. Phys. Semicond. **21**, 262 (1987)].

[16]G. L. Bir and G. E. Pikus, *Symmetry and Strain Effects in Semiconductors* (Nauka, Moscow, 1972).

[17]I. B. Bersuker, Electronic Structure and Properties of Coordination Compounds (Khimiya, Leningrad, 1986), p. 287.

[18]D. T. Hurle, J. Phys. Chem. Solids **40**, 639 (1979).

[19]M. J. Puska, O. Jepsen, O. Gunnarsson, and R. M. Nieminen, Phys. Rev. B **34**, 2695 (1986).

[20]G. Dlubek and R. Krause, Phys. Status Solidi A **102**, 443 (1987).

[21]A. A. Gutkin, M. A. Reshchikov, and V. R. Sosnovskiĭ, Fiz. Tekh. Poluprovodn. **27**, 1516 (1993) [Semiconductors **27**, 838 (1993)].

[22]K. D. Glinchuk., A. V. Prokhorovich, and V. E. Rodionov, Fiz. Tekh. Poluprovodn. **11**, 35 (1977) [Sov. Phys. Semicond. **11**, 18 (1977)].

[23]A. A. Gutkin, N. S. Averkiev, M. A. Reshchikov, and V. E. Sedov, in *Semiconductor Optics. Proc. Intl. Conf.* (Ulyanovsk State Univ. Publ., Ulyanovsk, 1998), p. 122.

Translated by Frank J. Crowne

SEMICONDUCTOR STRUCTURES, INTERFACES AND SURFACES

Using the temperature-dependent photovoltage to investigate porous silicon/silicon structures

E. F. Venger, É. B. Kaganovich, S. I. Kirillova, É. G. Manoilov, V. E. Primachenko, and S. V. Svechnikov

Institute of Semiconductor Physics, National Academy of Sciences of Ukraine, 252650 Kiev, Ukraine

Structures based on porous silicon por-Si/p-Si, both freshly prepared by chemical etching and aged, exhibit a temperature-dependent photovoltage at high levels of electron-hole pair generation by pulse trains of red and white light. These structures are investigated by measuring this photovoltage, which is shown to consist of two components: a photovoltage generated in p-Si, and an oppositely directed photovoltage that appears in por-Si, characterized by trapping of nonequilibrium holes at the surface of por-Si nanocrystals during the period of illumination by the first pulse of white light. For aged structures capture of electrons in the oxide of the por-Si is also observed. The concentration of interface electronic states and electron traps at the interface of p-Si with por-Si is determined by measuring the photovoltage induced by pulses of red light. © *1999 American Institute of Physics.* [S1063-7826(99)01111-4]

Photoluminescence of porous silicon in the visible region of the spectrum has prompted researchers to investigate its properties by various methods. Recently information about the electronic properties of porous silicon/p-silicon structures (por-Si/p-Si) prepared by electrochemical etching was obtained by investigating the photovoltage.[1–3] In Ref. 1, studies of the photovoltage by the Kelvin method revealed for the first time that the photovoltage signal arises not only from p-Si but also from por-Si. Studies of the kinetics of the photovoltage excited by laser pulses with various photon energies[2] revealed that nonequilibrium holes generated in the p-Si are captured in the por-Si. Experiments have shown[3] that the photovoltage which appears in layers of por-Si detached from the p-Si can be both positive and negative, depending on the type of electrochemical etching used to make the por-Si.

It is known[4,5] that por-Si layers obtained by chemical coloring etching also emit visible photoluminescence. However, in this case the process used to make the layers is more controlled, allowing finer layers ($<0.5-1$ μm) to be grown. In contrast, layers of por-Si grown by anodization are, as a rule, thicker and of nonuniform thickness.

Our goal in this study was to analyze the temperature dependence of the pulsed photovoltage and use the results to investigate por-Si/p-Si structures obtained by chemical etching of p-Si without applying an electric field, both immediately after preparation and after a half a year of aging in air.

EXPERIMENTAL PROCEDURE

Layers of porous silicon whose thickness was less than 1 μm were made on a polished surface of (100) p-Si (resis-

tivity $\rho = 10$ $\Omega\cdot$cm) by processing the latter for 10 min in a solution with composition $HF:HNO_3:H_2O=1:3:5$. For these layers we observed ''slow'' red and ''fast'' blue bands in the time-resolved photoluminescence spectra.[6] Control samples of p-Si with a smooth surface were made by etching in a solution with composition $HF:HNO_3=1:3$. The por-Si/p-Si structures were investigated both immediately after preparation and after six months of aging them under natural conditions.

In order to measure the photovoltage across these por-Si/p-Si structures, the latter were monitored together with a capacitor consisting of a semitransparent conducting layer of $SnO_2\langle Sb\rangle$ on mica. The capacitance of the capacitor was on the order of 100 pf/cm^2. The photovoltage signal was recorded on a memory oscilloscope when the capacitor was illuminated by light pulses from an ISSh-100 flash lamp with duration 10 μs and intensity 10^{21} photons/cm$^2\cdot$s. In order to obtain the magnitude of the photovoltage (V_{ph}) of the structure, the signal taken from the oscilloscope was multiplied by a calibration coefficient for the measurement surface, which was determined using a calibration electrical pulse.

The quantity V_{ph} was measured in vacuum in a cryostat at a residual pressure of 10^{-4} Pa as the temperature T was lowered from 300 to 100 K. The function $V_{ph}(T)$ was plotted twice as the por-Si/p-Si structure was exposed to pulse trains of both white and red light. In the latter case we used a KS-19 spectral filter, which was transparent to light with wavelengths of 700 to 2700 nm. This filter prevented the porous silicon from absorbing light.[2,3]

In most cases, the photovoltage V_{ph} measured after the first light pulse differed from its value after the second or any subsequent pulses, which arrive at a repetition rate of 1 Hz. This difference is associated with capture of nonequilibrium
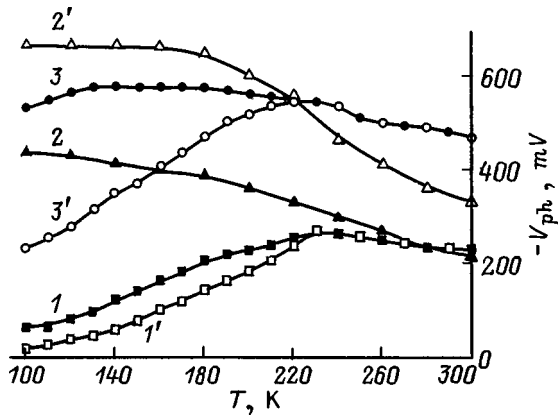
FIG. 1. Temperature dependences of the photovoltage V_{ph} for a *p*-Si surface (*1,1′*) and an as-grown *por*-Si/*p*-Si structure in white (*2,2′*) and red (*3,3′*) light. (*1—3*)—first light pulse, (*1′—3′*)—second light pulse.

FIG. 2. Temperature dependences of the photovoltage of aged structures of *por*-Si/*p*-Si in white (*1,1′*) and red (*2,2′*) light. *1,2*—first light pulse, *1′,2′*—second light pulse.

holes or electrons at surface traps during the first pulse, which are filled by the time it ends.[7] The time for retention of the captured charge in these traps increases greatly (to several hours) at low temperatures; therefore, in order to correctly measure the values of V_{ph}, the samples were heated to a temperature high enough to empty the traps of captured carriers after each measurement, and then once more cooled in the dark to the temperature of the next measurement. At this time, the first and second values of V_{ph} were measured again.

EXPERIMENTAL RESULTS AND DISCUSSION

The light intensity we used was high enough to flatten the energy bands of both *por*-Si and *p*-Si during the illumination pulse.[8] Therefore, when the samples were illuminated with red light the photovoltage V_{ph} became equal to the surface potential of *p*-Si φ_s, but with opposite sign. Note that the contribution of the Dember photovoltage to V_{ph} is insignificant due to the mutual scattering of carriers when the concentrations are high, which makes the diffusion coefficients of electrons and holes equal.[9]

Figure 1 shows the functions $V_{ph}(T)$ obtained from a control sample of *p*-Si with a normal surface (curves *1*, *1′*) and from as-grown *por*-Si/*p*-Si structure, along with curves for the same samples illuminated with white light (curves *2*, *2′*) and red light (curves *3*, *3′*). Curves *1*, *2*, and *3* were obtained after the samples were illuminated by the first light pulse, curves *1′*, *2′*, and *3′* after illumination by the second and subsequent light pulses. For the surface of *p*-Si, the values of V_{ph} obtained in white and red light coincided. In this case $-V_{ph}=\varphi_s$ at any temperature, which corresponds to downward bending of the energy bands $q\varphi_s$ (where q is the electron charge) for *p*-Si. The rather small increase in φ_s as the temperature decreases from 300 to 230 K (curve *1*) is connected with filling of surface electronic states by holes as the Fermi level in *p*-Si shifts toward the valence band. The decrease in φ_s for $T<230$ K is associated with reconstruction of the system of electronic states caused by reversible structural changes at the semiconductor-oxide film interface as the temperature varies.[10,11]. The difference between curves
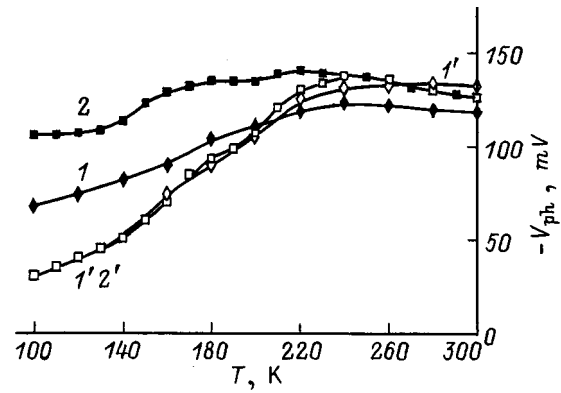
1 and *1′* for $T<220$ K is due to trapping of nonequilibrium electrons and surface traps within the illumination time by the first pulse, which gives rise to photomemory in the potential φ_s.[7]

It is clear from Fig. 1 that for as-grown *por*-Si/*p*-Si structure the functions $V_{ph}(T)$ measured in white and red light differ significantly. Over the entire temperature range, the values of $-V_{ph}$ obtained after the first pulse of red light are larger than $-V_{ph}$ obtained after the first pulse of white light (curves *3* and *2*, respectively). This implies that white light, in addition to generating a negative photovoltage by flattening the *p*-Si energy bands, which also happens with red light, generates a positive photovoltage V_{ph}^{por} when it is absorbed by *por*-Si nanocrystals. Recall that *por*-Si is believed to be a two-phase system containing quantum-well nanocrystals (*nc*-Si) in a porous SiO_x host. In this case the *por*-Si/*p*-Si interface is made up of regions where the interfaces are *nc*-Si/*p*-Si and SiO_x/*p*-Si. Light absorbed in *por*-Si also creates nonequilibrium holes that are captured at traps of the internal *nc*-Si/SiO_x surfaces within the time the first light pulse acts, leading to larger values of $-V_{ph}$ after subsequent light pulses (compare curves *2* and *2′*). This hole-generated photomemory is maintained at room temperature for ~ 30 s, which is much longer than the retention time at 230 K of the photomemory associated with capture of electrons at surface traps of the more narrow band *p*-Si when the sample is illuminated with red light (see curves *3* and *3′*). All these results suggest that the wider-band *por*-Si behaves like an *n*-type semiconductor, in contrast to *p*- Si, which is characterized by upward bending of the energy bands at the surface and trapping of holes as minority carriers at the surface under illumination.

For *por*-Si/*p*-Si structures aged for six months under natural conditions, the *por*-Si also behaves like an *n*-type semiconductor, but in this case the positive V_{ph}^{por} is smaller in value and the trapping of holes at the *nc*-Si/SiO_x surfaces is weaker (Fig. 2). It is clear that the difference between curves *1* and *2*, which were plotted after the first pulses of white and red light, respectively, is not as significant as it was for an as-grown structure. Clear evidence of the weaker trapping of holes in aged structures is the fact that in samples illuminated with white light at 220 K the photomemory changes

sign (curve *1'*). At $T > 220$ K trapping of holes at the surfaces of *nc*-Si dominates, while at $T < 220$ K trapping of electrons at the SiO_x/p-Si interface dominates. It is clear from curves *2* and *2'*, which were obtained under illumination with red light, that this begins even at $T = 240$ K.

Yet another peculiarity of the aged *por*-Si/*p*-Si structures is the photomemory that appears after a train of white-light pulses. This memory is connected with charging of traps in the silicon oxide by electrons,[12] whose thickness around the *nc*-Si increases with aging. While traps at the *nc*-Si surfaces are saturated with holes and traps at the *p*-Si/*por*-Si interface are saturated with electrons within the time the first light pulse acts, about 120 white light pulses are required to saturate the traps in the SiO_x. In this case, at room temperature the value of $-V_{ph}$ changes from 120 to 34 mV, while the time the photomemory is maintained exceeds 10^5 s. The number of electrons captured at oxide traps, which can be estimated from calculations based on measurement of the photovoltage in red light, is found to exceed 3×10^{10} cm^{-2}. Note that since no detectable photomemory of this kind was observed on an aged surface of *p*-Si, capture of electrons in *por*-Si/*p*-Si structures takes place within this *por*-Si oxide.

As we already noted, when red light pulses are used $-V_{ph}$ equals the potential φ_s of the *p*-Si substrate at the interface with *por*-Si. It is clear from Figs. 1 and 2 that the surface potential φ_s is always positive (depletion-related bending of the energy bands downward), and is larger in magnitude on as-grown *por*-Si/*p*-Si structure. Furthermore, once a certain temperatude is reached, φ_s no longer increases with decreasing temperature and starts to decrease. On the segment where φ_s increases with decreasing temperature, which is due to charging of surface electronic states of *p*-Si by holes as the Fermi level shifts towards the valence band, we can calculate[13] the density of electronic surface states for the region of the *p*-Si band gap that is being probed. We found that the density of electronic surface states in the energy range 0.14–0.17 eV above the midpoint of the band gap E_i for an as-grown structure amounts to 3×10^{11} cm^{-2} ·eV^{-1}, while for an aged structure it is 4×10^{10} cm^{-2} ·eV^{-1} in the energy range 0.14–0.22 eV below E_i. At the surface of *p*-Si the density of states is only 3×10^{10} cm^{-2} ·eV^{-1} in the interval 0.08–0.13 eV below E_i. Thus, the density of states clearly increases when a *por*-Si layer is grown on *p*-Si, and decreases as the *por*-Si/*p*-Si structure ages. The segment of the function $\varphi_s(T)$, where φ_s is found to decrease with decreasing temperature, is explained by reconstruction of the system of surface electronic states due to structural changes at the *p*-Si/por-Si interface as the temperature changes. For an aged *por*-Si/*p*-Si structure these structural changes begin at a higher temperature than for a freshly prepared structure.

Illumination with red light at temperatures below 230–220 K indicates that the photomemory of φ_s is connected with capture of nonequilibrium electrons at surface traps of *p*-Si (Figs. 1 and 2). Figure 3 shows calculated[7] dependences of the number of captured electrons on temperature $N(T)$ at a planar surface of *p*-Si (Fig. 1) and at a *p*-Si/por-Si interface for freshly prepared (curve *2*) and aged (curve *3*) structures.
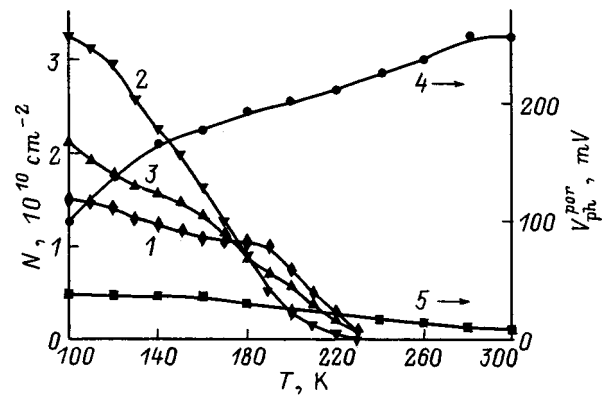

FIG. 3. Temperature dependences of the concentration N of captured electrons at the surface of *p*-Si (*1*), and at the interface of an as-grown (*2*) and an aged *por*-Si/*p*-Si structure (*3*), and also the temperature dependences of the photovoltage V_{ph}^{por} that appears in *por*-Si for as-grown (*4*) and aged (*5*) structures.

Because the traps are saturated with electrons by the first light pulse, the functions $N(T)$ also reflect the temperature dependences of the trap concentration. The increase in the value of N with decreasing temperature is attributable to the participation of increasing number of shallow traps located near the conduction band in trapping and holding electrons. From Fig. 3 it is clear that while at higher temperatures slightly more electrons are trapped by deep trapping centers at the surface of *p*-Si, at lower temperatures the traps with the highest rate of electron capture ($\sim 3 \times 10^{10}$ cm^{-2}) are shallow traps at the interface for an as-grown *por*-Si/*p*-Si structure. Note that the number of holes captured at surfaces of *nc*-Si when the structure is illuminated with white light at low temperatures can turn out to be even larger than 3×10^{10} cm^{-2}, because the quantity $-V_{ph}$ at the second pulse increases despite the same capture of electrons taking place in this case as occurs in red light (Fig. 1).

Figure 3 also shows the temperature dependences of the photovoltage V_{ph}^{por} that appears in porous silicon, obtained by subtracting the values of V_{ph} measured after the first pulses of white and red light. It is clear that the values of V_{ph}^{por} for an as-grown structure (curve *4*) are considerably larger than for an aged structure (curve *5*). This implies that the *por*-Si in an as-grown structure has a larger band bending upward at the *nc*-Si than *por*-Si in an aged structure. The fact that the temperature dependences of V_{ph}^{por} are so distinct for freshly prepared and aged structures clearly indicates that the amount of oxidation of *nc*-Si and the structural changes at the nanocrystal surfaces with decreasing temperature strongly affect the band bending.

CONCLUSIONS

We measured the temperature dependence of the pulsed photovoltage in order to investigate the electronic properties of *por*-Si/*p*-Si structures in which the *por*-Si was obtained by chemical etching without applying an electric field. By illuminating the *por*-Si/*p*-Si structures with white light pulses, which were absorbed in both the *por*-Si and the *p*-Si, and red light pulses, which were absorbed only in the

por-Si, we were able to measure the temperature dependences of the magnitude of the photovoltage at high levels of electron-hole pair generation in both materials. Our results proved that the photovoltage that appears in *por*-Si is opposite in polarity to the photovoltage that appears in *p*-Si. Moreover, we found that in as-grown *por*-Si/*p*-Si structures capture of nonequilibrium holes takes place within the time the first white light pulse acts over the entire temperature range 300–100 K, whereas in aged *por*-Si/*p*-Si structures capture of nonequilibrium holes dominates at $T > 220$ K, but at $T < 220$ K capture of nonequilibrium electrons dominates. This gives rise to corresponding photovoltage memory effects. For aged structures we also observed a photovoltage memory connected with charging of traps in the silicon oxide of *por*-Si by electrons after the structure is illuminated by a train of white light pulses.

By investigating the photovoltage generated by illumination with red light we can determine the band bending of the *p*-Si at the interface with *por*-Si in the temperature range 300–100 K, and also estimate the density of electronic surface states of *p*-Si. As the temperature decreases, we reach a certain temperature at which the system of electronic surface states reconstructs. We calculated the temperature dependences of the number of captured electrons at the interface of *p*-Si with *por*-Si for the structures under study.

[1] A. B. Matveeva, E. A. Konstantinova, V. Yu. Timoshenko, and P. K. Kashkarov, Fiz. Tekh. Poluprovodn. **29**, 2179 (1995) [Semiconductors **29**, 1136 (1995)].

[2] V. Yu. Timoshenko, E. A. Konstantinova, and T. Dietrich, Fiz. Tekh. Poluprovodn. **32**, 613 (1998) [Semiconductors **32**, 549 (1998)].

[3] L. Burstein, Y. Shapira, J. Partee, J. Shinar, Y. Lubianiker, and I. Balberg, Phys. Rev. B **55**, R1930 (1997).

[4] R. W. Fathauser, T. George, A. Ksendzov, and R. P. Vasquez, Appl. Phys. Lett. **60**, 995 (1992).

[5] S. V. Belov, Pis'ma Zh. Tekh. Fiz. **18**, 16 (1992) [Sov. Tech. Phys. Lett. **18**, 247 (1992)].

[6] L. L. Fedorenko, A. D. Sardarly, E. B. Kaganovich, S. V. Svechnikov, S. P. Dikiĭ, and S. V. Baranets, Fiz. Tekh. Poluprovodn. **31**, 6 (1997) [Semiconductors **31**, 4 (1997)].

[7] V. E. Primachenko and O. V. Sitko, *Physics of Semiconductor Surfaces Doped by Metals* (Naukova Dumka, Kiev, 1988).

[8] A. V. Sachenko and O. V. Sitko, *Photoeffects in Surface Layers of Semiconductors* (Naukova Dumka, Kiev, 1988).

[9] Z. S. Gribnikov and V. I. Mel'nikov, Fiz. Tekh. Poluprovodn. **2**, 1352 (1968) [Sov. Phys. Semicond. **2**, 1133 (1968)].

[10] S. I. Kirillova, V. E. Primachenko, O. V. Sitko, and V. A. Chernoban, Optoelektron. i Poluprovodn. Tekh. No. 20, 15 (1991).

[11] S. I. Kirillova, V. E. Primachenko, V. A. Chernoban, and O. V. Sitko, Surfaces No. 11, 74 (1991).

[12] S. N. Kozlov and S. N. Kuznetsov, Fiz. Tekh. Poluprovodn. **12**, 1680 (1978) [Sov. Phys. Semicond. **12**, 995 (1978)].

[13] E. F. Venger, S. I. Kirillova, V. E. Primachenko, and V. A. Chernoban, Ukr. Fiz. Zh. **42**, 1333 (1997).

Translated by Frank J. Crowne

Electrical characteristics and structural properties of ohmic contacts to p-type 4H-SiC epitaxial layers

K. V. Vasilevskiĭ, S. V. Rendakova, I. P. Nikitina, A. I. Babanin, and A. N. Andreev

A. F. Ioffe Physicotechnical Institute, Russian Academy of Sciences, 194021 St. Petersburg, Russia

K. Zekentes

Microelectronics Research Group, Institute of Electronic Structure and Lasers, F.O.R.T.H., Heraklion, Crete, Greece

Epitaxial films grown by low-temperature liquid phase epitaxy on p-type 4H-SiC were used as strongly doped subcontact layers for making low-resistance contacts to the p-type material. The layers had a bulk resistivity of $\sim 0.02\,\Omega\cdot$cm and an aluminum atom concentration of $\sim 1.5 \times 10^{20}\,$cm^{-3}. The absence of polytype inclusions and the distinct crystalline quality of the strongly doped subcontact layers was confirmed by x-ray diffraction methods. Ohmic contacts with resistivities less than $10^{-4}\,\Omega\cdot$cm^2 were prepared by depositing and then annealing multilayer metal mixtures containing Al and Ti. The structural properties and energy characteristics of the resulting ohmic contacts are discussed. © *1999 American Institute of Physics.* [S1063-7826(99)01211-9]

INTRODUCTION

Silicon carbide is one of the most promising semiconductor materials for making devices used in solid-state high-power and microwave electronics. In fabricating silicon-carbide bipolar devices, the creation of low-resistance contacts to 4H- and 6H-SiC with p-type conductivity remains a key problem, because these polytypes of silicon carbide have wide band gaps (3.28 and 3.09 eV at room temperature, respectively). In nature there are no metals with work functions greater than 6 eV, which would make it possible to obtain ohmic contacts by decreasing the height of the Schottky barrier. Hence, such contacts can be obtained only by creating tunneling-transparent barriers to strongly doped SiC, or by creating highly defective layers at the metal-semiconductor boundary. The best contacts to polytype 4H-SiC are obtained by magnetron sputtering of Al + Si with a subsequent annealing for 20 min at 700 °C.[1] The minimum resistivity (R_{cont}) that can be achieved in this way is $3.8 \times 10^{-5}\,\Omega\cdot$cm^2, but reproducibly obtainable values are about $R_{\text{cont}} \simeq 10^{-4}\,\Omega\cdot$cm^2. The epitaxial layers have an acceptor concentration of $5 \times 10^{19}\,$cm^{-3}. The best contact to polytype 6H-SiC ($R_{\text{cont}} \simeq 4 \times 10^{-6}\,\Omega\cdot$cm^2) was obtained on expitaxial layers with an acceptor concentration of 2×10^{19} cm^{-3}, using Co + Si metallization and a long anneal: 5 hours at 500 °C plus 2 hours at 900 °C, leading to the formation of cobalt silicide.[2] This value of the contact resistivity is in rather good agreement with experimental dependence of R_{cont} on the doping level for Ti- and Al/Ti-contacts to p-type 6H-SiC,[3,4] which in turn repeat the dependence of the Schottky barrier transparency on the doping level of the silicon carbide subcontact region. In Ref. 3 it was concluded that the dependence of the resistivity of Ti/Al-contacts on the concentration of acceptor impurities is also typical of all

other metallizations, because it is determined by the dependence of the tunneling current through the Schottky barrier on the level of 6H-SiC doping. Thus, in order to obtain low-resistance contacts to 4H- and 6H-SiC with hole conductivity it is necessary, above all, to create a strongly doped subcontact semiconductor layer.

It is possible to increase the doping level of the semiconductor subcontact region by using aluminum and boron, i.e., chemical elements that are acceptor impurities in SiC, to create the contacts. Once they have diffused into silicon carbide, either during the time of deposition or after a subsequent annealing, they should increase the level of doping of the subcontact layer. However, because the diffusion coefficients of impurities in silicon carbide are extremely small, short-time annealing of contacts at temperatures of order 1000 °C does not increase the level of doping of the subcontact layer. Although annealing at higher temperatures – on the order of 1700 °C – or for longer annealing times does lead to the formation of a contact via recrystallization of the semiconductor surface layer,[5,6] such high-temperature annealing is not compatible with technologies for making devices with $p-n$ junctions just below the surface.

Another way to increase the doping level of the subcontact layer is to grow an additional strongly doped epitaxial layer or create one by ion doping. The maximum concentration of aluminum atoms that can be incorporated into the SiC crystal lattice and play the role of electrically active impurities depends on the methods of epitaxy or doping. The highest concentration of aluminum atoms ever incorporated into silicon carbide, on the order of $2 \times 10^{21}\,$cm^{-3}, was obtained by doping during epitaxy of 6H-SiC, using the sublimation sandwich method.[7] Epitaxial layers grown in this way have high crystal quality, and the aluminum atoms are almost all

electrically active. On the other hand, the higher growth temperature ($\sim 2000\,°C$) means that this method cannot be used for direct deposition of the contact layer onto a prepared device structure, and the impossibility of controlling the level of doping during the growth process prevents the creation of the working structure and the subcontact layer at the same time.

A strongly doped contact layer can also be obtained by ion implantation of aluminum with subsequent annealing. Thus, this method has been used to create subcontact layers for contacts to *p*-type 6*H*-SiC made of Ti/Al (Refs. 8–10) and Al (Ref. 11). The highest concentration of aluminum atoms in silicon carbide obtained by ion doping at room temperature was $2 \times 10^{19}\,cm^{-3}$. In this case the concentration of electrically active atoms was $10^{19}\,cm^{-3}$ (Ref. 12). Combined implantation of Al and C into 6*H*-SiC at room temperature, or at higher temperatures ($800\,°C$), makes it possible to increase the atomic concentration of Al to $2 \times 10^{21}\,cm^{-3}$ (Ref. 11), but activation of the impurities and recrystallization of the amorphous SiC layer that forms at such high implantation doses ($Al^+ \simeq 10^{15}\,cm^{-2}$) requires a long high-temperature anneal for 30 min at $1550\,°C$ in a special geometry that prevents the decomposition of the SiC surface layer. Although ohmic contacts with a contact resistivity on the order of $10^{-5}\,\Omega\cdot cm^2$ can be made to these layers,[11] strong diffusion of the implanted impurities is observed at the same time, leading to washing-out of the doping profile of the working structure and to depletion of the surface layer. The crystalline quality of the annealed layers, however, is considerably worse than the starting layer.[13]

Because vapor-phase epitaxy makes accurate control of the doping profile possible, strongly doped subcontact layers could be grown by this method at the same time as a device structure. However, the maximum concentration of aluminum that can be attained for doping during epitaxial growth from a vapor phase is roughly $2 \times 10^{20}\,cm^{-3}$ for epitaxial layers of 6*H*-SiC, i.e., almost an order of magnitude smaller than that obtained by the two preceding methods.[14] The growth rate of these layers was 2 μm/h at a growth temperature of $1550\,°C$. It was shown in Ref. 14 that practically all the Al atoms are electrically active. However, at the highest concentrations of around $2 \times 10^{20}\,cm^{-3}$ a number of triangular defects were observed in the layers. Those defects were interpreted as inclusions of the 3*C*-SiC polytype. A number of strongly broadened lines were also observed on the rocking curves obtained from these layers, which is evidence of strong disruption of the crystal lattice induced by the extremely high Al concentrations. Contacts to these layers were made by direct deposition of the composition Al/Ti/Al and annealing at temperatures from 650 to $950\,°C$. Because low-resistance contacts with resistivities of $\sim 10^{-4}\,\Omega\cdot cm^2$ were obtained only for Al concentrations of $\sim 2 \times 10^{20}\,cm^{-3}$ in the epitaxial layers, we may conclude that the presence of lattice defects and inclusions of the 3*C*-SiC polytype play an important role in lowering the contact resistivity. These defects and inclusions can affect the reliability and lifetime of the contacts, while in devices that are operating under extremely high power densities they can cause nonuniformities

in the current density, local heating, and consequently burning-out of the mesa structure.

Finally, strongly doped layers of *p*-type 4*H*- and 6*H*-SiC can be grown by low-temperature liquid-phase epitaxy (LTLPE).[15] The monitored rate of growth in this process is found to be in the range 0.1–1 μm/h, which makes it possible to grow thin layers, while the growth temperature is relatively low and lies in the range 1100–$1200\,°C$. The concentration of aluminum atoms in such layers, which was measured by secondary ion mass spectroscopy (SIMS), was found to be $7 \times 10^{20}\,cm^{-3}$, which is lower than the highest doping level obtained by the sublimation sandwich method and ionic doping but exceeds the maximum doping level obtained for vapor-phase epitaxy. The distinctive crystalline quality of these layers was confirmed by *x*-ray diffraction, as well as its successful use as a substrate for subsequent epitaxy of gallium nitride and the creation of *n*-GaN/*p*-SiC heterostructures.[16] All this makes the LTLPE method attractive for making strongly doped subcontact layers to decrease the resistivity of contacts to *p*-type 4*H*- and 6*H*-SiC.

The topic of this paper is the fabrication of low-resistance ohmic contacts to *p*-type 4*H*-SiC by growing strongly doped subcontact layers using LTLPE, and the investigation of structural properties and electrical characteristics of these contacts.

FABRICATION OF OHMIC CONTACTS TO *p*-TYPE 4*H*-SIC

Our strongly doped subcontact layer for making low-resistance contacts to *p*-type 4*H*-SiC was a *p*-type epitaxial layer grown by LTLPE (an LTLPE layer).[15,16] The substrate for this layer was provided by a homoepitaxial structure,[1)] consisting of an epitaxial layer of 4*H*-SiC with a thickness of 10 μm grown on the ''silicon'' facet of an *n*-type 4*H*-SiC semiconductor crystal having a concentration of uncompensated acceptors on the order of $0.9 \times 10^{18}\,cm^{-3}$. The LTLPE layer had a thickness of 300 nm, while the atomic concentration of aluminum in it, as measured by SIMS, was $1.5 \times 10^{20}\,cm^{-3}$.

In order to make ohmic contacts, metals were deposited onto the LTLPE layer by vacuum sputtering via evaporation of a target by an electron beam. Before deposition the samples were subjected to standard chemical cleaning, after which photoresist was deposited on them and patterns were created for measuring the contact resistance. Immediately before deposition the samples were held for 2 minutes in a 10% solution of hydrofluoric acid and washed in deionized water. Successive deposition of all the metals took place in a single process while the residual pressure in the chamber of the deposition apparatus was held below 4×10^{-7} Torr. The contact metallization consisted of metals deposited in the following sequence: Ti (3 nm) — adhesion layer; Al (50 nm)–Ti (100 mm) — contact layer; Pd (10 nm)–Ni (50 nm) — protective coating. After deposition and flash photolithograpy, the samples were annealed to create the ohmic contact. The annealing took place over various time intervals at a temperature of $\sim 1200\,°C$ in a hydrogen flux, and a pressure of 500 Pa in a quartz chamber with cooled walls. Before annealing, the chamber was evacuated to a pressure of 5 Pa.

The time required to increase the temperature from room temperature to the anneal temperature was 40 sec. Annealing in a hydrogen flux and the Pd–Ni coating were used to suppress oxidation of the metals during the anneal.

ENERGY CHARACTERISTICS OF OHMIC CONTACTS

We used the Shockley method to measure the contact resistance, modified for a cylindrical contact geometry, as described in Ref. 17. The low surface resistivity of the metallization compared to the resistance of the epitaxial layer is an important condition for the use of this method to be valid. The surface resistivity of the metallization was $0.5 \, \Omega/\square$ immediately after deposition, and increased to $4.2 \, \Omega/\square$ after annealing at $1150 \, °C$ for 11 min. Despite the fact that the resistance of the metallization increased as a result of the annealing, it remained much smaller than the surface resistivity of the p-SiC layer ($\sim 600 \, \Omega/\square$).

The pattern formed on the metallization to measure the contact resistance had a set of point contacts with diameter $d = 40 \, \mu m$, surrounded by outer contacts whose inner diameter (D) varied from 100 to 500 μm. The resistance of the ohmic contacts was determined by plotting the dependence of the total resistance between the inner and outer contact R_{tot} on $\ln(D/d)$. The tangent of the slope angle of the straight-line approximation to this function equals $R_S/2\pi$, where R_S is the surface resistivity of the epitaxial layer, while the intersection with the R_{tot} axis equals the resistance of the inner point contact R_{ct}. The value of the contact resistivity R_{cont} can be obtained by numerically solving the transcendental equation given by the function $R_{ct} = f(R_S, R_{cont})$.[17] Note that in this method of measuring the quantity R_{cont} the resistance of the outer contact is assumed to be negligible. In reality, the resistance of the outer contact ranged from $0.05R_{ct}$ to $0.25R_{ct}$ as the outer diameter of the mask varied from 500 to 100 μm for the anticipated values of $R_S \simeq 1000 \, \Omega/\square$ and $R_{cont} \simeq 10^{-4} \, \Omega \cdot cm^2$. This implies that the value of R_{cont} calculated from these measurements is an upper bound for the value of the contact resistivity.

The current-voltage (I-V) characteristics of the test samples became linear after annealing for 50 sec at $1150 \, °C$. Figure 1 shows the dependence of R_{tot} on $\ln(D/d)$ for several periods of the photolithographic mask. A considerable scatter in results at various points on the film is noticeable; however, plots of R_{tot} versus $\ln(D/d)$ based on points measured within a single period of multiplication (1200 μm) are well approximated by a straight-line function. The value of the specific contact resistance obtained from this function ranged from 6.0×10^{-5} to $8.9 \times 10^{-4} \, \Omega \cdot cm^2$ for various regions on the film, which also differed in their values of R_S. An average value of $R_{cont} = 1.5 \times 10^{-4} \, \Omega \cdot cm^2$ was obtained for $R_S < 600 \, \Omega/\square$. Subsequent annealings of these contacts for periods as long as 300 sec at $1200 \, °C$ led to an increase in the contact resistance to $8.5 \times 10^{-4} \, \Omega \cdot cm^2$, although the I-V characteristics remained linear in this case.
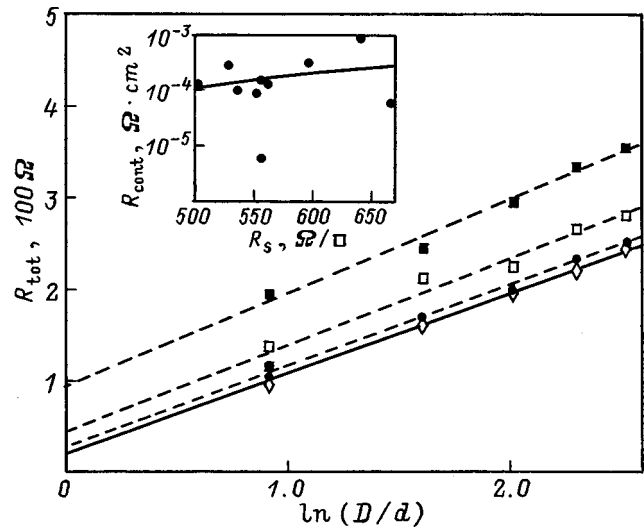

FIG. 1. Dependence of R_{tot} on $\ln(D/d)$ for an annealed Ti/Al/Ti/Pd/Ni contact to strongly doped 4H-SiC.

STRUCTURAL PROPERTIES OF THE STRONGLY DOPED SUBCONTACT 4H-SIC LAYER AND THE CONTACT METALLIZATION

The structural properties of the LTLPE 4H-SiC layer were studied by x-ray diffraction. Figure 2 shows rocking curves in modes (ω) and $(\omega, 2\theta)$ measured using two- and three-crystal spectrometers operating on the $(0004) \, CuK_\alpha$ reflection. Asymmetry of the peaks is observed in both curves. The half-widths of the rocking curves measured in modes (ω) and $(\omega, 2\theta)$ were comparable, allowing us to assume a uniform distribution of dislocations in the epitaxial layer. This assumption in turn allows us to decompose the rocking curves measured in both modes into a sum of curves described by Gaussian distributions.[18] As is clear from the figure, each rocking curve is well approximated by a sum of two curves that are signals from the strongly doped LTLPE layer (1) and the weakly doped p-type layer and substrate (2). The half-width of the peak of the rocking curve from the layer was $37.2''$ for a half-width of the peak from the substrate equal to $12''$ on the curve measured in the (ω)-mode, which shows the rather high structural quality of the strongly doped LTLPE p-type layer. The angular distance between the peaks from the substrate and the strongly doped p-type layer on the rocking curve measured in the $(\omega, 2\theta)$-scanning geometry is $0.00253°$, which corresponds to a concentration of Al in the LTLPE layer of about $1.5 \times 10^{20} \, cm^{-3}$ (Ref. 19). This value of the Al concentration is in good agreement with the results obtained from SIMS.

In order to study the changes that occur in the composition of the metallic layer as the ohmic contact forms, we measured Auger profiles of the samples immediately after deposition and after annealing. The results are shown in Fig. 3. It is clear that as a result of annealing, oxidation occurs only at the metallization surface, and that there is no oxygen at the ⟨silicon carbide⟩–metal boundary. Despite the fact that, on the whole, the protective Pd–Ni layer fulfilled its function and prevented oxidation of the contact Ti–Al layer during the anneal time, it must be noted that the Pd diffuses
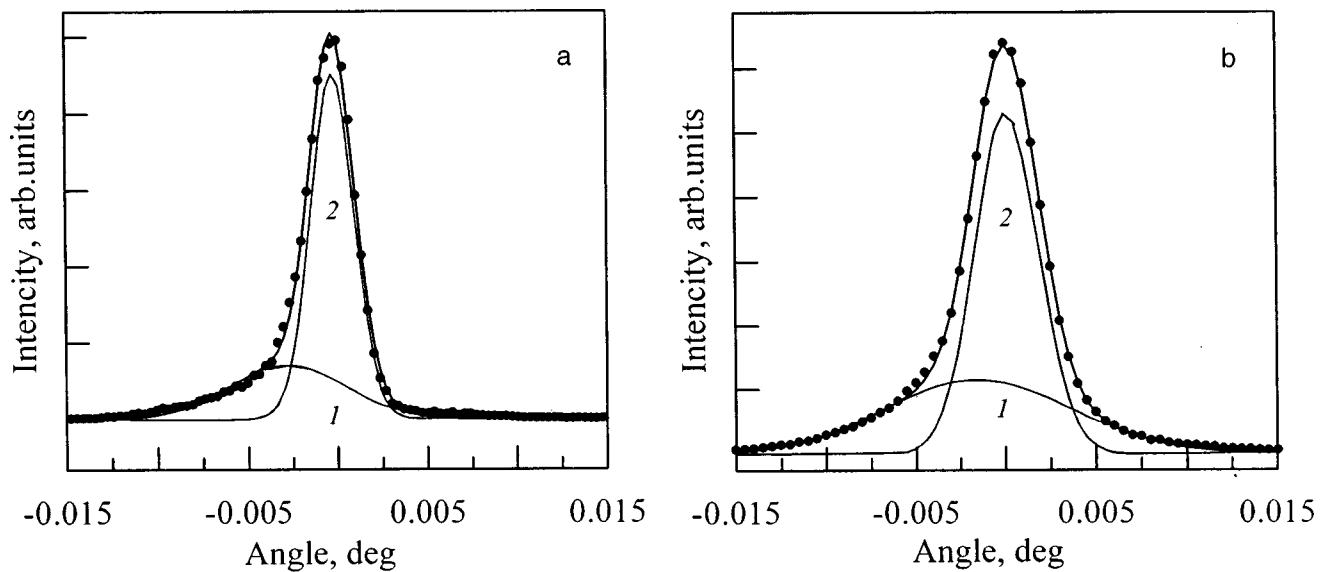
FIG. 2. Diffractive reflection curves in modes: a—(ω, 2θ), b—(ω). The experimental points lie on a curve that is the sum of two Gaussians which are shown by the thin curves and explained in the text.

in the Ti layer even during the deposition process. In fact, as shown in Ref. 20, it is necessary for oxygen to be present in the surrounding atmosphere in order that there be no mutual diffusion of Pd and Ti, because oxygen itself diffuses through the palladium and forms titanium oxide at the Pd–Ti boundary, which intrinsically plays the role of a barrier for Pd and prevents its diffusion into the Ti. For a deposition of metals under high-vacuum condition, i.e., in the absence of oxygen, the use of the additional Pd layer turns out to be unnecessary. Although the substrate was not heated intentionally, the deposited metal increased its temperature

enough for mutual diffusion of Pd and Ti. This process is also observable in the Auger profiles of the samples immediately after deposition.

Another distinctive feature of the metallization on samples after annealing is the presence of a layer containing carbon and titanium close to the ⟨silicon carbide⟩- metal boundary. X-ray phase analysis of the contact layer after annealing shows that peaks for pure Ni and Ti appear on the diffraction pattern, and also a peak that can be interpreted as corresponding to AlPd or TiC. Comparison with the results of Auger analysis, for which neither Al nor Pd were ob-
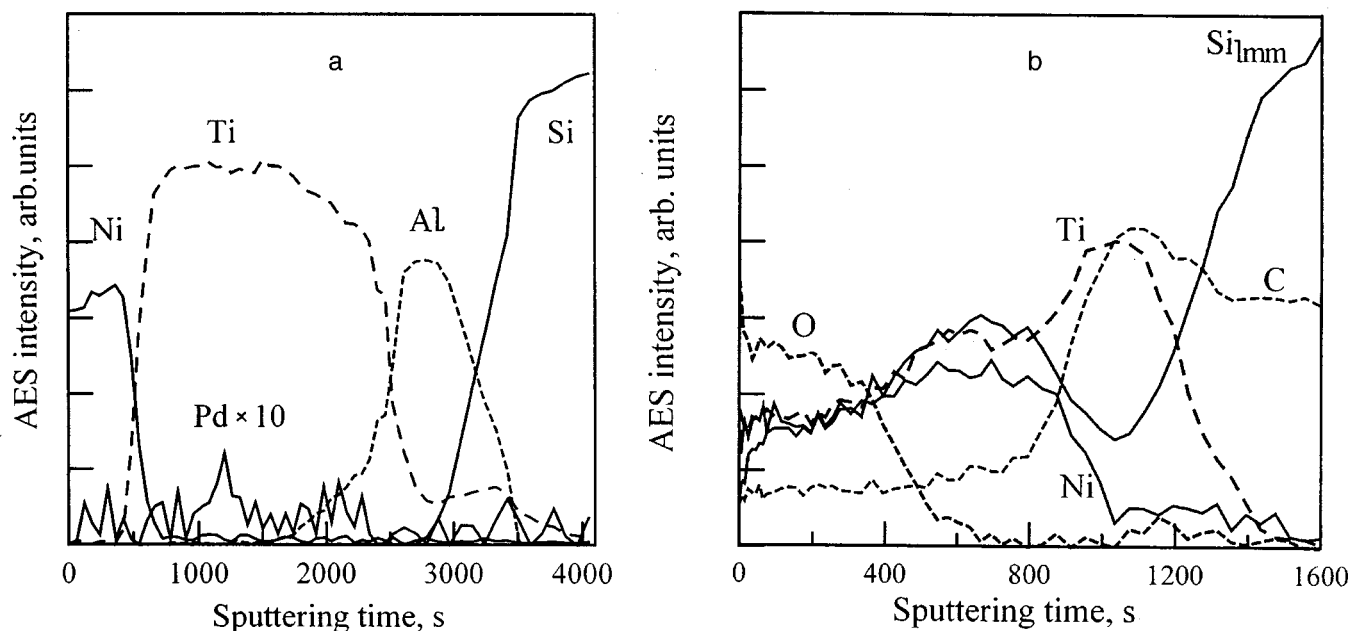

FIG. 3. Auger profile of the contact composition of the metals: a—immediately after deposition, b—after annealing for 50 sec at 1150 °C in a flux of hydrogen.
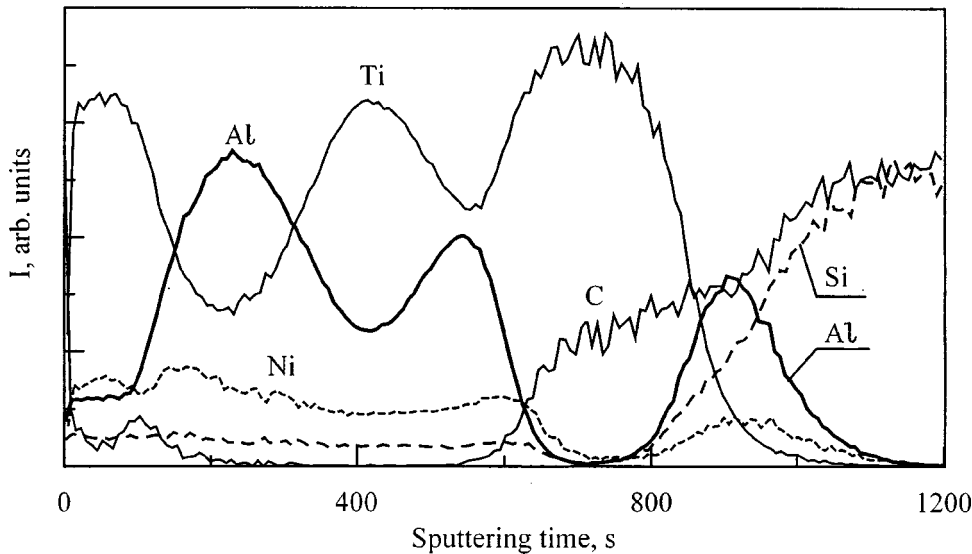
FIG. 4. SIMS profile of contact composition of metals after annealing for 50 sec at 1150 °C in a flux of hydrogen.

served (which implies that their concentrations do not exceed 1%), allows us to assert that titanium carbide forms in the contact layer as a result of annealing. In order to obtain the Al distribution in the contact layer we used SIMS, which allowed us to detect very low concentrations of Al down to $\sim 10^{17}\,\mathrm{cm}^{-3}$. The SIMS profile for the distribution of elements in the contact layer after annealing is shown in Fig. 4. Although the SIMS method does not give correct quantitative estimates for such high concentrations, the correlation between SIMS and the Auger profiles is quite clear: both methods show the presence of a layer enriched with Ti and C. It is also clear from Fig. 4 that some of the aluminum atoms diffuse through the titanium layer towards the surface, while the rest of the Al atoms remain close to the TiC-SiC boundary. We assume that the Al forms a high-temperature alloy with Ti in a very thin layer near the boundary, because the contact remains stable as a result of the subsequent anneal.

CONCLUSIONS

The layer grown by low-temperature liquid-phase epitaxy and used for making ohmic contacts to *p*-type 4*H*-SiC had an aluminum concentration of $1.5 \times 10^{20}\,\mathrm{cm}^{-3}$, which allowed us to obtain contacts with resistivities less than $10^{-4}\,\Omega \cdot \mathrm{cm}^2$. The high concentration of acceptor impurities is the most important, but by no means the only requirement on the subcontact layer of semiconductor in the course of device fabrication. In particular, the subcontact layer should have a low bulk resistivity in order to avoid additional losses due to the resistance connected in series with the working structure. The resistivity depends not only on the impurity concentration but also on the degree of activation of the impurities and the crystalline quality of the semiconductor material. Thus, when $2 \times 10^{21}\,\mathrm{cm}^{-3}$ atoms of aluminum were incorporated by ion implantation into 6*H*-SiC, a material was obtained with a resistivity less than $0.22\,\Omega \cdot \mathrm{cm}$ (Ref. 11), and when 6*H*-SiC was doped with aluminum during vapor-phase epitaxy up to levels of about $5 \times 10^{20}\,\mathrm{cm}^{-3}$, the resistivity of the epitaxial layer was $0.042\,\Omega \cdot \mathrm{cm}$ (Ref. 21).

The magnitude of the resistivity of the subcontact layer $R_S \simeq 600\,\Omega/\square$, obtained by measuring the contact resistance corresponds to a bulk resistivity of the LTLPE 4*H*-SiC layer of $\sim 0.02\,\Omega \cdot \mathrm{cm}$. From what we can gather from published data, this value is close to the resistivity of the very highest-conductivity epitaxial layers of *p*-type 4*H*-SiC ($0.025\,\Omega \cdot \mathrm{cm}$) made by doping during vapor-phase epitaxy.[21] Keeping in mind that layers grown by low-temperature liquid-phase epitaxy have high structural quality, these results should find application in making contacts in bipolar high-power and high-frequency silicon-carbide devices.

[1)]Silicon carbide films with an epitaxial layer were purchased at CREE Research, Inc., (USA).

[1]L. Kassamakova, R. Kakanakov, N. Nordell, and S. Savage, Mater. Sci. Forum **264−268**, 787 (1998).

[2]N. Lundberg and M. Ostling, Solid-State Electron. **39**, 1559 (1996).

[3]J. Crofton, P. A. Barnes, J. R. Williams, and J. A. Edmond, Appl. Phys. Lett. **62**, 384 (1993).

[4]J. Crofton, L. Beyer, J. R. Williams, E. D. Luckowski, S. E. Mohney, and J. M. Delucca, Solid-State Electron. **41**, 1725 (1997).

[5]R. N. Hall, J. Appl. Phys. **29**, 914 (1958).

[6]M. M. Anikin, M. G. Rastegaeva, A. L. Syrkin, and I. V. Chuiko, in *Amorphous and Crystalline Silicon Carbide* III [Springer Proceedings in Physics 56], Berlin, Springer-Verlag (1992), p. 183.

[7]Yu. Vodakov, E. N. Mokhov, M. G. Ramm, and A. D. Roenkov, in *Amorphous and Crystalline Silicon Carbide* III [Springer Proceedings in Physics 56], Berlin, Springer-Verlag (1992), p. 329.

[8]L. Spiegss, O. Nennewitz, and V. Breternitz, Appl. Surf. Sci. **91**, 347 (1995).

[9]L. Spiegss, O. Nennewitz, and J. Pezoldt, Inst. Phys. Conf. Ser. **142**, 585 (1996).

[10]L. Spiegss, O. Nennewitz, and J. Pezoldt, Diamond Relat. Mater. **6**, 1414 (1997).

[11]K. Tone, S. R. Weiner, and J. H. Zhao, Mater. Sci. Forum **264−268**, 689 (1998).

[12] G. Pensl, V. V. Afanas'ev, M. Bassler, M. Schadt, T. Troffer, J. Heindl, H. P. Strunk, M. Maier, and W. J. Choyke, Inst. Phys. Conf. Ser. **142**, 275 (1995).

[13] Z. C. Feng, I. Ferguson, R. A. Stall, K. Li, Y. Singh, K. Tone, J. H. Zhao, A. T. S. Wee, K. L. Tan, F. Adar, and B. Lenian, Mater. Sci. Forum **264–268**, 693 (1998).

[14] N. Nordell, S. Savage, and A. Schoner, Inst. Phys. Conf. Ser. **142**, 573 (1995).

[15] S. V. Rendakova, V. Ivantsov, and V. A. Dmitriev, Mater. Sci. Forum **264–268**, 163 (1998).

[16] A. E. Nikolaev, S. V. Rendakova, I. P. Nikitina, K. V. Vassilevski, and V. A. Dmitriev, Electron. Mater. **27**, 288 (1998).

[17] G. Boberg, L. Stolt, P. A. Tove, and H. Norde, Phys. Scr. **24**, 405 (1981).

[18] M. A. Krivoglaz, *Diffraction of X-Rays and Neutrons by Nonideal Crystals* (Naukova Dumka, Kiev, 1983), p. 325.

[19] R. N. Kutt, E. N. Mochov, and A. S. Tregubova, Solid State Phys. **23**, 3496 (1981).

[20] J. M. Poate, K. N. Tu, and J. W. Mayer, *Thin Films — Interdiffusion and Reaction* (A. Wiley–Interscience Publication, 1978).

[21] T. Kimoto, A. Itoh, N. Inoue, O. Takemura, T. Yamamoto, T. Nakajima, and H. Matsunami, Mater. Sci. Forum **264–268**, 675 (1998).

Translated by Frank J. Crowne

Effect of low-temperature charge redistributions on the conductivity of surface electron channels at the Si/SiO$_2$ interface

N. I. Bochkareva and S. A. Khorev

A. F. Ioffe Physicotechnical Institute, Russian Academy of Sciences, 194021 St. Petersburg, Russia
(Submitted April 27, 1999; accepted for publication April 27, 1999)
Fiz. Tekh. Poluprovodn. **33**, 1340–1344 (November 1999)

The behavior of the electron density at the Si/SiO$_2$ interface with temperature is investigated by measuring the rf conductivity of band-edge surface electronic channels that shunt Schottky barriers in *n*-type Si. The results are explained within a model in which the ''metallic'' character of the temperature behavior of the conductivity reflects a redistribution of electron charge between the oxide and the silicon lattice in the vicinity of characteristic temperatures of the oxygen subsystem of the oxide. © *1999 American Institute of Physics.* [S1063-7826(99)01311-3]

1. The electronic properties of the Si/SiO$_2$ interface form the basis for devices used in silicon electronics and the classical two-dimensional electronic system, and as such have been studied extensively. However, recently there has been an ongoing elaboration of new model representations of electronic states at this interface and in the oxide. These new representations are required in order to understand the processes by which these states are modified by changes in temperature, electric field, and illumination, and the role of hydrogen in these processes.[1,2] Observations of a metal-insulator transition in the two-dimensional electron gas contained in silicon field-effect transistors at liquid-helium temperatures,[3] and its interpretation based on an assumed relation between the metallic conductivity and the temperature dependence of the occupation of scattering centers—charged hole traps in SiO$_2$ (Ref. 4) — has also attracted attention to this problem. Note that the ''metallic'' behavior of the conductivity of electron channels at the Si/SiO$_2$ boundary at liquid-nitrogen temperatures is connected with the dominance of electron-phonon scattering.[5] However, the nonmonotonic temperature behavior of the mobility observed in experiments (see, e.g., Ref. 6) requires that other mechanisms be invoked.

One such mechanism could be a low-temperature change in the spectrum of surface states and band bending of the sort observed in Ge,[7] Si,[8] and GaAs.[9] In these cases, measurements of the conductivity of surface channels can give information about the nature of electrical activity of surface centers. In Ref. 10 it was shown that the temperature dependence of the high-frequency conductivity of shunting surface electronic channels in barrier structures and relaxation spectra of the conductivity can also be informative. In Ge and Si, for example, these dependences are found to have well-defined steps and peaks near the same temperatures when surface structural defects are present,[10,11] allowing us to hypothetically associate them with the intrinsic behavior of oxygen and hydrogen-oxygen complexes at the boundary between the crystals and the natural oxide.[10] Such investigations of barrier structures with electronic surface channels induced by positive charge that forms in the oxide during the

thermal oxidation of silicon are of considerable interest.

Our goal was to investigate and compare the temperature behavior of the conductivity of surface channels in Schottky diodes made from *n*-type Si, channels that form at the interface between the Si and natural and thermally generated oxides, and to take into account a possible relationship between the ''metallic'' temperature character of the conductivity and redistributions of electron charge between the oxide and crystal silicon at the Si/SiO$_2$ interface that occur in the neighborhood of ''intrinsic'' temperatures of the oxide's oxygen subsystem.

2. In these investigations we used films of high-resistivity *n*-type Si with resistivities of 2 k$\Omega\cdot$cm which contain surface stacking faults surrounded by partial dislocations that penetrate to a depth of $<1\mu$m. The defects are introduced by oxidizing the Si in dry oxygen at an oxidation temperature $850-1050\,°$C for 1 hour, according to the method described in Ref. 10. In order to create the Schottky barrier, a layer of SiO$_2$ is first removed within a window with area 3×5 mm^2. A layer of Au is then deposited on the film with area 3.5×5.5 mm^2, forming a structure with a wide electrode. In control samples, the layer of thermally generated oxide is removed from the entire Si surface before depositing the Au. In order to measure the layer conductivity in a portion of the film, the thermal oxide with the defective surface is not removed. Ohmic Ni contacts are made on the backside of the films.

3. Structures with a wide electrode exhibit a considerable excess current which increases as the temperature is lowered. This is illustrated by the temperature dependence of the dc conductivity $G(T)$, shown in Fig. 1 by curve *1*. At high frequencies the active conductivity $\tilde{G}(T)$ of all the diodes exhibits a tendency toward nonmonotonic changes with decreasing temperature (curves *2*, *3*, *6*, and *7*). The change in the capacitive component of the rf conductance $\omega C(T)$ with temperature (where C is the measured capacity of the diodes, and $\omega=2\pi f$; here f is the frequency of the probing voltage) is illustrated by the function $\tilde{B}(T)$, where $\tilde{B}\equiv\omega(C-C_0)$, $C_0\equiv C(T=300$ K) (Fig. 1, curve *4*). The correlation between the traces of curves $\tilde{G}(T)$ and $\tilde{B}(T)$ indicates that the tem-
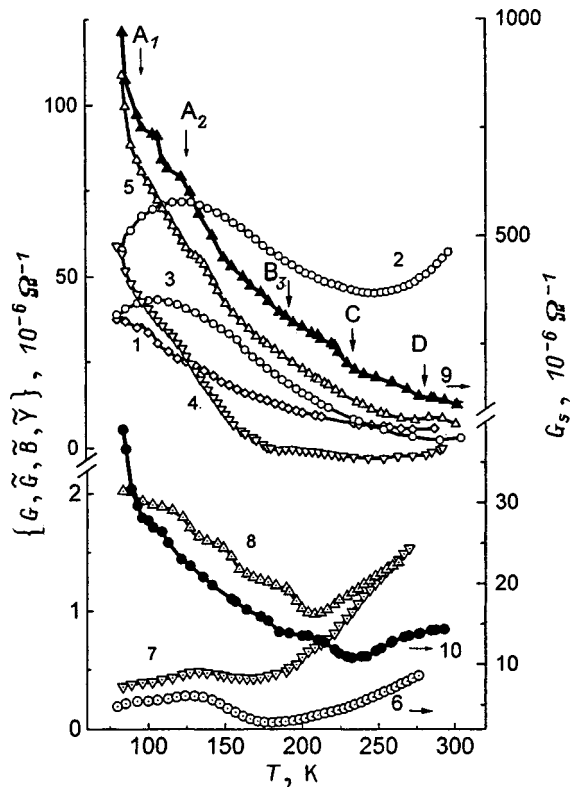
FIG. 1. Temperature dependences of the dc conductance $G(T)$ (*1*), its active component $\widetilde{G}(T)$ (*2, 3, 6, 7*), its capacitive component $\widetilde{B}(T)$ (*4*), and the modulus of the rf conductivity $\widetilde{Y}(T)$ (*5, 8*) of surface channels at the boundaries between Si and its thermal (*1–5*) and natural oxides (*6–8*), and also the layer conductance of a Si sample with a thermal oxide $G_s(T)$ after holding the sample for several days (*9*) and several months (*10*) under natural conditions. The arrows denote temperature positions of the peaks of spectrum 1 in Fig. 2. For curves *1–5, 7*, and *8* the left-hand scale is used, for curves *6, 9*, and *10* the right-hand scale. The oxidation temperature, °C: (*1–8*) — 1050, (*9, 10*) — 850. *U*, *6* — 0.5; *2* — 1.5; *3, 4* — 2.5; *1, 5, 7* — 3.5; *8* — 8. $f = 160$ kHz.

FIG. 2. Relaxation spectra of the capacitive component of the rf conductivity of a surface channel at the boundary of Si with its natural (*1*) and thermally grown oxide (*2, 3*). $t_1 = 2$ ms, $t_2 = 10$ ms. $f = 160$ kHz. Switching: *1, 2* — (0→4.5 V), *3* —(1→2.5 V).

perature features of the measured capacitance are caused by changes in the reactive conductivity of the leakage channel with temperature. Note that the functions $G(T)$, $\widetilde{G}(T)$, and $\omega C(T)$ are reversible under thermal cycling.

The temperature dependences of the modulus of the high-frequency admittance $\widetilde{Y} \equiv (\widetilde{G}^2 + \widetilde{B}^2)^{1/2}$ are shown in Fig. 1 by curves *5* and *8*. The temperature curves of the layer admittance of the samples $G_s(T)$ are similar in character, reflecting the temperature behavior of the surface admittance $\sigma_s(T)$, because the measured value of G_s exceeds the bulk conductivity ($\sim 1 \times 10^{-5}\ \Omega^{-1}$ at 300 K) (Fig. 1, curves *9* and *10*). From Fig. 1 it is clear that the nonmonotonic nature of the curves $\widetilde{G}(T)$, $\widetilde{B}(T)$, and $\widetilde{Y}(T)$ in samples with a thermal oxide is less clearly defined than in the control samples, but the changes in slope are observed at similar temperatures.

Such behavior of the conductivity with temperature in the samples under study is even more strikingly evident in the relaxation spectra (Fig. 2), which consist of temperature curves for the nonstationary capacitive admittance $\Delta\widetilde{B}(T) = \omega[C(t_2) - C(t_1)]$ and which are obtained by the standard method used for capacitive deep-level transient spectroscopy. As already noted in Ref. 10, the choice to investigate
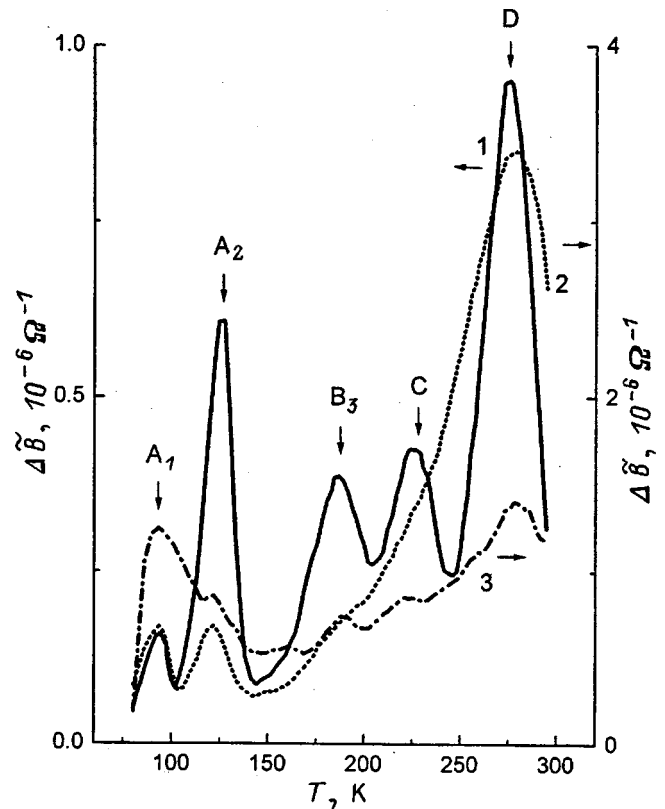
high-resistance Si excludes the possibility that effects of charging deep levels will appear in the spectra, because the width of the depletion region even under equilibrium conditions greatly exceeds the penetration depth of the stacking faults ($<1\ \mu$m) and when the voltage is switched, the edge of the space-charge region sweeps through a region without defects. The spectra of control samples are identical to those observed in Ref. 10 in Si with surface packing faults; they contain five basic peaks with maxima A_1 (94 K), A_2 (126 K), B_3 (187 K), C (226 K), and D (273 K). From Fig. 2 it is clear that in structures with a wide electrode, despite the considerable monotonic background, peaks in the spectra are observed near the same temperatures.

4. The correlation of the temperature dependences $\widetilde{Y}(T)$ and $\Delta\widetilde{B}(T)$ with the function $G_s(T)$ can be interpreted within the model discussed in Ref. 10, which established a relation between the density of electrons at the Si/SiO$_2$ interface and the admittance of the electron channel that shunts the potential barrier. In this model it is assumed that an external voltage changes not only the width of the space-charge region and the depth of the channel, but also the width of the channel, because a transverse field appears at its boundary due to the different distributions of longitudinal field in the channel and in the depletion region. When this field is screened, the channel narrows at the source and broadens towards the drain. Negative feedback in the channel affects the screening time significantly. When the voltage is in-

creased in a stepwise manner, for example, the increase in current as a result of broadening of the channel at the drain suppresses the redistribution of voltage along the channel, causing narrowing of the channel at the source. The subsequent decay of the current and narrowing at the drain slows down the broadening at the source. Negative feedback broadens the frequency characteristics both in the regions of high and low frequencies, decreasing the time $\tau_f(T) \sim \sigma_s^{-1}(T)$ for the current to grow and increasing the time $\tau_s(T) \sim \sigma_s(T)$ in which it slowly falls off.[10] At high frequencies, due to the oscillating width of the channel, measurements of the admittance reflect the conductivity of an ''opened'' channel and the temperature dependences $\sigma_s(T)$ are clearly manifested in the functions $\tilde{G}(T)$, $\tilde{B}(T)$, and $\tilde{Y}(T)$ but more weakly in the functions $G(T)$, which to a large degree reflects the overlap of the channel by the depletion region and the effect of an increase of the diffusion potential as the temperature is lowered. In addition, at $\omega\tau_f \sim 1$ the temperature change in σ_s leads to a change in the ratio $\tilde{G}/\tilde{B}$, which also makes itself felt in the shapes of the curves $\tilde{G}(T)$ and $\tilde{B}(T)$. The dependence $\tau_s = f(\sigma_s)$ accounts for a number of peaks in the relaxation spectra as $\Delta\tilde{B}(T) = \omega[C(t_2) - C(t_1)]$ changes for a given choice of t_2 and t_1 for the relaxation time window.

5. We have presented some information about possible connections between the temperature-dependent changes in the admittance of surface band-edge channels and the surface density of electrons and temperature-induced redistributions of electron charge between the oxide and silicon, based on low-temperature properties of oxygen in adsorbed oxygen and hydrogen-oxygen condensates that are known from the literature, and also in the solid phase.

Analogy with the temperature transition from donor to acceptor activation of oxygen adsorbed complexes. Oxygen can be both an acceptor and a donor of electrons. Donor-like behavior of oxygen centers at the surface of Si crystals, like oxygen thermal donors in its bulk, is connected with electrons of unshared-pair orbitals in super-coordinated oxygen atoms. Increasing the number of oxygen atoms in a complex, and also increasing the binding energy and decreasing the interatomic distances, leads to ejection of electronic levels into the conduction band.[12] The force that drives the temperature dependence of the electronegativity and the conversion of submonolayer oxygen adsorbed on a cold substrate from donor to acceptor is a structural transition that is observed with increasing temperature. Oxygen adsorbed at 100 K on a Si surface, for example, exhibits electropositive properties, and decreases the work function, forming a downward band bending at the surface. Upon heating, the work function increases and the bands bend upwards, which is attributable to a changeover from molecular adsorbed oxygen to chemisorbed oxygen.[13] The transformation of the molecular form of oxygen to its atomic form observed in Ref. 14 in submonolayers of oxygen adsorbed at 100 K at the surface of Cu is accompanied by a step-like increase in the work function, at the same temperatures as the peaks A_2, B_3, C, D in the relaxation spectra in this paper. An analogous change in the work function is also observed in the system $H_2O/O_2/Cu$ (Ref. 15). In this case, in the region of the same temperatures

as the peaks B_3, C, and D in our study, the authors of Ref. 15 observed peaks in the thermodesorbed spectra, reflecting a loss of stability of hydrogen-oxygen complexes at 190, 220, and 280 K.

Redistribution of charge at a silicon-oxide interface at intrinsic temperatures of the oxygen subsystem of the oxide. Within the same temperature intervals as the peaks A_1, A_2, B_3, C, and D, a succession of structural phase transitions is observed when solid hydrogen-oxygen condensates synthesized at 80 K are heated: amorphous condensate $\rightarrow$ sintering $\rightarrow$ softening $\rightarrow$ viscous liquid $\rightarrow$ crystallization $\rightarrow$ melting $\rightarrow$ liquid $\rightarrow$ gas,[16] as well as amorphous solid water α-H_2O (Ref. 17). As a result of these transformations, the concentrations of molecular ions of oxygen peroxide O_2^{2-} and O_2^- ions, and also O_3 and O_4 structures containing a -OO- bond, decrease nonmonotonically with temperature, while the concentrations of atomic ions O^- and O^{2-} increase: $O_2 \rightarrow O_2^- \rightarrow O_2^{2-} \rightarrow O^- \rightarrow O^{2-}$ (Ref. 16). Note also that in the temperature range corresponding to peaks A_2, B_3, C, and D, the authors of Ref. 18, using ESR, observed a stepwise decrease in the concentration of peroxide radicals $\equiv$Si-OO- during post-irradiation annealing of amorphous SiO_2 with a high content of dissolved O_2 molecules.

The analogies formulated here allow us to assume that in the oxygen subsystem of SiO_2 there are a number of temperatures in the range 77−300 K at which the interaction energy in the oxygen complexes containing the bond -OO- change reversibly, which is accompanied by a change in their electronegativity and a redistribution of electron charge between the oxide and the silicon crystal. As a result, the density of bound and free electrons at the Si surface can also change. These temperatures in the final analysis are related to temperature phase transitions: boiling of the oxygen (90 K) and ozone (161 K); breaking of the molecular bond -OO- in molecular O_2^- ions (145 K) and oxygen peroxide O_2^{2-}; the beginning of decomposition of the solid condensate $H_2O_2-H_2O$ (190 K) and melting of the eutectic $H_2O_2-H_2O$ (220 K); melting of ice (273 K), sintering ($\sim$100 K), glassification ($\sim$ 136 K) and crystallization ($\sim$ 158 K) of the solid hydrogen-oxygen condensates.[16,17] In this case the change in electron density at the Si/SiO_2 interface in the neighborhood of these temperatures depends on real structural features of SiO_2 and defects at the Si surface, and also the presence of hydrogen in SiO_2.

Analogy with the temperature mechanism for interlayer charge transfer in layered oxides. The qualitative model considerations stated above are also based on the ''oxygen-hole'' model of quasi-two-dimensional conductivity and superconductivity in layered oxides based on the spatial separation of electrons and holes between planes with differing oxygen concentrations[19] and on the decisive role of the oxide's oxygen subsystem. In these models, the binding of electrons in a layer with an oxygen deficit leads to an increase in the concentration of holes in the conducting layer. It is assumed that dimerization of holes $2O^{2-} - 2e \rightarrow 2O^- \rightarrow O_2^{2-}$ and binding of the holes at oxygen peroxides O_2^{2-} leads to superconductivity in the neighborhood 90 K (Refs. 20 and 21) and that the temperature dependence of the

conductivity is controlled by thermal drift of oxygen atoms in oxygen bridges between layers.[22] Comparison of the experimental data allows us to identify the general characteristic temperatures for changes of interatomic distances in layered oxides controlled by the density of holes in conducting layers,[22] and changes in the density of electrons at the Si/SiO$_2$ interface based on data from our study. This is an indication of a possible generality of electronic chemical processes responsible for interlayer charge redistribution. The analogy we have mentioned is confirmed by the model representation put forth in this paper for microscopic phase transitions at the Si/SiO$_2$ interface as the physical cause of the temperature correlation of electronic and structural properties, and indirectly confirms that the temperature transformations between molecular and atomic forms of oxygen in the oxide are reversible under temperature cycling. This analogy also allows us to assume that the increase in electron density at the Si/SiO$_2$ interface as a result of cooling can be accompanied by an increase in the bond length of the bridging oxygen (oxygen in the structural fragment $\equiv$ Si-O-SiO$_3$) with the Si lattice.

Temperature analogies between the relaxation spectrum of the conductivity and the spectra of internal friction. Additional confirmation of these conclusions comes from analogous behavior of temperature features in the rf conductivity of surface channels found here and also in Refs. 10 and 11, and absorption of ultrasonic waves in the kilohertz spectral region observed as anomalies in the conductivity in Ge and Si crystals containing dislocations in the bulk and in the skin layer reported in Refs. 23 and 24. For example, peaks were observed in the spectra of internal friction in Si crystals[23] in the temperature range 80–200 K at 91, 124, and 192 K, which are close to the temperature peaks A_1, A_2, and B_3 in the relaxation spectra of the conductivity. Similar peaks in layered oxides, accompanied by abrupt changes in the parameters of the oxide lattice,[25] are observed at 90, 126, 180, and 220 K, which correspond to the temperature positions of peaks A_1, A_2, B_3, and C. The mechanisms for low-energy relaxation processes in oxides, just as in semiconductor crystals, remain matters of dispute, despite a long history of discussion. Anomalies in the absorption of elastic waves in Si are connected with freeze-out of the rotational motion of point defects, including oxygen[26] or hydrogen defects,[27] which brake the elastic vibrations of dislocations. In oxides these anomalies are often related to the oxide's oxygen subsystem, i.e., internal structural instability connected with oxygen vacancies, changes in the spectrum of vibration of oxygen- containing complexes, etc. (see, e.g., the review artice[28]).

Note also that we can find an explanation within the framework of these model representations of the temperature changes in electronegativity of oxygen and hydrogen-oxygen complexes for the temperature anomalies observed previously in the mobility of electron inversion channels in silicon field-effect ransistors,[6] and also the post-irradiation positive built-in charge in SiO$_2$ (Ref. 18) and the density of dangling bonds of silicon at the Si/SiO$_2$ surface.[29] This prompts us to claim that our model could provide the key to understanding the mechanism for modification of interface states at the

Si/SiO$_2$ interface upon exposure to electric field, illumination, and temperature.

6. Based on analysis of the results obtained here, and using literature data that are relevant, we may conclude that the observed nonmonotonic increase in the conductance of electronic channels at the Si/SiO$_2$ boundary with decreasing temperature is controlled by temperature-induced redistribution of electrons and holes between Si and SiO$_2$ in the neighborhood of intrinsic temperatures of the oxide's oxygen subsystem, leading to the formation of a surface layer enriched by electrons near 80 K.

[1] E. H. Poindexter, C. F. Young, and G. J. Gerardy, in *Fundamental Aspects of Ultrathin Dielectrics on Si-based Devices*, edited by E. Garfunkel *et al.* (Kluwer Academic Publishers, Netherlands, 1998).

[2] J. M. M. de Nijs, K. G. Druijf, V. V. Afanas'ev, E. van der Drift, and P. Balk, Appl. Phys. Lett. **65**, 2428 (1994).

[3] S. V. Kravchenko, W. E. Mason, G. E. Bowker, J. E. Furneaux, V. M. Pudalov, and M. D'Iorio, Phys. Rev. B **51**, 7038 (1995).

[4] B. L. Altshuler and D. L. Maslov, Phys. Rev. Lett. **82**, 145 (1999).

[5] T. Ando, A. B. Fowler, and F. Stern, Rev. Mod. Phys. **54**, 437 (1982).

[6] K. Rais, G. Ghibaudo, and F. Balestra, Phys. Status Solidi A **146**, 853 (1994).

[7] A. V. Rzhanov, *Electronic Processes at the Surfaces of Semiconductors* (Nauka, Moscow, 1971).

[8] S. I. Kirillova, M. D. Moin, V. E. Primachenko, S. V. Svechnikov, and V. A. Chernoban, Fiz. Tekh. Poluprovodn. **26**, 1399 (1992) [Sov. Phys. Semicond. **26**, 784 (1992)].

[9] Yu. V. Dubrovskiĭ and S. V. Morozov, *Surfaces. Physics, Chemistry, Mathematics* N9, 143 (1987).

[10] N. I. Bochkareva and A. V. Klochkov, Fiz. Tekh. Poluprovodn. **32**, 1432 (1998) [Semiconductors **32**, 71 (1998)].

[11] N. I. Bochkareva, Fiz. Tekh. Poluprovodn. **25**, 537 (1991) [Sov. Phys. Semicond. **25**, 323 (1991)].

[12] P. Deak, L. C. Snyder, and J. W. Corbett, Phys. Rev. B **45**, 11 612 (1992).

[13] D. Schmeisser, Surf. Sci. **137**, 197 (1984).

[14] A. Spitzer and H. Luth, Surf. Sci. **118**, 136 (1982).

[15] P. A. Theil and T. E. Madey, Surf. Sci. Rep. **7**, 211 (1987).

[16] T. V. Yagodovskaya and L. I. Nekrasov, Zh. Fiz. Khim. Zh. Fiz. Khim. **51**, 2434 (1977).

[17] G. P. Johari, A. Hallbrucker, and E. L. Mayer, J. Chem. Phys. **95**, 2955 (1991).

[18] D. L. Griscom, Phys. Rev. B **40**, 4224 (1989).

[19] J. D. Jorgensen, B. W. Veal, A. P. Paulikas, L. J. Nowicki, G. W. Grabtree, H. Claus, and W. K. Kwok, Phys. Rev. B **41**, 1863 (1990).

[20] M. S. Hegde and P. Ganguly, Phys. Rev. B **38**, 4557 (1988).

[21] I. Ya. Dzyaloshinskiĭ, JETP Lett. **49**, 142 (1989).

[22] J. Konstantinovic, G. Parette, and Z. Diordjevic, Solid State Commun. **70**, 163 (1989).

[23] L. P. Khiznichenko, P. F. Kromer, D. K. Kaipnazarov, E. Otenyazov, D. Yusupova, and L. G. Zotova, Phys. Status Solidi **21**, 805 (1967).

[24] B. M. Mecs and A. S. Nowick, Appl. Phys. Lett. **8**, 75 (1966).

[25] Y. Wang, H. Shen, Z. Zhu, Z. Xu, M. Gu, Z. Niu, and Z. Zhang, J. Phys. C **20**, L665 (1987).

[26] V. S. Postnikov, V. I. Kirillov, Yu. A. Kapustin, and V. S. Borisov, Fiz. Tekh. Poluprovodn. **27**, 1906 (1985) [Sov. Phys. Semicond. **27**, 1148 (1985)].

[27] A. Novik and B. Berry, *Relaxation Phenomena in Crystals* (Atomizdat, Moscow, 1975).

[28] V. I. Belomestnykh, O. L. Khasanov, and Yu. Kon-Chiu, Superconductivity **2**, 119 (1989).

[29] D. L. Griscom, J. Appl. Phys. **58**, 2524 (1985).

Statistical delay of microplasma breakdown in GaP $p-n$ junctions

S. V. Bulyarskiĭ

Ulyanovsk State University, 432700 Ulyanovsk, Russia

Yu. N. Serëzhkin and V. K. Ionychev

Mordovian State University, 430000 Saransk, Russia

The mechanism for switching on a microplasma in gallium phosphide $p-n$ junctions is investigated. It is shown that changing the distribution function of the statistical breakdown delay with respect to distance makes it possible to determine the energy spectrum of deep levels localized in the microplasma channels. In these experimental studies, commercial gallium phosphide AL102 red-light LEDs were used. In the temperature range 100–380 K the influence of a number of energy levels was detected. In these diodes, deep levels were observed to have an unusually strong effect on the statistical breakdown delay when their charge states are changed by a fractional decrease in the voltage across the $p-n$ junction. © *1999 American Institute of Physics.* [S1063-7826(99)01411-8]

INTRODUCTION

Avalanche breakdown of $p-n$ junctions usually has a microplasma character with a delay.[1] Deep levels located in the space-charge region of a $p-n$ junction are found to have a large effect on the breakdown delay.[2–6] At high concentrations of these levels, when the electric field intensity in the $p-n$ junction changes appreciably during their charging, a relaxational breakdown delay appears.[4] If the concentration of deep levels is low, then they affect the statistical breakdown delay of the microplasma. For silicon $p-n$ junctions these issues were investigated in Ref. 5, and in Ref. 6 for gallium phosphide $p-n$ junctions. However, the results obtained, as the authors of these papers themselves remark, are too imprecise and contradictory.

In our view, many of the problems are connected with the fact that charging of deep levels takes place by passage of the avalanche current through the microplasma channel. In this case, the deep levels can capture both electrons and holes. The occupation of deep levels occurs over the entire space-charge region, including the region of maximum field. Therefore, effects of Frenkel–Poole type or tunneling can manifest themselves during re-emission of the captured charge carriers. The passage of a filling current pulse heats the channel of the microplasma. Because emission of carriers occurs over a short time, problems arise with the definition of temperature.

In this paper we study the effect of deep levels on statistical breakdown delay as these levels are filled by decreasing the reverse voltage across a $p-n$ junction. In this case trapping of only charge carriers (electrons from the *n*-base side and holes from the *p*-base side) occurs. Filling of deep levels can take place within a bounded region near the edges of the space-charge region, where the electric field intensity is considerably lower than its maximum field intensity in the $p-n$ junction.

We will consider the influence of deep levels in a microplasma channel on the probability of the channel switching on, and the possibility of determining deep-level parameters from measurements of the distribution function for the length of delay before static breakdown of the microplasma.

## DISTRIBUTION OF STATIC BREAKDOWN DELAY VERSUS DISTANCE

Consider a $p-n$ junction in which a uniform distribution of deep levels is present with an energy level in the upper half of the band gap. In this case, as a rule, the emission of electrons from a deep level is considerably larger than the emission of holes, i.e., $e_n \gg e_p$. Let the $p-n$ junction support a voltage U_m for a sufficiently long time so that stationary occupation of the deep levels is achieved. Let us discontinuously increase the voltage from U_m to $U > U_M$, where U_M is the voltage for microplasma breakdown. The situation in the microplasma channel for a certain time t after the discontinuous change in voltage is shown schematically in Fig. 1.

When $e_n \gg e_p$, the deep levels in the region from $-L_p$ to L_m are nearly empty, and from them we will alternately see emission of holes and electrons. In the region from L_m to L_n, starting with the instant of the voltage jump, all the deep levels will be completely occupied by electrons. In this region we will observe primarily electron emission.

The probability of switching on the microplasma after applying an overvoltage can be expressed in the form[2]

$$P_M = 1 - \exp\left[-\int_0^t P_{01}(t)dt \right],$$

where P_{01} is the probability of a transition from the ''switched off'' state to the ''switched on'' state per unit time. It is determined by the frequency for the appearance of triggering carriers in the microplasma channel and the prob-
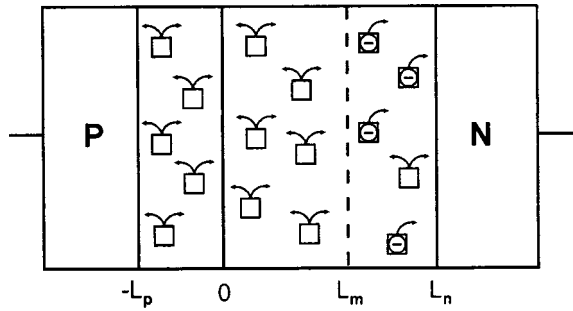
FIG. 1. Schematic illustration of a $p-n$ junction.

ability of avalanche being triggered by them. In the case under study, switching on of the microplasma is caused by electrons and holes emitted from the deep levels.

The probability that in a time t after applying the overvoltage the microplasma does not switch on is determined by the expression

$$1 - P_M = \exp\left\{ -S_M \int_0^t \int_{-L_p}^{L_n} [G_n(x,t)P_n(x,t) + G_p(x,t)P_p(x,t)]dxdt \right\}, \tag{1}$$

where $G_n(x,t)$ and $G_p(x,t)$ are the rates of emission of electrons and holes from the deep levels, respectively; $P_n(x,t)$ and $P_p(x,t)$ are the probabilities that they will trigger an avalanche, and S_M is the cross section of the microplasma channel.

In the first portion of the space-charge region from $-L_p$ to L_m we have a stationary occupation of the deep levels and the rate of emission of electrons and holes is the same:

$$G_{n1} = G_{p1} = \frac{e_n e_p}{e_n + e_p} N_t, \tag{2}$$

where e_n and e_p are emission coefficients for electrons and holes from the deep levels, and N_t is the deep level concentration.

In the second region from L_m to L_n there is nonstationary occupation of the deep levels. The rate of emission in this region is given by the relations

$$G_{n2} = e_n N_t \left(\frac{e_n}{e_n + e_p} e^{-\frac{t}{\tau}} + \frac{e_p}{e_n + e_p} \right), \tag{3}$$

$$G_{p2} = \frac{e_n e_p}{e_n + e_p} N_t \left(1 - e^{-\frac{t}{\tau}} \right), \quad \tau = (e_n + e_p)^{-1}. \tag{4}$$

In this case it is assumed that at $t = 0$ occupation of the deep levels is complete in this region. We also assume that the concentration of deep levels N_t is small compared to the concentration of doping impurities, and that the electric field has is no effect on the emission of charge carriers from the deep levels. In this case e_n and e_p do not depend on the coordinates, while L_n, L_p, P_n, and P_p are independent of time.

Based on Eqs. (1)–(4) for the distribution function of the breakdown delay with respect to distance (the probability that during time t the microplasma will not switch on) we then have

$$1 - P_M = \exp\left\{ -S_M N_t \left[\frac{e_n e_p}{e_n + e_p} t \int_{-L_p}^{L_n} \left(P_n(x) \right. \right.\right.$$
$$\left. + P_p(x) \right) dx + \frac{e_n^2}{(e_n + e_p)^2} \left(1 - e^{-\frac{t}{\tau}} \right)$$
$$\left.\left. \times \left(\int_{L_m}^{L_n} P_n(x)dx - \frac{e_p}{e_n} \int_{L_m}^{L_n} P_p(x)dx \right) \right] \right\}. \tag{5}$$

In GaP the coefficients of collisional ionization of electrons and holes are equal, i.e., $\alpha_n = \alpha_p = \alpha$. In this case the probability of triggering an avalanche by an electron $P_n(x)$ and a hole $P_p(x)$ starting from a point x in the space-charge region is determined by the expressions[1]

$$P_n(x) = 1 - \exp\left[-P_{np} \int_x^{L_n} \alpha(x')dx' \right],$$

$$P_p(x) = 1 - \exp\left[-P_{np} \int_{-L_p}^x \alpha(x')dx' \right], \tag{6}$$

where P_{np} is the probability of triggering an avalanche by an electron-hole pair. When the ionization of electrons is the same as that of the holes, this quantity does not depend on the location of the pair generation, and is determined by the transcendental equation

$$1 - P_{np} = \exp\left[-P_{np} \int_{-L_p}^{L_n} \alpha(x)dx \right]. \tag{7}$$

It follows from Eq. (5) that in a semilogarithmic system of coordinates the distribution function for breakdown delay consists of linear and nonlinear parts:

$$f(t) = -\frac{M}{L} \int_{-L_p}^{L_n} [P_n(x) + P_p(x)]dx \frac{e_n e_p}{e_n + e_p} t, \tag{8}$$

$$\varphi(t) = -\frac{M}{L} \left[\int_{L_m}^{L_n} P_n(x)dx - \frac{e_p}{e_n} \int_{L_m}^{L_n} P_p(x)dx \right]$$
$$\times \frac{e_n^2}{(e_n + e_p)^2} \left(1 - e^{-\frac{t}{\tau}} \right), \tag{9}$$

where M is the number of deep levels in the microplasma channel.

For purely electronic traps ($e_p = 0$), the linear term equals zero, and the distribution function for breakdown delay has the form

$$1 - P_M = \exp\left[A \left(1 - \exp\left(-\frac{t}{\tau} \right) \right) \right]. \tag{10}$$

In this case A is always negative, which corresponds to a decrease in the statistical breakdown delay. If, however, $e_p \neq 0$, then the linear term can be eliminated from consideration if we measure the distribution function without filling the deep levels. In this case for small overvoltages $L_m \cong L_n$
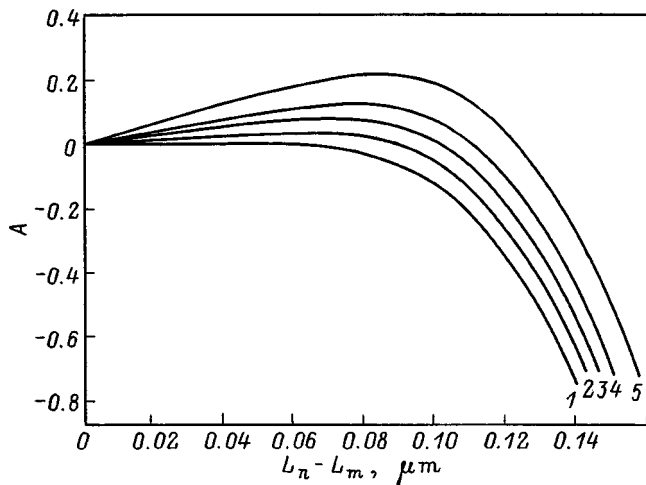
FIG. 2. Dependence of the parameter A on the width of the filled region. The concentration gradient was 4×10^{22} cm^{-4}; $T = 300$ K; $U_M = 17.80$ V; $U - U_M = 0.7$ V. e_p/e_n: *1* — $\leqslant 10^{-3}$, *2* — 10^{-2}, *3* — 2×10^{-2}, *4* — 3×10^{-2}, *5* — 5×10^{-2}.

and, according to Eq. (5), $f(t)$ is measured. Thus, the question can be reduced to analyzing the function $\varphi(t)$ which contains the basic information about the influence of deep levels on the breakdown delay, and which also has the form of Eq. (10). It follows from Eq. (9) that in this case A can have both negative and positive signs. The latter implies that the filling of deep levels by majority carriers increases the statistical delay of the microplasma.

Figure 2 shows the change in the parameter A with increasing width of the region of filling for a smooth gallium phosphide $p - n$ junction with $M = 100$. In these calculations we used ionization coefficients from Ref. 7. It is clear from the figure that for equal ionization coefficients of electrons and holes it is harder to see the increase in the static breakdown delay than it is to observe its decrease. As the deep levels fill near the edge of the space-charge region, $A > 0$, but in absolute value it is small. This hinders its separation from the overall distribution functions for breakdown delay. The situation is somewhat more favorable in abrupt asymmetric $p - n$ junctions. When other conditions are approximately the same, the values of A near maximum are an order of magnitude greater in these junctions.

It is even easier to observe the increase in the statistical breakdown delay when the collisional ionization coefficient for majority carriers is smaller than the coefficient for minority carriers (for example, in silicon $n^+ - p$ junctions). Here the occupation of deep levels by holes leads to a time-dependent decrease in electron emission, whose contribution to triggering avalanche is considerably higher.

We easily can obtain the distribution function for breakdown delay for the case where the voltage is switched on with a built-in delay. In other words, we increase the voltage from U_m to U_M, pause for a time t_d, and then increase the voltage to $U > U_M$. For rather small overvoltages $U - U_M$ this reduces to adding a factor $\exp(-t_d/\tau)$ to the expression for the nonlinear part in Eq. (9). The effect of such a delay t_d is equivalent to incomplete occupation of the deep levels in the region from L_m to L_n.

In real $p - n$ junctions, along with emission of carriers from the deep levels there are some other mechanisms which supply carriers for triggering an avalanche. Another term, usually a linear term,[1] in this case should be added to the exponent on the right side of expression (5). Its contribution can also be included when measuring the distribution function of the breakdown delay without filling of the deep levels (background triggering).

EXPERIMENTAL RESULTS

By studying the effect of deep levels on the breakdown delay of the microplasma we can determine the parameters of the deep levels located in the microplasma channels. This can be done either by measuring the distribution function of the breakdown delay, or by studying the effect of the delay t_d for a voltage U_M. We restrict the analysis to determining the parameters of the deep levels directly from the distribution function for breakdown delay.

Measurements were made on a series of gallium phosphide red-light emitting diodes AL102. The capacitance-voltage characteristics are shown for the example of a distribution of doping impurities that is linear in character within the space-charge region for a concentration gradient of about 4×10^{22} cm^{-4}. The steady-state breakdown voltage of the first microplasmas in various diodes varied in the range of 18 to 19 V. For these measurements we chose diodes in which the breakdown voltage for the second microplasma exceeded by more than 1 V the voltage for first breakdown.

Analysis of the LEDs under study showed that the appearance of a microplasma is always accompanied by the appearance of a glowing point that is yellow-orange in color. In all cases, these points are located outside the edge of the $p - n$ junction contour. This is probably explained by the fact that near the edges of the space-charge region the concentration of doping impurities is $\sim 6 \times 10^{17}$ cm^{-3}. Surface states at such high concentrations of impurities are unable to have any important effect on the field distribution, and the $p - n$ junction breakdown is bulk-like in character.

The temperature range for these investigations was 100 to 380 K. The samples were placed in a cryogenic thermostat that emitted no light, which accurately maintained a temperature of ~ 0.1 K. The temperature of the samples was controlled by a platinum resistance thermometer TSPM-5. The voltage across the $p - n$ junction was varied using a generator of step voltages with a leading edge whose width was about 10 μs. The breakdown delay time was measured by a CHZ-54 frequency meter.

When observed at constant voltage, the microplasma pulses had a well-defined ''packet'' character in the entire temperature range. This observation was evidence of the presence of deep levels in the microplasma channel. However, no relaxation of the barrier capacitance with time was observed. The temperature dependence of the capacitance had a smooth monotonic character. All of this indicates either a low concentration of deep levels in the diodes or their localization in the microplasma channels.

In order to eliminate the influence of previous breakdown cycles, in measuring the breakdown delay we allowed
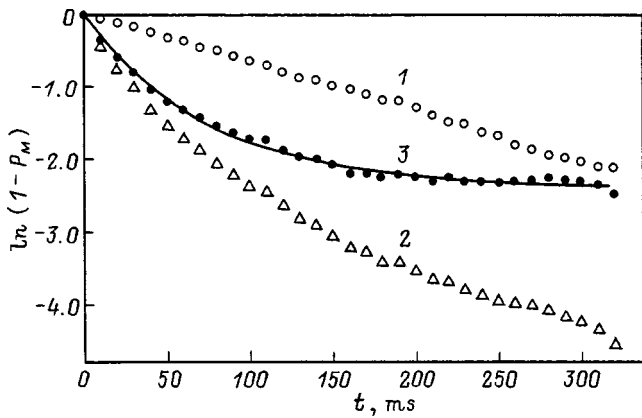
FIG. 3. Distribution function for the static breakdown delay with respect to time. *1*—Without filling of deep levels, *2*—with filling of deep levels, *3*—the difference curve corresponding to expression (10) for $A = 2.40$ and $\tau = 78.2$ ms. $T = 320.9$ K; $U_M = 18.45$ V; $U - U_M = 0.35$ V; $U_m = 13.0$ V.

FIG. 4. Arrhenius curves for the observed levels.

enough of a time lag for the diode to undergo a filling voltage U_m. Depending on temperature, this time was either fractions of a second at high temperatures or several seconds at low temperatures.

Without filling of the deep levels, the distribution function for breakdown delay is linear in semilogarithmic coordinates. If re-emission of trapped carriers from the deep levels is eliminated, then avalanches are triggered by electron-hole pairs that were generated (the entry of minority carriers into the microplasma channel from the base regions is equivalent to the generation of electron-hole pairs at the edge of the space-charge region). It is easy to show that the average duration of breakdown delay t_0 for equal collisional ionization coefficients of electrons and holes can in this case be written in the form

$$t_0 = (\nu P_{np})^{-1}, \tag{11}$$

where ν is the frequency of appearance of electron-hole pairs in the microplasma channel. Here P_{np} does not depend on the location where the pairs were generated and is given by expression (7). Using Eq. (11), we find that ν changes very slowly with temperature and depends strongly on the applied voltage. This indicates that in the temperature interval under study a large contribution to the supply of charge carriers for triggering an avalanche comes from a tunneling mechanism for generating electron-hole pairs.

In order to experimentally measure the distribution function for breakdown delay it is necessary to ensure the condition $t_0 > 2\tau$. This can be done by choosing the overvoltage $(U - U_M)$ at the diode or by varying the temperature.

Figure 3 shows the distribution function for breakdown delay $1 - P_M$ at $T = 320.9$ K. The function $1 - P_M$ is defined as the ratio of the number of step-voltage pulses for which breakdown delay exceeds a time t to the total number of applied pulses (1000). It is clear from the figure that all the curves correspond to relations (5) and (8)–(10). At certain temperatures the resulting curve *3* is described by the sum of two exponentials of the form (10) with time constants that differ by almost an order of magnitude. This allows us to separately determine τ in these cases.
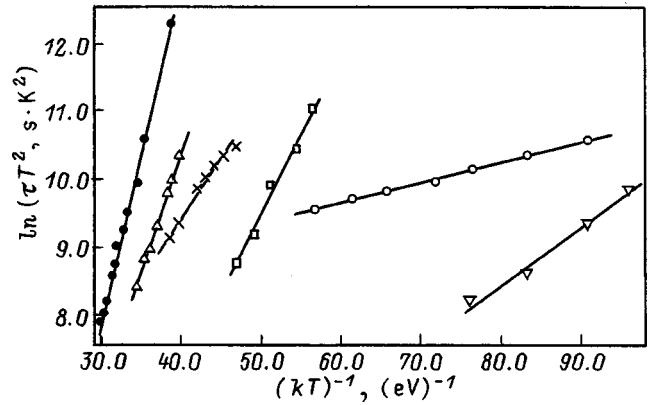
Figure 4 shows dependences of τ on T in the form of Arrhenius curves. Six values of activation energy were found (in eV): 0.49 ± 0.01, 0.35 ± 0.01, 0.23 ± 0.01, 0.16 ± 0.01, 0.084 ± 0.005, and $0.030 \pm .001$. The first five values of activation energy can be assigned to individual energy levels. However, it is impossible to determine from which band we should measure these energy values, because the diodes under study have almost symmetrical structure. The lost activation energy appears at low temperatures over a rather wide range. Possibly it is connected with fluctuations in the band potential from the space-charge region of the $p - n$ junction.[8] Near the boundaries of the space-charge region they can lead to the appearance of local regions that capture majority carriers and hold them for a long time.

It should be noted that within the entire temperature range the occupation of deep levels by decreasing the voltage led to a decrease in the statistical breakdown delay. In this case an anomalously high sensitivity was observed to the filling of deep levels, especially at low temperatures. Even for a rather small change in the voltage across the $p - n$ junction ($U_M - U_m \cong 0.5 - 4$ V) a decrease in the average delay to breakdown was observed and the value of the parameter A reached $1 - 2$ in absolute value. Meanwhile, calculations using the ionization coefficients of Ref. 7 for reasonable assumptions about the geometric dimensions of the microplasma and deep level concentrations give values for A that are smaller by ten orders of magnitude. As follows from Fig. 2, for the diodes under study the considerable increase in A with increasing range of occupation should be observed for $L_n - L_m \geq 0.3 L_B$, where L_B is the width of the space-charge region at the microplasma breakdown voltage.

In order to explain the anomalously high sensitivity of breakdown delay to deep level filling we offer the following assumptions.

1. The electric field distribution in the microplasma channel differs considerably from the distribution of field in the $p - n$ junctions under study and is more similar to the field distribution in a $p^+ - n - n^+$ structure. In this case, even when the deep levels near the edges of the space-charge region are filled, they turn out to be in regions of relatively high field. The increase in sensitivity to filling of deep levels with decreasing temperature is connected with the increase in

the width of edge layer of the space-charge region, in which the deep levels are always completely filled.

2. The collisional ionization coefficients in GaP and their temperature dependences in weak fields are considerably larger than the values obtained by extrapolating the data of Ref. 7 would suggest. In this paper the ionization coefficients were measured in the range of fields $(5-13) \times 10^5$ V/cm, whereas the maximum value of the field in the region where the deep levels are filled for $U_M - U_m \cong 4$ V is on the order of 10^5 V/cm.

3. Although the distribution function for carriers in GaP in strong fields is assumed to be spherically symmetric, there are a small number of carriers that are able to avoid collisions with phonons (Shockley electrons). These carriers play the primary role in triggering an avalanche as carriers are emitted from the deep levels. In this case, in calculating the probability for triggering an avalanche the use of average values of the collisional ionization is inadequate, and the theory of avalanche triggering should be reconsidered.

At this time, there is no basis for preferring one of these assumptions over the others.

[1] I. V. Grekhov and Yu. N. Serezhnin, *Avalanche Breakdown in Semiconductor p−n Junctions* (Energiya, Leningrad, 1980).

[2] C. Kimura and J. Nishizawa, Jpn. J. Appl. Phys. **7**, 1453 (1968).

[3] M. W. Nield and J. H. Leck, Br. J. Appl. Phys. **18**, 185 (1967).

[4] P. V. Akimov, I. V. Grekhov, and Yu. N. Serezhnin, Fiz. Tekh. Poluprovodn. **4**, 2099 (1970) [Sov. Phys. Semicond. **4**, 1802 (1970)].

[5] K. I. Nuttal and M. W. Nield, Solid-State Electron. **18**, 13 (1975).

[6] G. Ferenczi, Solid-State Electron. **17**, 903 (1974).

[7] R. A. Logan and H. G. White, J. Appl. Phys. **36**, 3945 (1965).

[8] S. V. Bulyarskiĭ and N. S. Grushko, *Generation-Recombination Processes in Active Elements* (Moscow State Univ. Publ., Moscow, 1995).

Translated by Frank J. Crowne

On the transformation of the potential barrier at a GaAs/Au interface during heat treatment

B. I. Bednyĭ*[)]

N. I. Lobachevskiĭ Nizhegorod State University, 603600 Nizhniĭ Novgorod, Russia
(Submitted April 20, 1999; accepted for publication May 19, 1999)
Fiz. Tekh. Poluprovodn. **33**, 1350–1354 (November 1999)

The effect of vacuum heat treatment on the electronic state of a GaAs(100) surface coated with island layer of gold is investigated. It is found that the effective band bending in the depletion layer decreases monotonically with increasing anneal temperature in the range 100–500 °C. The Fermi level at the surface remains approximately 0.8 eV below the conduction-band bottom. The transformation of the potential barrier is due to the formation of a strongly doped region near the surface with high tunneling transmittance. It is shown that the photoelectric properties of thin GaAs films can be controlled by adsorption of gold and heat treatment. © *1999 American Institute of Physics.* [S1063-7826(99)01511-2]

1. INTRODUCTION

The high density of electron states localized on a free GaAs surface and at interfaces between GaAs and metals or insulators is one of the most important physicotechnical problems impeding the full realization of the well-known advantages of gallium arsenide over silicon in practical applications. In Schottky diodes, surface states cause the Fermi level to be pinned near the center of the band gap in GaAs, thereby sharply decreasing the ''sensitivity'' of the potential barrier to the work function of the metal.[1] Pinning makes the technology for fabricating diodes with a low barrier height,[2–4] which are necessary for a number of technical applications (for example, the production of millimeter-range detectors and mixers[4]), much more complicated. Definite difficulties also arise in the development of GaAs-based thin-film photosensitive components.[5]

The possibility of controlling the electric characteristics of a number of III–V–metal contact systems by heat treatment (right up to a transition of contacts from rectifying into ohmic) has been reported elsewhere.[6–8] The changes occurring in the electric properties of Schottky diodes are explained by the ''repinning'' of the Fermi level near the conduction-band bottom as a result of the rearrangement of the energy spectrum of surface states.[8] In the present paper we report the first results of an experimental investigation of the effect of heat treatment on the electrical and photoelectric properties of a GaAs surface coated with an island layer of gold. They attest to a change in the shape and effective height of a barrier near the surface while the Fermi level remains pinned near the center of the band gap.

2. EXPERIMENTAL METHODS

A GaAs surface coated with an island layer of gold is a methodologically convenient model system whose electronic properties are similar to those of a completely metallized GaAs surface.[9] The methodological advantages are due to the absence of a surface conducting phase with relatively small fillings of the surface with the adsorbate. This makes it

possible to use for diagnostics of metal–semiconductor interfaces photosensitive methods based on the study of longitudinal carrier transport near the semiconductor surface (planar conduction, photoconduction, field effect, and others). Of great interest is the possibility of controlling the potential barrier near the surface in GaAs by photoelectric methods, since photoelectronic processes in this material are especially sensitive to the state of the surface because the photocarriers are located primarily within the depletion layer near the surface.[10]

We have investigated the submicron n-GaAs films (about 0.5 μm thick) doped (Ge) to $\sim 10^{17}$ cm^{-3} and grown by vapor-phase epitaxy (MOCVD) on the (100) surface of semi-insulating GaAs. An island surface structure was obtained by adsorption of gold from a water solution of $HAuCl_4$, using the method described in Ref. 9. The Au concentration in the solution was $\sim 1.6 \times 10^{-4}$ g-ions/liter, and the adsorption time was ~ 2 min. Electron-microscopic analysis confirmed the island character, established in Ref. 9, of the adsorbed gold layer. Typical values of the island density were $\sim 10^{11}$ cm^{-2}, the characteristic size of the islands was ~ 10 nm, and the degree of filling of the surface with metal was $\sim 0.4 - 0.5$.

Heat treatment was conducted in a $\sim 10^{-4}$ Pa vacuum for 1 h. The anneal temperature T_{ann} was varied in the range 100–500 °C. Control specimens, which were subjected to all stages of preliminary treatment except treatment in the $HAuCl_4$ solution, were prepared for identifying the effects due to the presence of gold atoms on the semiconductor surface.

The surface band bending U_S, the position U_{FS} of the Fermi level relative to the conduction-band bottom at the surface, and the density g_{SS} of surface states near the Fermi level were determined from combined measurements of the planar (surface-barrier) photoconductivity, surface photovoltage, and differential field effect. The algorithm used to analyze the results of the photoelectric measurements has been described previously.[10–12] The electrostatic potential of
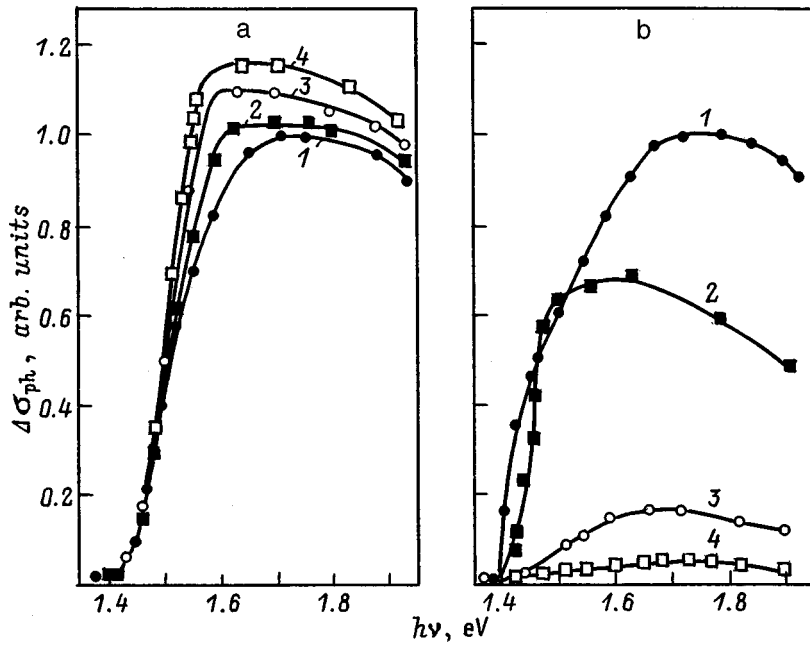
FIG. 1. Photoconductivity spectra for samples with a free surface (a) and a surface coated with a gold layer (b) with annealing temperature T_{ann}, °C: *1*—100, *2*—200, *3*—400, *4*—480.

the surface (the work function χ) and the photovoltage V_{ph} on the surface barrier were measured by the dynamic capacitor method (Kelvin probe).

3. RESULTS AND DISCUSSION

Comparing the properties of a surface coated with an island layer of gold and the properties of the initial surface showed that band bending in the first case ($\sim 0.75-0.8$ eV) is much greater than in the second case ($\sim 0.55-0.6$ eV). According to the field-effect data, the increase in band bending and the corresponding shift of the Fermi level to the valence band ($\Delta U_{FS} \simeq 0.2$ eV) are due to an increase in the density of surface states. As a result of the adsorption of Au, the value of g_{SS} increased from $(1-2) \times 10^{12}$ to $(4-5) \times 10^{12}$ cm$^{-2} \cdot$ eV^{-1}. Therefore the position of the Fermi level on a GaAs surface coated with islands of gold $U_{FS} \simeq 0.8$ eV is close to the usual barrier height in Au–GaAs Schottky diodes (~ 0.9 eV; Refs. 13–15).

Figure 1 shows the typical photoconductivity (PC) spectra obtained at various heating temperatures on the control and gold-coated samples. The photoconductivity was measured with modulated illumination in a weak-signal (linear in the illumination intensity) regime and resulted in the same number of photons incident on the sample. It is evident that the adsorption of Au changes the character of the effect of heat treatment on the magnitude of the PC signal ($\Delta\sigma_{ph}$). An increase $\Delta\sigma_{ph}$, reaching $\approx 20\%$ for $T_{ann} \gtrsim 400$ °C (Fig. 1a), is observed with increasing T_{ann} for samples with a free surface. When an island gold structure is present, the photoconductivity decreases in the entire spectral range. Starting at $T_{ann} \approx 400$ °C, $\Delta\sigma_{ph}$ decreases by more than an order of magnitude (Fig. 1b).

Figure 2 shows the surface photovoltage V_{ph} versus the anneal temperature and the corresponding changes in the work function χ. When the control samples were annealed, V_{ph} and χ iuncreased. Taking into account the previous

results,[16,17] it can be concluded that the effect of vacuum heat treatment on the electronic state of a GaAs surface is due to reconstruction of the skin layer as a result of the desorption of arsenic and the formation of a polycrystalline phase of Ga_2O_2. The additional structural surface disordering arising in the process results in a higher density of surface states and surface band bending (according to our data, at $T_{ann} \approx 450 -500$ °C the band bending increases by an amount of the order of 0.2 eV). A consequence of these processes is the experimentally observed increase in the work function and surface photovoltage.

For samples with a gold layer the effect of heat treatment on the photovoltage had the opposite sign and was more
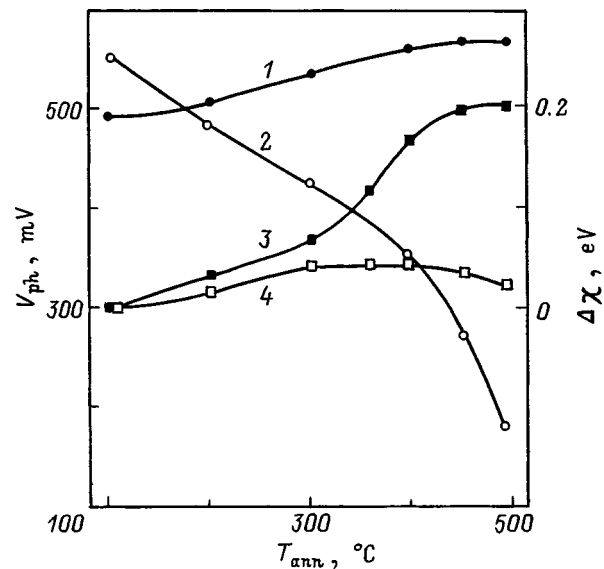

FIG. 2. Surface photovoltage V_{ph} (left-hand scale, curves *1* and *2*) and change $\Delta\chi$ of the work function (right-hand scale, curves *3* and *4*) versus the annealing temperature for the control sample (*1*, *3*) and a sample with a gold layer on the surface (*2*, *4*).
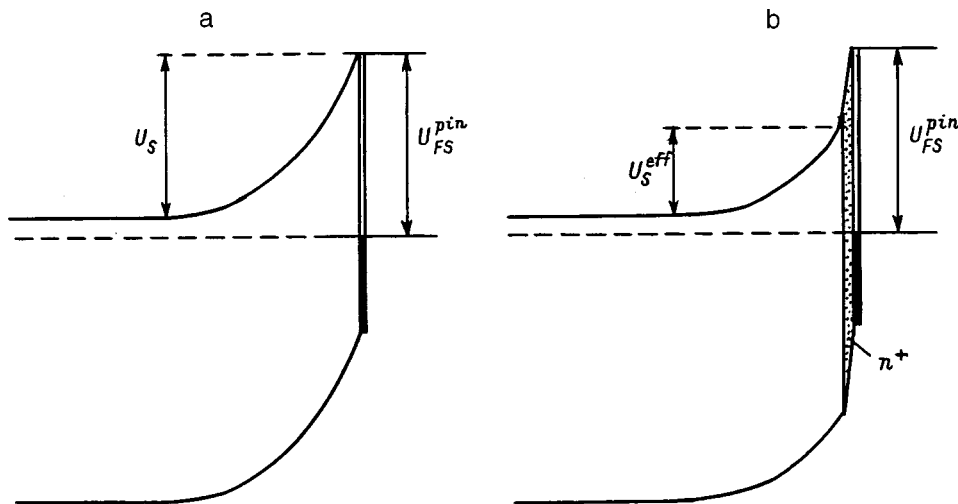
FIG. 3. Model of the energy band diagram of a GaAs/Au interface before (a) and after (b) heat treatment.

pronounced. At $T_{ann} \approx 500\,°C$, for example, the photovoltage decreased in magnitude by more than 0.4 eV. Interestingly, no substantial changes of the work function could be discerned in the process. As one can see from Fig. 2, $\Delta\chi \leqslant 0.05$ eV, irrespective of the annealing temperature. This shows that the heat-treatment-induced change in the position of the Fermi leve at a surface modified with Au atoms is negligible. Estimates show that after annealing at temperatures $T_{ann} > 350\,°C$ the density of states of such a surface exceeds 10^{13} cm$^{-2} \cdot$eV^{-1} (the value of g_{SS} could not be determined more accurately because of the extremely low values of the mobility in the presence of the field effect).

Therefore, to interpret the experimental data it is necessary to take into consideration the fact that during vacuum heat treatment the position of the pinned Fermi level $U_{FS} \approx 0.8$ eV remains essentially the same at a GaAs surface coated with an island layer of gold. This result agrees with the data obtained in a study of the internal photoemission of Au–GaAs Schottky diodes,[18] and it can be easily interpreted from the standpoint of the theory of disorder-induced surface states (DIGS model[19]). Indeed, thermal activation of interphase interactions and reactions at a metal–semiconductor interface is accompanied by an increase in the structural–chemical disordering of the boundary layer.[14,15] According to theory,[19] disordering of this kind should result in higher values of g_{SS} and in pinning of the Fermi level near the electric-neutrality level of the system of surface states. Calculations based on the DIGS model (see, for example, Ref. 14) show that in GaAs the electric-neutrality level lies approximately 0.9 eV below the conduction-band bottom; this is close to the experimental value of U_{FS}.

A phenomenological analysis of the data on the effect of heat treatment on the photoelectric properties of a gold-modified GaAs surface, just as analysis of the current–voltage and capacitance–voltage characteristics of Schottky diodes,[6–8] leads to the conclusion that the surface band bending decreases with increasing T_{ann}. A calculation of U_S from the dependence of the stationary photoconductivity on the photovoltage on a surface barrier shows that for $T_{ann} \approx 450$–$500\,°C$ the band bending does not exceed 0.3 eV. The conclusion that the band bending decreases is formally

at variance with the data on the pinning of the Fermi level at the surface. However, this discrepancy can be easily removed by assuming that heat treatment gives rise to a thin, heavily doped, n^+ region with a high transmittance for electron tunneling near the boundary with a metal. The part of the contact potential that falls across the n^+ region, because of the tunneling transmission of carriers through the top of the barrier, will then virtually have no part in barrier photoeffects. For this reason, the photoconductivity and photovoltage under these conditions should be determined not by the true height but rather by the effective height of the surface barrier U_S^{eff}, equal to the band bending in the depletion layer outside the n^+ region (Fig. 3).

The transformation of the barrier increases with T_{ann}: The voltage drop in the n^+ region increases and U_S^{eff} decreases. The effective barrier height can therefore be controlled by varying the annealing temperature, similarly to the way this is done in Schottky diodes by special subsurface δ doping of a semiconductor before metallization.[20]

The hypothesis that a heavily doped layer appears near the surface agrees with the existing theory of interphase interactions in the system Au–GaAs.[6,14,15] According to these ideas, the restructuring of the GaAs/Au interface as a result of heat treatment is accompanied by a breakdown of stoichiometry in the skin layer as a result of gallium atoms escaping from the semiconductor into the metal (autdiffusion) and the formation of an Au–Ga solid solution and an intermetallic phase Au$_3$Ga (at $T_{ann} > 350\,°C$). It is natural to infer that favorable conditions for the localization of germanium (dopant) in the Ga sublattice and manifestation of its donor properties arise as a result of gallium autdiffusion and the generation of point defects of the type V_{Ga}. Thus, as a result of the accumulation of germanium near the surface, partial compensation of the initial negative charge of the surface by the positive charge of donor centers of the type Ge$_{Ga}$ and, as a result, a decrease of the effective height of the barrier near the surface occur.

The above-examined mechanism of transformation of a barrier at a GaAs surface coated with an island layer of gold also agrees with the results of an experimental investigation of the morphology and chemical composition of the interface

in a GaAs–Au system with a solid metal film.[7] Secondary ion mass spectrometry has revealed[7] surface segregation of the volume dopant at $T_{ann} \geqslant 400\,°C$. The thickness of the destroyed region near the surface with high dopant density ($>10^{18}$ cm^{-3}) reached hundreds of angstroms. Under these conditions the potential barrier should be completely contained within the n^+ region and should enable carrier tunneling through the interface. This seems to be the main reason for the transformation, which was observed in Refs. 6 and 8 of the contacts from rectifying type into ohmic type as a result of heat treatment.

4. CONCLUSIONS

Thermal activation of the interphase interaction at a GaAs/Au interface results in the transformation of the surface potential barrier — decrease of the effective band bending accompanying rigid pinning of the Fermi level on the surface approximately 0.8 eV below the conduction-band bottom. The effect is due to the formation of a strongly doped n^+ region with high transmittance for tunneling electrons near the semiconductor surface. The results of this work show that the effective barrier height and the characteristics of surface photoeffects in GaAs can be controlled by adsorption of gold and by choosing an appropriate heat-treatment regime.

We wish to thank R. V. Kudryavtseva and A. B. Ozerov for assisting in the experiment.

*)E-mail: Bednyi@sandy.ru; Fax: (8312)657523

[1] J. M. Woodall, P. D. Kirchner, J. L. Freeouf, D. T. McInturff, M. R. Melloch, and F. H. Pollak, Philos. Trans. R. Soc. London, Ser. A **344**, 521 (1993).

[2] M. P. Patkar, T. P. Chin, J. M. Woodall, M. S. Lundstrom, and M. R. Melloch, Appl. Phys. Lett. **66**, 1412 (1995).

[3] T. A. Bryantseva, V. E. Lyubchenko, and E. O. Yunevich, Radiotekh. Élektron., No. 8, 1306 (1995).

[4] N. A. Maleev, V. V. Volkov, A. Yu. Egorov, A. E. Zhukov, A. R. Kovsh, M. F. Kokorev, and V. M. Ustinov, Fiz. Tekh. Poluprovodn. **33**, 346 (1999) [Semiconductors **33**, 345 (1999)].

[5] S. A. Kostylev, E. F. Prokhorov, and A. T. Ukolov, *Transport Phenomena in Thin-Film Gallium-Arsenide Structures* (Naukova dumka, Kiev, 1990), Chap. 2, p. 34.

[6] Z. Liliental-Weber, R. Gronsky, J. Washburn, N. Newman, W. E. Spicer, and E. R. Weber, J. Vac. Sci. Technol. B **4**, 966 (1986).

[7] P. H. Holloway and C. H. Mueller, Thin Solid Films **221**, 254 (1992).

[8] Yu. A. Gol'dberg and E. A. Posse, Fiz. Tekh. Poluprovodn. **32**, 200 (1998) [Semiconductors **38**, 181 (1998)].

[9] N. L. Dmitruk, G. Y. Kolbasov, O. I. Maeva, and V. I. Poludin, Thin Solid Films **65**, 341 (1981).

[10] I. A. Karpovich, B. I. Bednyĭ, N. V. Baĭdus', S. M. Plankina, M. V. Stepikhova, and M. V. Shilova, Fiz. Tekh. Poluprovodn. **23**, 2164 (1989) [Sov. Phys. Semicond. **23**, 1340 (1989)].

[11] B. I. Bednyĭ, N. V. Baĭdus', and Yu. A. Danilov, in *Vestnik Nizhegorodskogo universiteta im. N. I. Lobachevskogo,* Ser. *Fizika tverdogo tela* (Nizhniĭ Novogorod State University Press, Nizhniĭ Novgorod, 1998), No. 2, p. 40.

[12] B. I. Bednyĭ, I. A. Karpovich, and N. V. Baĭdus', Fiz.-Khim. Mekh. No. 1, 94 (1991).

[13] D. P. Wang and T. L. Shen, Jpn. J. Appl. Phys. **33**, Pt. 1, 1253 (1994).

[14] F. Bechstedt and R. Enderlein, *Semiconductor Surfaces and Interfaces* [Berlin, Akademie-Verlag, 1988; Mir, Moscow, 1990].

[15] V. I. Belyĭ and V. R. Belosludov, in *Current Problems of the Physical Chemistry of Semiconductor Surfaces* (Nauka, Novosibirsk, 1988), p. 43.

[16] B. I. Bednyĭ, Yu. A. Benediktov, A. N. Kalinin, and I. A. Karpovich, Izv. Vyssh. Uchebn. Zaved. Fiz., No. 3, 30 (1980).

[17] T. A. Bryantseva, G. G. Dvoryankina, Z. M. Lebedeva, A. B. Ormont, A. G. Petrov, and E. O. Yunevich, Neorg. Mater. **22**, 889 (1986).

[18] T. P. Chen, Y. C. Liu, S. Fung, and C. D. Beling, J. Appl. Phys. **77**, 6724 (1995).

[19] H. Hasegawa and H. Ohno, J. Vac. Sci. Technol. B **4**, 1130 (1986).

[20] V. I. Shashkin, A. V. Murel', Yu. N. Drozdov, V. M. Danil'tsev, and O. I. Khrykin, Mikroelektronika **26**, 57 (1997).

Translated by M. E. Alferieff

LOW-DIMENSIONAL SYSTEMS

Absorption of a strong electromagnetic wave by electrons in a superlattice in a quantizing electric field

D. V. Zav'yalov and S. V. Kryuchkov

Volgograd State Pedagogical University, 400013 Volgograd, Russia
(Submitted July 21, 1998; accepted for publication March 10, 1999)
Fiz. Tekh. Poluprovodn. **33**, 1355–1358 (November 1999)

Intraminiband absorption of light by electrons in a quantum superlattice in a quantizing electric field is investigated theoretically taking into account the electron–phonon interaction. It is assumed that the interaction with optical dispersion-free phonons makes the main contribution to electron scattering. It is shown that the point $\omega = \omega_0$ (ω is the light frequency, and ω_0 is the optical phonon frequency) conditionally divides the ω dependence of the absorption into two parts: $\omega < \omega_0$, the region of exponentially weak absorption and $\omega > \omega_0$, the region of ''strong'' absorption. An electric field shifts the region of strong absorption in the red direction of the spectrum. © *1999 American Institute of Physics.* [S1063-7826(99)01611-7]

Electroabsorption of light in semiconductor structures could become a basis for the development of a variety of optoelectronic devices[1] (optical modulators,[2] optical logic gates,[3] laser diodes with mode locking,[4] and others). In addition, experiments on interband electroabsorption[5] have reliably confirmed the Stark quantization of the energy spectrum of charge carriers in superlattices (SLs).

The theory of interband absorption of light in a SL in a quantizing electric field has been developed by Zhilich.[6] Intraband absorption of light in a classically strong electric field has been investigated theoretically by Malevich,[7] who took into account the dynamic effect (not associated with carrier heating) of a constant electric field on the electron scattering by phonons.

In the present paper we report the results of an experimental study of the multiphoton intraband absorption of light by a semiconductor SL in a quantizing electric field. We point out several specific features of this effect which are promising in terms of their use for practical applications.

We assume that the electronic energy spectrum in the absence of an external perturbation can be approximated by the relation

$$\epsilon(\mathbf{p}) = \frac{p_y^2 + p_z^2}{2m} + \Delta\left[1 - \cos\left(\frac{p_x d}{\hbar}\right)\right], \qquad (1)$$

where Δ is the half-width of a conduction miniband, p_x, p_y, and p_z are the projections of the quasimomentum onto the coordinate axes, m is the effective mass of current carriers in a plane perpendicular to the SL axis (the x axis), and d is the period of the SL.

When a strong electric field oriented along the axis of the superstructure is applied, the energy spectrum of the electrons becomes quasidiscrete:[8,9]

$$\epsilon(p_z, p_y, \nu) = \frac{p_y^2 + p_z^2}{2m} + \nu\hbar\Omega. \qquad (2)$$

Here Ω is the Stark frequency, $\Omega = eE_x d/\hbar$ is the Stark frequency, E_x is the strength of the electric field, and ν is an integer.

Stark quantization appears when the following conditions are satisfied:

$$\Omega\tau \gg 1, \qquad (3)$$

$$\hbar\Omega \ll E_g. \qquad (4)$$

Here τ is the relaxation time, and E_g is the miniband gap. The condition (4) means that we restrict the analysis to the single-miniband approximation. The inequality (3) corresponds to discrete levels which are not broadened by electron collisions with lattice irregularities.

Let us assume that a strong, linearly polarized electromagnetic wave, whose electric field vector lies in the zy plane, is incident on the SL. Under these conditions the electron wave function (disregarding the photon momentum) has the form

$$\Psi(p_z, p_y, \nu) = \sqrt{\frac{L_x}{dV}} J_{\nu - x/d}\left(\frac{\Delta}{\hbar\Omega}\right)$$

$$\times \exp\left\{\frac{i}{\hbar}[p_y y + p_z z + f(\mathbf{p}_\perp) - \epsilon(\mathbf{p})t]\right\}, \qquad (5)$$

$$f(\mathbf{p}_\perp) = \frac{e\mathbf{E}\mathbf{p}_\perp}{m\omega^2}\sin(\omega t) - \frac{e^2 E^2}{8m\omega^3}\sin(2\omega t),$$

where L_x is the size of the normalization volume V along the x axis, $J_\nu(x)$ is a first-order Bessel function, $\mathbf{E}$ is the electric field vector of the electromagnetic wave, $\mathbf{p}_\perp$ is the component of the electron quasimomentum in the $z0y$ plane, and ω is the angular frequency of the incident wave.

The wave function (5) is a product of two functions corresponding to a constant Stark ladder[8,9] and a state that takes into account exactly the influence of a strong electromagnetic wave.[10]

Treating the interaction between electrons and optical phonons as a perturbation, we find the absorption, which we determine in the standard manner (as the ratio of the energy absorbed per unit volume of the matter per unit time to the flux density of the incident light). We assume the phonons to be dispersion-free and the phonon frequency $\omega_0 =$ const.

Thus, we write the light absorption as

$$\alpha(\omega) = \frac{2\pi\omega n_0}{cuV} \sum_{\nu,\nu'} \sum_{\mathbf{p}_\perp,\mathbf{p}'_\perp} \sum_{\mathbf{q}} n(\mathbf{p}_\perp) H^2 |M_{\nu,\nu'}(q_x)|^2$$

$$\times \sum_{s=-\infty}^{\infty} s|G_s(\mathbf{q}_\perp)|^2 \delta[\epsilon(\mathbf{p}'_\perp) - \epsilon(\mathbf{p}_\perp) + \hbar\omega_0$$

$$- \hbar\Omega(\nu - \nu') - s\hbar\omega]\delta_{\mathbf{p}'_\perp,\mathbf{p}_\perp - \hbar\mathbf{q}_\perp}. \tag{6}$$

Here u is the radiation energy density, c is the velocity of light in vacuum, n_0 is the refractive index of the medium, $n(\mathbf{p}_\perp)$ is the function for electron distribution over perpendicular values of the quasimomentum $\mathbf{p}_\perp$, $H = \sqrt{\hbar/(2\omega_0\rho V}C_{\mathbf{q}}$, $C_{\mathbf{q}}$ is a coupling constant, ρ is the density of the crystal, $M_{\nu\nu'}(q_x)$ $[G_s(\mathbf{q}_\perp)]$ is the matrix element of the operator $\exp(iq_x x)$ $[\exp(i\mathbf{q}_\perp \cdot \mathbf{r}_\perp)]$ which takes into account the effect of a static field (light) on the absorption; specifically, for the energy spectrum (2) we have

$$|M_{\nu\nu'}(q_x)|^2 = J_{\nu-\nu'}^2\left[\frac{\Delta}{\hbar\Omega}\sin\left(\frac{dq_x}{2}\right)\right], \tag{7}$$

$$|G_s(\mathbf{q}_\perp)|^2 = J_s^2(\mathbf{a}_0\mathbf{q}_\perp), \tag{8}$$

where $\mathbf{a}_0 = e\mathbf{E}/m\omega^2$ is the amplitude of electron oscillations in the field of the wave. The expression (7) is presented, for example, in Refs. 8 and 9, and the expression (8) can be obtained using the standard relation[11] (see also Ref. 10),

$$e^{-iz\sin(\alpha)} = \sum_{s=-\infty}^{+\infty} J_s(z)e^{-is\alpha}.$$

In the expression (6), processes with absorption of a phonon are ignored (this is possible when $\hbar\omega_0 \gg kT$).

In general, substantial difficulties arise in the calculation of $n(\mathbf{p}_\perp)$. We shall therefore restrict the discussion to the case

$$\hbar\Omega \gg \frac{\Delta^2}{2\hbar\omega_0}\coth\left(\frac{\hbar\omega_0}{2kT}\right), \tag{9}$$

$$\frac{e^2E^2}{\hbar m\omega^3} \ll \frac{kT}{\hbar\omega} \ll 1. \tag{10}$$

The inequality (9) signifies that there are virtually no transitions between Stark sublevels, and that equilibrium is established within each Stark subband.[12] We note that numerical values of ω on the order of Ω are important in the problem, so that on the basis of Eq. (3) we assume $\omega\tau \gg 1$. The condition (10) then makes it possible to ignore the heating of current carriers by the field of the electromagnetic wave.[13,14]

The function $n(\mathbf{p}_\perp)$ can therefore be written in the form[12]

$$n(\mathbf{p}_\perp) = \frac{2\pi dn\hbar^2}{mkT}\exp\left(-\frac{\mathbf{p}_\perp^2}{2mkT}\right), \tag{11}$$

where n is the electron density in the conduction miniband.

Investigating the case of ultraquantum fields ($\Delta/\hbar\Omega \ll 1$), we can expand expression (7) in a series and retain the terms of order $(\Delta/\hbar\Omega)^2$. Only the terms with $\nu - \nu' = 0, \pm 1$ will then remain in the sum over ν and ν'.

If the intensity of the incident light is moderately high, so that $a_0 \ll a$ (a is the period of the crystal lattice along the $0y$ and $0z$ axes), then the expression (8) can also be expanded in a series, retaining the first nonvanishing terms.

Retaining in the sum over s only terms of order $(\mathbf{a}_0 \cdot \mathbf{q}_\perp)^2$, we shall examine the single-photon absorption ($s = \pm 1$).

For a nonpolar crystal we have $C_{\mathbf{q}} = C_0 =$ const. In this case we obtain an expression for $\alpha(\omega)$ in the zeroth-order approximation in $(\Delta/\hbar\Omega)^2$

$$\alpha(\omega) = \frac{A}{\omega^3}\sum_{s=-1}^{1}\exp\left[\frac{\hbar}{2kT}(\kappa - |\kappa|)\right]\left(1 + \frac{\hbar|\kappa|}{2kT}\right), \tag{12}$$

$$A = \frac{C_0^2 ne^2kT\pi}{dn_0\hbar^3c\rho\omega_0},$$

where $\kappa = s\omega - \omega_0$.

For a polar crystal $C_{\mathbf{q}} = C/q$. In this case the absorption coefficient has the form

$$\alpha(\omega) = \frac{B}{\omega^3}\sum_{s=-1}^{1} s\exp\left(\frac{\hbar\kappa}{2kT}\right)|\kappa|K_1\left(\frac{\hbar|\kappa|}{2kT}\right), \tag{13}$$

$$B = \frac{\sqrt{2\pi}C^2 ne^2}{2cn_0\rho\omega_0\hbar\sqrt{mkT}},$$

where Q_1 is a modified Bessel function of the first kind.

From the expressions (12) and (13) and Fig. 1 (curve *1*) and Fig. 2 (curve *1*) it is evident that the point $\omega = \omega_0$ conditionally divides the single-photon absorption as a function of ω into two parts: $\omega < \omega_0$, the region of exponentially weak absorption and $\omega > \omega_0$, the region of strong absorption. The width of the region of exponentially weak absorption is $\Delta\omega \sim kT/\hbar$. We note that the point $\omega = \omega_0$ corresponds to the threshold for the creation of an optical phonon.

A similar situation is also observed in the absence of a quantizing field.

In the next approximation in $(\Delta/\hbar\Omega)^2$ the absorption has the following form for a nonpolar crystal:

$$\alpha(\omega) = \frac{A}{\omega^3}\sum_{s=-1}^{1}\sum_{l=-1}^{1} sM_l\exp\left[\frac{\hbar}{2kT}(\kappa - |\kappa|)\right]\left(1 + \frac{\hbar|\kappa|}{2kT}\right) \tag{14}$$

and for a polar crystal it is

$$\alpha(\omega) = \frac{B}{\omega^3}\sum_{s=-1}^{1}\sum_{l=-1}^{1} s\exp\left(\frac{\hbar\kappa}{2kT}\right)f_l(\kappa) \tag{15}$$
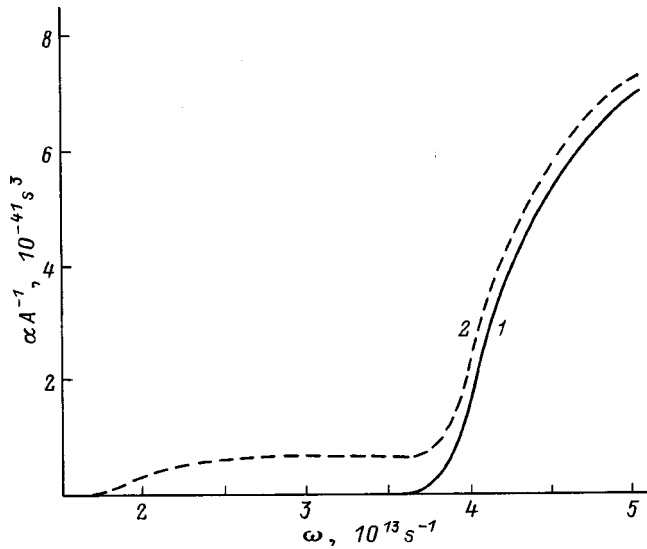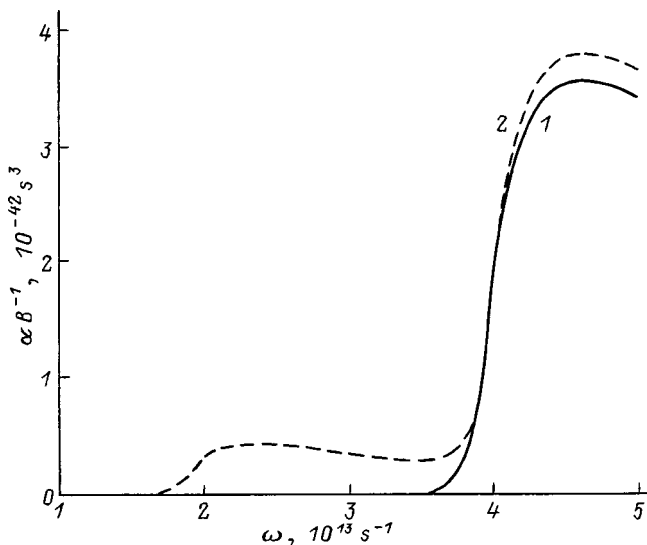
FIG. 1. Absorption coefficient for a nonpolar crystal in the zeroth approximation (*1*) and in the first approximation (*2*) with respect to $(\Delta/\hbar\Omega)^2$. $\omega_0 = 4 \times 10^{13}\,\text{s}^{-1}$, $\Omega = 2 \times 10^{13}\,\text{s}^{-1}$, and $T = 5$ K.

Here

$$M_0 = 1 - \frac{1}{4}\left(\frac{\Delta}{\hbar\Omega}\right)^2,$$

$$M_1 = M_{-1} = \frac{1}{8}\left(\frac{\Delta}{\hbar\Omega}\right)^2,$$

$$f_0(\kappa) = \left[1 - \frac{1}{4}\left(\frac{\Delta}{\hbar\Omega}\right)^2\right]F(\kappa) + \frac{1}{4}\left(\frac{\Delta}{\hbar\Omega}\right)^2 I(\kappa),$$

$$f_{-1}(\kappa) = f_1(\kappa) = \frac{1}{8}\left(\frac{\Delta}{\hbar\Omega}\right)^2 [F(\kappa) - I(\kappa)],$$

FIG. 2. Absorption coefficient for a polar crystal in the zeroth approximation (*1*) and in the first approximation (*2*) with respect to $(\Delta/\hbar\Omega)^2$. $\omega_0 = 4 \times 10^{13}\,\text{s}^{-1}$, $\Omega = 2 \times 10^{13}\,\text{s}^{-1}$, and $T = 5$ K, $m = 10^{-27}$ g.

$$F(\kappa) = |\kappa| K_1\left(\frac{\hbar|\kappa|}{2kT}\right),$$

$$I(\kappa) = \frac{\hbar}{4m}\int_0^\infty \exp\left(-\frac{\hbar^2}{8mkT}\xi^2 - \frac{\kappa^2 m}{2kT}\frac{1}{\xi^2} - \xi d\right)\xi\,d\xi,$$

$$\kappa = s\omega - \omega_0 - l\Omega.$$

It is evident from the expressions (14) and (15) and Fig. 1 (curve *2*) and Fig. 2 (curve *2*) that the region of strong single-photon absorption in the first-order approximation in $(\Delta/\hbar\Omega)^2$ shifts in the direction of lower frequencies by the amount Ω. An appreciable absorption of light with frequency less than the frequency of an optical phonon is therefore possible. Specifically, the inequality $\omega > \omega_0 - \Omega$ should be satisfied. However, the absorption of light at frequency $\omega \sim \omega_0 - \Omega$ is suppressed by the factor $(\hbar\Omega/\Delta)^2$. This situation resembles the Franz–Keldysh effect in interband absorption, where an electric field shifts the absorption edge into the interior region of the band gap. A physical reason for the shift of the region of strong single-photon absorption is the possibility of an electron hopping downwards along the Stark ladder. As a result, the energy required to excite an optical phonon is taken not only from the electromagnetic wave but also from the static field.

Let us write the expression for the two-photon absorption for a nonpolar crystal in an approximation of zeroth-order in $(\Delta/\hbar\Omega)^2$:

$$\alpha(\omega) = \frac{A}{\omega^3}\sum_{i=-1}^{1}\sum_{l=-1}^{1} iM_l\left\{\exp\left[\frac{\hbar}{2kT}(\kappa - |\kappa|)\right]\left(1 + \frac{\hbar|\kappa|}{2kT}\right)\right.$$
$$+ \frac{3e^2E^2kT}{4m\hbar^2\omega^4}\exp\left[\frac{\hbar}{2kT}(\kappa - |\kappa|)\right]$$
$$\times\left[3 + 3\frac{\hbar|\kappa|}{2kT} + \left(\frac{\hbar|\kappa|}{2kT}\right)^2\right] + \frac{3e^2E^2kT}{8m\hbar^2\omega^4}$$
$$\left.\times\exp\left[\frac{\hbar}{2kT}(\kappa' - |\kappa'|)\right]\left[3 + 3\frac{\hbar|\kappa'|}{2kT} + \left(\frac{\hbar|\kappa'|}{2kT}\right)^2\right]\right\},$$

$$(16)$$

where $\kappa = i\omega - \omega_0 - l\Omega$, and $\kappa' = 2i\omega - \omega_0 - l\Omega$.

Thus it is evident that the dependence of the two-photon absorption on the light frequency can also be conditionally divided into two regions: For absorption not to be exponentially small, the condition $2\omega > \omega_0$ must be satisfied.

We shall now make some numerical estimates. The ideas developed here are applicable for $\hbar\omega_0 \simeq 3 \times 10^{-2}$ eV, $T \leqslant 10$ K, $E \leqslant 5 \times 10^2$ V/cm (~2 CGS units), $\Delta \leqslant 10^{-2}$ eV, and $\hbar\Omega \simeq 2 \times 10^{-2}$ eV. If, moreover, the density is $n \simeq 10^{16}$ cm^{-3}, then a numerical estimate of the light absorption gives $\alpha(\omega) \simeq 10^2$ cm^{-1}.

Finally, we note that the above-described characteristic features of electroabsorption of light are strongly coupled with the fact that electrons are scattered by dispersion-free optical phonons. In general, dispersion of optical phonons and interaction of electrons with acoustic phonons can change the picture described above. To observe the charac-

teristic features predicted in our study, dispersion must be quite weak. This effect can be estimated by expressing the phonon frequency as $\omega = \omega_0 - \alpha q^2$ (q is the quasiwave vector of a phonon, in order of magnitude α is estimated to be $\alpha \sim \hbar/2M$, and M is the mass of an atom). Dispersion can be ignored if $\hbar^2 q^2/2M \ll \hbar\Delta\omega \sim kT$. The actual values of q in our problem are $q_{ac} \sim (2m\omega_0/\hbar)^{1/2}$. The condition $m\hbar\omega_0/M \ll kT$ must therefore be satisfied. For the numerical values chosen above for the parameters and for $m/M \sim 10^{-5}$ (which is characteristic of Ga and As, which are used to synthesize typical SLs) the latter inequality holds well.

To estimate the role of acoustic phonons we shall use the following circumstance — in uniform materials with electrons being scattered by acoustic phonons the intraband absorption α_{ac} is related, in order of magnitude, to the absorption α_{opt} at deformational acoustic phonons (for conditions similar to ours, $\hbar\omega \sim \hbar\omega_0 \gg kT$) by the relation[15]

$$\alpha_{ac} = \alpha_{opt}\left(\frac{\varepsilon_{ac}\omega_0}{C_0 U_s}\right)^2.$$

Here ε_{ac} is a constant in the acoustic deformation potential, and U_s is the speed of sound. Therefore in the materials where $\varepsilon_{ac}\omega \ll C_0 U_s$ or scattering by polar optical phonons predominates, it can thus be expected that the above-described features of electroabsorption of light can be observed experimentally.

[1] L. Solymar and D. Walsh, *Lectures on the Electrical Properties of Materials* [Oxford University Press, New York, 1988; Mir, Moscow, 1991].
[2] T. K. Woodward, Teodor Sizer (II), D. L. Sivco, and A. Y. Cho, Appl. Phys. Lett. **57** (6), 548 (1990).
[3] D. A. B. Miller, D. S. Chemla, T. C. Damen, and A. C. Gossard *et al.*, Appl. Phys. Lett. **45** (1), 13 (1984).
[4] Y. Silberberg, P. W. Smith, D. J. Eilenberger, and D. A. B. Miller *et al.*, Opt. Lett. **9**, 507 (1984).
[5] K. Fujiwara, H. Shneider, R. Cingolani, and K. Ploog, Solid State Commun. **72** (9), 935 (1989).
[6] A. G. Zhilich, Fiz. Tverd. Tela (Leningrad) **34** (11) 3501 (1992) [Sov. Phys. Solid State **34**, 1875 (1992)].
[7] V. L. Malevich, JETP Lett. **57**, 175 (1993).
[8] M. Saitoh, J. Phys. C: Sol. St. Phys. **5** (9), 914 (1972).
[9] K. Hacker, Phys. Status Solidi **33** (2), 607 (1969).
[10] V. A. Pazdzerskiĭ, Fiz. Tekh. Poluprovodn. **6**(4), 758 (1972) [Sov. Phys. Semicond. **6**, 658 (1972)].
[11] I. N. Bronshteĭn and K. A. Semendyaev, *Handbook of Mathematics* (Nauka, Moscow, 1980).
[12] I. B. Levinson and Ya. Yasevichyute, Zh. Éksp. Teor. Fiz. **62**(5), 1902 (1972) [Sov. Phys. JETP **35**, 991 (1972)].
[13] V. L. Ginzburg and A. A. Rukhadze, *Waves in Magnetoactive Plasma* (Nauka, Moscow, 1970).
[14] É. M. Épshteĭn, JETP Lett. **13**, 364 (1971).
[15] K. Seeger, *Semiconductor Physics* [Springer-Verlag, Berlin, 1974; Mir, Moscow, 1977].

Translated by M. E. Alferieff

X-Ray diffraction analysis of multilayer InAs–GaAs heterostructures with InAs quantum dots

N. N. Faleev,[*] A. Yu. Egorov, A. E. Zhukov, A. R. Kovsh, S. S. Mikhrin, and V. M. Ustinov

A. F. Ioffe Physicotechnical Institute, Russian Academy of Sciences, 194021 St. Petersburg, Russia

K. M. Pavlov and V. I. Punegov

Syktyvkar State University, 167001 Syktyvkar, Russia

M. Tabuchi and Y. Takeda

Department of Materials Science and Engineering, Nagoya University, 464–8603 Nagoya, Japan

Multilayer InAs–GaAs structures with an array of vertically aligned InAs quantum dots in a GaAs matrix, grown by molecular-beam epitaxy, were investigated by crystal truncation rods and high-resolution x-ray diffractometry methods. It was shown that the formation of scattering objects such as vertically aligned quantum dots in the structures strongly influences the mechanism of diffraction scattering of x-rays and changes the spatial distribution of the diffracted radiation. This is explained by the appearance of additional long-range order in the lateral arrangement of the scattering objects in the periodic structures, by the curving of the crystallographic planes in the periodic part of the structure, and by the quasiperiodicity of the deformation profile due to the vertically coupled quantum dots. The observed spatial distribution of the diffracted intensity can be explained qualitatively on the basis of a new model where the scattering layers with quantum dots consist of defect-free, coherently coupled, InAs and GaAs clusters. © *1999 American Institute of Physics.* [S1063-7826(99)01711-1]

1. INTRODUCTION

Epitaxial heterostructures with arrays of vertically aligned quantum dots[1–8] are interesting objects for studying their possible applications in various optomicroelectronic devices, for example, laser diodes. In this connection, it is important to investigate the structural properties of such structures, to study the mechanisms of epitaxial growth and relaxation of elastic stresses, and to determine the characteristic features of the diffraction interaction of x-rays with scattering objects of this type. It is well known that the formation of an array of quantum dots (QDs) on a growth surface changes the mechanism of epitaxial growth of intermediate GaAs layers and influences the distribution of the elastic stresses in and the planarity of the layers. During growth of multilayer structures an ordered structure of QDs is formed in the direction of epitaxial growth (q_z) — an array of vertically aligned dots — and in the plane of the heterojunction (lateral directions q_x and q_y). The parameters of QDs and the character of their spatial ordering are determined by the conditions of epitaxial growth.

It is known that the formation of quantum dots in the structures substantially changes the physical parameters of the structures. Specifically, a change produced in the spatial distribution of deformation in epitaxial layers by the presence of QDs should appreciably affect the conditions of diffraction of x-rays and change the character of the spatial distribution of the intensity. The results of x-ray diffraction studies will help to establish the mechanism leading to the formation of QDs and to determine the characteristic features of the relaxation of elastic stresses in structures of this type. All this is important for understanding the physical characteristics of low-dimensional quantum-well objects.

2. EXPERIMENTAL METHODS

The experimental samples were grown on precisely oriented n^+-GaAs(001) substrates by molecular-beam epitaxy in a Riber 32P system with a solid-state arsenic source. To decrease segregation and reevaporation of In, the substrate temperature during formation of a multilayer structure with QDs and deposition of a 100-Å-thick GaAs layer covering the array of quantum dots was lowered to 480 °C. The growth temperature for the rest of the structure was 620 °C. Growth was conducted under As-stabilized conditions. An array of vertically aligned dots was formed on approximately 1.2-μm-thick GaAs buffer layers as a result of three-, six-, and tenfold deposition of QD layers separated by 50-Å-thick GaAs layers. The effective thickness of InAs layers was 5.5–6.0 Å. The InAs–GaAs periodic structures were buried with a GaAs layer of the order of 0.4–0.5 μm thick. Transmission electron microscopy (TEM) showed the InAs QDs formed in this manner to be close in shape and size and weakly ordered in lateral directions. Correspondingly, the periodic structures containing InAs QDs are arrays of vertically aligned QDs in a GaAs matrix.[9] However, because TEM methods are local,

the presence of long-range order in the lateral arrangement of InAs QDs requires that these data be confirmed by x-ray diffractometry, which is highly sensitive to structural ordering.

Structures with additional spatial ordering of layers in the direction of epitaxial growth (superlattices) as objects of investigations were chosen because in x-ray diffraction experiments on perfect periodic structures, just as on structures of interference type, spatial resolution comparable to the resolution of transmission electron microscopy[10,11] can be attained and substantial information about the structure of the layers and interfaces can be obtained.

Measurements by the crystal truncation rods (CTR) method were performed on a two-crystal diffractometer at station BL6A of the photon factory in Tsukuba, Japan using synchrotron radiation from a storage ring with 2.5-GeV positrons (the ring current — 380–250 mA). Monochromatization and collimation of the synchrotron radiation were performed using a curved quartz mirror and a triangular Si(111) crystal, curved to form a quasiparallel beam of monochromatized radiation. Special light-sensitive plates (imaging plate — IP) were used to record the two-dimensional diffraction patterns. Information from the plates was read optically.[12]

The CTR patterns were recorded near the (004) GaAs reflection at the wavelength 1.6 Å of the synchrotron radiation. After information was read from the IP and the incoherent background was removed, the diffraction curves were reconstructed from the complete two-dimensional patterns in the direction of the diffraction vector q_z (analogs of $\omega - 2\theta$ x-ray diffraction curves) and in a perpendicular direction q_x

(analogs of ω curves). These curves were later used to obtain numerical data on the structures.

The high-resolution x-ray diffraction studies were performed on a Rigaku (Japan) high-transmission, double-crystal $\theta - \theta$ diffractometer with a slit-type Ge(001) double monochromator using $CuK_{\alpha 1}$ radiation. The $\omega - 2\theta$ and ω scanning methods were used to record the diffraction reflection curves (DRCs) and the intensity distribution in reciprocal space (reciprocal space mapping — RSM). A narrow receiving slit in front of the detector was used to separate the coherent and diffuse components of the diffracted radiation.

3. EXPERIMENTAL RESULTS

For accurate estimation of the crystallographic structural perfection, the samples were first investigated near the (004) GaAs reflection in a TRS-1 double-crystal diffractometer with high angular resolution [the divergence of the radiation after the asymmetric Ge(001) monochromator was 1.0-1.2″]. A characteristic feature of the experimental structures is that the intermediate layers containing InAs QDs serve as interference interlayers for radiation diffracted by the top GaAs layer. As a result of the large mismatch of the average lattice parameters in layers with QDs, the top GaAs layer is spatially shifted relative to the substrate and the GaAs buffer layer. In turn, the latter is spatially displaced relative to the substrate because of the presence of a silicon-doped GaAs layer on its bottom interface. In crystallographically perfect heterostructures the presence of such interlayers results in the appearance of extended interference patterns in the DRCs.
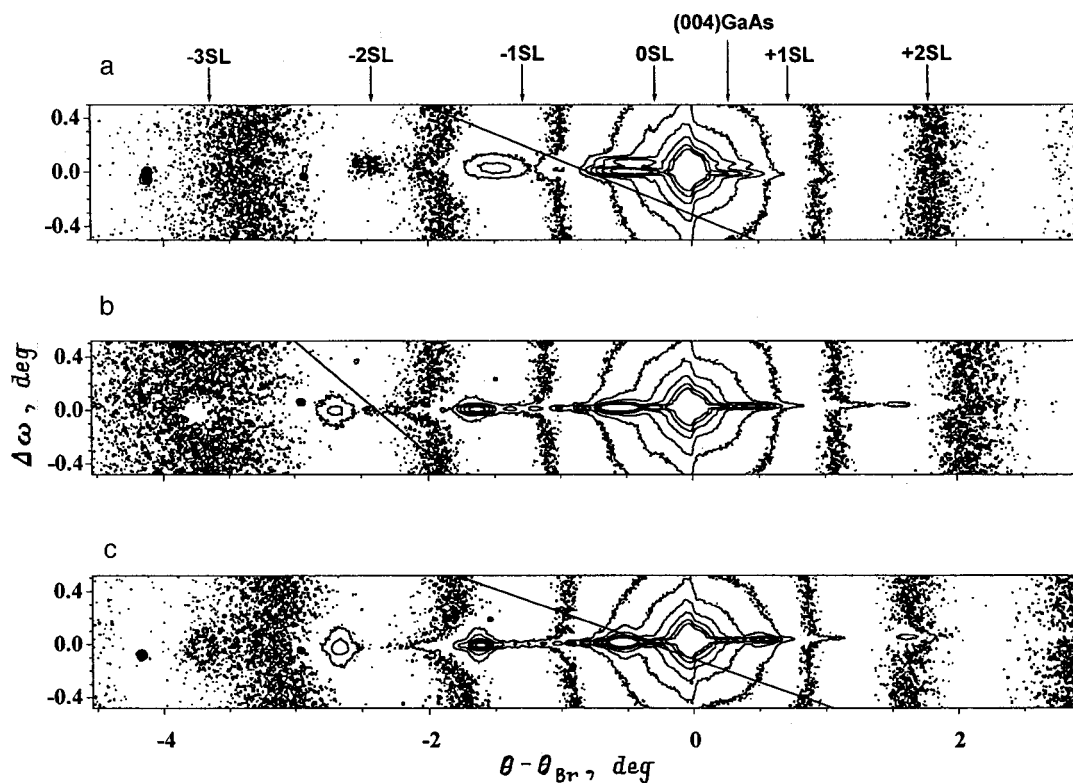

FIG. 1. CTR patterns of the spatial distribution of the radiation intensity near the (004) GaAs reflection for structures with 3 (a), 6 (b), and 10 (c) pairs of InAs–GaAs layers. The wavelength of the synchrotron radiation is 1.6 Å.

TABLE I. Parameters, obtained by the CTR method, for the experimental structures.

Sample No.	n	t_{SL}, Å	Δt_{if}, Å	Δa_{SL}, 10^{-2} Å	x_{InAs}, %	t_{InAs}, Å
1	3	54.6	9.6	6.44	7.63	4.15
2	6	52.7	9.2	7.69	9.1	4.80
3	10	52.0	9.0	7.57	9.00	4.65

Note: n — number of pairs of InGA–GaAs layers; t_{SL} — period of the InAs(QDs)–GaAs superstructure; Δt_{if} — broadening of the interface in the superstructure; Δa_{SL} — mismatch of the lattice parameters in the InAs(QDs)–GsAs superstructure, determined by x-ray diffractometry methods according to the position of the 0SL peak, corresponding to the average composition (mismatch) in the superstructure, in the diffraction curve; x_{InAs} — InAs concentration in the superstructure (estimated according to the mismatch parameter and the period of the superstructure); t_{InAs} — InAs thickness in the superstructure (scaled to pure InAs).

The crystallographic perfection of the buffer and top GaAs layers can be determined according to the shape and parameters of these patterns, and the planarity of epitaxial layers producing the interference pattern can be estimated from the angular extent of the thickness oscillations.[13] The measurement results showed that the experimental structures possess high crystalline perfection, and the density of growth defects (predominantly of the point type) is low. Extended structural defects of the type dislocation loops and (or) misfit dislocations are virtually completely absent in the experimental structures.

It is known that most crystallographic defects in epitaxial structures are formed during epitaxial growth.[14–16] Migrating along the structure, defects formed on the growth surface strongly affect the crystallographic perfection of both the upper- and lower-lying layers, including the substrate.[14,15] For this reason, data on the structural perfection of thick adjoining layers make it possible to estimate the degree of perfection of the intermediate layers that contain quantum dots and to interpret correctly the results of further diffraction studies. For heterostructures with a high crystallographic perfection, determined by the structural perfection of each layer individually, this makes it possible to compare directly the characteristic features of the x-ray diffraction data with the true structure of the experimental objects, for example, quantum dots. For epitaxial layers with low crystallographic perfection, the structural defects formed have a predominant effect on x-ray scattering, changing the character of the diffraction patterns substantially.

Analysis of the CTR diffraction patterns (Fig. 1) shows that the character of the spatial distribution of intensity in the direction q_z and in the direction $q_x(q_y)$ changes as the total number of pairs of layers (InAs + QD)–GaAs increases. Appreciable changes in the q_z direction — decrease of the linear extent of superstructural spots, appearance of additional thickness oscillations — are all manifestations of a dynamical effect due to an increase of the coherent-scattering volume. But the shape of the superstructural peaks also changes at the same time in a perpendicular (lateral) direction. Becoming narrower in the q_z direction, the distant superstructural spots become appreciably extended in the q_x direction, and chords, whose length increases from the -1SL peak to the -3SL peak, appear near them. The shape and parameters of the CTR ω curves for the -1SL and -2SL peaks showed that the broadening of the spots in the q_x direction is much greater than the instrumental error of the method due to the finite size of the incident beam. It can therefore be inferred that the experimentally observed elongation of the diffraction spots in the lateral direction is due to the appearance of certain features, due primarily to the formation of InAs QDs, in the periodic part of the structures.

Numerical analysis of the $\omega - 2\theta$ CTR curves showed that the thicknesses of the quantum-well layers in multilayer structures are close to the prescribed values (Table I). The planarity of the InAs/GaAs heterojunctions of the periodic part of the structures, estimated according to the total extent of the diffraction patterns, was 3–4 monolayers. The differences between the CTR and x-ray diffraction data did not exceed 1.5 Å, despite the much higher ($>10^4$ times) intensity of the synchrotron radiation.

Comparison with the results of investigations of InAs–GaAs periodic structures of different types[17,18] shows that such broadening of the InAs/GaAs heteroboundaries is characteristic of a GaAs(001) surface and is determined by the morphology of the growth surface.[19] This allows us to assert that in epitaxial structures with a low density of growth defects ($\leqslant 10^4 - 10^5$ cm^{-2}) the broadening or nonplanarity of the heteroboundaries, which is due to the morphology of the growth surface, is the main factor which decreases the extent of the informative part of the coherent DRCs and limits the spatial resolution of diffraction methods.

Data from high-resolution x-ray diffraction measurements (Table II) confirmed the results obtained by the CTR method. A comparison shows that the differences in the structural parameters are negligible and fall within the measurement error. Numerical simulation of the coherent diffraction reflection curves was used to refine the geometric parameters of the structures. The calculations were performed using the standard dynamical theory of diffraction based on

TABLE II. Structural parameters obtained from high resolution x-ray diffractometry data and by numerical simulation of experimental diffraction reflection curves. .

Sample No.	t_{capL}, nm	t_{SL}, Å	Δt_{if}, Å	Δa_{SL}, 10^{-2} Å	x_{InAs}, %	t_{InAs}, Å	Computed values		
							t_{SL}^{calc}, Å	x_{InAs}^{calc}, %	t_{InAs}^{calc}, Å
1	505 ± 24	54.2	11	6.58	7.8	4.22	55	9.8	5.40
2	410 ± 28	52.3	10.8	7.60	9.0	4.70	53	9.5	5.04
3	450 ± 23	52.4	10.5	7.66	9.05	4.75	52	9.6	5.00

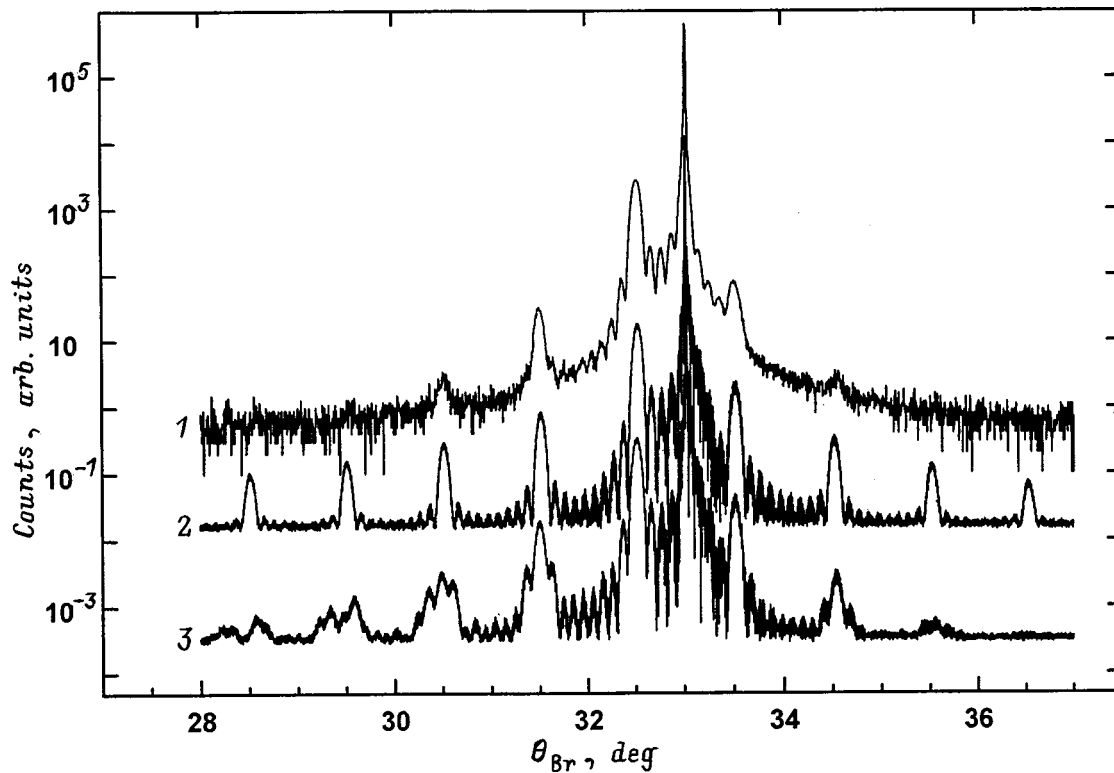*Note*: t_{capL} — thickness of the top GaAs layer in the structure

FIG. 2. Experimental (*1*) and computed (*2* and *3*) coherent $\theta - 2\theta$ diffraction curves for a structure containing 10 pairs of InAs–GaAs layers. (004) GaAs reflection, Cu$K_{\alpha 1}$ radiation.

the Takagi equations.[20] Quantum dots were simulated by a InGaAs layer of variable composition with an InAs wetting layer at the heterojunction. In the dynamical approximation, ignoring the real broadening of the InAs/GaAs boundaries and the characteristic features of the internal structure of the layers containing quantum dots, good agreement was obtained between the experimental curves (Fig. 2, curve *1*) and the computed curves only in a limited angular range — near the central (0SL) and the closest (± 1 SL) superstructural peaks (Fig. 2, curve *2*). Taking into account the broadening of the InAs/GaAs boundaries somewhat changed the shape of the distant superstructural peaks, but, as expected, it did not lead to any fundamental changes in the pattern as a whole (Fig. 2, curve *3*). The computational results are also presented in Table II. The computed values of the periods of the superstructures agree well with the experimental values, while the thicknesses of the InAs layers calculated taking into account Vegard's law are closer to the technological parameters. This can be explained by the dynamical effect of scattering by thin layers, shown for single-layer structures in Ref. 21.

The results of the x-ray diffraction analysis of the spatial distribution of the diffracted intensity (RSM) and the shape and parameters of the ω curves completely confirmed the CTR data. The RSM patterns (Fig. 3) showed that the spatial distribution of the diffracted intensity differs substantially from similar curves for planar periodic structures or structures with an artificially produced periodicity in the lateral direction.[22] The largest differences in the intensity distribution are observed near the substrate peak and the superstruc-

tural peaks. Just as in the CTR patterns, the size of the main diffraction spots decreases in the q_z direction but increases in the $q_x(q_y)$ direction upon transition from the central superstructural maximum (0SL peak) to the lateral superstructural maxima. Moreover, a distinguishing feature of the RSM patterns is the presence of extended ω chords not only in the superstructural peaks but also in the substrate peak.

The ω curves measured near the superstructural peaks showed that instead of a single peak characteristic of planar structures the curves can possess two or more diffraction peaks, whose shape and parameters seem to be determined by the ordering in the system of quantum dots. In the symmetric (004) reflection the most extended chords in the $q_x(q_y)$ direction are observed for the -1 SL peak and the central (004) GaAs reflection. In the central section of the -1 SL peak, for example, two maxima are observed in the ω curves (Fig. 4), and away from the exact angular position corresponding to the -1 SL peak their number increases to 5. The average sizes of the scattering clusters in the azimuthal direction [110], estimated according to the distance between the peaks in the ω curves, correspond to scattering by complexes with average sizes 64 ± 4 and 26 ± 2 nm, which is close to the average sizes of GaAs and InAs clusters. For the (100) azimuthal direction the character of the distribution of the diffractive intensity does not change as a whole. The average size of GaAs clusters is 90.0 nm. The change in the shape of the ω curves and the appearance of additional peaks in them attest to the formation of long-range order in the arrangement of the scattering centers. The character of the change in the shape of the superstructural spots in the RSM
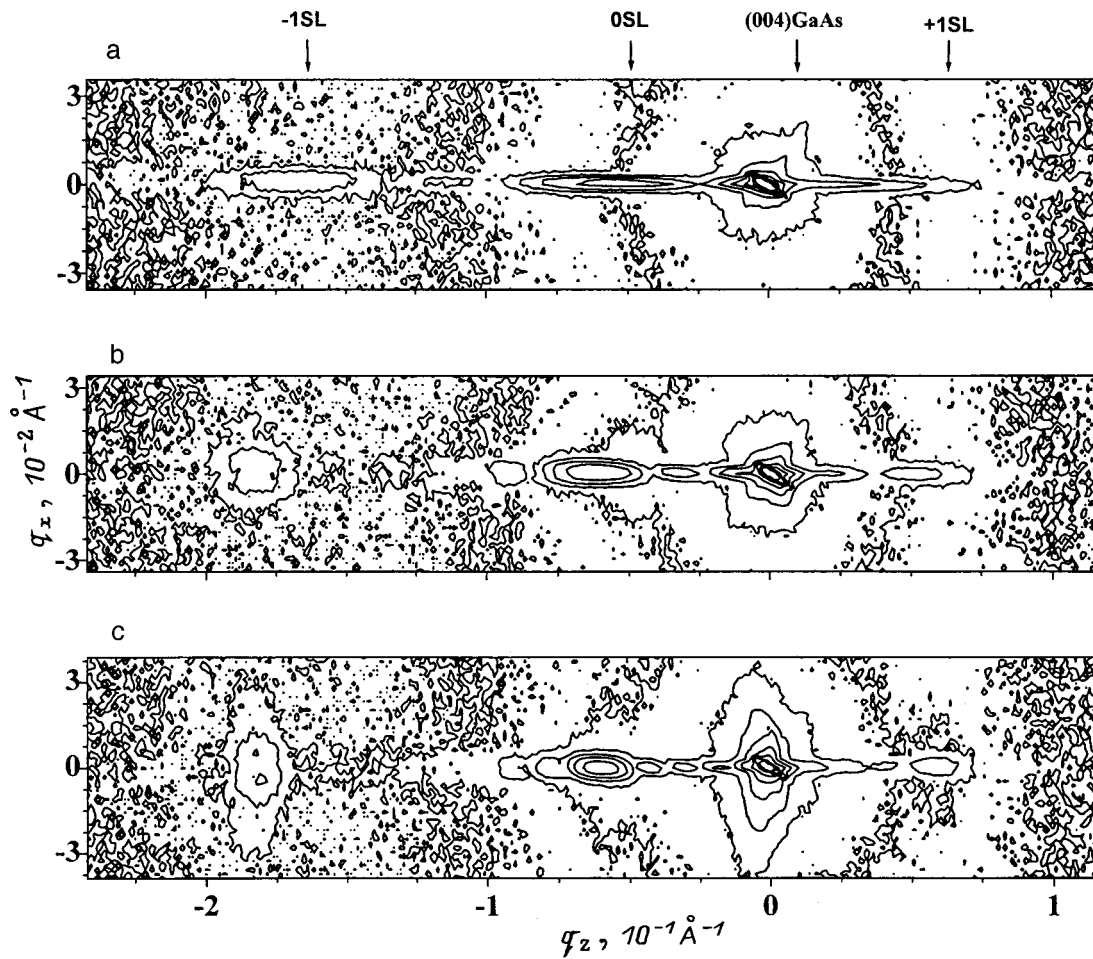
FIG. 3. Diffraction patterns of the diffracted intensity distribution in reciprocal space near the (004) GaAs layers for structures with 3 (a), 6 (b), and 10 (c) pairs of InAs–GaAs layers. Radiation — $CuK_{\alpha 1}$.
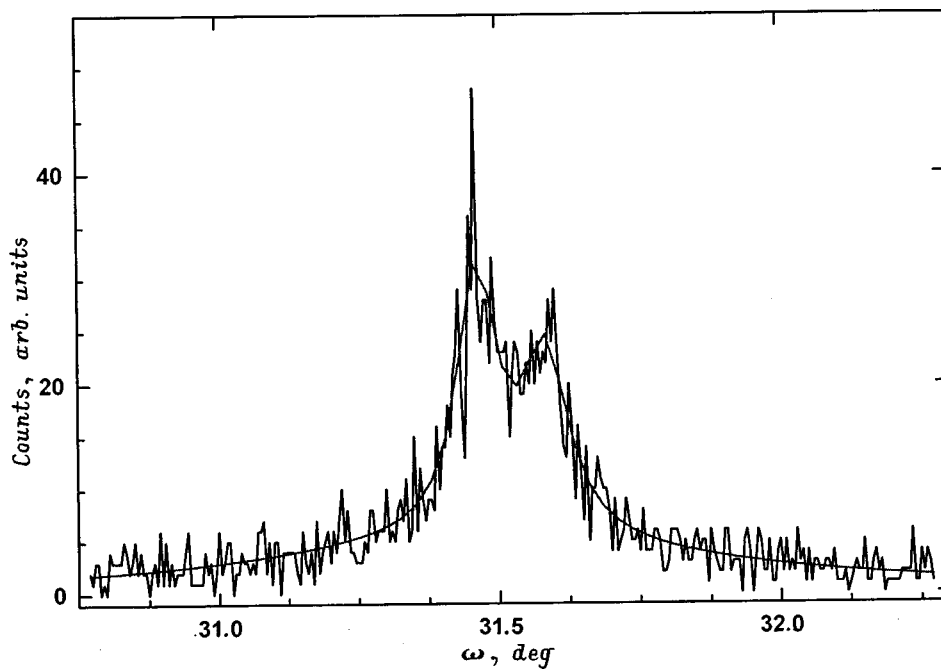

FIG. 4. ω curve near the center of the superstructural peak -1SL. The resulting fit of the curve with a Lorentzian is presented. (004) GaAs reflection, $CuK_{\alpha 1}$ radiation.

patterns suggests that the degree of lateral ordering in layers with QDs increases with increasing total number of pairs of layers, which is confirmed by the calculations and the experimental (TEM) data.[23,24]

The x-ray diffraction measurements gave a detailed picture of the spatial distribution of the diffracted intensity near the (004) GaAs central diffraction spot. The RSM pattern showed clearly the presence of an ω chord for the substrate peak, while because of the limited dynamic range of the detecting plates, strong background illumination is always present in the CTR patterns near the main structural maxima, making it difficult to study the details of the spatial distribution of the diffracted intensity.

4. DISCUSSION OF THE RESULTS

Analysis of the experimental results shows that the lateral scattering of x-rays is influenced mainly by InAs–GaAs superlattices containing InAs QDs. In addition, it is necessary to take into account the appreciable bending of the crystallographic planes due to the presence of QDs on the diffraction scattering of x-rays as well as the effect of the quasiperiodic deformation potential induced by vertically aligned quantum dots in the adjoining part of the GaAs layer.

This suggested a structural model of the scattering layers that qualitatively explains the experimental results. In the standard model the InAs quantum dots lying on an InAs wetting layer are treated coherently as ideal, elastically stressed InAs clusters of definite size and shape, i.e., without structural defects, built into a perfect GaAs matrix. It is assumed that the elastic stresses introduced by the QDs do not strongly influence the structure of the intermediate GaAs layers and the stress distribution in them, i.e. the GaAs layers are planar and uniform with respect to structural parameters. The curvature of the crystallographic planes is disregarded.

In such a model the main factor that can appreciably influence the diffraction scattering of x-rays are the InAs QDs. In the case of random spatial distribution and if the intrinsic sizes are markedly nonuniform, they will contribute only to diffuse scattering, which will be weak because their total scattering volume is negligible and there are no extended structural defects associated with them. Comparison with the experimental results shows that this model disregards certain features of the structure of scattering layers and requires refinement.

The results obtained show that the elastic stresses introduced by quantum dots strongly affect the structure of the intermediate GaAs layers. Taking into account the characteristic features of the formation of quantum-well layers with elastically strained clusters and the character of the stress distribution in them,[25] the GaAs layers with built-in InAs quantum dots cannot be regarded as planar and uniform. In our model the periodic structure is formed by layers consisting of pyramidal InAs clusters separated by coherently coupled GaAs clusters in the form of inverted pyramids. A layer of such clusters is bounded below by an InAs wetting layer and above by a thin GaAs layer. In contrast to the preceding model, where the GaAs layer containing InAs QDs was regarded as a standard epitaxial layer, unbounded
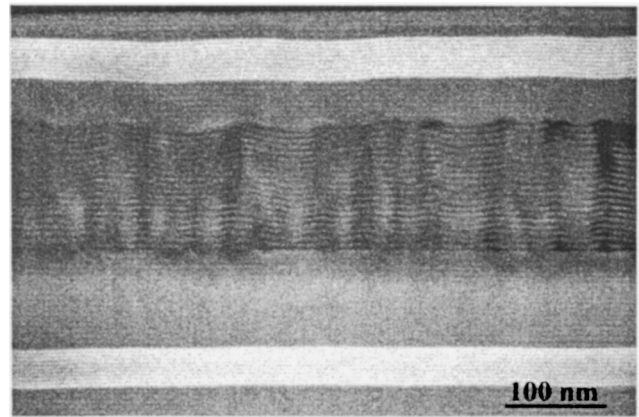

FIG. 5. Electron-microscopic image of a structure with 20 pairs of InAs–GaAs layers in the cross-sectional geometry, **g** (002).

in the lateral directions, in the new model the GaAs layer containing InAs QDs is regarded as a system of quantum-well InAs and GaAs clusters that possess finite sizes in all directions. It is assumed that under optimal growth conditions clusters are formed without formation of extended structural defects along the boundaries. As a monolayer structure grows, the variance of their intrinsic sizes decreases, and a system of InAs–GaAs clusters with indications of long-range order in lateral directions forms as a result of vertical alignment of the QDs. In addition, the curvature of the crystallographic planes, which is due to coherent embedding of strained InAs QDs in the matrix of the main material (Fig. 5), must be taken into account. It is evident in photomicrographs that the curvature of the crystallographic planes increases with the total number of pairs of layers in the periodic part of the structure. In addition, the curvature is inherited by the upper-lying GaAs layer, gradually decreasing away from the layers with QDs.

Using the model presented here, we shall examine the process of relative ordering of GaAs and InAs clusters in the (001) plane and we shall analyze the associated features of the spatial distribution of the diffracted intensity. For a completely disordered arrangement of clusters, diffraction scattering will be diffuse and due mainly to scattering by GaAs clusters as a result of their large scattering volume (on the order of 90% of the total volume of the periodic structures). As a result, the scattering will be localized near the corresponding GaAs site, as shown in Ref. 26. In the presence of periodicity in the direction of epitaxial growth (q_z), diffuse scattering should also appear near the superstructural peaks. Ordering of a cluster system in the vertical and lateral directions, as well as the variance of the characteristic sizes of InAs and GaAs clusters should increase the local static Debye–Waller factor[26] and, ultimately, the intensity of coherent scattering in the q_x (q_y) direction near the superstructural peaks and lead to the appearance of additional peaks in the ω curves.

The sharp increase in length of the chords for the $-1SL$ and $-2SL$ peaks, as compared with the 0SL peak, can be explained by the fact that as the angular deflection from the central peak increases, the sensitivity of the shape of the

superstructural peaks to nonuniformities in the structural parameters, for example, to the gradient of the period of the superstructure and the curvature of the crystallographic planes increases substantially. At the same time, the relative contribution of the top part of the structure to scattering increases.[13] This is very important, since the vertical and lateral ordering of the cluster system increases in each subsequent layer.[23,24] As a result, the position of clusters at the top of the structures is more ordered, and their sizes are more uniform. At the same time, the curvature of the crystallographic planes also increases. This should be most clearly seen as a change in the shape of the ω curves — appearance of additional peaks in them (lateral ordering) and increase in length of the ω chords near the distant superstructural peaks and the substrate peak (additional diffuse scattering due to local deformation of the crystal lattice near the QDs, resulting in curvature of the crystallographic planes), as is observed experimentally. The large difference in the shape of the chords for the -1SL and $+1$SL satellites seems to be due to a difference in the mechanisms of phase interaction of the waves diffracted by the substrate and epitaxial structure.

Using the above-described physical model as a basis, we shall use as a computational model the ordered, on the average, arrangement of quantum dots in the directions of the x and y axes with the same average step. To describe this system we introduce an n-dimensional normal distribution, where n is the average number of quantum dots in one period of the superlattice. For simplicity, we assume that the random displacements of the QDs from the average positions are uncorrelated, i.e., they are statistically independent. We also assume that in each period the variances of the displacements, the QD sizes, and the average distances between QDs are the same. By changing the variance, the average distance between QDs, and the average QD size from period to period we can simulate the variation of the vertical and lateral correlations in the QD parameters. The intensity distribution in reciprocal space was simulated on the basis of the theory which was described by Pavlov and Punegov[27] and which was extended to a multicrystal diffraction scheme. The simulation results are presented in Fig. 6. The form of the computed coherent intensity distribution in the reciprocal space is in many respects the same as the experimental results, which confirms the assumption that the coherent component makes the main contribution to the scattered intensity. We note that the working model makes it possible to describe only the most general features of the structure of the quantum dots that are actually formed. As a result, only qualitative agreement between the experimental and theoretical data was attained. In the future, we plan to use multiparticle correlation functions in the calculations in order to obtain a more accurate description of correlations in the parameters of quantum dots.

It is also necessary to take into account in the model the effect on the scattering of x-rays of the curvature of the crystallographic planes and elastic stresses that penetrate from layers with QDs into the upper-lying GaAs layer. Allowance should also be made for the changes due to the built-in quantum dots, which affect the distances that are large compared with the sizes of the QDs themselves (see Fig. 5) and ac-

count, together with the curvature of the planes, for the non-uniformly distributed deformation profile in the GaAs lying at the top. In aggregate, this should result in the appearance of additional quasicoherent scattering in the directions q_x (q_y) near the (004) GaAs peak, as was indeed observed in the experimental RSM data in the form of narrow ω ties. The difference in the experimental and theoretical patterns can likewise be explained by the fact that diffuse scattering was ignored in the simulation, and it undoubtedly makes a substantial contribution to the distribution of the diffracted radiation.

In general, the question of the degree of coherence of the diffracted radiation is very complicated, and it is now in the investigatory stage. We note only the following circumstance, referring to the question of the degree of coherence of the radiation. In the direction q_z the half-width of the ω chords, observed in the RSM patterns, in any x section does not exceed their half-width in the central $\theta - 2\theta$ section, which is determined by the total thickness of the periodic structure. Just as narrow chords in the directions q_x and q_y are also observed in the asymmetric (115) reflection with a small entry angle. This can be explained by the fact that the degree of spatial ordering of the system in the direction of epitaxial growth is much greater than in the lateral direction, primarily because of the radical difference in the mechanisms leading to their formation. For this reason, the phase correlations in the direction q_z are stronger than in the directions q_x and q_y, in which further ordering of the statistically disordered clusters (or QDs) only starts to appear. Nonetheless, our data show that the rate of lateral ordering of clusters in real structures is much higher than in the computed model,[23] since the choice of the initial position for InAs quantum dots and their conditions of formation in a real structure are not random but rather are determined by the mechanism of epitaxial growth and the quality of the initial growth surface in the process of formation of layers with quantum dots.

We note another important circumstance concerning the question of the coherence of the diffracted radiation. The data obtained show that in the investigated structures deformation curvature of the crystallographic planes, in contrast to the breakdown of planarity of the layers and heteroboundaries, does not seem to have a large effect on the coherence of the diffracted radiation and therefore on the spatial resolution of x-ray diffractometry methods.

5. CONCLUSIONS

The crystal truncation rods (CTR) and high-resolution x-ray diffractometry methods were used to investigate the crystallographically perfect multilayer periodic InAs–GaAs structures with InAs quantum dots. The characteristic laws of the diffraction scattering of x-rays by structures of this type were found. Using the CTR patterns and the patterns of the spatial distribution of the diffracted intensity, it was shown that long, narrow chords in the q_x (q_y) direction form parallel to the surface near the superstructural peaks and reflec-
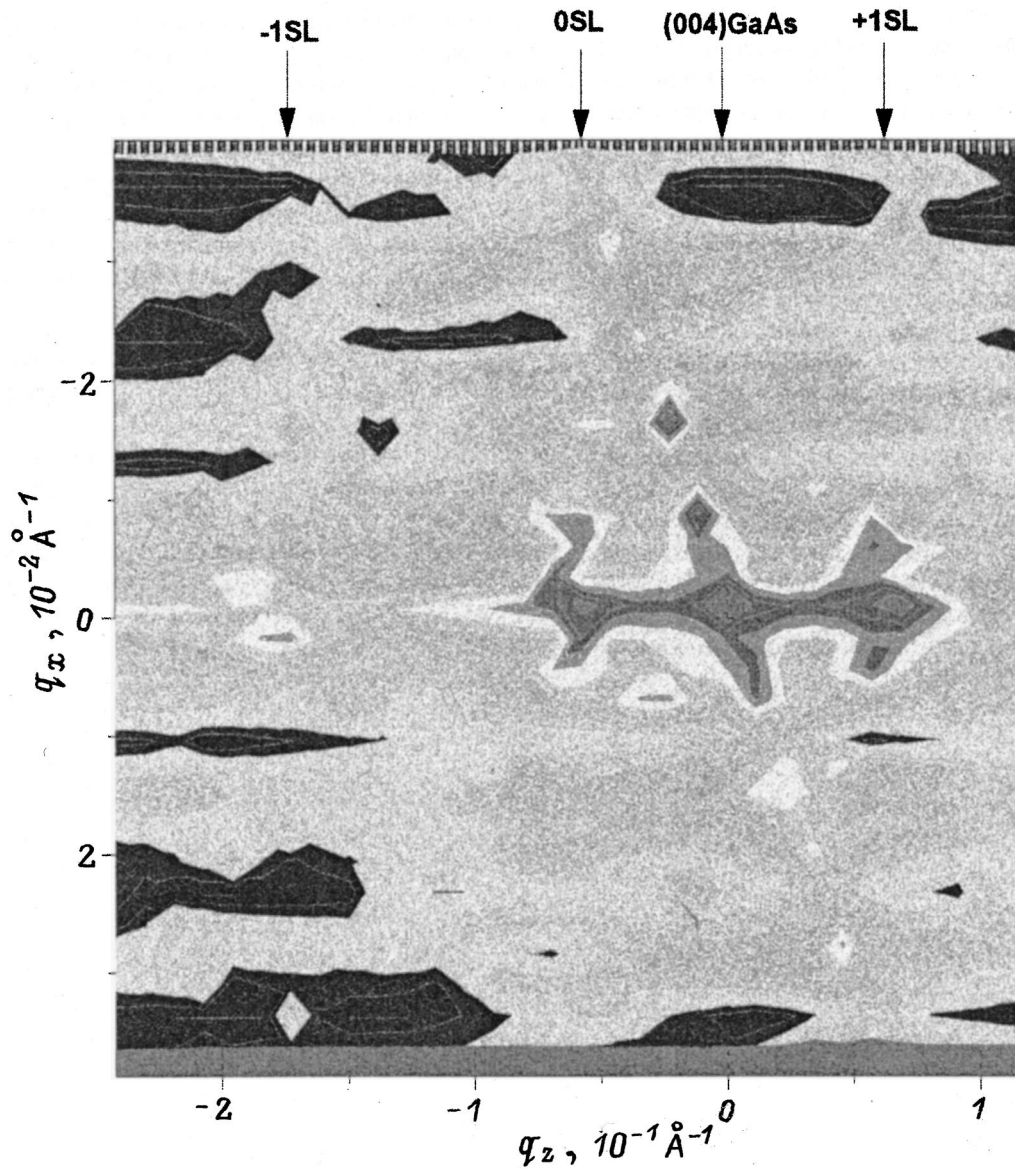
FIG. 6. Computed diffracted intensity distribution in reciprocal space near a (004) GaAs reflection for a structure with 10 pairs of InAs–GaAs layers. Radiation — $CuK_{\alpha 1}$.

tions from the substrate. This indicates curvature of the crystallographic planes in regions containing QDs and in the upper adjoining layers.

It is shown that as the number of pairs of layers in a periodic structure increases, the length of the ω chords increases and the pattern of the spatial distribution of the diffracted intensity changes. The shape and parameters of the ω curves near the superstructural peaks attest to the formation of long-range order in the lateral arrangement of the scattering centers (QDs, GaAs clusters) in multilayer periodic structures. It was shown that in a direction toward the surface lateral ordering of clusters grows in the layers and the size variance decreases.

A new model of quantum-well layers of quantum dots was proposed. The layers consist of defect-free, coherently coupled InAs and GaAs clusters. The formation of a system of clusters is due to the presence of nonuniformly distributed elastic strains around the buried InAs quantum dots. The

model takes into account the curvatures of the crystallographic planes, due to local deformations near InAs QDs, and the additional deformation potential induced in the upper-lying GaAs layer. The calculations performed on the basis of the proposed model showed that the results obtained largely agree with the experimental results, thereby confirming that the coherent component of the diffracted radiation makes a large contribution to the scattered intensity. It was shown that the formation of an additional deformation potential and the adjoining GaAs layer at the top and the curvature of the crystallographic plane strongly influence the spatial distribution of the diffracted intensity and lead to the appearance of an additional ω chord for the substrate peak.

It was shown that the nonplanarity or broadening of the interfaces in perfect heterostructures is the main factor limiting the spatial resolution of x-ray diffractometry methods. In contrast to this effect, the deformation curvature of crys-

tallographic planes does not seem to greatly influence the spatial resolution of the method.

The crystal truncation rods and high-resolution x-ray diffractometry methods complement one another, making it possible to establish the particular features of the diffraction scattering of x-rays by complex scattering objects.

*)E-mail: Faleev@pop.ioffe.rssi.ru

[1] Y. Arakawa and H. Sakaki, Appl. Phys. Lett. **40**, 939 (1982).

[2] M. Asada, Y. Miyamoto, and Y. Suematsu, Jpn. J. Appl. Phys. **24**, L95 (1985).

[3] L. Goldstein, F. Glas, J. Y. Marzin, M. N. Charasse, and G. LeRoux, Appl. Phys. Lett. **47**, 1099 (1985).

[4] Y. Arakawa and A. Yariv, IEEE J. Quantum Electron. **QE-22**, 1887 (1986).

[5] M. Asada, Y. Miyamoto, and Y. Suematsu, IEEE J. Quantum Electron. **QE-22**, 1915 (1986).

[6] M. Tabuchi, S. Noda, and A. Sasaki, in *Science and Technology of Mesoscopic Structures*, edited by S. Namba, C. Hamaguchi, T. Ando (Springer-Verlag, Tokyo, 1992).

[7] *Nanostructures and Qantum Effects*, edited by H. Sakaki and H. Noge (Springer-Verlag, Berlin, 1994).

[8] *Epitaxial Microstructures*, edited by A. C. Gossard (*Semiconductors and Semimetals*, Academic Press, Boston, 1994, Vol. 40).

[9] P. N. Brunkov, A. A. Suvorova, N. A. Bert, and A. R. Kovsh, Fiz. Tekh. Poluprovodn. **32**, 1229 (1998) [Semiconductors **32**, 1096 (1998)].

[10] L. Tapfer and K. Ploog, Phys. Rev. B **40**, 9802 (1989); L. Tapfer, M. Ospelt, and H. Kanel, J. Appl. Phys. **67**, 1298 (1990).

[11] N. N. Faleev, I. K. Solomin, L. I. Flaks, S. V. Batashova, and S. G. Konnikov, Phys. Status Solidi A **120**, 327 (1990).

[12] T. Shimura and J. Harada, J. Appl. Crystallogr. **26**, 151 (1993).

[13] A. M. Afanas'ev, P. A. Aleksandrov, S. S. Fanchenko, V. A. Chaplanov, and S. S. Yakimov, Acta Crystallogr. **42**, 116 (1986).

[14] N. Faleev, R. Stabenow, M. Sinitsyn, B. Yavich, A. Haase, and A. Grudsky, Mater. Sci. Forum **166–169**, 293 (1994).

[15] V. G. Gruzdov, A. O. Kosogov, and N. N. Faleev, Pis'ma Zh. Tekh. Fiz. **20**(14), 1 (1994) [Tech. Phys. Lett. **20**, 561 (1994)].

[16] L. Dong, J. Schnitker, R. W. Smith, and D. J. Srtolovitz, J. Appl. Phys. **83**, 217 (1998).

[17] M. A. Bert, Yu. G. Musikhin, V. V. Preobrazhenskiĭ, M. A. Putyato, B. R. Semyagin, A. A. Suvorova, V. V. Chaldyshev, and P. Werner, Fiz. Tekh. Poluprovodn. **32**, 769 (1998) [Semiconductors **32**, 683 (1998)].

[18] N. N. Faleev, V. V. Chaldyshev, A. E. Kunitsyn, V. V. Preobrazhenskiĭ, M. A. Putyato, B. R. Semyagin, and V. V. Tret'yakov, Fiz. Tekh. Poluprovodn. **32**, 24 (1998) [Semiconductors **32**, 19 (1998)].

[19] D. Suzuki, H. Yamaguchi, and Y. Horikoshi, Jpn. J. Appl. Phys. **37**, 758 (1998).

[20] S. Takagi, J. Phys. Soc. Jpn. **26**, 1239 (1969).

[21] P. F. Fewster and C. J. Curling, J. Appl. Phys. **62**, 4154 (1987).

[22] V. Holy, A. A. Darhuber, G. Bauer, P. D. Wang, Y. P. Song, C. M. Sotomayor Torres, and M. C. Holland, Phys. Rev. B **52**, 8348 (1995).

[23] J. Tersoff, C. Teichert, and M. G. Lagally, Phys. Rev. Lett. **76**, 1675 (1996).

[24] S. Rouvimov, Z. Liliental-Weber, W. Swider, J. Washburn, E. R. Weber, A. Sasaki, A. Wakahara, Y. Furkawa, T. Abe, and S. Noda, J. Electron. Mater. **27**, 427 (1998).

[25] M. Grundmann, O. Stier, and D. Bimberg, Phys. Rev. B **52**, 11 969 (1995).

[26] A. A. Darhuber, V. Holy, J. Stangl, G. Bauer, A. Krost, F. Heinrichsdorff, M. Grundmann, D. Bimberf, V. M. Ustinov, P. S. Kop'ev, A. O. Kosogov, and P. Werner, Appl. Phys. Lett. **70**, 955 (1997).

[27] K. M. Pavlov and V. I. Punegov, Acta Crystallogr. **54**, 214 (1998).

Translated by M. E. Alferieff

Quantum Hall effect in a single-mode wire

Z. D. Kvon,*) E. B. Ol'shanestkiĭ, M. I. Katkov, A. E. Plotnikov, A. I. Toropov, and N. T. Moshegov

Institute of Semiconductor Physics, Siberian Branch of the Russian Academy of Sciences, 630090 Novosibirsk, Russia

M. Casse

High Magnetic Field Laboratory CNRS, F-38042 Grenoble, France

J. C. Portal

INSA—Toulouse, F-31077 Toulouse, France

The quantum Hall effect in a single-mode wire is studied for the first time. It is established that a well-expressed quantum Hall resistance for filling factors $i = 1$ and 2 is observed in magnetic fields in which the magnetic length becomes less than the width of the wire. Breakdown of proportionality with respect to the magnetic field in the arrangement of the Hall quantization plateau and the dissipative conductivity minima is observed. © *1999 American Institute of Physics.* [S1063-7826(99)01811-6]

The behavior of the quantum Hall effect (QHE) in wires and point contacts is one of the interesting features arising in the study of this effect. Unitl now, however, it has not been studied exhaustively. There are several works[1–3] devoted to an experimental investigation of the QHE in wires. The object of investigation in all of these cases were wide wires whose width W was much greater than the electron wavelength; i.e., in fact, in those studies the QHE in a situation where the energy spectrum was essentially the same as in the macroscopic situation was studied, and all effects analyzed in Refs. 1 and 2 were studied in a situation where the width of the wire was much greater than the electron wavelength. We have carried out for the first time a study of the quantum Hall effect in a one-mode quantum wire, where the situation is reversed in some sense, i.e. the wire width is such that in a zero magnetic field the wire is a conducting channel where the electrons fill only the ground quantum-well subband. At first glance, a QHE should be impossible in such a wire. However, since a single-mode wire has a finite width on the order of λ, it can be inferred that the QHE will still occur in magnetic fields such that the magnetic length $l_h < \lambda$. Our objective was to verify this conjecture experimentally and to study the possible features of the QHE in a one-mode quantum wire.

The experimental samples consisted of wires curved into a ring and equipped with potentiometric contacts, which consisted of the same kind of wires (see the inset in Fig. 1). They were fabricated on the basis of a two-dimensional electron gas with high mobility on a AlGaAs/GaAs heterojunction with a 60-nm-thick spacer. The electron density and mobility were 2×10^{11} cm^{-2} and 10^6 cm^2/(V·s), respectively. Next, a TiAu metal gate was deposited on the structure. It was used to change the width of the wire. The dissipative R_L (R_{1234} or R_{1256}) and Hall R_H (R_{1235} or R_{1246})

resistances of the samples described were measured. The measurements were performed at 40 mK temperature in magnetic fields up to 15 T. The measuring current was 0.1–1 nA in order to prevent effects due to heating. It should be noted that in the absence of a bias on the gate all experimental samples were closed, and a conducting channel appeared only when a positive bias was applied to the gate.

Figure 2 shows the results of measurements of the Aharonov–Bohm oscillations of one of the above-described structures with $V_g = 455$ mV and $T = 30$ mK. It is evident that the amplitude of these oscillations is not uniform in the magnetic field, but rather it is marked with beats. This is clearly seen in the inset in Fig. 2, which shows the same oscillations but without the constant component. The Fourier spectrum, shown in the same figure, also confirms the existence of beats. As was established in Refs. 3 and 4, the presence of beats of the Aharonov–Bohm oscillations is important evidence of uniformity of the wires used to fabricate the ring. The beats are due to the lifting of the clockwise–anticlockwise degeneracy in a finite-size ring by a magnetic field. Besides the indications of a single mode, the beats, more accurately their frequency, also make it possible to estimate the wire width, which is 40–60 nm in order of magnitude, i.e. the electron wavelength in the initial–dimensional gas. The Aharonov–Bohm oscillations described above therefore make it possible to talk more or less uniquely about a single-mode nature of the experimental wires, where the resistance of a wire at $B = 0$ exceeds 20 kΩ.

Figure 1 shows typical results of measurements of the Hall R_H and dissipative R_L resistances of wires in strong magnetic fields. The curves are presented for two values of the gate voltage $V_g = 630$ mV (a) and $V_g = 580$ mV (b). We consider first the curves in Fig. 1a, which correspond to a large, positive bias and actually larger wire width. In the first

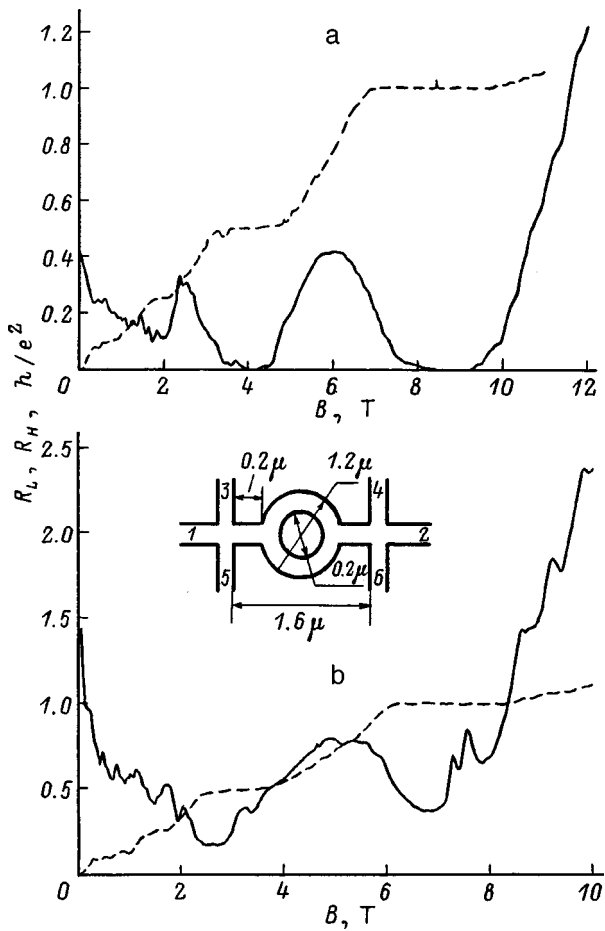FIG. 1. Dissipative (R_L, solid lines) and Hall (R_H, dashed lines) resistances with different gate voltages V_g, mV: a — 630, b — 580. Inset: Schematic diagram of the geometry of the experimental samples.

place, it is evident that the resistance R_L of a wire in a zero magnetic field is 11.2 kΩ, which would suggest that at least two one-dimensional subbands are filled. In this case, even in magnetic fields $B > 2$ T clearly defined quantum Hall resistance is observed for filling factors $i = 4, 2$, and 1 and the corresponding minima of R_L. The observation of a plateau with $i = 4$ confirms the assumption made above that a wire with $V_g = 630$ mV is not a single-mode system. As the magnetic field increases, the plateau width and correspondingly the width and depth of the minima in R_L increase, as is usually observed in macroscopic samples and wide wires. Resistance fluctuations which are of a mesoscopic nature and are characteristic of submicron-long wires are also observed. Let us now analyze the curves in Figs. 1b, corresponding to a lower value of the gate voltage and actually a smaller wire width. They are of special interest. The resistance of a wire in the absence of a magnetic field for this state of the sample is 37 kΩ, which attests to realization of a single-mode regime. As one can see, in a strong magnetic field clearly expressed Hall quantization plateaus are observed for filling factors $i = 2$ and $i = 1$. A more detailed comparison and analysis of the curves in Figs. 1a and 1b shows two unexpected effects: In the first place, even though the deep minima vanish, when $R_L^{\min}$ is several orders of magnitude less than $R_L^{\max}$ (in Fig. 1b the value of R_L at a minimum is greater than the value of R_L at a maximum by only a factor of 2 or 3), in the curves $R_H(B)$ the Hall–quantization plateaus for the same filling factors are essentially identical to the plateaus in Fig. 1a. In the second place, the position of the center of the plateau is no longer proportional to the filling factor: the center of the first plateau corresponding to $i = 2$ occurs at $B = 3.2$ T, and the center of the plateau corresponding to $i = 1$ occurs at $B = 7$ T. Therefore, the experi-
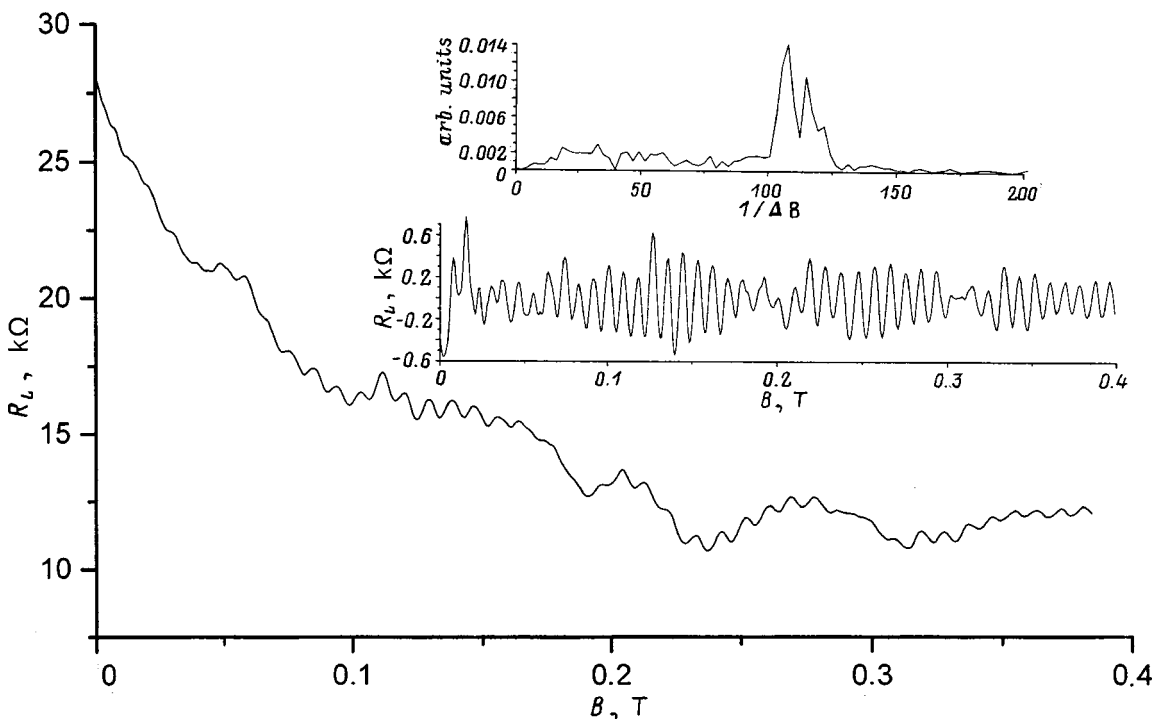

FIG. 2. Dissipative resistance $R_L(B)$ of a structure in weak magnetic fields. Inset: Same dependence without the constant component and its Fourier spectrum.

mental results presented above show that the Hall quantization in a one-mode wire of submicron length exhibits a number of features which do not fit into the standard picture of the QHE.

We shall now briefly discuss the possible reasons for this behavior. It is obvious that the QHE in a one-mode wire must be analyzed in terms of edge current states (ECSs), which describe well the QHE in bounded wires.[4,5] From the standpoint of the theory of ECSs the described anomalies in the behavior of the QHE in a one-mode wire can be explained as follows. When edge current states are introduced, it is always implicitly assumed that the wire width is such that states can be sharply divided into localized volume states and edge states that transport the current. This division results in a unique correspondence between the position of the Hall-quantization plateau and the filling factor, as is observed in experiments with wide wires.[1,2] It also suppresses backscattering between ECSs, which results in quantization of R_H and vanishing of R_L. Such a separation cannot be made in a single-mode wire. This is probably the reason for the peculiarities of the QHE in such a wire. Still, an exhaustive explanation of the results described in this paper requires further theoretical and experimental investigations.

*)E-mail: kvon@thermo.isp.nsc.ru

[1] H. Z. Zhang, K. K. Choi, D. C. Tsui, and G. Weimann, Phys. Rev. Lett. **55**, 1144 (1985).

[2] J. A. Simmons, S. W. Hwang, D. C. Tsui, H. P. Wei, L. W. Engel, and M. Shayegan, Phys. Rev. B **44**, 12 933 (1991).

[3] W.-C. Tan and J. C. Inkson, Phys. Rev. B **53**, 6947 (1996).

[4] A. A. Bykov, Z. D. Kvon, and E. B. Olshanetsky, in *Proceedings of the 22nd International Symposium on Compound Semiconductors* (Cheju Island, Korea, 1996) p. 909.

[5] M. Buttiker, *Semiconductors and Semimetals* (1992) v. 35, p. 191.

Translated by M. E. Alferieff

Molecular-beam epitaxy of a strongly lattice-mismatched heterosystem AlN/Si(111) for application in SAW devices

D. G. Kipshidze[*)]

A. F. Ioffe Physicotechnical Institute, Russian Academy of Sciences, 194021 St. Petersburg, Russia

H. P. Schenk, A. Fissel, U. Kaiser, J. Schulze, and Wo. Richter

Institut für Festkörperphysik, Friedrich-Schiller-Universität Jena, 07743 Jena, Germany

M. Weihnacht and R. Kunze

Institut für Festkörper- und Werkstofforschung Dresden, 01171 Dresden, Germany

J. Kräusslich

Institut für Optik und Quantenelektronik, Friedrich-Schiller-Universität Jena, 07743 Jena, Germany

The results of using molecular-beam epitaxy for growing piezoelectric AlN films on Si (111) substrates suitable for device applications are reported. The technological conditions for growth of stoichiometric AlN by controlling the surface reconstruction occurring under various thermodynamic conditions on the growth surface are determined. The films of the hexagonal polytype of AlN possess high crystalline perfection and an atomically smooth epitaxial surface. The mechanism for relaxation of the AlN crystal lattice over a distance of one monolayer from the heterojunction is found. It is demonstrated that the AlN film is piezoelectric. Investigations of the temporal characteristics of a SAW attest to a low level of scattering of the wave during propagation. The electromechanical coupling constant is measured in interdigital transducer geometry ($\lambda = 16$ mm) and is found to be 0.07 % at a frequency $f = 286$ MHz, in good agreement with the theoretical value for a 1.04-μm-thick AlN film. © *1999 American Institute of Physics.* [S1063-7826(99)01911-0]

1. INTRODUCTION

One of the promising applications of aluminum nitride involves the development of new SAW devices[1,2] and its use as a buffer layer for subsequent deposition of heterostructures based on the solid solutions AlN–GaN and InN–GaN. Its high SAW velocity,[3,4] excellent insulating properties, and chemical and thermal stability make AlN a promising material for transducers operating at frequencies above 1 GHz.[5–10] Today, quartz and LiNbO$_3$ are widely used for these applications, especially in radiotelecommunications technology. Most papers published thus far reported mainly the results of experimental studies of the acoustic properties of the system AlN/Al$_2$O$_3$, obtained by reactive sputtering,[5] vapor-phase epitaxy,[6] vapor-phase epitaxy from metalloorganic compounds (MOCVD),[7] and molecular-beam epitaxy (MBE).[8]

It is of interest to use silicon substrates for growing piezoelectric AlN layers. This is promising for integration of the technology of group III metal nitrides with the cheap and well-developed silicon technology. Only a few papers considered the application of the piezoelectric AlN layers grown on silicon substrates for SAW filter devices: the high growth temperature required in the MOCVD method ($\approx 1200\,°C$) makes this method less promising for use in the conventional technology of structures.[1] Positive results in this direction

have been obtained by reactive rf sputtering, where the AlN growth temperature was lowered to 500 °C.[9–11] Nonetheless, the decrease in the propagation velocity of SAW in AlN epitaxial layers is due mainly to the roughness of the surface and the defectiveness of the AlN layers.[1,5] Although the structures in the interdigital transducer geometry with a period of several microns can be obtained on AlN layers with a rough surface, layers with an atomically smooth surface make it possible to decrease the period of the transducer to 0.5 μm, which is an important achievement in applications of SAW devices.[5,7] In some cases, the surfaces of the AlN films must be polished in order to improve their piezoelectric properties.[1,4,6]

Thus, the use of AlN layers as a basis for SAW devices and as a buffer layer for subsequent deposition of the working optoelectronics components based on AlGaN and InGaN heterostructures imposes stringent requirements on the crystalline perfection of AlN layers, on the quality of their surface, and on their transport properties.

AlN has been less studied than GaN. Many problems attributable to the thermodynamic conditions of epitaxy, which are necessary for initiating and growing crystal-perfect AlN layers on strongly lattice-mismatched substrates, have not yet been resolved. Previous investigations of epitaxial growth of AlN by MBE, MOCVD, and reactive sput-

tering on Si substrates attest to a columnar structure of these layers.[12–17]

The relatively low epitaxy temperatures and growth rates, as well as the better controllability of the epitaxy process make the method of modified molecular-beam epitaxy with a plasma-activated nitrogen source very promising for growth of piezoelectric AlN layers. Recently published papers have reported the successful application of this method for growing AlN layers in a two-dimensional growth mode on GaN (Ref. 18) and Si(111) (Refs. 19–21). In addition, there exists some information on the surface reconstruction of AlN: (2×2) and (3×3) surface reconstructions of AlN epitaxial layers grown on Si(111) were noted in Refs. 20 and 22 and in Refs. 23 and 24, respectively. Surface reconstruction of the type $(\sqrt{3}\times\sqrt{3})R30°$ for MBE-grown AlN on SiC has been reported in Ref. 25. However, the physical picture of nucleation and epitaxy and the appearance of the above-indicated reconstructions as a function of the flux ratios of group-V and group-III elements were not considered in Refs. 18–24.

In this paper we will determine the thermodynamic conditions for initiation and epitaxial growth of AlN on Si(111) substrates. We will consider the structural properties and surface morphology of the grown AlN epitaxial layers, which allow us to use this heterosystem AlN/Si(111) as composite substrates for growing other nitride compounds and solid solutions based on them. We will describe the mechanism for relaxation of the crystal lattice of the strongly mismatched AlN/Si(111) system. We will also present the results of an investigation of the SAW characteristics for one of the epitaxial layers of aluminum nitride.

2. EXPERIMENTAL PROCEDURE

The AlN films were grown in a three-chamber molecular-beam epitaxy system. The growth chamber was equipped with a standard aluminum effusion cell and a turbomolecular pump with an effective evacuation rate of 1500 liters/s. The background pressure in the growth chamber was 10^{-10} mbar. An MPD21 (Oxford Applied Research) high-frequency (13.56 MHz) source of plasma-activated nitrogen was used to activate the nitrogen. At a working pressure of 10^{-5} mbar the flow of molecular nitrogen N_2 into the growth chamber was one standard cubic centimeter per minute (sccm); the purity of Al and N_2 was 6*N*. The growth mode, the structure of the layers, and the surface reconstructions were monitored by RHEED.

The AlN epitaxial layers were grown on *p*-type Si(111) substrates with resistivity exceeding 5 k$\Omega\cdot$cm. A modified Chirac method was used to prepare the substrates.[21] The substrates were heat-cleaned in a growth chamber at 920 °C. Removal of the passivating layer from the surface was accompanied by the appearance of (7×7)−type surface reconstruction of Si(111) at a temperature on the order of 780 °C; this reconstruction was replaced by (1×1)−type volume reconstruction with sharp Kikuchi lines at a temperature of the order of 830 °C. Lowering the substrate temperature restored the previous RHEED pattern.

The roughness of the surface of the epitaxial layers was measured with a TMX-2010 topometric atomic-force microscope. X-ray diffraction analysis and transmission electron microscopy (TEM) method were used to estimate the degree of crystalline perfection of the epitaxial layers. TEM and high-resolution TEM investigations were performed with JEM-1200 and JEM-4000 microscopes.

An aluminum structure with the configuration of a 100-nm-thick interdigital transducer with 20 pairs of fingers and an 8-μm period was deposited on one of the epitaxial AlN films to determine the piezoelectric parameters of AlN. The delay line was 2986 μm long.
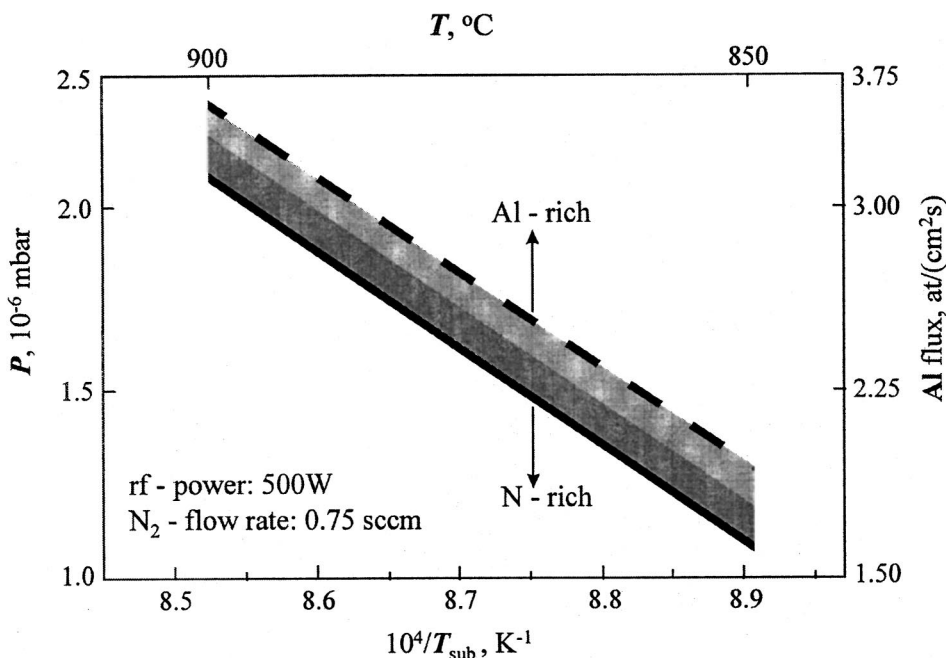

FIG. 1. Phase diagram of AlN surface reconstructions on a Si(111) substrate as a function of the Al flux given by the equivalent pressure P and versus the reciprocal of the substrate temperature T_{sub}. The solid line corresponds to $(\sqrt{3}\times\sqrt{3})R30°$ surface reconstruction, the dark-gray region corresponds to (1×1) reconstruction, and the light-gray region and the region above it correspond to (2×6) reconstruction. The layers grown under conditions corresponding to the dashed line possess triangular cracks.

3. EXPERIMENTAL RESULTS AND DISCUSSION

The development of the modern nitride MBE technology has led in the last few years to the publication of a large number of studies devoted primarily to the study of the surface reconstruction of GaN epitaxial layers using RHEED. The presence of surface reconstruction attests to an atomically smooth surface of the growing layer and can be a decisive factor for determining the stoichiometric balance between different modifications of activated nitrogen and group-III metal atoms under various thermodynamic conditions on the growth surface. To determine the stoichiometric growth conditions by controlling the surface reconstruction we heve therefore investigated the superstructures arising during epitaxial growth of AlN as a function of the Al flux pressure on the growth surface and as a function of the substrate temperature. The N_2 flux (0.75×10^{-5} mbar) and the plasma discharge power (500 W) were held constant in all experiments in a given series.

AlN film growth was initiated at substrate temperature 700 °C by depositing a 1/3 monolayer of Al on a (7×7) reconstructed Si(111) substrate surface. As a result of this process, the (7×7) surface reconstruction was replaced by $(\sqrt{3} \times \sqrt{3})R30°$ reconstruction. An extensive analysis of the (7×7) surface reconstruction on a Si(111) surface [Si(111)-(7×7)] and the effect of the deposition of the 1/3 monolayer of Al on the energetics of a Si(111)-(7×7) surface are described in Ref. 26. After the plasma-activated nitrogen source was switched on, nitriding of the 1/3 monolayer of Al was performed. AlN growth commenced immediately after the RHEED pattern changed from $(\sqrt{3} \times \sqrt{3})R30°$ to (1×1)−type reconstruction with linear reflections. Next, the substrate temperature was gradually raised to the final epitaxy temperature.

A different method for initiating AlN growth commenced with brief (2–3 s) nitriding of the Si(111)-(7×7) surface. As a result, the (7×7) surface reconstruction was replaced by (3×3) reconstruction. More prolonged nitriding of the surface resulted in vanishing of the superstructure and formation of a layer of polycrystalline silicon. For this reason, after nitriding of the Si(111)-(7×7) surface for 2–3 s, AlN film growth was started by opening the shutter of the Al effusion cell. However, the epitaxial processes initiated by this method were not accompanied by growth surface reconstructions, except for a (1×1) volume-type reconstruction. For this reason, this method for initiating growth was not used in the experiments designed to construct the phase diagram of AlN surface reconstructions, which we shall examine below.

Figure 1 shows a phase diagram where AlN surface reconstructions are followed as a function of the Al fluxes required to stabilize the reconstructions and as a function of the reciprocal of the substrate temperature T_{sub} with a constant atomic-nitrogen flux. Under the conditions of excess nitrogen we observed only the three-dimensional RHEED pattern of a wurtzite-type crystal lattice. Films grown under these conditions possess a compact structure in the form of columns.[14] The transition to two-dimensional growth was observed with a decrease of the excess nitrogen and was
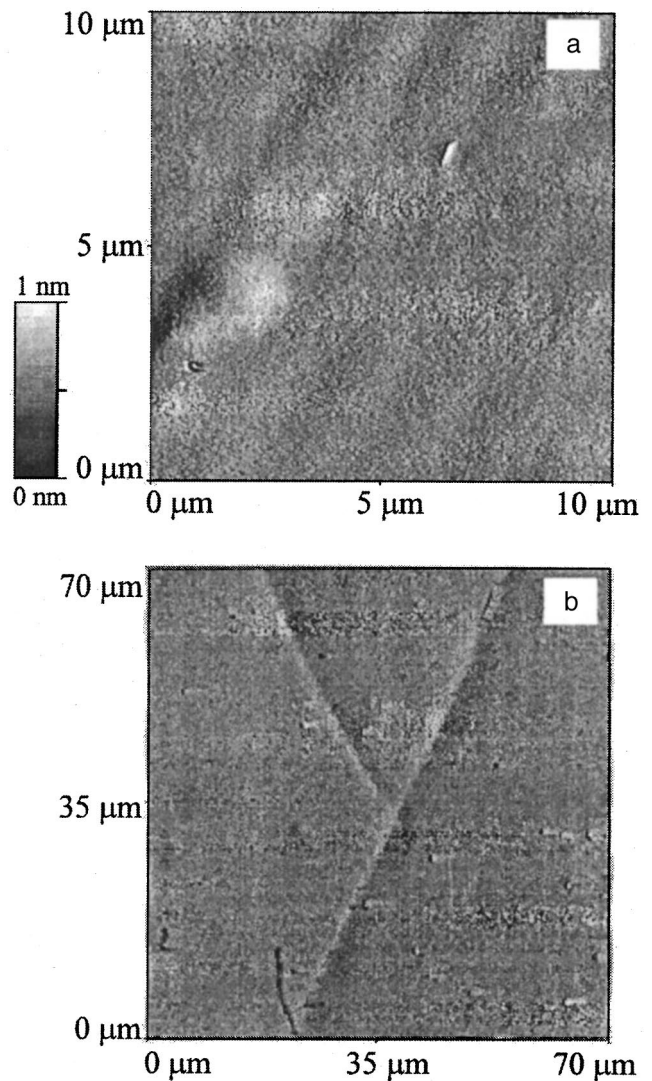

FIG. 2. Surface morphology of single-crystal AlN layers, as determined by atomic-force microscopy: a — topometric image of an atomically smooth epitaxial surface with roughness at the measurement level RMS ≈ 0.5 nm; b — differential image of an AlN film with triangular cracks with the film grown under excess-Al conditions (the roughness corresponds to a depth of 1 nm).

accompanied by the appearance of a $(\sqrt{3} \times \sqrt{3})R30°$ superstructure. In Fig. 1 the solid line corresponds to the technological conditions under which AlN growth occurs in the $(\sqrt{3} \times \sqrt{3})R30°$ surface reconstruction regime. As the Al flux was gradually increased, successive linear reflections corresponding to (1×1) and (2×6) surface reconstructions, designated in the diagram by dark- and light-gray regions, respectively, appeared. A further increase of the Al flux decreased the intensity of the RHEED pattern because of the formation of aluminum drops on the surface. The dashed line in the diagram corresponds to boundary conditions after which formation of aluminum drops on the surface of the epitaxial layer starts. The existence of transitional lines between different reconstruction regions can be explained by taking into consideration the evaporation of aluminum from the growth surface. In turn, this fact shows that under the

indicated thermodynamic conditions the aluminum attachment coefficient is different from 1.

This diagram enabled us to calculate the activation energy required for Al desorption, 1.3 eV. Nitrogen desorption was not observed in the temperature range investigated by us. We assume that the AlN growth rate under excess-Al conditions is limited by the amount of atomic nitrogen.

The layers grown in the temperature range from 850 to 900 °C under conditions corresponding to the region between the solid and dashed lines in Fig. 1 possess the best crystalline properties. These layers possessed an atomically smooth surface and roughness at the level of atomic-force microscopy measurements RMS $\approx 0.2-0.5$ nm (Fig. 2a). However, the layers grown under technological conditions corresponding in Fig. 1 to the dashed line possessed cracks in the directions $\langle \bar{2}110 \rangle$ and $\langle 0\bar{1}10 \rangle$ (Fig. 2b).

TEM investigations showed that the layers grown in the two-dimensional growth mode (under the conditions designated by the region between the solid and dashed lines in Fig. 1) possess a single-crystal structure free of oriented domains. The characteristic lattice defects of these layers are filamentary dislocations.[27] High-resolution TEM investigations of the AlN/Si(111) heterojunction show a sharp boundary between the epitaxial layer and the substrate (Fig. 3a). Relaxation of the crystal lattice of aluminum nitride on a characteristic distance of one monolayer from the heterojunction is observed here, even though there is a 23.4% mismatch between the lattice constants. The literature contains data on the correspondence between the unit cells of the AlN and Si lattices.[16,24] Under our experimental conditions, the results of the Fourier analysis of the high-resolution TEM photomicrographs served as proof that the crystal lattices of these materials match (Fig. 3b). The large 23.4% mismatch d_e/d_s-1 between lattice constants of the epitaxial layer d_e and substrate d_s decreases to $f=(nd_e-md_s)/md_s = -0.013$ (1.3%), taking into consideration the condition $m{:}n=4{:}5$. A similar matching of the crystal lattices of the epitaxial layer and substrate was observed in Ref. 28 for the
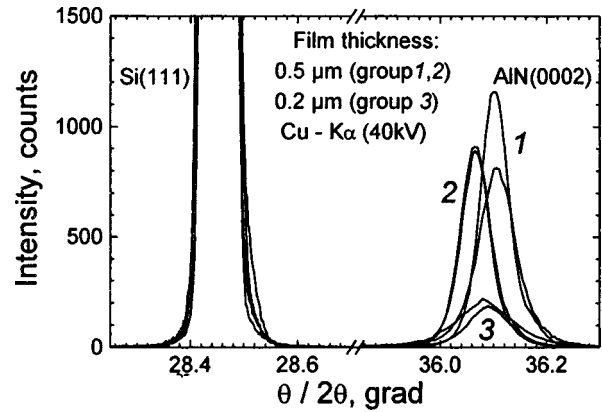

FIG. 4. X-Ray rocking curves for AlN layers grown on Si(111). The measurements were performed using a detector aperture with a 0.22-mm slit. The group-*1* AlN layers (curve *1*) were grown under excess-Al conditions. They possess a single-crystal structure and triangular cracks on the surface. The group-*2* AlN single-crystal layers (curves *2*) were grown in a regime close to a stoichiometric ratio of group-V and -III elements in the vapor phase. The group-*3* layers (curves *3*) possess a compact columnar structure and were grown under excess-nitrogen conditions.

heteroboundary of the system GaN(001)/GaAs(001). Based on the calculations presented here, we assume that the decrease in the strain energy of the epitaxial layer as a result of the 4:5 correspondence for the planes of the crystal lattice of Si($\bar{1}$10) and AlN($\bar{2}$110) is responsible for the two-dimensional growth mode of AlN on Si(111).

The results of the x-ray diffraction studies are shown in Fig. 4. The lattice parameters of the epitaxial layers with compact columnar structure (group *3*) and single-crystal layers with cracks (group *1*) are $c=4.977\pm0.001$ Å and $c=4.976\pm0.001$ Å, respectively. These crystalline parameters are close in value to those of the relaxed AlN layers, which is most likely a consequence of the columnar structure of these layers or the formation of cracks. The lattice parameters of AlN layers grown under two-dimensional growth conditions (group *2*), i.e., under technological conditions cor-
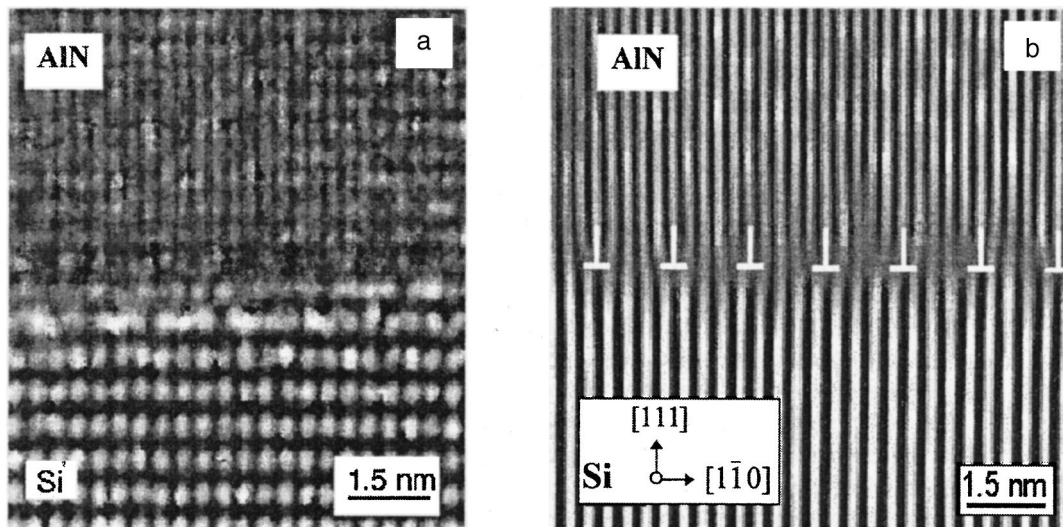

FIG. 3. AlN/Si(111) heterojunction: a — high-resolution TEM image in the Si[11$\bar{2}$] direction; b — Fourier analysis of high-resolution TEM photomicrographs demonstrating a 4:5 correspondence between the unit cells of AlN and Si in the AlN($\bar{2}$110) and Si($\bar{1}$10) directions.
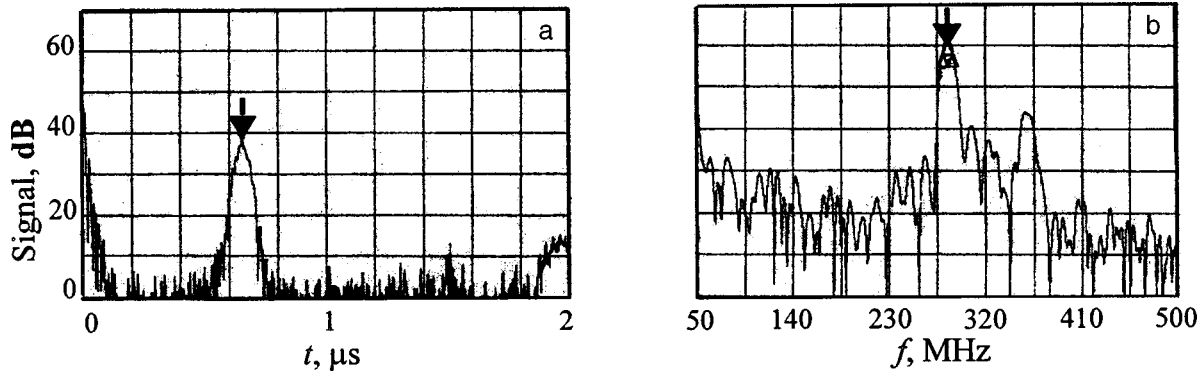
FIG. 5. Characteristics of the surface-acoustic wave of a transducer prepared on the basis of an AlN/Si(111) heterojunction. The wave propagates in AlN in the $(\bar{2}110)$ direction, corresponding to the $(\bar{1}10)$ direction in the Si substrate (see Fig. 3b): a — temporal (marker at $t = 653.5$ ns), b — frequency (marker at $f = 285.7$ MHz).

responding to the region between the solid and dashed lines in Fig. 1, are $c = 4.981 \pm 0.001$ Å . We infer that the compression of the unit cell of the crystal lattice along the a axis as a result of the 4:5 correspondence of the lattices (see Fig. 3b) is the reason for the expansion of the AlN unit cell along the c axis.

The group-*1* and group-*2* single-crystal layers exhibit the most intense reflection peaks of the x-ray rocking curves (Fig. 4). The characteristic widths of the x-ray rocking curves of group-2 AlN layers (415 nm thick) are 0.06° ($\omega/2\theta$ scanning) and 0.32° for ω scanning. These results, as compared with those published in the literature,[12,14,20] attest to a substantial improvement in the quality of the layers under the epitaxial growth conditions employed by us.

A single-crystal film with thickness $h = 1040$ nm, grown at temperature 900 °C, corresponding to the phase diagram (Fig. 1), under conditions stabilizing (1×1)−type surface reconstruction, was chosen to determine the piezoelectric properties of aluminum nitride. The propagation of a Rayleigh wave along the AlN surface was investigated. Measurements of the temporal and frequency characteristics (Figs. 5a and 5b) were performed, and the electromechanical coupling constant and SAW phase velocity were compared with the theoretically predicted values of these parameters (Figs. 6a and 6b). A definite interdigital transducer geometry with acoustic wavelength $\lambda = 16$ μm, equal to twice the period of the fingers, was used to study the piezoelectric characteristics. This value corresponds to an average frequency of 286 MHz (Fig. 5b) and SAW phase velocity 4569 m/s (Fig. 6a) in the $[\bar{2}110]$ direction in AlN. The value 0.07% obtained for the electromechanical coupling constant (Fig. 6b) is in good agreement with the theoretically predicted value, taking into consideration the elasticity constants $c_{11} = 345$, $c_{12} = 125$, $c_{13} = 120$, $c_{33} = 395$, and $c_{44} = 118$ GPa and the piezoelectric moduli $e_{31} = -0.58$, $e_{33} = 1.55$, and $e_{24} = -0.48$ C/m² (Refs. 1 and 2). This agreement attests to the very good piezoelectric properties of the AlN crystal (thickness $h = 1040$ nm), which are suitable for use in SAW devices. The maximum electromechanical coupling constant 0.19% corresponds to the ratio $h/\lambda = 0.2$ (Fig. 6b). For the same AlN layer thickness this corresponds to wavelength $\lambda = 5.2$ μm, phase velocity $v = 4630$ m/s, and frequency $f = 890$ MHz.

The large difference, approximately 40 dB (Fig. 5a), between the background and signal attests to weak SAW scattering. The relatively high level of the parasitic frequencies that is observed on the frequency characteristic (Fig. 5b) could be due to the nonuniformity of the film over the thickness, giving rise to distortions of the SAW wavefront along its propagation path, which is about 3 mm. The frequency characteristics of this film are not quite as good as those
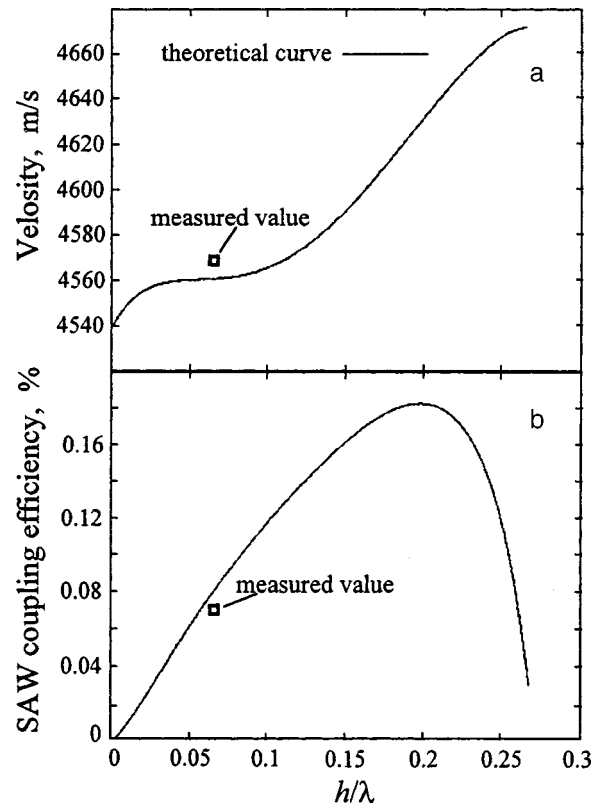

FIG. 6. Parameters of a surface-acoustic wave versus the ratio of the thickness h of the AlN layer to the wavelength λ in a transducer prepared on the basis of an AlN/Si(111) heterojunction. The wave propagates in AlN in the $(\bar{2}110)$ direction, corresponding to the $(\bar{1}10)$ direction in the Si substrate. a — Phase velocity, b — electromechanical coupling constant. Solid lines — computed curves; squares — measured values.

obtained recently[7,8] in the AlN/Al$_2$O$_3$ system, but they do show a large improvement of the piezoelectric properties of AlN obtained on Si(111).[10]

4. CONCLUSIONS

In summary, we have demonstrated that growth of layers of the hexagonal polytype of AlN can be initiated on a (7×7) reconstructed Si(111) surface by MBE using a source of plasma-activated nitrogen. The basic types of AlN surface reconstruction during growth were determined. In the excess-nitrogen regime, two-dimensional growth of AlN occurs under $(\sqrt{3} \times \sqrt{3})R30°$ surface reconstruction conditions, and in the excess-aluminum regime it occurs under (2×6) reconstruction conditions. AlN growth under (1×1) surface reconstruction conditions is stoichiometric, since excess-nitrogen conditions can result in three-dimensional growth, while excess-aluminum conditions can result in the formation of cracks or aluminum drops on the surface.

Investigations of the AlN/Si(111) heterojunction demonstrated a 4:5 correspondence between the unit cells of the AlN and Si lattices in the AlN($\bar{2}110$) and Si($\bar{1}10$) directions. The epitaxial layers possess an atomically smooth surface and a single-crystal structure free of oriented domains.

Propagation of a Rayleigh-type surface-acoustic wave (SAW) was successfully demonstrated in an AlN film grown on Si(111) in the two-dimensional growth mode. The epitaxial layer possesses very good piezoelectric properties which are suitable for device applications. This is indicated, in particular, by the results of the experimental study of the time-dependent characteristics of SAW, which show weak scattering during wave propagation.

*)E-mail: gela@nano.ioffe.rssi.ru

[1] K. Tsubouchi and N. Mikoshiba, IEEE Trans. Sonics Ultrason. **SU−32**, 634 (1985).

[2] K. Shimada, T. Sota, and K. Suzuki, J. Appl. Phys. **84**, 4951 (1998).

[3] G. D. O'Clock, Jr., and M. T. Duffy, Appl. Phys. Lett. **23**, 55 (1973).

[4] J. K. Liu, K. M. Lakin, and K. L. Wang, J. Appl. Phys. **46**, 3703 (1975).

[5] H. Okano, N. Tanaka, K. Shibata, and S. Nakano, Jpn. J. Appl. Phys. **32**, 4052 (1993); H. Okano, N. Tanaka, Y. Takahashi, T. Tanaka, K. Shibata, and S. Nakano, Appl. Phys. Lett. **64**, 166 (1994).

[6] K. Kaya, H. Takahashi, Y. Shibata, Y. Kanno, and T. Hirai, Jpn. J. Appl. Phys. **36**, 2837 (1997).

[7] T. Suetsugu, T. Yamazaki, S. Tomabechi, K. Wada, K. Masu, and K. Tsobouchi, Appl. Surf. Sci. **117/118**, 540 (1997).

[8] C. Deger, E. Born, H. Angerer, O. Ambacher, M. Stutzmann, J. Hornsteiner, E. Riha, and G. Fischerauer, Appl. Phys. Lett. **72**, 2400 (1998).

[9] F. S. Hickernell and H. M. Liaw, in *Proceedings of the 9th IEEE International Symposium on the Applications of Ferroelectrics* (1995), p. 543.

[10] Y.-J. Yong and J.-Y. Lee, J. Vac. Sci. Technol. A **15**, 390 (1997).

[11] L. G. Pearce, R. L. Gunshor, and R. F. Pierret, in *Proceedings of the 1981 IEEE Ultrasonics Symposium* (1981), p. 381.

[12] K. S. Stevens, M. Kinniburgh, A. F. Schwartzman, A. Ohtani, and R. Beresford, Appl. Phys. Lett. **66**, 3179 (1995).

[13] K. S. Stevens, M. Kinniburgh, and R. Beresford, Appl. Phys. Lett. **66**, 3518 (1995).

[14] S. Karmannr, H. P. D. Schenk, U. Kaiser, A. Fissel, and Wo. Richter, Mater. Sci. Eng., B **50**, 228 (1997).

[15] K. Dovidenko, S. Oktyabrsky, J. Narayan, and M. Razeghi, J. Appl. Phys. **79**, 2439 (1996).

[16] W. J. Meng, J. A. Sell, T. A. Perry, L. E. Rehn, and P. M. Baldo, J. Appl. Phys. **75**, 3446 (1994).

[17] I. Ivanov, L. Hultman, K. Järrendahl, P. Martensson, J.-E. Sundgren, B. Hjörvarsson, and J. E. Greene, J. Appl. Phys. **78**, 5721 (1995).

[18] B. Daudin and F. Widmann, J. Cryst. Growth **182**, 1 (1997).

[19] A. Osinsky, S. Gangopadhyay, J. W. Yang, R. Gaska, D. Kuksenkov, H. Temkin, I. K. Shmagin, Y. C. Chang, J. F. Muth, and R. M. Kolbas, Appl. Phys. Lett. **72**, 551 (1998).

[20] M. A. Sánchez-García, E. Calleja, E. Monroy, F. J. Sánchez, F. Calle, E. Muñóz, and R. Beresford, J. Cryst. Growth **183**, 23 (1998).

[21] H. P. D. Schenk, U. Kaiser, G. D. Kipshidze, A. Fissel, J. Kräusslich, H. Hobert, J. Schulze, and Wo. Richter, Mater. Sci. Eng., B **59**, 84 (1999).

[22] M. A. L. Johnson, S. Fujita, W. H. Rowland, Jr., K. A. Bowers, W. C. Hughes, Y. W. He, N. A. El-Masry, J. W. Cook, Jr, J. F. Schetzina, J. Ren, and J. A. Edmond, J. Vac. Sci. Technol. B **14**, 2349 (1996).

[23] U. Rössner, Thesis, CEA, Grenoble, 1995.

[24] A. Bourret, A. Barski, J. L. Rouvière, G. Renaud, and A. Barbier, J. Appl. Phys. **83**, 2003 (1998).

[25] K. Järrendahl, S. A. Smith, T. Zheleva, R. S. Kern, and R. F. Davis, Mater. Sci. Forum **264−268**, 1181 (1998).

[26] W. Mönch, *Semiconductor Surfaces and Interfaces* (Springer, Berlin, 1993), p. 257.

[27] U. Kaiser, P. D. Brown, I. Khodos, C. J. Humphreys, H. P. D. Schenk, and Wo. Richter, J. Mater. Res. (in press).

[28] A. Trampert, O. Brandt, H. Yang, and K. H. Ploog, Appl. Phys. Lett. **70**, 583 (1997).

Translated by M. E. Alferieff

AMORPHOUS, GLASSY, AND POROUS SEMICONDUCTORS

Reversible and irreversible changes in the photoluminescence spectra of porous silicon held in water

B. R. Dzhumaev

Institute of Semiconductor Physics, Ukrainian National Academy of Sciences, 252650 Kiev, Ukraine
(Submitted March 9, 1999; accepted for publication April 13, 1999)
Fiz. Tekh. Poluprovodn. **33**, 1379–1383 (November 1999)

The change induced in the photoluminescence spectra and photoluminescence excitation spectra by holding porous silicon in water is investigated. It is found that submerging a sample in water gives rise simultaneously to reversible and irreversible changes in the intensity and position of the photoluminescence maximum. It is shown that the irreversible changes are due to the same processes that occur in air: oxidation and desorption of substances which participate in the photoluminescence and which give rise to the visible-range band of the excitation spectrum, from the surface of the porous layer. It is established that the rate of these processes in water is much higher than in air. It is shown that the reversible changes are due to the vanishing of the visible-range photoluminescence excitation band in water. It is inferred that this band is attributable to water clusters that contain components of the etchant. © *1999 American Institute of Physics.* [S1063-7826(99)02011-6]

Despite many investigations, the mechanism for the luminescence of porous silicon (*P*-Si) remains unresolved. It is obvious that the surface can play a large role in the photoluminescence (PL) process because its area is large and it contains a variety of substances (components of the etchant, reaction products). At the same time, determining the role of the surface is a rather difficult problem. To obtain such information, aging of *P*-Si in air[1–5] and in vacuum[5–7] and the changes occurring when samples are held in the etchant after anodization stops[8] were investigated. Since it was suggested in some papers that water plays a large role in PL,[6] we investigated the effect of holding porous silicon samples in water on the photoluminescence spectrum and the photoluminescence excitation spectrum (PES).

1. RESULTS AND DISCUSSION

The test samples were obtained by anodic etching of *p*-type Si wafers (resistivity $\rho = 5 - 10 \ \Omega \cdot$ cm) with (100) or (111) orientation in an alcohol solution of HF (HF:H_2O:C_2H_5OH=1:1:2) with current density $I_{etch} = 20$ mA/cm^2 and etch time $\tau = 2, 15,$ and 30 min. The PL was excited by light from a xenon lamp. The light was passed through an NDR-23 monochromator and detected with an IKS-12 monochromator.

Figure 1 shows the PES $W(\lambda_{exc})$ of three as-grown samples obtained with the same current density 20 mA/cm^2 and different etch times $\tau = 2, 15,$ and 30 min. In what follows, for simplicity, the samples obtained with $\tau = 2, 15,$ and 30 min are denoted as samples 1, 2, and 3, respectively. As one can see from the figure, the PES are nonelementary and consist of two bands — a wide visible band in the range $\lambda_{exc} = 310 - 500$ nm (band I) and an ultraviolet band in the

range $\lambda_{exc} = 250 - 310$ (band II). We note that band II was observed in all experimental samples and the position of its maximum was the same for different samples. At the same time, the position of the maximum of band I shifted in the long-wavelength direction with increasing etch time. Moreover, in some samples it was absent completely (Fig. 1, curve *1*).

The PL spectra $W(\lambda_{PL})$ of the as-grown sample 2, which were measured using excitation by light with different wavelengths (λ_{exc}), are presented in Fig. 2a. As one can see from the figure, the wavelength λ_{PL}^{max} of the maximum of the PL band depends on the excitation wavelength. As λ_{exc} shifts in the short-wavelength direction, the maximum of the PL band also shifts in the same direction (from 660 to 600 nm), attesting to the nonelementary nature of the PL band.
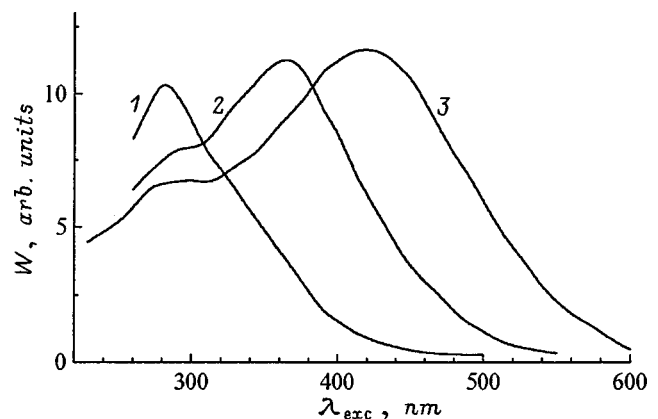

FIG. 1. Luminescence excitation spectra of three as-grown *P*-Si samples obtained with current density $I_{etch} = 20$ mA/cm^2 and etch times 2 (*1*), 20 (*2*), and 30 min (*3*).
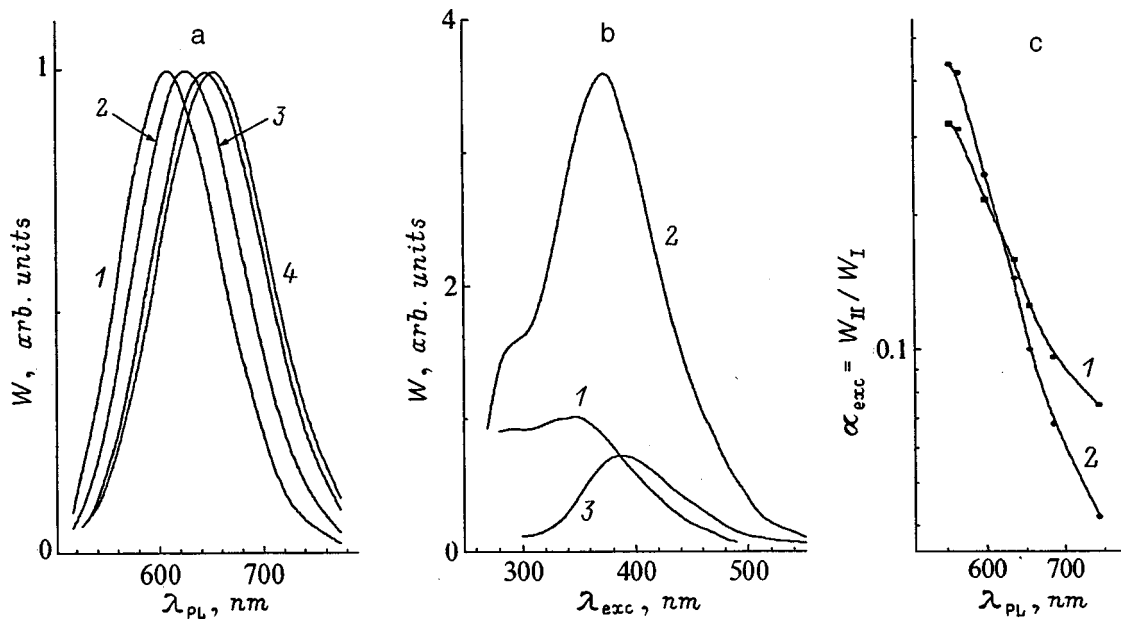
FIG. 2. a — PL spectra of *P*-Si sample 2 with excitation wavelengths λ_{exc} = 300 (*1*), 350 (*2*), 400 (*3*), and 450 nm (*4*). b — Luminescence excitation spectra measured for different wavelengths of the PL band λ_{PL} = 555 (*1*), 636 (*2*), and 744 nm (*3*). c — Ratio of intensities for different wavelengths of the luminescence excitation spectrum $\alpha_{exc} = W_{300}/W_{360}$ (*1*) and $\alpha_{exc} = W_{300}/W_{420}$ (*2*) versus λ_{PL}.

Figure 2b shows the PES of sample 2 in different sections of the PL band (different values of λ_{PL}): on the short-wavelength edge (λ_{PL} = 555 nm), at the maximum of PL (λ_{PL}^{max} = 636 nm), and on the short-wavelength edge (λ_{PL} = 744 nm). As one can see from Fig. 2c, the intensity ratio $\alpha_{exc} = W_{II}/W_{I}$ of band II (300 nm) and band I (360 and 420 nm) (W_{300}/W_{360} and W_{300}/W_{420}) depends on the PL wavelength λ_{PL}, for which the PES is measured, and it decreases with increasing λ_{PL}. This means that the long-wavelength part of the PL band is excited predominantly in the PES I band, and the short wavelength part is excited in band II. The continuous shift of the PL maximum with excitation wave-

length could be due to the simultaneous overlapping of the PL and PES bands.

It is significant that in samples 1 and 3 no dependence of the position λ_{PL}^{max} of the maximum of the PL band on the excitation wavelength λ_{exc} was observed, while the position λ_{PL}^{max} of the PL maxima accompanying excitation in these bands was different. This attests to the elementary nature of the PES bands with λ_{exc} = 290 − 300 and 420 − 430 nm and to the absence of strong overlapping of the bands.

It should be noted that band I can also have a compli-cated structure, and that a dependence of the ratio of the intensities of the subbands on λ_{PL} can also be observed in it.
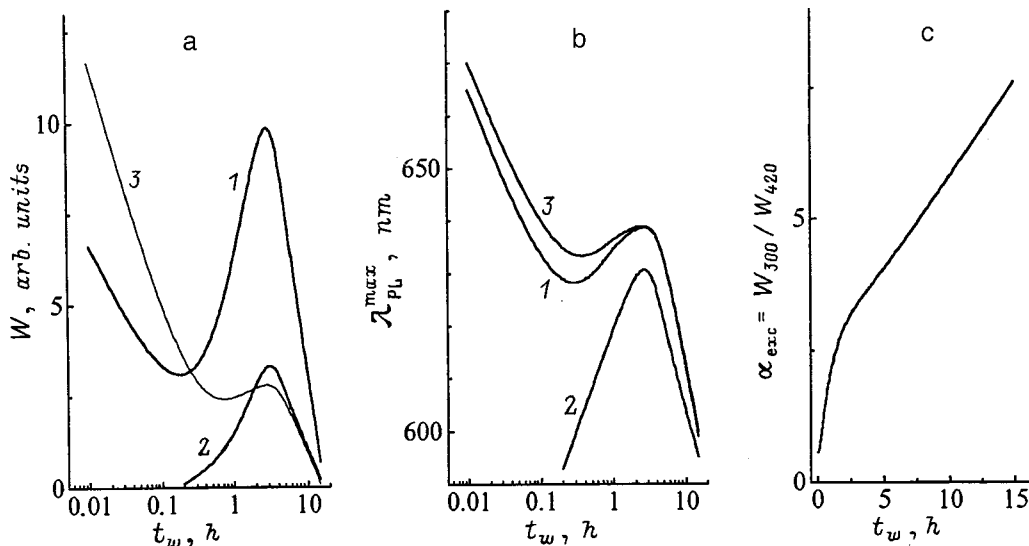

FIG. 3. Photoluminescence intensity W (a), wavelength of PL maximum λ_{PL}^{max} (b) with excitation by light with wavelength λ_{exc} = 300 (*1, 2*) and 420 nm (*3*), measured in air (*1, 3*) and in water (*2*), and $\alpha_{exc} = W_{300}/W_{420}$ (c) versus the aging time t_w of *P*-Si sample 3 in water.

This circumstance and the fact that its position is different in different samples indicate that band I could be nonelementary.

The results presented above thus suggest that in *P*-Si there exist at least two PL excitation channels and that each channel has its own PL band.

To trace the behavior of the components of the PL, which are excited in bands I and II, we present below the PL intensities of two wavelengths excited by light, which correspond to these bands ($\lambda_{exc} = 300$ and 420 nm).

The *P*-Si samples were aged in water at room temperature. The PL was measured in air (the sample was removed from the water during the measurement) and directly in water. The luminescence excitation spectra were measured only in air.

When the samples were submerged in water, the PL intensity measure directly in the water decreased and its maximum shifted in the short-wavelength direction (for example, from 665–670 to 590–600 nm for sample 3). After the samples were removed from the water, as they dried in air the PL intensity increased and its maximum shifted in the long-wavelength direction. However, the intensity and λ_{PL}^{max} did not return to their initial values (Fig. 3). After holding in water, the PES also changed: Besides an overall decrease in intensity, the ratio $\alpha_{exc} = W_{300}/W_{420}$ (Fig. 3c) increased, which is confirmed by curve *5* in Fig. 4a, which is the difference between curves *1* and *2*.

After repeated submersion of *P*-Si in water, λ_{PL}^{max} is again shifted in the short-wavelength direction and the PL intensity decreases. As the samples dried, the wavelength of the maximum and the intensity of PL were partially restored.

In summary, the change in the PL intensity and λ_{PL}^{max} occurring when the *P*-Si sample is submerged in water is due to the superposition of two effects: reversible and irreversible. The irreversible changes can be detected by measuring the PL and PES in air before and after submersion in water. We note that a reversible decrease in the PL intensity accompanying submersion in water was observed in all samples, irrespective of the form of the PES spectrum. At the same time, a reversible shift in the maximum occurred only in samples which possessed a PES I maximum, in addition to a PES II maximum. In the absence of the PES I band (sample 1) no shift was observed.

Irreversible effect. The magnitude and character of the irreversible changes depend on the submersion time t_w of the *P*-Si sample in water. As one can see from Fig. 3a (curve *1*, sample 3), when the PL is excited by light with $\lambda_{exc} = 300$ nm (PES band II), as t_w increases, the intensity of the PL initially decreases and then increases appreciably, and again decreases (measurement in air). In the process λ_{PL}^{max} in the section of decreasing PL intensity shifts in the short-wavelength direction, and in the increasing sections it shifts in the long-wavelength direction (Fig. 3b, curve *1*). When the PL is excited by light from the PES band I, the behavior of the curve $W(t_w)$ is similar to its behavior in the case $\lambda_{exc} = 300$ nm, but the dominant effect is a decrease in the PL intensity (Fig. 3a, curve *3*). The shift of λ_{PL}^{max} with $\lambda_{exc} = 420$ nm is also similar to the shift of λ_{PL}^{max} for $\lambda_{exc} = 300$ nm (Fig. 3b, curve *3*). It is significant that the PL decreases

predominantly in the PES I band and increases in the PES II band, which is manifested as a change in α_{exc} (Fig. 3c).

Comparing the results of aging of the samples of porous silicon in water and in air[5] shows that the same processes occur in water as in air (oxidation and removal of certain substances from the surface of the Si filaments), but the rate of these processes in water is much higher. The decrease in the PL intensity, the shift of λ_{PL}^{max} in the short-wavelength direction, and the decrease in the intensity of the PES I band are associated with removal of the substances participating in PL, and the increase in the PL intensity, the shift of λ_{PL}^{max} in the long-wavelength direction, and the increase in the intensity of the PES II band are associated with oxidation. The presence of a section of increasing PL intensity for excitation by light from the PES I band (Fig. 3, curve *3*) can be explained by overlapping of the PES I and II bands. The subsequent rapid decrease in the PL intensity can be explained
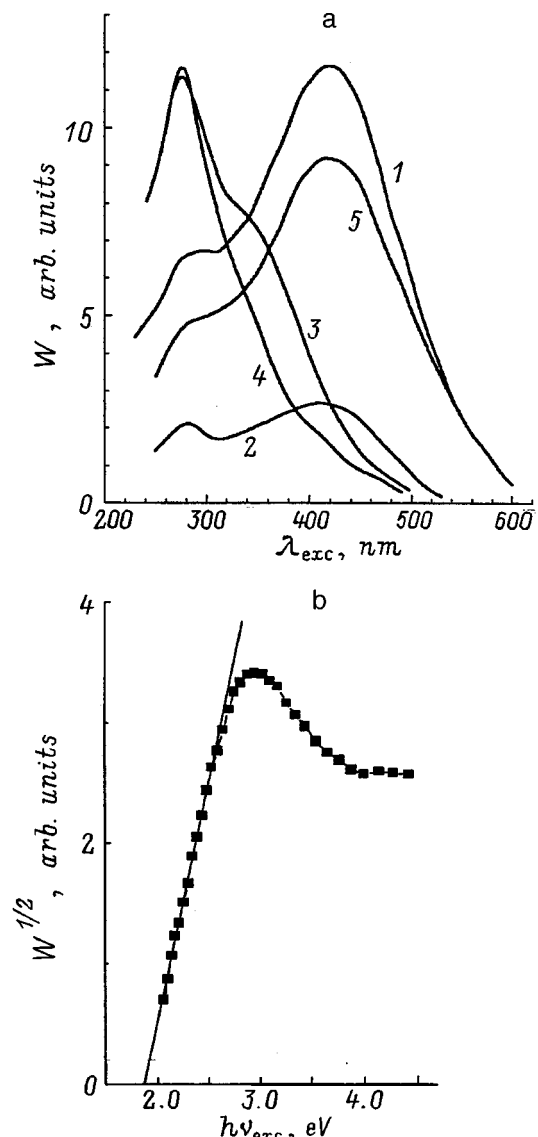

FIG. 4. a — Luminescence excitation spectra measured at different aging times of *P*-Si sample 3 in water: *1* — initial, *2* — $t_w = 10$ min, *3* — $t_w = 3$ h, *4* — $t_w = 15$ h; *5* — difference between curves *1* and *2*; *4* — the intensity scale is magnified by a factor of 10. b — Luminescence excitation spectrum in the coordinates $W^{1/2}–h\nu_{exc}$.

by complete oxidation of the porous silicon layer, which is observed, for example, for oxidation in oxygen.[9] We note that complete oxidation does not occur when the samples are stored in air at room temperature for 1 or 2 years. This is attributable to the lower rate of this process. The removal of the substances responsible for the PES I band from the surface of the Si filaments occurs because these substances dissolve in water and are then removed by diffusion, in agreement with the assumption made above that they include components of the etchant or reaction products.

The PES I band could be due to light absorption in water clusters that contain impurities (which could be etchant components or reaction products). This assumption agrees with the study of the influence of the evacuation and introduction of water vapor on the PL intensity.[6] In addition, it is known that clusters of water molecules containing impurities (Li, Na, K, H, CH_3, and others) give PL in the range 350–500 nm,[10] which corresponds to the spectral position of the PES I band. It can therefore be inferred that this band is due to the clusters that contain, for example, H, CH_3, or F present in the etchant.

This is indicated by an analysis of the shape of the long-wavelength edge of the PES, which makes it possible to estimate the spectral behavior of the optical absorption $\alpha(h\nu)$, assuming that the magnitude of the PES signal is proportional to absorption in the limit of an optically thin sample provided that the quantum efficiency does not depend on the energy of the incident photons. It was found that the low-energy edge of the PES I band can be described by the function $(\alpha)^{1/2} \sim (h\nu - E_e)$, where E_e is in the range 1.8–2.2 eV (Fig. 4b). This dependence is characteristic of indirect transitions and agrees with the assumption that the absorbing object is a cluster.

Reversible effect. One could infer that the reversible changes occurring in the PL when the *P*-Si samples are submerged in water are due to the characteristic features of light transmission in water (absorption and refraction). This can explain the change in the PL intensity. In this case, however, the reversible shift of λ_{PL}^{max} in the short wavelength direction, observed only if band I is present in the PES spectrum, remains incomprehensible.

In summary, the shift of λ_{PL}^{max} is due to the presence of the PES I band and occurs in the same direction as for desorption of the adsorbents with which it is associated.[5] We assume, therefore, that this displacement is attributable to the weakening of the contribution of band I in PES when the samples are submerged in water. In the irreversible effect,

such weakening seems to be due to the removal of impurities that appear in the clusters from the surface of the porous layer (filaments) as a result of diffusion. If there has not been enough time for such diffusion to occur, the PES I band is restored by drying, making it possible to explain the partial reversibility of the effect.

On this basis, the vanishing of excitation in the band PES I in the reversible effect can be attributed to the appearance of a continuous layer of water on the surface of the porous layer (filaments). The idea that the PES I band is due to light absorption by water clusters containing etchant components as impurities makes it possible, therefore, to explain both the irreversible and reversible effects and the fact that in the latter case the intensity of PES I decreases and λ_{PL}^{max} shifts more strongly than in the irreversible effect. The decrease in the intensity of the band PES I in the irreverisble effect should be determined by the rate of removal of impurities, and in our samples it occurs in ten minutes, while the formation of a continuous layer of water results in vanishing of the clusters immediately after submersion in water.

In conclusion, we note that measurements of the intensity and position of the PL in water with excitation by light with $\lambda_{exc} = 300$ nm (Fig. 3, curve *2*) reflect the character of the irreversible changes. The absence of the first aging section signifies that this section in air is due to overlapping of the excitation bands I and II.

[1] Y. M. Weng, Zh. N. Fan, and X. F. Zong, Appl. Phys. Lett. **63**, 168 (1993).

[2] R. T. Collins, M. A. Tischler, and J. H. Stathis, Appl. Phys. Lett. **61**, 1649 (1992).

[3] M. A. Tischler, R. T. Collins, J. H. Stathis, and J. C. Tsang, Appl. Phys. Lett. **60**, 639 (1992).

[4] M. S. Brandt, H. D. Fuchs, M. Stuzmann, J. Weber, and M. Cardona, Solid State Commun. **81**, 307 (1992).

[5] N. E. Korsunskaya, T. V. Torchinskaya, B. R. Dzhumaev, L. Yu. Khomenkova, and B. M. Bulakh, Fiz. Tekh. Poluprovodn. **31**(8), 908 (1997) [Semiconductors **31**, 773 (1997)].

[6] M. S. Brodin, V. N. Bykov, D. B. Dan'ko, A. A. Kipen', G. A. Naumovets, R. D. Fedorovich, and N. I. Yanushevskiĭ, Ukr. Fiz. Zh. **40**(9), 933 (1995).

[7] N. E. Korsunskaya, T. V. Torchinskaya, B. R. Dzhumaev, B. M. Bulakh, O. D. Smiyan, A. L. Kapitanchuk, and S. O. Antonov, Fiz. Tekh. Poluprovodn. **30**(8), 1507 (1996) [Semiconductors **30**, 792 (1996)].

[8] S. Letant and J. C. Vial, J. Appl. Phys. **80**, 7018 (1996).

[9] A. Bsiesy, J. C. Vial, F. Gaspard, R. Herino, M. Legion, F. Muller, R. Romestain, A. Wasiela, A. Halimaoui, and G. Bomchil, Surf. Sci. **254**, 195 (1991).

[10] D. N. Sitharamarao and J. F. Duncan, J. Phys. Chem. **67**, 2126 (1963).

Conductivity and absorption edge of amorphous silicyne

A. I. Mashin*) and A. F. Khokhlov

N. I. Lobachevskiĭ Nizhegorod State University, 603600 Nizhniĭ Novgorod, Russia
(Submitted April 5, 1999; accepted for publication April 28, 1999)
Fiz. Tekh. Poluprovodn. **33**, 1384–1387 (November 1999)

Experimental results on the temperature dependence of the conductivity and the spectrum of the absorption coefficient of amorphous silicyne — the linear allotropic form of silicon — are reported. Silicyne is found to be a semiconductor with a ~1.6-eV band gap. Near room temperature conduction occurs by a hopping mechanism, and the room-temperature conductivity is $\sim 10^{-8}\,\Omega^{-1}\cdot\text{cm}^{-1}$. The influence of the columnar structure of the initial film on silicyne formation during annealing of *a*-Si:H is studied. © *1999 American Institute of Physics.* [S1063-7826(99)02111-0]

1. INTRODUCTION

Until recently it was thought that, in contrast to carbon, which exhibits five allotropic forms (diamond, graphite, carbon, lansdalite, and fullerene), silicon in its elementary form cannot form compounds where the silicon atoms have sp^2 and (or) sp hybridization. The new modification of silicon, which we discovered and whose existence was proved by electron diffraction and x-ray spectroscopy methods,[1,2] is called silicyne by analogy with carbyne — the third allotropic modification of carbon, which consists of rectilinear carbon chains. We obtained silicyne samples in the form of thin films (from 100 to 500 nm). Silicyne consists of rectilinear chains in which each silicon atom is bound with two neighboring atoms by sp hybrid bonds. A few atoms are in the sp^2 hybrid state and possess three nearest neighbors. Because of this circumstance, the linear chains of atoms have kinks approximately every 5–10 atoms. The silicon atoms on these kinks possess one extra bond, which they can use to form a three-dimensional network. Moreover, intermolecular van der Waals forces can participate in the formation of the bulk material.

In the present paper we report the results of experimental studies of certain properties of the new material.

2. SAMPLE PREPARATION

Thin films of silicyne were obtained after vacuum annealing (at 500 °C) of hydrogenated amorphous silicon *a*-Si:H films. The anneal time was 30 min. The initial ~400-nm-thick *a*-Si:H was deposited during decomposition of silane in an rf glow discharge on a crystalline silicon, fused quartz, and polychore substrates. The substrate temperature during deposition was 250 °C.

As noted in Ref. 1, the films remain amorphous after annealing at 500 °C. Silicyne does not form in all cases. In particular, the initial films of amorphous silicon must be free of foreign impurities.[3] The oxygen concentration, for example, should not exceed 0.2 at.%. The possibility for the existence of a linear allotropic form of silicon and the effect of foreign impurities on silicyne formation agree well with our previous quantum-mechanical calculations.

3. RESULTS AND DISCUSSION

We studied the surface morphology of amorphous silicon and silicyne films (Fig. 1) by scanning probe microscopy on a TMX-2100 ''Accurex'' atomic-force microscope in the contact mode using standard procedures. As one can see from Figs. 1a and 1b, the silicyne films which we obtained and the *a*-Si:H films which were used to prepare the silicyne are structurally nonuniform. The surface contour of the *a*-Si:H films, in which no silicyne was observed after annealing, is identical to that of the substrate (Fig. 1c). The structural nonuniformity of the initial *a*-Si:H film has been observed previously in certain deposition regimes. The surface morphology which we observed can be explained, on the basis of Ref. 4, by the columnar structure of the amorphous silicon film. Under standard conditions for preparing *a*-Si:H, the columns are oriented perpendicular to the substrate surface, which results in a loose, cauliflower-like surface on the film. The sizes of the columns, in which the material also remains amorphous, depend on many technological parameters governing the fabrication of the *a*-Si:H film, the thickness of the film, and the structure of the substrate surface and can vary from hundreds of angstroms to several microns. According to Ref. 4, in addition to the columns mentioned above, *a*-Si:H films can contain microscopic columns ~10 Å in diameter, making an angle with respect to the surface. These columns consist of a material which is highly enriched with hydrogen. As a result, the hydrogen becomes bound predominantly in disclinations of amorphous silicon.

Since *a*-Si:H films without a columnar structure generally are used to fabricate solar cells, the deposition regimes were found and various methods for suppressing the formation of a columnar structure of the films during growth were developed. This is probably the explanation for why the properties and structure of amorphous hydrogenated silicon films with structural nonuniformities have been studied so little. However, in our case the presence of a columnar structure and other linear defects in *a*-Si:H films plays a positive role. With annealing at 500 °C, the structural rearrangements in such a material occur in the presence of a high concentration of dangling bonds because of the intense evaporation of
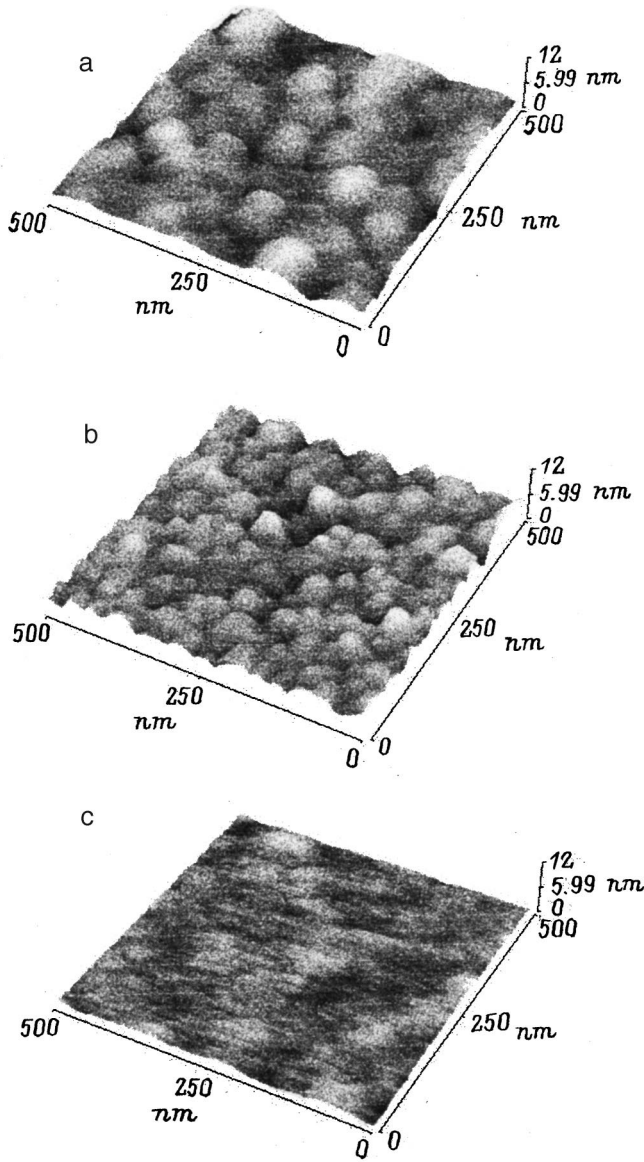
FIG. 1. Surface morphology of silicyne (a) and *a*-Si:H (b, c) films. b — Initial *a*-Si:H film used to produce silicyne. c — *a*-Si:H film whose annealing at 500 °C does not lead to the formation of silicyne.

FIG. 2. Temperature dependences of the conductivity of *a*-Si:H films with columnar structure (*1*), isotropic structure before (*3*) and after (*4*) annealing at 500 °C and of silicyne (*2*).

hydrogen and orienting action of the column walls, which stimulate the formation of linear chains of silicon atoms. Thus, the presence of linear defects in the initial *a*-Si:H film, in our view, promotes the formation of silicyne during annealing. The effect of the columnar structure on silicyne formation increases as the diameter of the columns decreases.

Figure 2 shows the temperature dependences of the conductivity of the experimental films. It is evident that the conductivity of the initial amorphous-silicon films is of an activational character in the entire experimental temperature range and can be described by the expression

$$\sigma = \sigma_0 \exp(-\Delta E/kT), \tag{1}$$

where $\Delta E = E_c - E_f$ is the activation energy, and E_c and E_f are the energies corresponding to the conduction-band bottom and the position of the Fermi level. Conduction is realized by carriers excited from the Fermi level into delocalized
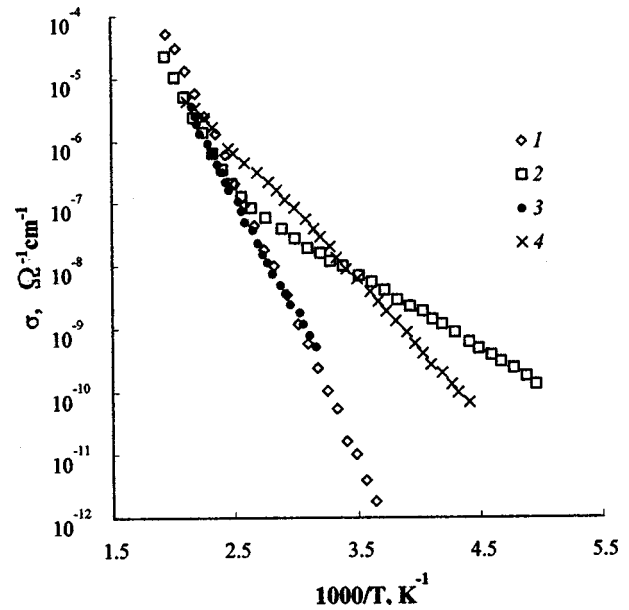
states located above the conduction-band bottom. The activation energy is essentially independent of the conditions under which the films are prepared: ~0.88 eV for *a*-Si:H films with columnar structure and ~0.84 eV for films with isotropic structure.

After annealing at 500 °C, the temperature dependence of the conductivity of isotropic samples in our entire experimental temperature range satisfies the law (1) with activation energy ~0.45 eV. At the same time, two sections with a different conduction mechanism are observed in the temperature dependence of the conductivity of silicyne in the experimental range. At high temperatures (>420 K) the conductivity is of a band character. The activation energy is ~0.8 eV. If the Fermi level is assumed to lie close to the center of the band gap of the amorphous semiconductor, then the band gap of silicyne is $\Delta E_g \approx 1.6$ eV. Near room temperature conduction is realized by charge-carrier hopping along localized states in the band tails. The temperature dependence of the conductivity in this temperature range can also be described by a law of the form (1), but the corresponding activation energy is $\Delta E = (E - E_f + W) \approx 0.25$ eV, where E is the energy near which hops of the charge carriers occur, and $W \approx 0.01$ eV is the hopping energy. Thus, when amorphous silicyne is formed from *a*-Si:H, defects whose energy lies 0.2–0.25 eV above the Fermi energy are produced.

The band gap obtained from the conductivity data agrees well with the results of optical experiments. As follows from Fig. 3, the absorption spectrum for most of the tested amorphous films in the experimental photon-energy range can be described by a power law of the form

$$\alpha \propto (\hbar\omega - E_g)^r, \tag{2}$$

where $E_g = E_c - E_v$, $\hbar\omega$ is the photon energy, and the exponent r depends on the conditions under which the amorphous film is fabricated. The Tauc law[5]
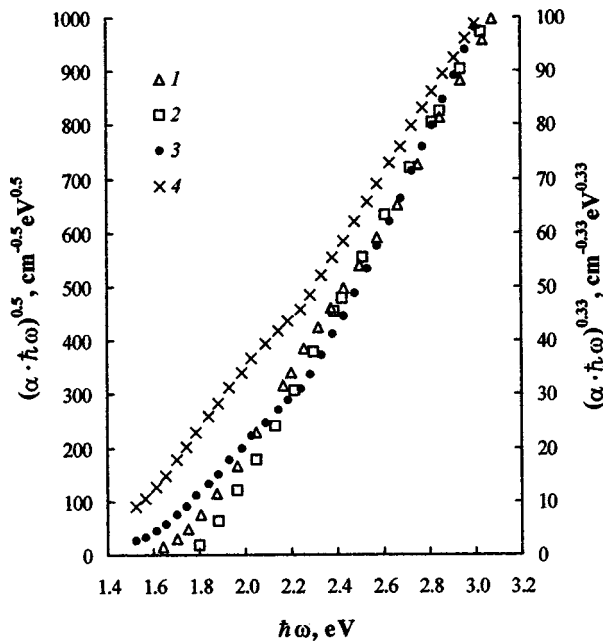
FIG. 3. Spectra of the absorption edge of a-Si:H before (1) and after (2) annealing at 350 °C in Tauc coordinates and of silicyne in Tauc (3) and Klazes (4) coordinates.

$$\sqrt{\alpha \hbar \omega} \propto (\hbar \omega - E_g) \qquad (3)$$

is ordinarily used to determine the band gap. This law holds well if the density of states in the delocalized states can be described by a simple parabolic law. It should be noted, however, that the linearity range of the absorption edge in the Tauc coordinates is large only for the initial a-Si:H film and the film annealed at 350 °C. The band gap determined from the Tauc law is 1.86 and 1.83 eV, respectively, for these samples. For silicyne the linearity range in Tauc coordinates is strongly limited. At the same time, linearity is observed in a wider photon energy range if Klazes' law

$$\alpha \hbar \omega \propto (\hbar \omega - E_g)^3 \qquad (4)$$

is used for the absorption edge spectrum instead of Eq. (3) (Ref. 6). For comparison, Fig. 3 shows the absorption edge of silicyne in both sets of coordinates. The energy dependence (4) for the absorption edge means that the density of delocalized states is a linear function of the energy near E_c and E_v in such a material. Klazes' law gives $E_g \sim 1.6$ eV. As we can see, the optical band gap of silicyne is approximately 0.20–0.25 eV less than in a-Si:H. Such a value of E_g cannot

be explained by a decrease in E_g as a result of the evaporation of hydrogen from the amorphous hydrogenated silicon during annealing. According to Ref. 4, annealing of a-Si:H at 500 °C decreases E_g by no more than 0.1 eV.

4. CONCLUSIONS AND DISCUSSION

In summary, structural nonuniformities of amorphous hydrogenated silicon strongly influence the process leading to the formation of silicyne during annealing of the silicon. Amorphous silicyne is a semiconductor with a ~ 1.6 eV band gap. It possesses defects that produce localized states in the band gap which are situated ~ 0.25 eV from the Fermi level. As a result, near room temperature conduction occurs by a hopping mechanism, and at 300 K we have $\sigma \sim 10^{-8} \, \Omega^{-1} \cdot cm^{-1}$. The density of delocalized states near the conduction-band bottom and the valence-band top in this material is a linear function of the energy.

Unfortunately, silicyne is now available only in the amorphous state, so that it is still too early to talk about its possible applications. However, if microcrystals of this material can be obtained, then we believe that they will possess unique properties. It can be expected that in the crystalline state this will be a one-dimensional semiconductor with a soliton conduction mechanism and unequalled high charge-carrier mobility. It is also possible that silicyne crystals consisting of linear atomic chains will be able to ''operate'' as a system of quantum wires, which is important for producing nanoelectronics devices.

*)E-Mail:mashin@phys.unn.runnet.ru

[1] A. F. Khokhlov, A. I. Mashin, and D. A. Khokhlov, JETP Lett. **67**, 675 (1998).

[2] Ph. F. Schewe and B. Stein, *The American Institute of Physics Bulletin of Physics News*, No. 388, Sept. 3, 1998.

[3] A. I. Mishin, A. F. Khokhlov, I. V. Kol'chugin *et al.*, Vestn. NNGU, Ser. Fiz. Tverd. Tela, 112 (1998).

[4] *The Physics of Hydrogenated Amorphous Silicon*, edited by J. D. Joannopoulos and G. Lucovsky (Springer-Verlag, New York, 1984; Mir, Moscow, 1987].

[5] J. Tauc, R. Grigorovici, and A. Vancu, Phys. Status Solidi **15**, 627 (1966).

[6] R. H. Klazes, van der M. H. L. M. Brock, J. Bezemer, and S. Radelaar, Philos. Mag. B **25**, 377 (1982).

Translated by M. E. Alferieff

THE PHYSICS OF SEMICONDUCTOR DEVICES

Classification of single-electron devices

I. I. Abramov*) and E. G. Novik

Belorussian State University of Informatics and Radio Electronics, 220027 Minsk, Belorus

A classification based on the principles identified in this paper is proposed for single-electron devices. A large number of currently known nanoelectronic devices of the type considered here can be described on the basis of this classification. This classification can be used to propose new single-electron devices. © *1999 American Institute of Physics.* [S1063-7826(99)02211-5]

1. INTRODUCTION

Structures based on single-electron tunneling (Coulomb blockade)[1] hold promise for the development of a wide spectrum of solid-state devices,[2–4] including a new generation of integrated circuits with a superhigh degree of integration. A large number of structures of the type examined with various configurations intended for various purposes are now known, and the number of publications in this field continues to grow. It is becoming quite difficult to find one's bearing in this field, since a complete classification of devices for single-electron electronics is not available. In view of this circumstance, our objective in this study is to construct a classification of device structures of a single type (single-electron structures), whose operation is based predominantly on the effect noted above. The advantage of the classification is that currently known structures of the type considered can be described using this classification, and it can be used as a basis for proposing new devices for single-electron electronics.

2. PRINCIPLES OF THE CLASSIFICATION

The proposed classification is based on the following principles.

I. The following **classes** of single-electron electronic structures can be distinguished on the basis of the characteristic active regions of the devices.

1) Single-tunneling devices. Such structures contain only one tunnel junction. An example is the single-electron diode,[5] which contains a $p–n$ junction with a degenerate charge-carrier gas, or a single-electron box,[6] where the tunnel junction is connected to the voltage source through a capacitor.

2) Chains of tunnel junctions. This class incorporates structures containing two or more tunnel junctions, connected in series, in the active region. One of the best studied devices in this class is the single-electron transistor.[7–9] It contains two tunnel junctions, separating a very small semiconductor ''island'' from the source and drain regions. Most other currently known single-electron devices belong to

this class: ''pump,''[10,11] modulator,[11,12] single-electron memory,[13] and others.

3) Matrix of tunnel junctions. Structures of this class contain in the active region tunnel junctions, connected in series and parallel, in a plane. An example of such a structure is a granular microbridge.[14]

4) Arrays of tunnel junctions. Such structures contain tunnel junctions, connected in series and parallel, in various dimensions.

A definite number of dimensions can be associated to each class noted above, specifically, single-tunneling devices — zero-dimensional component ($0D$); chains of tunnel junctions — one-dimensional array ($1D$); matrices — two-dimensional components ($2D$); and arrays of tunnel junctions — three-dimensional array of components ($3D$).

II. Each class of structures noted above (with the corresponding number of dimensions) can be represented by a definite type of **fundamental structural scheme.** We shall present the structural schemes of devices belonging to the classes enumerated above.

1) Box (single-tunneling device). The structural scheme of this device corresponds to zero dimensions $0D$ (Fig. 1). An intermediate electrode between a tunnel junction and a gate capacitor appears as an island.

2) A transistor (a chain of tunnel junctions) contains two tunnel junctions connected in series and an island between them. The current through the structure is controlled by means of a gate. Figure 1 shows one variant of the fundamental structural schemes of this device. The corresponding number of dimensions of this scheme is $1D$. Other variants of fundamental structural schemes of the single-electron transistor also exist.[15] These schemes differ by the arrangement of the island and the gate relative to the source and sink and by the configuration of the gate. The island can lie in the plane of the source and sink or above or below this plane. The configuration of the gate can be different. One configuration, often used in single-electron structures, is a split gate.[11] The gate can lie in the plane of the island (to the side of it) and above (below) the island, directly above (below) it or to the side of it. In a real transistor the number of gates can be different, and gates with different configurations and a
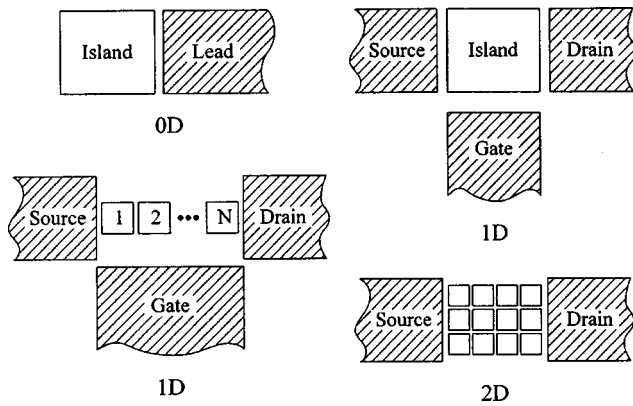
FIG. 1. Fundamental structural diagrams of some single-electron structures.

different arrangement relative to the island can be used in the same device.

3) The fundamental structural scheme for a ''multi-island'' chain of tunnel junctions differs from the transistor scheme by the number of islands (Fig. 1). Just as for a transistor, the arrangement of the islands relative to the source and sink and the configuration, number, and arrangement of gates can be different.[15]

4) Microbridge (matrix of tunnel junctions) — the fundamental structural scheme of this device, shown in Fig. 1, corresponds to $2D$ dimensions. The scheme contains a two-dimensional array of islands. The current through the structure is controlled by a gate located above the islands (the gate is not shown in the diagram).

III. We shall single out conditionally (since single-electron structures usually consist of various materials) the following **types** of single-electron structures according to the materials used for the island (islands).

1) Metal. These incorporate film structures in which the metal islands are separated by tunnel barriers in the form of insulating layers[16–18] or structures based on granular films,[14,19] or structures based on metal colloidal particles[20] and so on. In such structures a three-dimensional electron gas is confined in islands.

2) Semiconductor. An example of such structures are, for example, devices based on the heterostructures GaAs/AlGaAs,[21–24] GaAs with a δ-doped layer,[10,13] AlGaAs/InGaAs/GaAs,[24] and others. In these structures a two-dimensional electron gas (DEG) is confined in small puddles (islands) by various methods: by applying a bias to the gates,[21,22] by electron-beam lithography and etching of the structure,[23] by ion-beam implantation of Ga,[24] and so on. Such structures also include silicon single-electron structures based on a MOS field-effect transistor,[8,25] structures obtained by depositing nanosize silicon crystals,[26] structures prepared on a silicon-on-insulator substrate,[9,27] structures based on δ-doped SiGe,[28] and others.

3) Dielectric. In this case the dielectric islands must be separated by layers with a lower permeability than the island material. No such structures have been facbricated as yet.

4) Organic. An example of such a structure is a transistor based on a film consisting of a mixture of stearic acid and carbonate clusters.[29] The latter appear as islands.

5) Composite. In this case the islands consist of a composite material or various materials. These include structures which do not match with any of the previously identified single-electron structures.

IV. Different **modifications** of single-electron structures can be singled out according to the technological fabrication methods, materials forming the different regions of devices, control electrodes, and other principles. We shall present some of them.

For example, metal single-electron structures can be distinguished according to the technological fabrication process. At present, the following methods are used to obtain such structures: 1) electron-beam lithography (EBL) and sputtering,[16,17] 2) linear self-alignment,[30] 3) oxidation using a scanning tunneling microscope (STM),[18] 4) SECO (step edge cut-off);[31] 5) anodization of junctions fabricated by the EBL method and sputtering,[32] and others.

Semiconductor structures have the following modifications:

Silicon structures based on III–V semiconductors are distinguished according to the materials forming the active region (for example, GaAs structures and others). In turn, among silicon structures the following are distinguished according to the method used to form the active regions: 1) structures obtained in the inversion layer of a silicon MOS double-gate, field-effect transistor;[8,33] 2) structures formed on a silicon-on-insulator substrate using EBO and reactive ionic etching;[9,27,34,35] 3) structures based on nanosize silicon crystals which are obtained by treatment in an rf plasma and which are used as islands,[26] and others.

Various technological methods for producing silicon and single-electron structures based on GaAs are available. They differ mainly by the method used to confine the DEG in the structures, whose small ''puddles'' are used as islands. At present, the following methods of confinement (or formation of single-electron structures based on GaAs) are known: 1) confinement of a two-dimensional electron gas in a GaAs/AlGaAs heterostructure using split Schottky gates;[11,21] 2) EBL and reactive ionic etching of a GaAs/AlGaAs heterostructure for formation of the source, sink, channel, and gate regions;[23] 3) EBL and etching of mesa structures in GaAs/AlGaAs and formation of Schottky gates;[36,37] 4) confinement of a DEG in a δ-doped GaAs by a lateral gate (the contours of the structure are traced by EBL and etching);[13,38] 5) ion-beam implantation of Ga in selectively doped GaAs/AlGaAs and AlGaAs/InGaAs/GaAs heterostructures,[24,39] and so on.

In summary, currently known single-electron device structures can be associated to a definite class, type, and modification. They are characterized by a definite type of fundamental structural scheme (Fig. 1). We shall illustrate this point for specific nanoelectronic devices.

3. SINGLE-ELECTRON DEVICES

A. Metal structures

We shall examine a number of metal single-electron structures. The best studied device of this type at present is the single-electron transistor. As noted above, it belongs to the class of chains of tunnel junctions and corresponds to $1D$
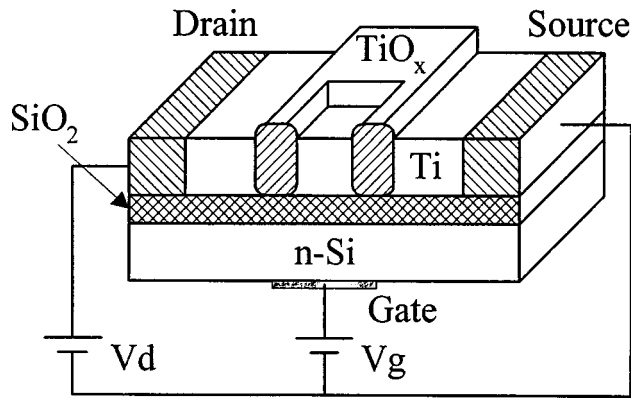
FIG. 2. Transistor fabricated by oxidation using a scanning tunneling microscope.

FIG. 3. Transistor fabricated by the step edge-cutoff method.

(Fig. 1). Metal single-electron transistors (one type of single-electron transistor) can be distinguished by the fabrication method and certain other indicators, which will be described below.

For example, single-electron transistor structures based on Al/AlO$_x$/Al–⟨tunnel junction⟩, fabricated by EBL and sputtering, have been proposed by Zimmerli et al.[16] In addition, the gate configuration in these devices is different: one possesses an interdigital capacitor–gate configuration and the other contains parallel gate and island planes. These structures operate at temperatures near 0.1 K. Another well-known method for fabricating transistors based on Al/ALO$_x$/Al tunnel junctions is the method of linear self-alignment.[30] The basic idea of this method is as follows: Tunnel junctions are formed along the edges of a base electrode (island), which confines one dimension of the junctions by its thickness. Forming a very narrow strip of the base electrode by sputtering and explosive lithography, the second dimension of the tunnel junctions is also low. The source and sink are formed by secondary deposition of a metal layer. The device operates at temperatures up to 1 K.

Metal single-electron transistors based on other materials are known. Figure 2 shows a transistor based on Ti/TiO$_x$/Ti tunnel junctions. It was obtained by oxidation using an STM.[18] After a metal film (Ti) is deposited, the surface of the film is oxidized by anodizing, using the STM tip as the cathode. Such a transistor can operate at room temperature. The structure in Fig. 3 is a transistor structure based on Cr/Cr$_2$O$_3$/Cr tunnel junctions, which is prepared by the step edge cutoff method.[31] The basic idea of the method is that a conducting film of thickness $d1$ is deposited on a preprepared insulating step of thickness $d2$. For $d1 < d2$ the electrodes have no contacts on the step edges, and current flows through the structure by tunneling. The device operates at temperatures near 15 K. All transistor structures described above can also be classified as modifications of film structures.

Besides transistors, multi-island chains belong to the class of chain tunnel junctions. A modification of such structures are devices based on granular films. An example is a structure based on a Au/Al$_2$O$_3$ granular film,[19] obtained by combined deposition of Au and Al$_2$O$_3$ on an Au substrate.
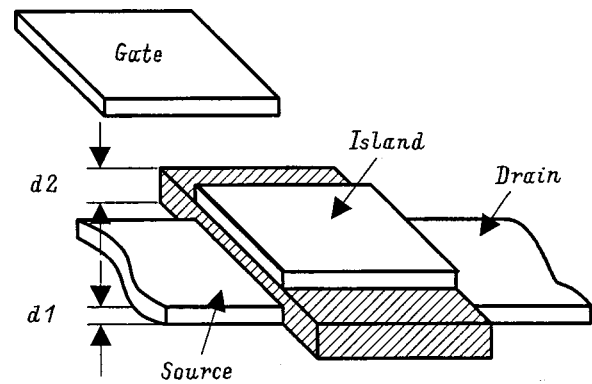
The STM tip is positioned above this film. The electric characteristics of this structure have been measured, and they agree well with the theoretically computed characteristics for a chain of tunnel junctions. Single-electron tunneling in the structure depends largely on the Au content in the film and the position of the STM tip. The structure operates at temperatures up to 77 K. Another example of a device belonging to the class of granular structures is a microbridge based on a granular NbN film (Fig. 4). The dimensions of the film are chosen to be less than the effective size of a charged soliton. As a result, the properties of the electronic conductivity of the structure are quasi-zero-dimensional. The device is fabricated by an ''edge-dependent method'' (edge-defined process).[14] The current through the structure is controlled by means of a gate located above the islands. The microbridge operates at temperatures near 4.2 K. In contrast to previously presented structures, this device belongs to the class of matrix tunnel junctions. Its fundamental structural layout is two-dimensional ($2D$) (Fig. 1).

Another modification of metal single-electron structures are devices based on chains of colloidal gold particles with molecular bonds.[20] These Au particles are the islands and the organic molecules are the binders — tunnel barriers. The Au particles are deposited using an aminosilane adhesive on a substrate with preprepared metal (Au) source, sink, and gate electrodes. Appropriate treatment forms organic molecules which bind the deposited colloidal particles and the source and sink electrodes. Electron transport in such a structure
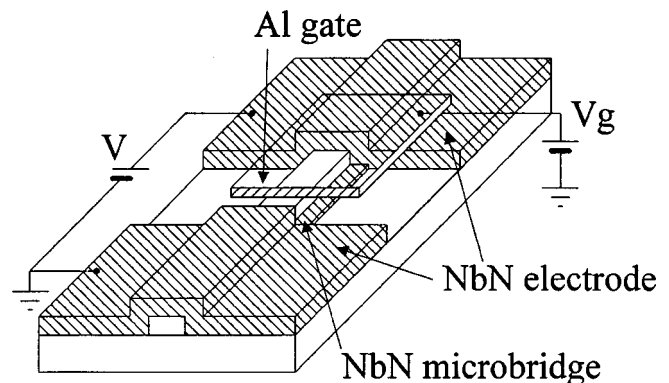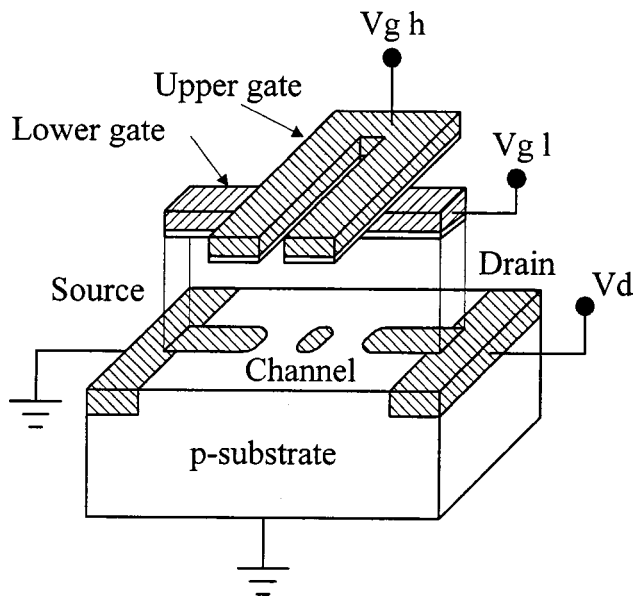

FIG. 4. Microbridge based on a granular NbN film.

FIG. 5. Single-electron transistor formed in the inversion layer of a MOS double-gate field-effect transistor.

FIG. 6. Quantum-dot transistor with a polysilicon gate.

occurs by tunneling of electrons through a chain of colloidal particles. Therefore this device is a multi-island chain and can be described by a 1D fundamental structural scheme (Fig. 1). The device operates at temperatures near 4.2 K, although the current-voltage characteristic remains nonlinear at 77 K.

An interesting method for fabricating metal single-electron structures has been proposed by Park et al.[40] An Ag film was deposited on a substrate with an Sb layer on the surface. Because there is no wetting of this film, small drops of Ag (islands) were formed on the substrate surface. Using an STM, whose tip was positioned above one such island, a ⟨STM tip⟩ — island — substrate structure was obtained. This structure is a double tunnel junction (a particular case of a multi-island chain). Tne I-V characteristic of the structure is sensitive to the horizontal position of the STM tip. Single-electron tunneling in the structure has been observed at room temperature.

B. Semiconductor structures

Let us now examine a number of modifications of semiconductor structures according to their fabrication method.

The silicon single-electron transistors (members of the class of chains of tunnel junctions) are now studied extensively. We shall therefore describe various modifications of this structure. Figure 5 shows a silicon single-electron transistor formed in the inversion layer of a MOS field-effect transistor with a double gate.[8] The bottom and top gates were obtained by the EBL method and dry chemical etching. The bottom gate (positively biased) forms an inversion channel and the top gate (negatively biased) forms potential barriers. The device operates at temperatures near 4.2 K.

Another modification is a quantum-dot transistor (Fig. 6).[9] This device is fabricated on the basis of a silicon-on-insulator structure using EBL and reactive ionic etching. A channel with an island is formed in the top silicon layer of
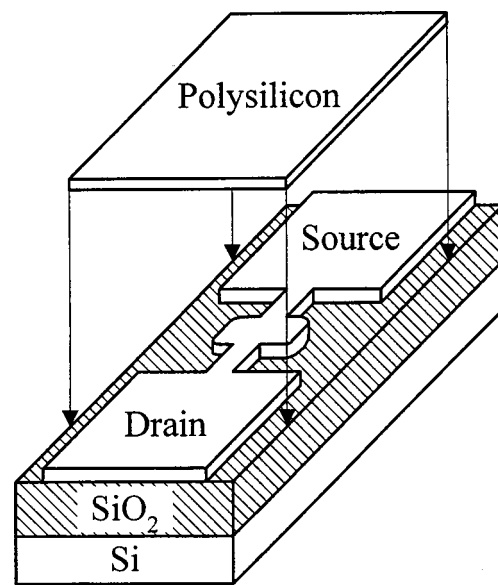
the substrate. In contrast to the preceding device, this transistor has only one polysilicon gate, which is located above the channel. In the tunneling regime, current oscillations are observed in the structure as a function of the gate voltage as a result of two effects: quantum confinement and single-electron tunneling. In addition, quantum-dot transistors with n- and p-type channels have been fabricated. The n-channel transistor operates at temperatures up to 100 K and the p-channel transistor operatures up to 81 K.[41] The realization of such structures opens up new possibilities for producing and using complementary pairs of quantum-dot transistors. Based on the fabrication method this modification includes other devices, for example, single-electron memory.[27,42] The structure of this device is similar to that of the quantum-dot transistor (Fig. 6), so that it also belongs to the class of chains of tunnel junctions. It differs from the transistor by the fact that the island is a quantum-dot floating polysilicon gate. An electron stored on the floating gate screens the channel from the potential on the control gate and shifts the threshold voltage. Different methods are available for obtaining a floating gate: deposition and the second stage of EBL and reactive ionic etching,[27] and the self-alignment method.[42] This device can operate at room temperature. Another example of this modification is a multi-island chain based on a quantum wire with a double lateral gate.[34] Tunnel junctions are formed by formation of depleted regions in a quantum wire by applying voltages to the lateral gates. The device operates at temperatures near 2 K, although nonlinearity on the I-V characteristic is observed up to 46 K.

Structures based on nanosize silicon crystals used as islands can be considered as a modification of silicon devices based on the fabrication method.[26] Nanosize crystals were obtained by treatment in a microwave plasma and are coated with an oxide layer. Next, they were deposited on a structure with preprepared electrodes. The structure is a quasi-one-dimensional chain of tunnel junctions since current flows along the path with the lowest resistance. Single-electron
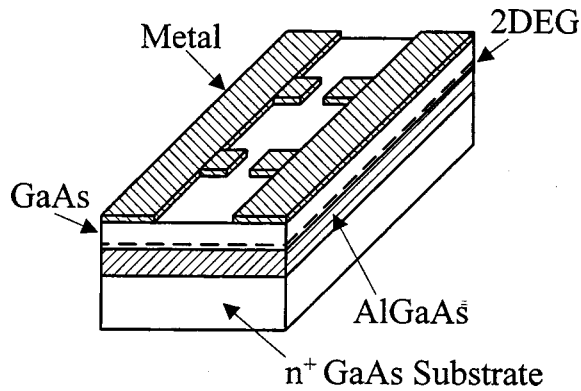
FIG. 7. GaAs/AlGaAs-based structure with a split Schottky gate.

tunneling is observed in the structure at room temperature.

Single-electron semiconductor structures based on GaAs are also being rapidly developed. In such structures the DEG is confined in islands by different methods. A number of modifications of such structures can be singled out by the method used for such confinement. We shall examine them for specific devices.

Figure 7 shows a device which is a double tunnel junction based on a GaAs/AlGaAs heterostructure.[21] In this device the DEG is confined in islands by applying a voltage to the metal split Schottky junctions which are located on the surface of the structure. A DEG is formed at the interface of the GaAs and AlGaAs layers, and its density is controlled by the voltage applied to the conducting substrate. When negative voltages are applied to the split gates, the DEG beneath them becomes depleted. As a result, a channel with small segments (islands) between the depleted sections (barriers) is formed in the DEG.[43,44] The device operates at temperatures near 0.5 K.

Another modification is a GaAs/AlGaAs-heterostructure-based transistor in which the gates, source, sink, island, and channel regions are obtained by EBL and reactive ionic etching of channels in the initial wafer.[23] As a result of this technological process, the DEG is confined in these regions. In contrast to the device presented in Fig. 7, the gates in such a structure lie in the same plane as the source, sink, and island regions (planar gates). The device operates at temperatures near 22 mK.

An example of such structures is a GaAs/AlGaAs-based transistor which is fabricated by the EBL method and liquid chemical etching of a mesa structure and formation of Schottky gates.[36] The DEG is formed at the interface of the GaAs and AlGaAs layers. Planar Schottky barriers are formed by the electrochemical method on the side walls of the channel, obtained by etching, with the DEG. The voltage applied to these gates confines the DEG in the islands. If the electric field in the structure with a split gate (Fig. 7) is applied perpendicular to the DEG, then the horizontal electric field produced by the voltage on a planar Schottky gate acts on the electrons in a direction parallel to the DEG, giving rise to strong confinement of the DEG. The device operates at temperatures up to 20 K.

There exist a number of single-electron structures with a

DEG in δ-doped GaAs wafer.[13,38] In such structures the DEG lies above the δ-doped layer. The contours of the structures (source, sink, gates, and channel) are traced by EBL and etching of a mesa structure in a GaAs wafer with a δ-doped layer. As a result of applying a voltage to the lateral gates, and also because of the presence of impurities and the roughness of the boundary, in the structure the channel with the DEG is divided into a number of islands. Such structures belong to the class of chains of tunnel junctions and can be used to produce single-electron memory. Structures with a DEG in a δ-doped GaAs structure operate at temperatures near 4.2 K.

C. Organic structures

An example of an organic structure is a transistor based on a film consisting of a mixture of stearic acid and carbonate clusters, which are the islands.[29] A device has been fabricated as follows. A mixed film of stearic acid with inclusions of carbonate clusters was deposited on an atomically smooth surface of graphite with a preformed control electrode. The electrode consisting of thin bilayered strips (Au layer on Al_2O_3) was formed by electronic nanolithography. The characteristics of such a structure were investigated using an STM, whose tip was positioned above the clusters. Single-electron tunneling is observed in the device at room temperature.

4. CONCLUSIONS

Several single-electron devices have been omitted in this paper because of their great diversity[45,46] and because of space limitations. Some of them operate on the basis of not only single-electron tunneling but also other transport mechanisms[47–49] (mixed-type device structures), including quantum interference,[50] for example, quantum interferometers based on split Aharonov–Bohm rings with a quantum dot in one arm.[51,52] Structures that can be classified as functionally integrated components or very simple integrated circuits have recently appeared,[53,54] but they cannot be classified according to the principles presented in this paper.

In summary, a classification of device nanoelectronics structures of a single type, which are based on the principles identified in this paper, has been proposed. A large number of existing nanoelectronic devices of the type considered here can be described on the basis of this classification. New single-electron devices can also be proposed on the basis of this classification.

*⁾E-mail: device@micro.rei.minsk.by

[1] D. V. Averin and K. K. Likharev, Zh. Éksp. Teor. Fiz. **90**, 733 (1986) [Sov. Phys. JETP **63**, 427 (1986)].

[2] *Single Charge Tunneling: Coulomb Blockade Phenomena in Nanostructures*, edited by H. Grabert and M. H. Devoret (NATO ASI Series B: Physics, Plenum, N. Y., 1992, Vol. 294).

[3] *Special Issue on Single Charge Tunneling*, edited by H. Grabert, Z. Physik B **85**, 3 (1991).

[4] Zh. I. Alferov, Fiz. Tekh. Poluprovodn. **32**, 3 (1998) [Semiconductors **32**, 1 (1998)].

[5] W. H. Richardson, Appl. Phys. Lett. **71**, 1113 (1997).

[6] P. Lafarge, H. Pothier, E. R. Williams, D. Esteve, C. Urbina, and M. H. Devoret, Z. Phys. B: Condens. Matter **85**, 327 (1991).

[7] K. K. Likharev, IEEE Trans. Magn. **23**, 1142 (1987).

[8] H. Matsuoka and S. Kimura, Appl. Phys. Lett. **66**, 613 (1995).

[9] E. Leobandung, L. Guo, Y. Wang, and S. Y. Chou, Appl. Phys. Lett. **67**, 938 (1995).

[10] K. Tsukagoshi and K. Nakazato, Appl. Phys. Lett. **71**, 3138 (1997).

[11] L. P. Kouwenhoven, A. T. Johnson, and N. C. van der Vaart, A. van der Enden, C. J. P. M. Harmans, C. T. Foxon, Z. Phys. B: Condens. Matter **85**, 381 (1991).

[12] L. J. Geerligs, V. F. Anderegg, P. A. M. Holweg, J. E. Mooij, H. Pothier, D. Esteve, C. Urbina, and M. H. Devoret, Phys. Rev. Lett. **64**, 2691 (1990).

[13] K. Nakazato, R. J. Blaikie, and H. Ahmed, J. Appl. Phys. **75**, 5123 (1994).

[14] N. Miura, N. Yoshikawa, and M. Sugahara, Appl. Phys. Lett. **67**, 3969 (1995).

[15] I. I. Abramov and E. G. Novik, Izv. Belorus. Inzh. Akad., No. 2 (6)/2, 4 (1998).

[16] G. Zimmerli, R. L. Kautz, and J. M. Martinis, Appl. Phys. Lett. **61**, 2616 (1992).

[17] T. A. Fulton and G. J. Dolan, Phys. Rev. Lett. **59**, 109 (1987).

[18] K. Matsumoto, M. Ishii, K. Segawa, Y. Oka, B. J. Vartanian, and J. S. Harris, Appl. Phys. Lett. **68**, 34 (1996).

[19] E. Bar-Sadeh, Y. Goldstein, C. Zhang, H. Deng, B. Abeles, and O. Millo, Phys. Rev. B **50**, 8961 (1994).

[20] T. Sato, H. Ahmed, D. Brown, and B. F. G. Johnson, J. Appl. Phys. **82**, 696 (1997).

[21] U. Meirav, M. A. Kastner, and S. J. Wind, Phys. Rev. Lett. **65**, 771 (1990).

[22] Y. Wang and S. Y. Chou, Appl. Phys. Lett. **63**, 2257 (1993).

[23] H. Pothier, J. Weis, R. J. Haug, and K. v. Klitzing, Appl. Phys. Lett. **62**, 3174 (1993).

[24] T. Fujisawa and S. Tarucha, Appl. Phys. Lett. **68**, 526 (1996).

[25] A. Ohata, A. Toriumi, and K. Uchida, Jpn. J. Appl. Phys. **36**, 1686 (1997).

[26] A. Dutta, M. Kimura, Y. Honda, M. Otobe, A. Itoh, and S. Oda, Jpn. J. Appl. Phys. **36**, 4038 (1997).

[27] L. Guo, E. Leobandung, and S. Y. Chou, Appl. Phys. Lett. **70**, 850 (1997).

[28] D. J. Paul, J. R. A. Cleaver, H. Ahmed, and T. E. Whall, Appl. Phys. Lett. **63**, 631 (1993).

[29] E. S. Soldatov, V. V. Khanin, A. S. Trifonov, S. P. Gubin, V. V. Kolesov, D. E. Presnov, S. A. Yakovenko, and G. B. Khomutov, JETP Lett. **64**, 556 (1996).

[30] M. Götz, K. Blüthner, W. Krech, A. Nowack, H.-J. Fuchs, E.-B. Kley, P. Thieme, Th. Wagner, G. Eska, K. Hecker, and H. Hegger, J. Appl. Phys. **78**, 5499 (1995).

[31] S. Altmeyer, B. Spangenberg, and H. Kurz, Appl. Phys. Lett. **67**, 569 (1995).

[32] Y. Nakamura, D. L. Klein, and J. S. Tsai, Appl. Phys. Lett. **68**, 275 (1996).

[33] H. Matsuoka, T. Ichiguchi, T. Yoshimura, and E. Takeda, Appl. Phys. Lett. **64**, 586 (1994).

[34] R. A. Smith and H. Ahmed, J. Appl. Phys. **81**, 2699 (1997).

[35] D. Ali and H. Ahmed, Appl. Phys. Lett. **64**, 2119 (1994).

[36] K. Jinushi, H. Okada, T. Hashizume, and H. Hasegawa, Jpn. J. Appl. Phys. **35**, 1132 (1996).

[37] Y. Nagamune, H. Sakaki, L. P. Kouwenhoven, L. C. Mur, C. J. P. M. Harmans, J. Motohisa, and H. Noge, Appl. Phys. Lett. **64**, 2379 (1994).

[38] K. Nakazato, T. J. Thornton, J. White, and H. Ahmed, Appl. Phys. Lett. **61**, 3145 (1992).

[39] T. Fujisawa, Y. Hirayama, and S. Tarucha, Appl. Phys. Lett. **64**, 2250 (1994).

[40] K.-H. Park, J. S. Ha, W. S. Yun, M. Shin, K.-W. Park, and E.-H. Lee, Appl. Phys. Lett. **71**, 1469 (1997).

[41] E. Leobandung, L. Guo, and S. Y. Chou, Appl. Phys. Lett. **67**, 2338 (1995).

[42] A. Nakajima, T. Futatsugi, K. Kosemura, T. Fukano, and N. Yokoyama, Appl. Phys. Lett. **70**, 1742 (1997).

[43] C. H. Crouch, C. Livermore, R. M. Westervelt, K. L. Campman, and A. C. Gossard, Appl. Phys. Lett. **71**, 817 (1997).

[44] R. H. Blick, R. J. Haug, J. Weis, D. Pfannkuche, K. v. Klitzing, and K. Eberl, Phys. Rev. B **53**, 7899 (1996).

[45] *Special Issue, Scanning Tunneling Microscopy*, edited by S. Hosok *et al.*, Jpn. J. Appl. Phys. **36**, Part 1, No 6B (1997).

[46] U. Meirav and E. B. Foxman, Semicond. Sci. Technol. **10**, 255 (1995).

[47] D. V. Averin, A. N. Korotkov, and K. K. Likharev, Phys. Rev. B **44**, 6199 (1991).

[48] T. Hiramoto, H. Ishikuro, T. Fujii, G. Hashiguchi, and T. Ikoma, Jpn. J. Appl. Phys. **36**, 4139 (1997).

[49] K. Yano, T. Ishii, T. Hashimoto, T. Kobayashi, F. Murai, and K. Seki, Appl. Phys. Lett. **67**, 828 (1995).

[50] T. J. Thornton, Rep. Prog. Phys. **57**, 311 (1994).

[51] A. Yacoby, M. Heiblum, D. Mahalu, and H. Shtrikman, Phys. Rev. Lett. **74**, 4047 (1995).

[52] E. Buks, R. Schuster, M. Heiblum, D. Mahalu, V. Umansky, and H. Shtrikman, Phys. Rev. Lett. **77**, 4664 (1996).

[53] A. Fujwara, Y. Takahashi, K. Murase, and M. Tabe, Appl. Phys. Lett. **67**, 2957 (1995).

[54] F. Hofman, T. Heinzel, D. A. Wharam, J. P. Kotthaus, G. Böhm, W. Klein, G. Tränkle, and G. Weimann, Phys. Rev. B **51**, 13 872 (1995).

Temperature dependence of the gain of lasers based on quantum-dot arrays with an inhomogeneously broadened density of states

A. E. Zhukov,*) A. R. Kovsh, and V. M. Ustinov

A. F. Ioffe Physicotechnical Institute, Russian Academy of Sciences, 194021 St. Petersburg, Russia
(Submitted May 12, 1999; accepted for publication May 19, 1999)
Fiz. Tekh. Poluprovodn. **33**, 1395–1400 (November 1999)

A model making it possible to describe analytically the temperature dependence of the optical gain and threshold current density in lasers based on quantum-dot arrays characterized by inhomogeneous broadening of the density of states is proposed. At high temperatures the dependence obtained is universal, i.e., it is determined exclusively by the broadening of the density of states, not by its specific form. © *1999 American Institute of Physics.*
[S1063-7826(99)02311-X]

A quantum dot (QD) is a center of zero-dimensional localization of charge carriers. In the ideal case, all QDs of an array can be characterized by a single, identical, size-well level. Thus the total density of states (TDS) of such an array, ignoring the homogeneous broadening, is a δ function. Used as the active region of an injection laser, such an array makes it possible, theoretically,[1] to lower substantially the threshold current density. For a δ-like TDS the relation between the current J and the gain G is given by the simple expression[2]

$$G = G^{\mathrm{sat}}\left(\frac{J-J_0}{J_0}\right), \tag{1}$$

where G^{sat} is the saturated (maximum possible) gain, J_0 is the transmission current, given by

$$J_0 = \frac{eN}{2\tau}, \tag{2}$$

τ is the radiative (spontaneous) recombination time, e is the electron charge, and $N = sN_{QD}$ is the total density of excitonic states, which is related to the density N_{QD} of the QD array and the degree of degeneracy s of the level equal to 2 for spin degeneracy.

The current–gain characteristic and hence the threshold current density in such a laser do not depend on temperature.

One of the most promising methods for producing real QD arrays for use in lasers is to make use of spontaneous self-organization at the initial stages of deposition of strained films.[3] In particular, lasers with threshold current densities less than $100\,\mathrm{A/cm^2}$ have been produced on the basis of self-organized In(Ga)As QDs in a (Al)GaAs host,[4] and continuous-wave lasing has been obtained with an initial power level greater than 3 W.[5]

The fundamental difference that distinguishes the array of self-organized QDs from the ideal case is the inhomogeneous broadening of the TDS due to dot-size variance. The TDS, therefore, cannot be described by a δ function, which means that Eqs. (1) and (2) are no longer applicable and that the current–gain relation now, in general, depends on temperature. Ordinarily, it is assumed that the main reason for the temperature dependence of the threshold current density in lasers based on self-organized QDs is the thermal filling of higher-lying states with carriers, including states of the wetting layer and host.[4] However, the higher energy levels of the QD array itself, which are due to smaller dots, can also served as a ''reservoir'' for transfer of carriers from QD states that participate in lasing. Indeed, a temperature dependence of the threshold characteristics can be observed even when the ground state of a QD is very strongly localized with respect to the host [QD lasers emitting at 1.3 μm (Ref. 6)].

In view of this circumstance, the question of an adequate description of the temperature dependence of the gain characteristics in lasers with an inhomogeneously broadened density of states becomes legitimate. This task is complicated by the fact that the exact TDS for a QD array is unknown. In the present paper we develop such a model of lasing from first principles. The results which we obtained can be used to relate in analytic form the gain and the current and plot them as a function of temperature. In addition, as will be shown below, at sufficiently high temperatures this dependence is universal, i.e., it does not depend on the specific form of the TDS of the QD array.

We assume that the carrier distribution over states within the TDS of arbitrary form $P(E)$ is described by the Fermi function

$$f(E,F) = \frac{1}{1 + \exp\left(\dfrac{E-F}{k_B T}\right)}, \tag{3}$$

where F is the quasi-equilibrium Fermi level. As a simplification, we shall examine a TDS which is symmetric with respect to the center of the band gap and we shall assume τ to be independent of the QD size. For correlated (excitonic) electron and hole trapping in QDs,[7] the radiative-recombination (spontaneous) current and the optical gain can be expressed, respectively, as

$$J(F) = \frac{e}{\tau}\int P(E)f(E,F)dE, \tag{4a}$$

$$G(F) = \mathrm{const} \cdot \max[(2f(E,F)-1)P(E)]. \tag{4b}$$

It is obvious that since the number of states that can participate in radiative recombination is limited by the finite density of the QD array, there exists a most likely value of the current in the spontaneous regime, equal to $2J_0$ [since $\int P(E)dE=N$] and a greatest (saturated) value of the gain $G^{sat}=$ const $\cdot P(E_0)$, where E_0 is the energy corresponding to the largest value of the TDS.

It is convenient to switch to dimensionless energy ($E\to\varepsilon=E-E_0/\sigma$; $F\to\varphi=F-E_0/\sigma$, where σ is the half-width of the TDS), temperature ($T\to t=k_BT/\sigma$), density of states $[P(E)\to\rho(\varepsilon)=\sigma P(\varepsilon)/N]$, current $[J(E)\to j(\varphi)=J(\varphi)/J_0]$, and gain $[G(F)\to g(\varphi)=G(\varphi)/g^{sat}]$. We can then write Eq. (4) in the form

$$j(\varphi,t)=2\int f(\varepsilon,\varphi,t)\rho(\varepsilon)d\varepsilon, \tag{5a}$$

$$g(\varphi,t)=\max[(2f(\varepsilon,\varphi,t)-1)\rho(\varepsilon)/\rho_0], \tag{5b}$$

where $\rho_0=\rho(0)$ corresponds to the value of the TDS at the maximum point.

These equations describe parametrically the current dependence of the gain $g(j)$ for a TDS function $\rho(\varepsilon)$ at a reduced temperature t.

Before seeking the temperature dependence of $g(j)$, we shall examine the limits corresponding to zero and infinite temperatures. In the first case, where the Fermi function is a step function,

$$j(\varphi)=2\int_{-\infty}^{\varphi}\rho(\varepsilon)d\varepsilon, \tag{6a}$$

$$g(\varphi)=\rho(\varphi)/\rho_0. \tag{6b}$$

It is obvious that in this case $g(j)$ is directly determined by the specific form of the function $\rho(\epsilon)$, i.e., it depends on the form of the density of states. In particular, it can be shown that for the TDS shown in Fig. 1 and described by Gaussian, Lorentzian, or parabolic functions (the values of ρ_0 correspond to the TDS normalization condition $\int\rho(\varepsilon)d\varepsilon=1$)

$$\rho(\varepsilon)=(1/\sqrt{\pi})\exp(-\varepsilon^2), \tag{7a}$$

$$\rho(\varepsilon)=\frac{1/\pi}{1+\varepsilon^2}, \tag{7b}$$

$$\rho(\varepsilon)=3/4(1-\varepsilon^2), \tag{7c}$$

the relation between the current and the gain has the form

$$j(g)^{gaussian}=2\Phi^*(-\sqrt{2\ln(1/g)}) \tag{8a}$$

where $\Phi^*(x)=\dfrac{1}{\sqrt{2\pi}}\int_{-\infty}^{x}\exp(-\varepsilon^2/2)d\varepsilon$ is the normal distribution function,

$$g(j)^{lorenzian}=\sin^2(\pi j/2), \tag{8b}$$

$$j(g)^{parabolic}=1-(1+g/2)\sqrt{1-g}. \tag{8c}$$

Plots of the corresponding functions are shown in Fig. 1b. We see that, as expected, these dependences differ substantially from the various TDS. A general property is the
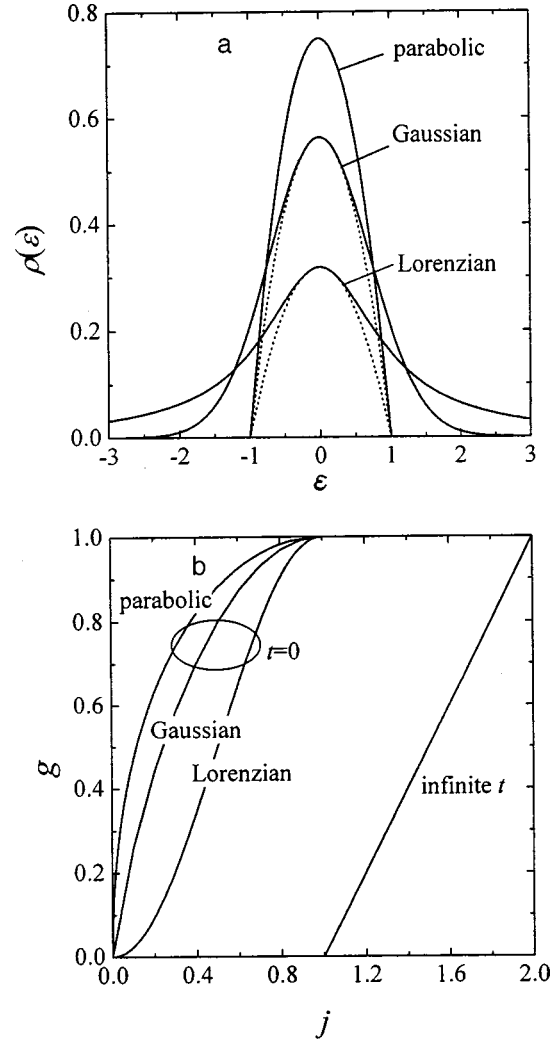

FIG. 1. a — Gaussian, Lorentzian, or parabolic density of states of a QD array (the dashed lines show the parabolic approximation); b — gain versus the pump current with zero and infinite temperatures for TDS shown in *a*.

actual absence of a transmission current, i.e., for an arbitrarily low current there exists a definite group of QDs for which the gain is positive.

In the limit of infinite temperature the Fermi function is the same within the TDS $[f(\varepsilon,\varphi.t\to\infty)\equiv f]$, and the maximum gain is reached at the maximum of the density of states. Therefore, $j=2f$, $g=2f-1$, and the relation between the ''reduced'' gain and current has the form

$$g=j-1, \tag{9}$$

which is similar to the expression (1) in dimensionless values.

Thus, the current dependence of the gain in a laser based on a QD array is different for the two limiting temperatures. In addition, at infinite temperature it is the same for any function $\rho(\varepsilon)$ describing the TDS and differs strongly in the limit of zero temperature. Therefore, it is pointless to seek the function $g(j)$ in the limit of low temperatures, since this relation is not universal (it depends on the form of the TDS, which, in general, is unknown). In addition, at low temperatures carrier transfer between different QDs, which estab-

lishes a global equilibrium within an ensemble of QDs, is suppressed, which results in nonequilibrium filling of the QD states by carriers that is not described by Fermi statistics.

We shall therefore consider a high but finite temperature. It can be assumed that the function $g(j)$ is the same for all TDS, and that it takes on the form of (9) in the limit $T \to \infty$. The requirement $k_B T \gg \sigma$ ($t \gg 1$) is too stringent and indefinite. How high the temperature must be will be clarified in the analysis below.

We note that the exact form of the TDS of a QD array is unknown, and since it is determined mainly by the QD-size variance, in general, it depends on the deposition conditions. To examine the characteristics of QD lasers, the function $\rho(\varepsilon)$ is usually approximated by functions of the form (7a) or (7b).[8] In contrast, we shall examine as the basic TDS the parabolic function (7c). Virtually any function $\rho(\varepsilon)$ [including a function of the form (7a) and (7b)] can be approximately represented in the form (7c) by expanding it in a Taylor series near the maximum (see Fig. 1a). On the other hand, this greatly simplifies the mathematical transformations. The validity of such a substitution will be discussed below.

To obtain results in an analytic form we shall employ the piecewise-linear approximation of the Fermi function

$$f(\varepsilon,\varphi,t) \approx 1, \quad \varepsilon < \varphi - 2t;$$

$$1/2 - (\varepsilon - \varphi)/4t, \quad \varphi - 2t < \varepsilon < \varphi + 2t;$$

$$0, \quad \varepsilon > \varphi + 2t. \tag{10}$$

Assuming the temperature to be sufficiently high ($t > 1/2$) and using Eq. (5), we can then write the expressions for the current and gain in the form

$$j(\varphi,t) \approx (3/2) \int_{-1}^{1} (1-\varepsilon^2)\left(1/2 - \frac{\varepsilon-\varphi}{4t}\right) d\varepsilon = 1 + \varphi/2t, \tag{11a}$$

$$g(\varphi,t) \approx \max\left[(1-\varepsilon^2)\left(\frac{\varphi-\varepsilon}{2t}\right)\right] \approx \left[(1-\varepsilon^2)\right.$$
$$\left.\times\left(\frac{\varphi-\varepsilon}{2t}\right)\right]_{\varepsilon \approx (-1/2)\varphi} \approx \frac{1}{2t}\left(\varphi + \frac{1}{4\varphi}\right). \tag{11b}$$

Using the relation (11a) between j and φ, we obtain the definitive expression for the current dependence of the gain at high temperatures,

$$g(j,t) \approx (j-1) + \frac{1}{16t^2(j-1)}. \tag{12}$$

As one can see, the expression (12) transforms into the expression (9) as t approaches infinity. Plots of this dependence at various temperatures are shown in Fig. 2a. The lowest current for which the expression (12) is approximately valid corresponds to $1 + 1/2t$, since in deriving it we assumed that $\varphi \approx 2t(j-1)$ is large. Physically this means that the expression (12) describes well the temperature-dependent relation between the gain and the current, when the Fermi level is sufficiently high. The maximum gain in this case is attained in the region of the TDS close to the maximum,
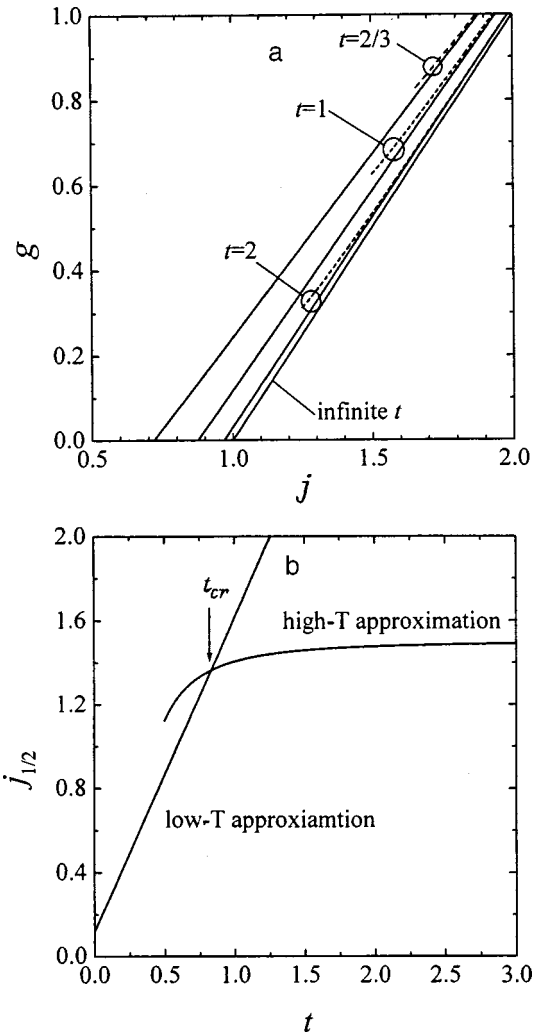

FIG. 2. a — Gain plotted as a function of the current for various temperatures in the approximation described by Eq. (12) (dashed lines) and in an approximation using a temperature-dependent differential gain and transmission current (14) (solid lines). b — Temperature dependence of the current, corresponding to gain $g = 1/2$, obtained in the high- and low-temperature (for a parabolic TDS) approximations. The arrow shows the critical temperature.

where virtually any TDS can be approximated by a convex parabola. In particular, it can be shown that for a Lorentzian TDS the function $g(j)$ at high temperatures also satisfies Eq. (12) if the terms on the order of $1/t^n$ with powers greater than $n = 2$ are disregarded. (In general, as $g \to 1$, the higher-lying excited states of both the QD and the states of the wetting layer and host play an increasingly larger role. A fairly comprehensive study of their influence is given in Ref. 2).

On the other hand, for low gains ($g \to 0$) the function $g(j)$ is determined primarily by the contribution of the "tail" of the TDS, which is not described by a parabolic approximation and, in general, is different for different TDS. But the relation between the gain and the current in this regime has virtually no effect on the device characteristics since nonzero internal losses exist even in laser diodes with four cleaved faces.

In summary, the best correspondence between the function (12) and the real function $g(j)$ is obtained for $g \approx 1$. Let

us expand the function (12) in a Taylor series in powers of $j - j_1$, so that $g(j_1) = 1$:

$$j_1 \approx 2 - \frac{1}{16t^2}, \tag{13a}$$

$$g(j) \approx 1 + (j - j_1) \frac{dg}{dj}\bigg|_{j = j_1}$$

$$\approx \left(1 - \frac{1}{16t^2}\right)\left[j - \left(2 - \frac{1}{16t^2}\right)\right] + 1. \tag{13b}$$

It is more convenient to explain this result in terms of a temperature-dependent transmission current j_{tr} and differential gain a:

$$g(j,t) = a(t)(j - j_{tr}(t)), \tag{14a}$$

$$a(t) \approx 1 - \frac{1}{16t^2}, \tag{14b}$$

$$j_{tr}(t) \approx 1 - \frac{1}{8t^2}. \tag{14c}$$

The current dependences of the gain described by Eqs. (14) are also shown in Fig. 2a for several temperatures. As the temperature is raised, the transmission current increases as a result of the "broadening" of the Fermi function; i.e., an increasingly larger number of higher-lying states (due to smaller QDs) becomes populated. At infinite temperature the transmission is 1; i.e. half of the states of a QD ensemble must be populated to achieve inversion, consistent with the expression (2).

The increase in the differential gain seems paradoxical, but it is easily explained since the total number of QD states is limited (we do not consider the higher-lying states), and hence the maximum current that can flow in the spontaneous recombination regime through the QD array is also limited. At high temperatures a large number of states is already populated (and hence the current is relatively high) to reach even a small gain. For further increase in gain the current can increase only negligibly since the number of unfilled states is small.

To estimate the lower temperature limit of applicability of the "high-temperature" approach presented above, we shall examine the current dependence of the gain at low temperatures for a parabolic TDS. [Again we note that as $t \to 0$, this function $g(j)$ will depend on the specific form of the TDS.] It is easy to show that the relationship between the current and the position of the Fermi level, described by Eq. (6a), remains valid if the terms with powers greater than t are disregarded and the expression for the gain [Eq. (5b)] becomes

$$g(\varphi,t) \approx \frac{1}{\rho_0}\left(\rho(\varphi) - 2t\frac{d\rho}{d\varepsilon}\bigg|_{\varepsilon = \varphi}\right). \tag{15}$$

In other words, the maximum gain is reached at an energy that is shifted by an amount on the order of $2t$ from the maximum of the TDS.
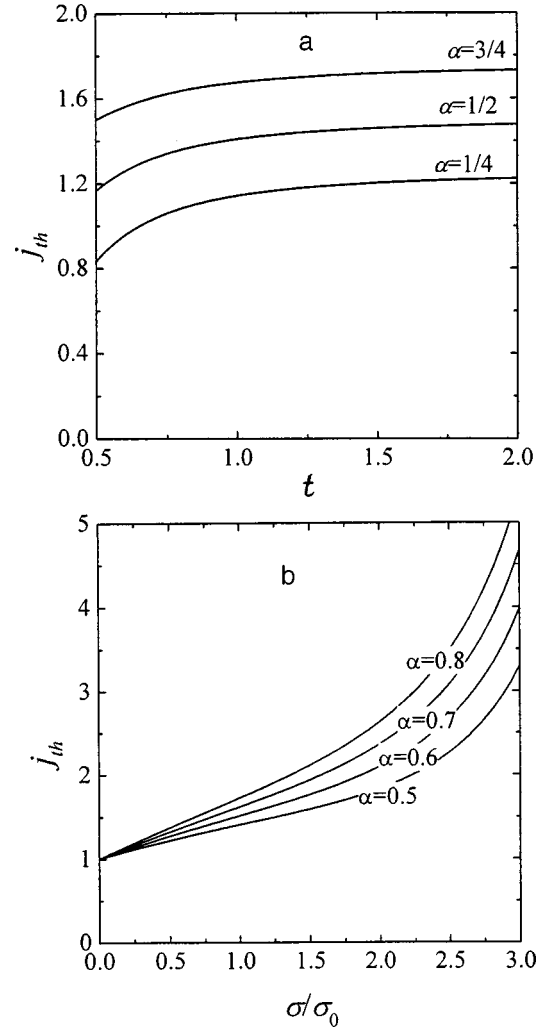

FIG. 3. Threshold current density versus the temperature (a) and versus the broadening of the density of states (b) for various values of the losses α.

For a parabolic TDS the temperature-dependent relation between the gain and the current is established in the form

$$j(g)^{\text{parabolic}} = 1 - \left[1 + g/2 - 3t\left(\frac{1}{\sqrt{1-g}} - \sqrt{1-g}\right)\right]\sqrt{1-g}. \tag{16}$$

It is evident that the relation (16) possesses the limit (8c) as $t \to 0$. For simplification, we assumed that $1 - g$ is large compared with t^2, so that we did not consider high gains (close to 1).

Let us consider the temperature dependence of the current corresponding to one-half gain, $g(j_{1/2}) = 1/2$. It is shown in Fig. 2b; it was calculated in both the high-temperature approximation [expression (14a)] and the low-temperature approximation [expression (16)]. The value $g = 1/2$ was chosen so as to make the most accurate comparison since the expression (14) works poorly in the limit $g \to 0$ and the expression (16) works poorly in the limit $g \to 1$. It is evident from Fig. 2b that both dependences intersect at a certain critical temperature $t_{cr} \approx 1$. It is obvious that this temperature

$T_{cr} \approx \sigma/k_B$ is the lower temperature limit up to which the expression (14) approximately describes the relation between the gain and the current.

In conclusion, we note that the typical values of the broadening of the density of states of arrays of self-organized QDs, which were determined according to the widths of the photo- and electroluminescence lines, lie in the range $2\sigma \approx 40 - 60$ meV. Therefore, T_{cr} is near room temperature, and the expression (14) is used to determine the temperature dependence of the threshold current density in the range that is important for practical applications. The threshold current density j_{th} (scaled to J_0) as a function of temperature is shown in Fig. 3a for various values of the threshold gain (in units of G^{sat}). It is evident that the existence of inhomogeneous broadening of the density of states of the QD array gives rise to an appreciable temperature dependence of the threshold in a QD laser.

If the temperature is fixed, then the expression (14) also makes it possible to estimate the effect of the broadening of the TDS on the threshold characteristics:

$$j_{th} = \frac{\sigma/\sigma_0}{\alpha(\sigma)} \alpha + j_{tr}(\sigma). \tag{17}$$

Here the total threshold losses α are expressed as fractions of the saturated gain which characterizes a QD array with broadening $\sigma_0 = k_B T$. The fact that the saturated gain G^{sat} itself is inversely proportional to σ is taken into account. Figure 3b shows the threshold current density versus σ for various losses α. It is evident that the threshold current density can be greatly decreased by decreasing σ, i.e., by forming more uniform QD arrays. We note that the limit is the value of σ, which is determined only by the homogeneous broadening associated with the finite exciton lifetime at the QD level.

In summary, we have studied the temperature dependence of the optical gain in lasers based on arrays of quantum dots with an inhomogeneously broadened density of states, such as lasers with self-organized QDs. We showed that at low temperatures the relation between the gain and the current is determined by the form of the function describing the density of states, while at high temperatures this dependence is universal in the sense that it is determined only by the broadening and not by the specific form of the density of states. This made it possible to describe analytically the temperature-dependent relation between the gain and the current (the threshold current density and threshold losses) at high temperatures and to estimate the limits of applicability of this model.

*)E-mail: zhukov@beam.ioffe.rssi.ru

[1] M. Asada, Y. Miyamoto, and Y. Suematsu, IEEE J. Quantum Electron. **QE-22**, 1915 (1986).

[2] A. R. Kovsh, A. E. Zhukov, A. Yu. Egorov, V. M. Ustinov, N. N. Ledentsov, M. V. Maksimov, A. F. Tsatsul'nikov, and P. S. Kop'ev, Fiz. Tekh. Poluprovodn. **33**, 215 (1999) [Semiconductors **33**, 184 (1999)].

[3] L. Goldstein, F. Glas, J. Y. Marzin, M. N. Charasse, and G. Le Roux, Appl. Phys. Lett. **47**, 1099 (1985).

[4] A. E. Zhukov, V. M. Ustinov, A. Yu. Egorov, A. R. Kovsh, A. F. Tsatsul'nikov, M. V. Maximov, N. N. Ledentsov, S. V. Zaitsev, N. Yu. Gordeev, V. I. Kopchatov, Y. M. Shernyakov, P. S. Kop'ev, D. Bimberg, and Zh. I. Alferov, J. Electron. Mater. **27**, 106 (1998).

[5] A. R. Kovsh, D. A. Lifshitz, A. E. Zhukov, A. Yu. Egorov, M. V. Maksimov, V. M. Ustinov, I. S. Tarasov, N. N. Ledentsov, P. S. Kop'ev, Zh. E. Alferov, and D. Bimberg, JETP Lett. (in press).

[6] A. E. Zhukov, A. R. Kovsh, N. A. Maleev, S. S. Mikhrin, V. M. Ustinov, A. F. Tsatsul'nikov, M. V. Maximov, B. V. Volovik, D. A. Bedarev, Yu. M. Shernyakov, P. S. Kop'ev, Zh. I. Alferov, N. N. Ledentsov, and D. Bimberg, Appl. Phys. Lett. (submitted).

[7] R. Heitz, M. Grundmann, N. N. Ledentsov, L. Eckey, M. Veit, D. Bimberg, V. M. Ustinov, A. Yu. Egorov, A. E. Zhukov, P. S. Kop'ev, and Zh. I. Alferov, Surf. Sci. **361/362**, 770 (1996).

[8] L. V. Asryan and R. A. Suris, Semicond. Sci. Technol. **11**, 554 (1996).

Translated by M. E. Alferieff